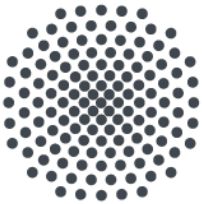

Nonlinear Dynamics of and Coherent Raman Imaging with Fiber-feedback Optical Parametric Oscillators

Von der Fakultät Mathematik und Physik der Universität Stuttgart
zur Erlangung der Würde eines Doktors der
Naturwissenschaften (Dr. rer. nat.) genehmigte Abhandlung

vorgelegt von

Moritz Flöß

aus Offenburg

Hauptberichter:	Prof. Dr. Harald Giessen
Mitberichter:	Prof. Dr. Peter Michler
Prüfungsvorsitzender:	Prof. Dr. Christian Holm

Tag der mündlichen Prüfung: 28.02.2024

4. Physikalisches Institut der Universität Stuttgart
2024

Moritz Flöß: *Nonlinear Dynamics of and Coherent Raman Imaging with Fiber-feedback Optical Parametric Oscillators*
2024

ABSTRACT

Nonlinear parametric frequency conversion is a widely used approach to provide coherent laser radiation with tunable wavelength output required for many spectroscopic applications, such as coherent RAMAN scattering spectroscopy, scanning near-field optical microscopy, or photoacoustic spectroscopy. Optical parametric oscillators form the core of such frequency conversion units. In particular, fiber-feedback optical parametric oscillators (FFOPO) offer superior performance in terms of wavelength stability, intenstity noise, as well as a small footprint, and low cost.

However, its stability depends on the precise control of the operational parameters. Therefore, it is important to understand the interplay of the linear and nonlinear effects governing the temporal and spectral dynamics of this system. This thesis provides an in-depth analysis of the nonlinear ultrafast transient dynamics in a femtosecond FFOPO system, establishing the groundwork for the implementation of additional functionalities. We provide insight into the spectral pulse evolution during the transient process on the timescale of individual resonator roundtrips. Moreover, the wavelength and pulse-to-pulse stability depending on the operational parameters and the intra-cavity dispersion regime are investigated in detail, demonstrating how to efficiently stabilize such a system.

Furthermore, we demonstrate how the nonlinear properties of this light source can be exploited to further extend its range of applications. First, we take advantage of the ultrafast signal buildup and realize burst-mode operation with the FFOPO system with burst rates ranging from DC all the way up to 5 MHz. Moreover, this system enables arbitrary pulse sequence generation with tunable wavelength output. These characteristics may find application in material processing, where the reduction of the average optical power is desired, while maintaining a high peak power level.

Next, we present a wavelength-tunable pulse picking system featuring a pulse contrast ratio of 130 dB, which thus exceeds the performance of conventional pulse pickers by 9 orders of magnitude. For this purpose, we exploit the nonlinear characteristics of the FFOPO system configured in an extended-cavity design. A wavelength-independent performance is demonstrated for variable repetition rates between 640 kHz and 41 MHz. Applications such as fluorescence lifetime imaging microscopy may benefit from the unique combination of a variable repetition rate, wavelength tunability, and exceptional temporal contrast ratio. The latter renders this system suitable as a

front-end seeding unit for high pulse energy amplification chains.

The generation of true random numbers is crucial for encryption to ensure secure money transfer, data storage, and communication. In this context, we discuss an approach to generate binary random numbers in an all-optical manner. Specifically, the occurrence of bistable period-doubling states in the FFOPO output can be exploited as binary sampling mechanism for random number generation. Here, the starting process of the transient signal buildup holds the potential to transfer its quantum noise characteristics to the randomly generated bit sequences. For practical applications such as encryption and decryption the generated bit strings must not exhibit any bias. For this reason, we characterize the intrinsic bias properties and the influence of optical pre-conditioning sequences on the binary outcome.

Additionally, we introduce stimulated RAMAN scattering (SRS) microscopy of biomedical and biological systems as a direct application of FFOPO systems as coherent and tunable light sources. Since SRS provides label-free chemical contrast, it presents an ideal method to study these systems quantitatively and non-invasively.

Hydrated pectin films form a strong physical bond with the surface of mammalian visceral organs. This renders pectin hydrogels an ideal material for medical applications such as surgical wound sealing. A potential mechanism of this efficient adhesion is the water-dependent entanglement of pectin polysaccharide chains with the organ surface layer. In order to gain a better understanding of this mechanism, we employ SRS spectroscopy to investigate the water transport dynamics in pectin hydrogel and to quantify the timescales of the hydration process. Moreover, label-free 3D SRS spectral imaging reveals insights into the adhesive interface without requiring sample fixation, dehydration, or staining.

Finally, we demonstrate monitoring of microplastics contamination in fish tissue using SRS spectral imaging. The inherent chemical contrast enables the differentiation of different types of plastic compounds in the fish tissue. Through studies on the size-dependent signal-to-noise ratio for microplastic particles, we establish a minimum detectable size threshold. Our results highlight the potential of SRS microscopy as a complementary approach to conventional RAMAN scattering imaging for the detection and identification of microplastic particles in fish tissue.

Future investigations may include monitoring the uptake of microplastics in specific organs associated with metabolic functions. What is more, quantifying the volume expansion of pectin hydrogels may further facilitate applications such as serosal wound healing and visceral tissue repair.

ZUSAMMENFASSUNG

Nichtlineare parametrische Frequenzkonversion ist ein weit verbreiteter Ansatz zur Erzeugung von kohärenter Laserstrahlung mit durchstimmbarer Wellenlänge, die für viele spektroskopische Anwendungen benötigt wird, z. B. für kohärente Raman-Streuungsspektroskopie, optische Rasternahfeldmikroskopie oder photoakustische Spektroskopie. Dabei stellen optisch-parametrische Oszillatoren den Kern solcher Frequenzkonversionseinheiten dar. Insbesondere optisch-parametrische Oszillatoren mit Faserrückkopplung (FFOPO) haben sich neben geringem Platzbedarf und niedrigen Kosten in Bezug auf Wellenlängen- und Puls-zu-Puls-Stabilität und Intenstitätsrauscheigenschaften als besonders leistungsfähig erwiesen.

Die Stabilität des Systems hängt jedoch empfindlich von den Betriebsparametern ab. Daher ist es wichtig, das Zusammenspiel der linearen und nichtlinearen Effekte zu verstehen, die die zeitliche und spektrale Dynamik dieses Systems bestimmen. Diese Arbeit bietet eine eingehende Analyse der nichtlinearen ultraschnellen transienten Dynamik in einem Femtosekunden-FFOPO-System. Wir geben Einblick in die spektrale Pulsentwicklung während des transienten Prozesses auf der Zeitskala einzelner Resonatorumläufe. Darüber hinaus werden sowohl die Wellenlängen- als auch die Puls-zu-Puls-Stabilität in Abhängigkeit der Betriebsparameter und der Dispersion innerhalb des Resonators im Detail untersucht, um einen Einblick in die effiziente Stabilisierung des Systems zu geben.

Desweiteren nutzen wir die nichtlinearen Eigenschaften dieser Lichtquelle, um weitere Anwendungsbereiche zu ermöglichen. Basierend auf dem ultraschnellen Einschwingvorgang realisieren wir einen Burst-Modus mit dem FFOPO-System mit Burst-Raten von DC bis hin zu 5 MHz und demonstrieren beliebige Pulssequenzen mit durchstimmbarer Wellenlänge. Dies kann bei der Materialbearbeitung Anwendung finden, wo eine Reduzierung der durchschnittlichen optischen Leistung bei gleichzeitiger Beibehaltung einer hohen Spitzenleistung erwünscht ist.

Als nächstes stellen wir ein durchstimmbares Pulspickersystem mit einem Pulskontrastverhältnis von 130 dB vor, das die Leistung herkömmlicher Systeme um 9 Größenordnungen übertrifft. Dazu nutzen wir die nichtlinearen Eigenschaften des FFOPO-Systems, welches hierfür in einem „extended-cavity design“ konfiguriert ist. Die Repetitionsrate kann variabel und wellenlängenunabhängig zwischen 640 kHz und 41 MHz gewählt werden. Anwendungen wie Fluoreszenzlebensdauer-Mikroskopie

können von diesen Eigenschaften profitieren. Das hohe Pulskontrastverhältnis macht dieses System zu einer geeigneten „front-end seeding“-Einheit für Verstärkerketten für hohe Pulsenergien.

Die Erzeugung echter Zufallszahlen ist für die Verschlüsselung entscheidend, um einen sicheren Geldtransfer, Datenspeicherung und Kommunikation zu gewährleisten. Wir diskutieren einen Ansatz zur Erzeugung binärer Zufallszahlen auf rein optischem Weg. Insbesondere bistabile Zustände im Pulszug des FFOPO können als Abtastmechanismus zur Erzeugung von binären Zufallszahlen genutzt werden. Der Startprozess des Einschwingvorgangs birgt das Potenzial, seine Quantenrauscheigenschaften auf die zufällig erzeugte Bitsequenz zu übertragen. Für eine effiziente Verschlüsselung dürfen die Bitsequenzen keine Abweichungen von einer Gleichverteilung aufweisen. Daher charakterisieren wir die intrinsischen Abweichungen und den Einfluss optischer Vorkonditionierungssequenzen auf die binäre Gleichverteilung.

Außerdem stellen wir die Mikroskopie mit stimulierter Raman-Streuung (SRS) biomedizinischer und biologischer Systeme als direkte Anwendung von FFOPO-Systemen. SRS ermöglicht „label“-freien chemischen Kontrast und ist daher eine ideale Methode, um diese Systeme quantitativ und nicht-invasiv zu untersuchen.

Hydratisierte Pektinfilme weisen eine starke Adhäsion mit der Oberfläche der inneren Organen von Säugetieren auf. Dies macht Pektinhydrogele zu einem idealen Material für medizinische Anwendungen wie die chirurgische Schließung von Wunden. Ein möglicher Mechanismus dieser effizienten Adhäsion ist die wasserabhängige Verschränkung von Polysaccharidketten im Pektin mit der äußersten Organschicht. Um diesen Mechanismus besser zu verstehen, nutzen wir SRS-Spektroskopie, um die Wassertransportdynamik in Pektinhydrogelen zu untersuchen und die Zeitskalen des Hydratationsprozesses zu quantifizieren. Darüber hinaus ermöglicht spektral aufgelöste 3D-SRS-Bildgebung Einblicke in die Adhäsionsgrenzfläche, ohne dass die Proben fixiert, dehydriert oder eingefärbt werden müssen.

Schließlich demonstrieren wir die Anwendung von spektral aufgelöster SRS-Bildgebung zur Untersuchung von Fischgewebe auf Kontaminierung mit Mikroplastik. Der intrinsische chemische Kontrast ermöglicht die Unterscheidung verschiedener Kunststoffverbindungen im Fischgewebe. Durch Bestimmung des größenabhängigen Signal-zu-Rausch-Verhältnisses für die Mikroplastikpartikel ermitteln wir einen Grenzwert für deren nachweisbare Größe. Unsere Ergebnisse unterstreichen das Potenzial von SRS-Mikroskopie als ergänzende Methode zu herkömmlicher Raman-Streuung für den Nachweis und die Identifizierung von Mikroplastikpartikeln in Fischgewebe.

Künftige Untersuchungen könnten die spezifische Aufnahme von Mikroplastik in verschiedenen Organen umfassen. Darüber hinaus könnte die Quantifizierung der Volumenexpansion von Pektin-Hydrogelen Anwendungen wie die Heilung von viszeralem Gewebe weiter erleichtern.

PUBLICATIONS

FULL LIST OF PUBLICATIONS

In scientific journals (first author):

1. **M. Floess**, M. Fagotto-Kaufmann, A. Gall, T. Steinle, I. Ehrlich, and H. Giessen
Limits of detection of microplastics in fish tissue using stimulated Raman scattering microscopy
Biomed. Opt. Express **15**, 1528–1539 (2024).

2. **M. Floess**, T. Steinle, and H. Giessen
Spectrally resolved ultrafast transient dynamics of a femtosecond fiber-feedback optical parametric oscillator
Opt. Express **31**, 44680–44692 (2023).

3. **M. Floess**, T. Steinle, F. Werner, Y. Wang, W. L. Wagner, V. Steinle, B. S. Liu, Y. Zheng, Z. Cheng, M. Ackermann, S. J. Mentzer, and H. Giessen
3D stimulated Raman spectral imaging of water dynamics associated with pectin-glycocalyceal entanglement
Biomed. Opt. Express **14**, 1460–1471 (2023).

4. **M. Floess**, T. Steinle, I. Gerhardt, and H. Giessen
Femtosecond tunable light source with variable repetition rate between 640 kHz and 41 MHz with a 130 dB temporal pulse contrast ratio
Opt. Express **30**, 1–11 (2022).

5. **M. Floess**, T. Steinle, and H. Giessen
Burst-mode femtosecond fiber-feedback optical parametric oscillator
Opt. Lett. **47**, 525–528 (2022).

In scientific journals (co-author):

6. C. Imiolczyk, T. Pfau, S. Thiele, J. Karst, **M. Floess**, M. Schmid, M. Hentschel, and H. Giessen
Ultracompact wavefront characterization of femtosecond 3D printed microlenses using double-frequency Ronchi interferometry
Opt. Express **32**, 9777–9789 (2024).

7. S. Doshi, D. Ludescher, J. Karst, **M. Floess**, J. Carlström, B. Li, N. M. Hemed, Y.-S. Duh, N. A. Melosh, M. Hentschel, M. Brongersma, and H. Giessen
Direct electron beam patterning of electro-optically active PEDOT:PSS
Nanophotonics (2024).

8. L. Schmid, F. Kadriu, S. Kuppel, **M. Floess**, T. Steinle, and H. Giessen
Photoacoustic spectroscopy with a widely tunable narrowband fiber-feedback optical parametric oscillator
Scientific Reports (2023, submitted).

9. D. de Jong, J. Karst, D. Ludescher, **M. Floess**, S. Moell, K. Dirnberger, M. Hentschel, S. Ludwigs, P. V. Braun, and H. Giessen
Electrically switchable metallic polymer metasurface device with gel polymer electrolyte
Nanophotonics **12**, 1397–1404 (2023).

10. J. Karst, Y. Lee, **M. Floess**, M. Ubl, S. Ludwigs, M. Hentschel, and H. Giessen
Electro-Active Metaobjective from Metalenses-On-Demand
Nat. Commun. **13**, 7183 (2022).

11. J. Karst, **M. Floess**, M. Ubl, C. Dingler, C. Malacrida, T. Steinle, S. Ludwigs, M. Hentschel, and H. Giessen
Electrically Switchable Metallic Polymer Nanoantennas
Science **374**, 612 (2021).

12. H. Linnenbank, T. Steinle, F. Mörz, **M. Floess**, H. Cui, A. Glidle, and H. Giessen
Robust and rapidly tunable light source for SRS/CARS microscopy with low-intensity noise
Adv. Photon. **1**(5), 055001 (2019).

Own contributions:

1. **M. Floess**, T. Steinle, F. Werner, Y. Wang, W. L. Wagner, V. Steinle, B. S. Liu, Y. Zheng, S. J. Mentzer, and H. Giessen
   3D stimulated Raman spectral imaging of water dynamics associated with pectin-glycocalyceal entanglement
   Conference Talk, DPG Spring Meeting 2023
   Dresden (Germany)

2. **M. Floess**, T. Steinle, I. Gerhardt, and H. Giessen
   Femtosecond Tunable Light Source with Variable Repetition Rate between 640 kHz and 41 MHz with a 130 dB Temporal Pulse Contrast Ratio
   Poster contribution, 2022 Siegman International School on Lasers
   Warsaw (Poland)

3. **M. Floess**, T. Steinle, and H. Giessen
   Transient Dynamics in a Femtosecond Fiber-feedback Optical Parametric Oscillator
   Conference Paper, CLEO 2022 (Online)
   San Jose (USA)

4. **M. Floess**, T. Steinle, I. Gerhardt, and H. Giessen
   Femtosecond Tunable Light Source with Variable Repetition Rate and Ultra-high Pulse Contrast Ratio
   Conference Talk, CLEO 2021 (Online)
   San Jose (USA)

5. **M. Floess**, F. Werner, T. Steinle, and H. Giessen
   Stimulated Raman scattering microscopy of biomedical systems
   Conference Talk, DPG Spring Meeting 2020
   Dresden (Germany)

6. **M. Floess**, T. Steinle, F. Mörz, H. Linnenbank, A. Steinmann, and H. Giessen
   Build-up dynamics in an optical parametric oscillator with synchronized pump modulation
   Conference Talk, DPG Spring Meeting 2019
   Munich (Germany)

Other contributions:

7. • H. Giessen, H. Linnenbank, T. Steinle, F. Mörz, **M. Floess**, and F. Werner
   Robust and rapidly tunable light source for SRS/CARS microscopy with extremely low-intensity noise
   Conference Talk, CLEO 2021
   San Jose (USA)

8. • J. Karst, **M. Floess**, M. Ubl, C. Dingler, C. Malacrida, T. Steinle, S. Ludwigs, M. Hentschel, and H. Giessen
   Electrically Switchable Metallic Polymer Nanoantennas and Metasurfaces
   Breakthrough Talk, NanoMeta 2022
   Seefeld (Austria)

9. • J. Karst, D. de Jong, **M. Floess**, D. Ludescher, Y. Lee, M. Ubl, S. Ludwigs, P. V. Braun, M. Hentschel, and H. Giessen
   Electrically switchable metallic polymer metasurfaces for beam switching and multi-focal metaobjectives
   Conference Talk, SPIE OPTO 2023
   San Francisco (USA)

10. • C. Imiolczyk, A. Steinmann, **M. Floess**, Z. Wang, M. Heymann, A. Toulouse, and H. Giessen
    Fiber-based femtosecond 3D printing
    Conference Talk, DPG Spring Meeting 2023
    Dresden (Germany)

• Presenting author

CONTENTS

1 INTRODUCTION

Nonlinear parametric frequency conversion is a widely used method to generate coherent laser radiation in wavelength regions, which might otherwise not be accessible. The lack of laser gain media for specific spectral regions in the near- and mid-infrared renders nonlinear parametric frequency conversion an indispensable tool for many spectroscopic applications, such as scanning near-field optical microscopy, coherent Raman spectroscopy, or photoacoustic spectroscopy.

Certain materials, e.g., lithium niobate ($LiNbO_3$), exhibit a strong nonlinear response upon irradiation with high-intensity laser radiation. This nonlinear response gives rise to newly generated wavelength components allowing to efficiently convert the input wavelength into other channels. In this context, the concept of optical parametric oscillation (OPO) allows to generate tunable wavelength output based on parametric frequency conversion. Therefore, optical parametric oscillators represent the core unit of wavelength-tunable parametric light sources.

The concept of a fiber-feedback optical parametric oscillator (FFOPO) improves the overall stability of such a system by transferring the largest part of the resonator into an optical fiber. Specifically, the wavelength and the output power stability are increased, and susceptibility to changes in ambient conditions is minimized. Besides a greatly reduced physical footprint, the intensity noise properties of the pump source are preserved, rendering FFOPO systems a superior light source for sensitive spectroscopy applications.

Stimulated Raman scattering (SRS) microscopy, being one of these applications, provides label-free, non-invasive, and chemically specific imaging contrast, which is based on probing Raman resonances. Due to the increased interaction cross-section, SRS allows orders of magnitude faster acquisition speeds compared to conventional Raman scattering imaging. Furthermore, the absence of non-resonant background signals and the linear signal scaling render this imaging modality an ideal choice for biological and biomedical imaging applications. SRS spectral imaging requires a coherent tunable light sources with pulsed output and excellent intensity noise prop-

erties. Consequently, FFOPO systems in combination with a solid-state laser oscillator as front-end are therefore the ideal choice for this purpose.

Within the scope of this work, we discuss the nonlinear dynamics of FFOPO systems and their application for SRS microscopy on biomedical and biological systems.

First of all, we provide a detailed investigation on the nonlinear transient dynamics in a FFOPO system depending on the intra-cavity dispersion regime and the operational parameters. We capture the intra-cavity pulse evolution spectrally resolved and on the timescale of individual cavity roundtrips. We furthermore provide insights into how to effectively stabilize the wavelength tuning behavior and the pulse-to-pulse output. Utilizing these insights on the ultrafast transient process, burst-mode operation of the FFOPO is demonstrated, which may be of interest for material processing applications. Moreover, we employ the nonlinear behavior of the FFOPO system to realize a pulse picking system with extraordinarily high suppression ratios independent of the operation wavelength, surpassing the performance of conventional systems by orders of magnitude. Owing to its nonlinearity and the self-feedback mechanism, the FFOPO output is subject to the emergence of nonlinear attractors, such as period-doubling states, limit cycles, or chaotic pulse trains. We demonstrate how period-doubling in particular in combination with the transient buildup process can be exploited to generate sequences of binary random numbers in an all-optical manner.

Last, we shift towards SRS spectral imaging of biomedical and biological systems as direct applications of FFOPO systems. We investigate the water transport dynamics in a novel pectin-based pleural sealant employed for surgical wound sealing of lung injuries. Furthermore, we employ the chemical specificity of SRS imaging for the detection of microplastics in fish tissue and provide quantitative detection limits for monitoring the microplastic contamination of our food chain.

THESIS OUTLINE

This thesis is structured into six main chapters. Chapter 3 to Chapter 6 discuss the transient dynamics in a FFOPO system and its applications for burst-mode operation, repetition rate tuning, and all-optical random number generation. Chapter 7 and Chapter 8 introduce SRS microscopy of biomedical and biological systems, where the FFOPO system finds a direct application for label-free and chemically specific coherent RAMAN imaging. As these topics have rather different scopes, each chapter features separate INTRODUCTION as well as CONCLUSION & OUTLOOK sections.

A main theory chapter precedes the other chapters to cover the most relevant theoretical background. The chapters are outlined as follows:

- Chapter 3 discusses the spectrotemporal transient dynamics in a femtosecond FFOPO system. Here, pump bursts are generated, which drive the FFOPO from its off-state into equilibrium via an intermediate transient state. Ultrafast real-time spectroscopy of individual signal pulses is employed to acquire the intra-cavity spectral evolution during the signal buildup process on the timescale of individual cavity roundtrips. Furthermore, we characterize the output wavelength as well as the pulse-to-pulse stability depending on the intra-cavity dispersion regime and the impact of spatial effects on the beam profile.

- The insights on the ultrafast signal buildup process are used to realize a burst-mode FFOPO, as will be discussed in Chapter 4. Essentially, the FFOPO system translates the pulse bursts generated in the pump beam line to its entire output wavelength tuning range without the disadvantage of wavelength-dependent pulse picking performance, which is usually the case for conventional pulse picking schemes. We demonstrate, that the ultrafast signal buildup dynamics enable arbitrary burst rates of up to 5 MHz with tunable wavelength output.

- In Chapter 5, we utilize the nonlinear properties of the FFOPO to realize a pulse picking system with an extremely high temporal pulse contrast ratio exceeding 130 dB. Therefore, an extended-cavity configuration is used for FFOPO system. We demonstrate that this design enables a tunable repetition rate while maintaining synchronous pumping, and thus, keeping the FFOPO in its equilibrium state. Hence, the excellent noise properties of the solid-state bulk pump oscillator are preserved.

- In Chapter 6, we discuss utilizing bistability in the FFOPO output in combination with the signal transients to generate binary random numbers. The idea is to harvest the inherent randomness of the starting process and exploit the bistable output attractor to generate random bit sequences. The FFOPO system therefore comprises both, the random process and a binary sampling mechanism to project a continuous random input onto two distinct output values. We find that the binary outcome exhibits an intrinsic bias. We discuss an all-optical approach based on employing a chaos attractor pre-sequence to reduce and potentially remove the bias.

- Chapter 7 introduces SRS microscopy as direct application of tunable FFOPO systems for vibrational imaging of biomedical systems. In particular, a novel pectin-based pleural sealant is investigated. Such pectin hydrogels are used to

surgically seal lung injuries, causing the lung to collapse (*pneumothorax*). This pectin hydrogel adheres extremely well on the pleura, which is the outermost layer covering the inner organs. We utilize label-free chemically specific SRS imaging to measure the interlink length of pectin with pleural tissue. Furthermore, SRS spectroscopy is used to investigate the water transport dynamics in the hydrogel. We quantify the time scales of two hydration mechanisms, i.e., direct contact with liquid water and water absorption from a humid ambient atmosphere.

- In Chapter 8 we employ SRS imaging for the detection of microplastics in fish tissue. The increasing abundance of microplastics debris in our environment causes contamination of our food chain. We quantitatively establish threshold for the minimum size and the signal-to-noise-ratio for unambiguous particle detection. In the next step, we demonstrate that the chemical specificity provided by SRS allows to identify and distinguish different plastic compounds from the surrounding tissue based on their specific RAMAN resonances. In addition, the excellent noise properties of the solid-state front-end laser system enable shot-noise limited detection.

2

THEORY

This chapter aims to provide an overview of the theoretical background relevant for the physical concepts discussed in this thesis. We will start with basic interactions between light and matter and shortly introduce dispersive effects on ultrashort laser pulses. In the next step, a brief introduction on nonlinear optical effects will be provided to lay the theoretical foundation for all chapters of this thesis. Special emphasis will be placed on parametric frequency conversion, as it forms the foundation for the fiber-feedback optical parametric oscillator (FFOPO) light sources used throughout this thesis.

We will continue discussing the basics of spontaneous as well as of stimulated Raman scattering to provide a background on coherent Raman scattering microscopy. The discussion will also cover the concepts of spatial resolution and fundamental properties of Gaussian beams.

In the last section, a brief overview on statistical quantities used for signal processing and data evaluation will be given.

NOMENCLATURE

Throughout this thesis, scalar quantities are written in standard font, e.g.:

λ (wavelength),

c (speed of light).

In order to denote vectorial quantities, bold characters are used, e.g.:

$\boldsymbol{E}$ (electric field vector),

$\boldsymbol{k}$ (wave vector).

2.1 LIGHT AND MATTER INTERACTIONS

The interaction between light and matter is fundamentally described by MAXWELL's equations. In differential form they read [1]

$$\nabla \cdot \boldsymbol{D} = \rho, \tag{2.1a}$$

$$\nabla \cdot \boldsymbol{B} = 0, \tag{2.1b}$$

$$\nabla \times \boldsymbol{E} = -\frac{\partial \boldsymbol{B}}{\partial t}, \tag{2.1c}$$

$$\nabla \times \boldsymbol{H} = \boldsymbol{j} + \frac{\partial \boldsymbol{D}}{\partial t}. \tag{2.1d}$$

These equations describe the relationship between the electric field $\boldsymbol{E}$ and the electric flux density $\boldsymbol{D}$ as well as between the magnetic field $\boldsymbol{H}$ and the magnetic flux density $\boldsymbol{B}$ via the vacuum permittivity ε_0 and permeability μ_0

$$\boldsymbol{D} = \varepsilon_0 \boldsymbol{E} + \boldsymbol{P}, \tag{2.2a}$$

$$\boldsymbol{B} = \mu_0 \left(\boldsymbol{H} + \boldsymbol{M} \right). \tag{2.2b}$$

The electric and magnetic polarization $\boldsymbol{P}$ and $\boldsymbol{M}$ account for the material-specific response to an external field.

Within the scope of this work, the linear and nonlinear optical effects governed by the electric polarization $\boldsymbol{P}$ are of importance. As mentioned, the macroscopic polarization $\boldsymbol{P}$ describes the response of the material upon the presence of an external electric field

$$\boldsymbol{P}(\omega) = \varepsilon_0 \chi(\omega) \boldsymbol{E}(\omega). \tag{2.3}$$

Here, χ denotes the susceptibility, which represents the corresponding response function. In order to account for anisotropic materials, χ in general is a tensorial quantity. Note that this representation as product between χ and $\boldsymbol{E}$ only holds in the frequency domain. In order to account for causality, the time domain representation requires a convolution between the two quantities. In the following, the frequency domain representation is assumed and the explicit ω-dependence will be dropped.

In this context, the susceptibility χ relates to the relative permittivity

$$\varepsilon = \chi + 1, \tag{2.4}$$

and thus, to the refractive index

$$n = \sqrt{\varepsilon} = \sqrt{\chi + 1}. \tag{2.5}$$

At this point it should be noted, that the frequency dependence of the response $\chi(\omega)$ translates to a frequency dependent refractive index $n(\omega)$, which is referred to as *dispersion*.

Details on the following derivation can be found in [2]. The electric susceptibility can be expanded into a TAYLOR series, such that the polarization reads

$$P_i/\varepsilon_0 = \sum_j \chi^{(1)}_{ij} E_j + \sum_{jk} \chi^{(2)}_{ijk} E_j E_k + \sum_{jkl} \chi^{(3)}_{ijkl} E_j E_k E_l + \dots, \tag{2.6}$$

where $\chi^{(n)}$ denotes the n^{th}-order susceptibility. In a more symbolic way, the polarization can be written as

$$\boldsymbol{P} = \underbrace{\varepsilon_0 \chi^{(1)} \boldsymbol{E}}_{\boldsymbol{P}_\text{l}} + \underbrace{\varepsilon_0 \chi^{(2)} \boldsymbol{E}^2 + \varepsilon_0 \chi^{(3)} \boldsymbol{E}^3 + \dots}_{\boldsymbol{P}_\text{nl}} \tag{2.7}$$

$\boldsymbol{P}_\text{l}$ accounts for the linear response, whereas $\boldsymbol{P}_\text{nl}$ contains the nonlinear contributions. As we will see later, the $\boldsymbol{P}_\text{nl}$ terms give rise to nonlinear optical effects.

In the following, we assume an uncharged ($\rho = 0$) and nonmagnetic ($\mu = 1$) material, which is valid within the scope of this work. Applying the *curl* to Eq. 2.1c and substituting Eq. 2.1d yields

$$\nabla \times \left(\nabla \times \boldsymbol{E}\right) = -\Delta \boldsymbol{E} = -\frac{\partial}{\partial t}\left(\nabla \times \boldsymbol{B}\right) = -\mu_0 \frac{\partial^2 \boldsymbol{D}}{\partial t^2}. \tag{2.8}$$

Here, we use the identity

$$\nabla \times \left(\nabla \times \boldsymbol{E}\right) = \nabla\left(\nabla \cdot \boldsymbol{E}\right) - \Delta \boldsymbol{E} = -\Delta \boldsymbol{E}, \tag{2.9}$$

where, according to Eq. 2.1a and due to the absence of free charges, the first term can be set to zero. Rewriting Eq. 2.8 and applying Eq. 2.2a and Eq. 2.7 yields

$$\begin{aligned} \Delta \boldsymbol{E} &= \varepsilon_0 \mu_0 \frac{\partial^2}{\partial t^2} \boldsymbol{E} + \mu_0 \frac{\partial^2}{\partial t^2} \boldsymbol{P} \\ &= \varepsilon_0 \mu_0 \left(\chi^{(1)} + 1\right) \frac{\partial^2}{\partial t^2} \boldsymbol{E} + \mu_0 \frac{\partial^2}{\partial t^2} \boldsymbol{P}_\text{nl}. \end{aligned} \tag{2.10}$$

Furthermore, we can use the vacuum light speed $c = 1/\sqrt{\varepsilon_0 \mu_0}$ and substitute Eq. 2.5 yielding the *nonlinear wave equation* [2]

$$\Delta \boldsymbol{E} = \frac{n^2}{c^2} \frac{\partial^2}{\partial t^2} \boldsymbol{E} + \frac{1}{c^2 \varepsilon_0} \frac{\partial^2}{\partial t^2} \boldsymbol{P}_\text{nl}. \tag{2.11}$$

In the absence of a nonlinear polarization contribution $\boldsymbol{P}_{\mathrm{nl}} = 0$, it reduces to the linear wave equation

$$\Delta \boldsymbol{E} = \frac{n^2}{c^2} \frac{\partial^2}{\partial t^2} \boldsymbol{E}, \tag{2.12}$$

which is solved by plane waves

$$\boldsymbol{E}(\boldsymbol{r}, t) = \boldsymbol{E}_0 \cos(\omega t - \boldsymbol{k} \cdot \boldsymbol{r} + \phi). \tag{2.13}$$

Here, $\omega = 2\pi f$ denotes the angular frequency and can be expressed in terms of the frequency f, $\boldsymbol{k}$ is the wavevector pointing in the direction of propagation. Its absolute value is known as *wavenumber* and is given by

$$k = |\boldsymbol{k}| = \frac{n\omega}{c} = \frac{2\pi n}{\lambda}, \tag{2.14}$$

where λ is the wavelength in vacuum. The intensity associated with an electric field is given by

$$I = \frac{1}{2} \varepsilon_0 n c |E|^2. \tag{2.15}$$

2.2 ULTRASHORT LASER PULSES AND DISPERSION EFFECTS

In this thesis, femtosecond laser pulses are employed for parametric frequency conversion. In practice, femtosecond laser pulses are generated by mode-locked laser oscillators, where a frequency comb of longitudinal modes is phase-locked, such that ultrashort pulses of light occur due to constructive interference of these modes. We will not go into detail here, however, the interested reader may refer to the following literature [3]. The following section aims to provide an overview on the most relevant aspects of ultrashort laser pulses with a particular focus of dispersive effects on pulse propagation. Further details can also be found in the work of T. Steinle [4], which lays the groundwork for the frequency conversion systems discussed in this thesis.

A laser pulse can be represented as a superposition of plane waves. For simplicity, we assume propagation in z-direction and drop the vectors, which yields

$$E(z, t) = \int_{-\infty}^{\infty} \tilde{E}(\omega) \exp(i\omega t - ik(\omega) z) \, \mathrm{d}\omega \tag{2.16}$$

with $\tilde{E}(\omega)$ being the field amplitude of the frequency compenent ω. In general, ultrashort laser pulses are subject to dispersion effects when propagating through media other than vacuum, given by the frequency dependent wavevector $\boldsymbol{k}(\omega)$. This

frequency dependence may lead to, e.g., temporal stretching of the laser pulses. For a quantitative description, the frequency dependent wavevector is expanded into a TAYLOR series around the center frequency ω_0

$$k(\omega) = k_0 + k_1(\omega - \omega_0) + \frac{1}{2}k_2(\omega - \omega_0)^2 + \dots \tag{2.17}$$

with

$$k_0 = k(\omega_0) \tag{2.18}$$

$$k_n = \left(\frac{\partial^n k}{\partial \omega^n}\right)_{\omega=\omega_0} \qquad (n = 1,\ 2, \dots). \tag{2.19}$$

The quantities k_n are directly linked to physical properties of the propagation of light pulses. The first term is associated with the *phase velocity* v_p, which is given by

$$v_\mathrm{p}(\omega_0) = \frac{\omega_0}{k_0} \tag{2.20}$$

and describes the propagation speed of the wavefronts. In contrast, the propagation speed of the laser pulse as a whole is given by the group velocity v_g, also denoting the propagation speed of the pulse envelope

$$v_\mathrm{g}(\omega_0) = \left(\frac{\partial \omega}{\partial k}\right)_{\omega=\omega_0} = \frac{1}{k_1(\omega_0)}. \tag{2.21}$$

Furthermore, the frequency components contained in a laser pulse might travel at different speeds in a medium, e.g., in an optical fiber, leading to temporal stretching of the pulse, also known as *chirp*. This is quantified by the *group velocity dispersion* (GVD)

$$\mathrm{GVD} = k_2(\omega_0) = \left(\frac{\partial^2 k}{\partial \omega^2}\right)_{\omega=\omega_0} = \frac{\partial}{\partial \omega}\frac{1}{v_\mathrm{g}} = \left(-\frac{1}{v_\mathrm{g}^2}\frac{\partial v_\mathrm{g}}{\partial \omega}\right)_{\omega=\omega_0}, \tag{2.22}$$

which is usually given in units of $\mathrm{fs}^2/\mathrm{mm}$ and quantifies the amount of second-order dispersion per unit length. It can also be expressed in the wavelength domain, given by the so-called *dispersion parameter*

$$D(\lambda) = -\frac{2\pi c}{\lambda^2} \cdot \mathrm{GVD} \tag{2.23}$$

with units of $\mathrm{ps}/(\mathrm{nm} \cdot \mathrm{km})$. The overall *group delay dispersion* (GDD) is the GVD multiplied by the propagation length x, yielding

$$\mathrm{GDD}(\lambda, x) = D(\lambda) \cdot x. \tag{2.24}$$

In the context of single-pulse spectral measurements discussed in Chapter 3, the group delay dispersion (GDD) is the quantity of interest to determine the overall temporal pulse stretching, and therefore, the spectral resolution of the dispersive FOURIER transformation (DFT) spectrometer.

2.3 NONLINEAR OPTICS

The higher-order terms of the susceptibility χ, as given by Eq. 2.7, account for the occurrence of nonlinear optical effects, which will be introduced in this section. Within the scope of this thesis, second- and third-order nonlinear optical effects play a role. In particular, the following nonlinear effects and their application are relevant:

Second-order ($\chi^{(2)}$) effects:

- Second-harmonic generation (SHG): frequency conversion process, that will be used for coherent RAMAN spectroscopy (Chapter 7 and Chapter 8).
- Sum-frequency generation (SFG): will be exploited for an optically gated cross-correlation measurement (Chapter 5).
- Difference-frequency generation (DFG): frequency conversion process employed for optical parametric amplification and oscillation.

Third-order ($\chi^{(3)}$) effects:

- Self-phase modulation (SPM): occurs in the nonlinear feedback of the OPO system used throughout this work.

2.3.1 *Second-order Nonlinear Effects*

As mentioned above, second-order frequency mixing processes are employed to generate tunable wavelength output. Here, we will shortly introduce the relevant effects. A more detailed discussion can be found in [2].

The second-order nonlinear polarization $\boldsymbol{P}^{(2)}(t)$ is calculated in the following. Here, we assume linearly polarized light and the nonlinear response of the medium to be independent of the polarization and propagation direction of the interacting waves. For simplicity, we also consider the absolute values of the involved fields. Generally, the spatial dependence of the interaction has to be taken into account. Nevertheless, this simplified discussion conveys the general concept of nonlinear frequency mixing sufficiently. For a more detailed discussion the reader may refer to [2].

We consider two plane waves with frequencies ω_1 and ω_2 being incident on the medium

$$E = E_1 \cdot \mathrm{e}^{-i\omega_1 t} + E_2 \cdot \mathrm{e}^{-i\omega_2 t} + \text{c.c.}, \tag{2.25}$$

driving the second-order polarization

$$\begin{aligned} P^{(2)}(t) =& \varepsilon_0 \chi^{(2)} E^2(t) \\ =& \varepsilon_0 [\chi^{(2)}_{2\omega_1} E_1^2 \cdot \mathrm{e}^{-2i\omega_1 t} + \chi^{(2)}_{2\omega_2} E_2^2 \cdot \mathrm{e}^{-2i\omega_2 t} \\ &+ 2\chi^{(2)}_{\omega_1+\omega_2} E_1 E_2 \cdot \mathrm{e}^{-i(\omega_1+\omega_2)t} \\ &+ 2\chi^{(2)}_{\omega_1-\omega_2} E_1 E_2^* \cdot \mathrm{e}^{-i(\omega_1-\omega_2)t} \\ &+ 2\chi^{(2)}_0 (E_1 E_1^* + 2E_2 E_2^*)] \\ &+ \text{c.c.} \end{aligned} \tag{2.26}$$

Note that this representation in the time domain is only valid for lossless and dispersionless media. Here, the frequency dependence of the susceptibility is denoted in terms of an index $\chi^{(2)}_{\omega_j} \equiv \chi^{(2)}(\omega_j)$ in order not to falsely suggest a multiplication. The individual contributions to $P^{(2)}(t)$ can be expressed as

$$P^{(2)}(t) = \sum_n \tilde{P}^{(2)}(\omega_n) \cdot \mathrm{e}^{-i\omega_n t}, \tag{2.27}$$

where the frequency components are given by

$$\tilde{P}^{(2)}(2\omega_1) = \varepsilon_0 \chi^{(2)}_{2\omega_1} E_1^2 \qquad \text{(SHG)} \tag{2.28a}$$

$$\tilde{P}^{(2)}(2\omega_2) = \varepsilon_0 \chi^{(2)}_{2\omega_2} E_2^2 \qquad \text{(SHG)} \tag{2.28b}$$

$$\tilde{P}^{(2)}(\omega_1 + \omega_2) = 2\varepsilon_0 \chi^{(2)}_{\omega_1+\omega_2} E_1 E_2 \qquad \text{(SFG)} \tag{2.28c}$$

$$\tilde{P}^{(2)}(\omega_1 - \omega_2) = 2\varepsilon_0 \chi^{(2)}_{\omega_1-\omega_2} E_1 E_2^* \qquad \text{(DFG)} \tag{2.28d}$$

$$\tilde{P}^{(2)}(0) = 2\varepsilon_0 \chi^{(2)}_0 \left(E_1 E_1^* + E_2 E_2^* \right). \qquad \text{(OR)} \tag{2.28e}$$

The first two contributions are known as *second-harmonic generation* (SHG), the third and fourth are referred to as *sum-frequency generation* (SFG) and *difference-frequency generation* (DFG), respectively. The last term represents a constant DC field, called *optical rectification* (OR). In particular, DFG is the process governing optical parametric amplification (OPA), and therefore, optical parametric oscillation (OPO). As OPO-based nonlinear frequency conversion plays a significant role, we will later discuss this separately.

In practice, however, usually only one of these components is generated with significant intensity, whereas the other effects are negligible. This is governed by the *phase-matching condition* which will be introduced in the context of parametric frequency conversion in Section 2.4.

2.3.2 *Self-phase Modulation*

The $\chi^{(3)}$ nonlinearity gives rise to the KERR effect. Essentially, this effects describes the intensity dependence of the refractive index, which becomes important in context of the interaction between intense ultrashort laser pulses and condensed matter. The KERR effect includes a number of effects, such as *self-focusing* and *self-phase modulation* (SPM), where the latter plays a substantial role in the passive nonlinear optical feedback in the cavity of the FFOPO system, which is employed throughout this work. Particularly, SPM generates additional frequency components and its interplay with dispersion and parametric gain gives rise to the occurrence of several different attractors, as we will see in Chapter 3. Therefore, the effect of SPM will be shortly introduced, which can also be found in textbooks such as [2] and [3].

The refractive index n experiences an intensity-dependent change $\Delta n(I)$ in the presence of an intense electric field. This results in

$$n(I) = n_0 + \Delta n(I) = n_0 + n_2 \cdot I, \tag{2.29}$$

where n_2 represents the *nonlinear index*. It can be expressed in terms of the $\chi^{(3)}$ nonlinearity as [2, p. 210]

$$n_2 = \frac{3\chi^{(3)}}{4\varepsilon_0 c n_0^2}. \tag{2.30}$$

Since the refractive index enters the (absolute value of the) wave vector

$$k = \frac{2\pi n}{\lambda_0}, \tag{2.31}$$

the optical phase will also be affected

$$\Phi(t) = \omega_0 t - kz = \omega_0 t - \frac{2\pi n(I)}{\lambda_0} \cdot L. \tag{2.32}$$

In this context, L denotes the distance the optical pulse has propagated. Therefore, the instantaneous frequency yields

$$\begin{aligned} \omega(t) = \frac{\mathrm{d}\Phi(t)}{\mathrm{d}t} &= \omega_0 - \frac{2\pi}{\lambda_0} \cdot \frac{\mathrm{d}n(I)}{\mathrm{d}t} \cdot L \\ &= \omega_0 - \frac{2\pi n_2}{\lambda_0} \cdot \frac{\mathrm{d}I(t)}{\mathrm{d}t} \cdot L. \end{aligned} \tag{2.33}$$

In the following, the resulting instantaneous frequency will be derived for the case of a GAUSSIAN-shaped ultrashort laser pulse. The temporal intensity profile of the pulse can be written as

$$I(t) = I_0 \cdot \exp\left(-t^2/\tau^2\right), \tag{2.34}$$

where τ represents half of the pulse duration. According to Eq. 2.33, this intensity profile induces an instantaneous frequency

$$\omega(t) = \omega_0 + \frac{4\pi n_2 I_0 L}{\lambda_0 \tau^2} \cdot t \cdot \exp\left(-t^2/\tau^2\right). \tag{2.35}$$

Plotting the resulting instantaneous frequency, as depicted in Fig. 2.1, reveals a redshift for the leading slope of the pulse and a blueshift for its trailing slope.

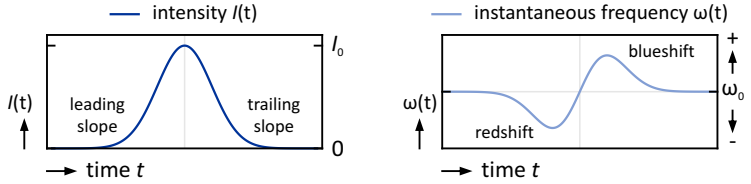

FIGURE 2.1. **SPM frequency shift.** Temporal evolution of the intensity (left) and the instantaneous frequency (right) of a GAUSSIAN pulse. The front of the pulse is blueshifted, whereas the back of the pulse experiences a redshift. An approximately linear chirp is present around the center of the pulse. Figure adopted from [3, p. 134].

Furthermore, an approximately linear frequency chirp around the peak position of the laser pulse

$$\omega(t) = \omega_0 + a \cdot t, \tag{2.36}$$

with a chirp rate

$$a = \left.\frac{\mathrm{d}\omega(t)}{\mathrm{d}t}\right|_{t=0} = \frac{4\pi n_2 I_0 L}{\lambda_0 \tau^2}. \tag{2.37}$$

The peak itself does not experience any frequency shift.

2.4 PARAMETRIC FREQUENCY CONVERSION

In contrast to laser activity, where energy is stored in the medium in the form of excited states with a finite lifetime, parametric processes do not involve energy deposition in the medium, except for heating through residual absorption. In the following section, we will introduce frequency conversion based on nonlinear parametric gain by means of the $\chi^{(2)}$ response of a nonlinear medium. The concept of phase matching will be discussed in order to understand the required conditions for efficient parametric frequency conversion. In particular, we will cover quasi phase matching based on periodically poled nonlinear crystals.

2.4.1 *Optical Parametric Amplification*

Optical parametric amplification (OPA) refers to a three-wave mixing process involving three different frequencies, called *pump*, *signal*, and *idler*. This process obeys energy conversion

$$\hbar\omega_\mathrm{p} = \hbar\omega_\mathrm{s} + \hbar\omega_\mathrm{i}. \tag{2.38}$$

By definition, the signal has higher energy than the idler, such that $\omega_\mathrm{p} > \omega_\mathrm{s} > \omega_\mathrm{i}$. Fig. 2.2 illustrates this process schematically. Here, the terminology *parametric amplification* refers to the intended amplification of the weak seed field at the input by energy transfer from the pump field. Strictly speaking, OPA is basically a DFG process, where the difference frequency (idler) between the pump and the signal (called *seed* at the input channel) is generated. Instead of intentionally generating the idler field in the first place, the idler is an inherent by-product in the amplification process of the signal channel.

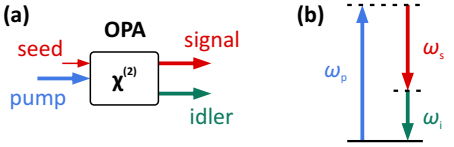

FIGURE 2.2. **Optical parametric amplification (OPA) process. (a)** A weak seed and a strong pump field are present at the input, which gives rise to parametric amplification via energy transfer from the pump to the seed field, which is referred to as *signal* at the output. **(b)** To fulfill energy conservation, an additional field is created, known as *idler*.

2.4.2 *Coupled Amplitude Equations*

The three-wave interaction in a nonlinear medium is described by the coupled amplitude equations. In particular, they provide the temporal evolution of the amplitudes $A_{\{\mathrm{p,s,i}\}}$ of pump, signal, and idler for the propagation through a nonlinear medium. Assuming the slowly-varying amplitude approximation $|\frac{\mathrm{d}^2 A}{\mathrm{d}z^2}| \ll |2k\frac{\mathrm{d}A}{\mathrm{d}z}|$, they can be written as [5]

$$\frac{\partial A_\mathrm{p}}{\partial z} + \frac{1}{v_{\mathrm{g,p}}}\frac{\partial A_\mathrm{p}}{\partial t} = -i\frac{\omega_\mathrm{p} d_\mathrm{eff}}{n_\mathrm{p} c} A_\mathrm{i} A_\mathrm{s} \exp\left(+i\Delta k z\right) \tag{2.39a}$$

$$\frac{\partial A_\mathrm{s}}{\partial z} + \frac{1}{v_{\mathrm{g,s}}}\frac{\partial A_\mathrm{s}}{\partial t} = -i\frac{\omega_\mathrm{s} d_\mathrm{eff}}{n_\mathrm{s} c} A_\mathrm{i}^* A_\mathrm{p} \exp\left(-i\Delta k z\right) \tag{2.39b}$$

$$\frac{\partial A_\mathrm{i}}{\partial z} + \frac{1}{v_{\mathrm{g,i}}}\frac{\partial A_\mathrm{i}}{\partial t} = -i\frac{\omega_\mathrm{i} d_\mathrm{eff}}{n_\mathrm{i} c} A_\mathrm{s}^* A_\mathrm{p} \exp\left(-i\Delta k z\right), \tag{2.39c}$$

where d_eff denotes the effective nonlinear coefficient, $v_{\mathrm{g},\{\mathrm{p,s,i}\}}$ the group velocity of the three waves, and Δk the wavevector mismatch. A net gain is achieved if this phase mismatch vanishes. The following section will discuss this concept in more detail.

2.4.3 *Phase Matching*

The phase mismatch occurring in the coupled amplitude equations is given by

$$\Delta \boldsymbol{k} = \boldsymbol{k}_\mathrm{p} - \boldsymbol{k}_\mathrm{s} - \boldsymbol{k}_\mathrm{i} = 0, \tag{2.40}$$

which is referred to as the *phase-matching condition* [2]. This condition essentially represents momentum conservation for this process, where the photon momentum is given by $\boldsymbol{p} = \hbar \boldsymbol{k}$. In order to fulfill Eq. 2.40, the interacting fields have to maintain a constant phase relation over the interaction length. In practice, however, dispersion leads to dephasing between the different frequency components. This becomes evident by rewriting equation Eq. 2.40 in terms of $k = \omega n(\omega)/c$, such that

$$\omega_\mathrm{p} n_\mathrm{p} = \omega_\mathrm{s} n_\mathrm{s} + \omega_\mathrm{i} n_\mathrm{i}. \tag{2.41}$$

In general, the frequency-dependent refractive index $n(\omega)$ prevents the phase matching condition from being fulfilled. Using birefringent materials, phase matching can be achieved by choosing the correct crystal orientation. Further details on phase matching based on birefringent crystals can be found in [2, p. 79].

2.4.4 *Quasi Phase Matching*

Apart from employing birefringence for phase matching, a phase mismatch can be compensated by periodic modulation of the susceptibility in a crystal, known as *quasi phase matching* (QPM). The spatially modulated susceptibility adds a grating vector

$$k_{\mathrm{gr},m} = \frac{2\pi}{\Lambda} m, \tag{2.42}$$

which compensates a non-zero wavevector mismatch [2]. The quantity Λ denotes the (fundamental) grating period. The phase matching order m accounts for the fact that the spatial modulation of the crystal susceptibility generally is not purely sinusoidal, but rect-shaped. Therefore, higher-order spatial frequency components are present as well. However, first-order ($m = 1$) phase matching yields the highest conversion efficiency, hence, we will assume this case in the following. The compensated wavevector mismatch thus reads

$$\begin{aligned} \Delta k &= k_\mathrm{p} - k_\mathrm{s} - k_\mathrm{i} - k_\mathrm{gr} \\ &= k_\mathrm{p} - k_\mathrm{s} - k_\mathrm{i} - \frac{2\pi}{\Lambda}. \end{aligned} \tag{2.43}$$

By imprinting varying grating periods Λ into a nonlinear crystal, k_gr can be adjusted, and therefore, the phase matching condition can be set to different signal wavelengths.

Fig. 2.3 depicts a comparison between the case of perfect phase matching, QPM, and of a non-zero phase mismatch. In case of QPM, the interacting waves dephase over the distance of one coherence length $L_\mathrm{coh} = \Lambda/2$, until the crystal susceptibility is flipped again. Instead of further dephasing, this flip resets the relative phase by π, which then starts to grow again. The periodic alternation of the crystal susceptibility therefore ensures constructive interference on average, leading to a net gain after propagating through the crystal [6].

Throughout this work, periodically poled lithium niobate (PPLN) crystals are employed for nonlinear frequency conversion. Therefore, we will briefly discuss the dispersion properties of lithium niobate and the associated influence on the phase matching bandwidth.

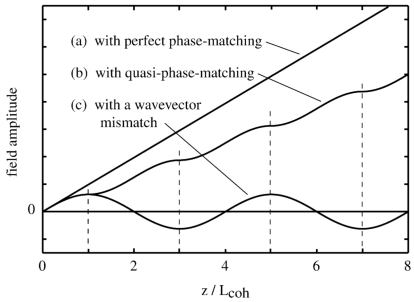

FIGURE 2.3. **Quasi phase matching. (a)** For perfect phase matching the field amplitude grows linearly while passing through the crystal. **(b)** In the quasi-phase-matched case, the wavevector mismatch is periodically compensated after a distance of $2L_{\mathrm{coh}}$ employing an artificially imprinted alternating crystal orientation. The field amplitude grows monotonically, though not as rapidly as for perfect phase matching. **(c)** In case of a wavevector mismatch the field amplitude oscillates periodically around zero, and thus, no net amplification is obtained. This figure is taken from [2, p. 86].

Fig. 2.4 depicts the wavelength-dependent refractive index of lithium niobate ($LiNbO_3$) for the range between 1.3 and 5 µm, calculated from SELLMEIER data provided by [7].

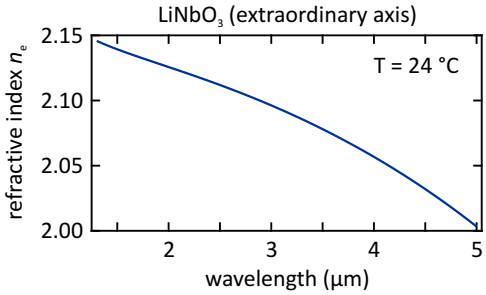

FIGURE 2.4. **Refractive index of $LiNbO_3$** along the extraordinary crystal axis at a temperature of 24 °C. Normal dispersion in the signal and idler wavelength range between 1.3 and 5 µm. The SELLMEIER data are taken from [7].

Using the calculated refractive index for lithium niobate, the wavenumbers k are plotted across the wavelength range of interest, see Fig. 2.5. As plotted in Fig. 2.5(b), the sum of the signal and idler wavenumbers $(k_{\mathrm{s}} + k_{\mathrm{i}})$ increases steadily for longer signal wavelengths, until the maximum is reached at the degeneracy point ($\lambda_{\mathrm{deg}} = 2\lambda_{\mathrm{p}}$). As we will see in the following discussion, this behavior causes donut-shaped

beam profiles, which occur asymmetrically only towards longer wavelengths with respect to the phase matching position.

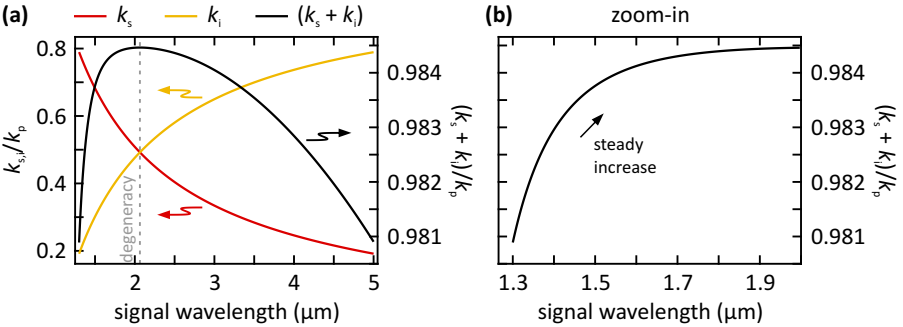

FIGURE 2.5. **Wavevectors of signal and idler in lithium niobate.** A pump wavelength of 1032 nm is assumed. **(a)** The absolute values $k_{s,i} = |\boldsymbol{k}_{s,i}|$ of the wavevectors of signal (red) and idler (yellow), as well as their sum (black) are normalized to the absolute value of the pump wavevector. The degeneracy wavelength of 2064 nm is indicated by the dashed line. At this point, $(k_s + k_i)$ is maximized. **(b)** Zoom-in to the signal range between 1.3 and 2 μm, where the $(k_s + k_i)$ is steadily increasing.

Let's consider that the QPM condition is optimized for a signal wavelength $\lambda_s = \lambda_{PM}$, i.e., the grating vector is fixed at k_g, see Fig. 2.6(a) in the center. Consequently, no phase matching can be achieved for signal wavelengths $\lambda_s < \lambda_{PM}$, as the sum

$$k_s + k_i + k_g < k_p, \tag{2.44}$$

see Fig. 2.6(a) on the left. In contrast, for $\lambda_s > \lambda_{PM}$ the wavenumber sum of signal, idler, and the grating exceeds the wavenumber of the pump

$$k_s + k_i + k_g > k_p. \tag{2.45}$$

In this case, a noncollinear wavevector geometry between pump, signal, and idler allows to maintain phase matching, even though the QPM condition is not optimized for this wavelength. This situation, known as *noncollinear phase matching* (NPM), is depicted in Fig. 2.6(a) on the right. These findings predict that the phase matching bandwidth is asymmetrically extended towards longer signal wavelengths with respect to the optimum QPM condition. In Chapter 3, we will demonstrate this asymmetry for the signal output of a FFOPO system, see Fig. 3.5 and Fig. 3.7.

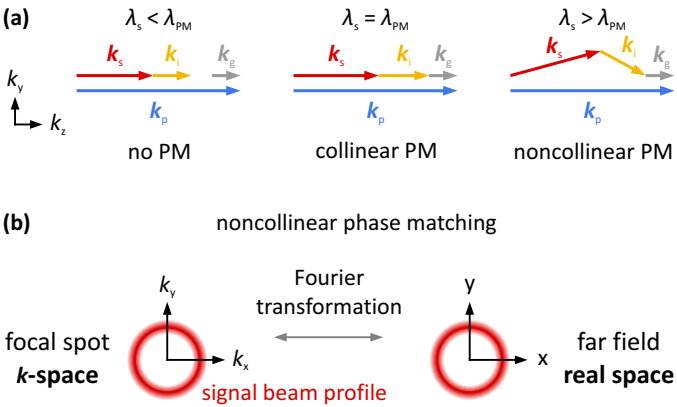

FIGURE 2.6. **Asymmetric noncollinear phase matching** in $LiNbO_3$. **(a)** QPM and the involved $\boldsymbol{k}$-vectors. The grating vector $\boldsymbol{k}_g$ is fixed for a given poling period and crystal temperature, such that optimal QPM is given for $\lambda_s = \lambda_{PM}$, which results in collinear phase matching. According to Fig. 2.5(b), signal wavelengths shorter than the phase-matched wavelength $\lambda_s < \lambda_{PM}$ lead to a phase mismatch. In case of $\lambda_s < \lambda_{PM}$, however, a noncollinear geometry between pump, signal, and idler supports phase matching. This extends the gain profile of the PPLN crystal asymmetrically towards longer signal wavelengths. **(b)** In the focal spot, noncollinear phase matching causes the signal wavevector to form a donut-shaped distribution perpendicularly to the optical axis. In the far field this donut shape manifests in the real-space beam profile.

The noncollinear wavevector geometry has implications for the beam profile of signal and idler. Fig. 2.6(b) illustrates the case of NPM for the signal in the plane perpendicular to the direction of propagation (z-axis). Both $\boldsymbol{k}$-space and real space are illustrated. In the focal spot, i.e., in the nonlinear crystal, the noncollinear geometry leads to a donut-shaped distribution in the $k_x k_y$-plane.

In the far field, the donut shape appears in the real space beam profile in the xy-plane. This can be understood if we consider the relation between near field and far field through a FOURIER transformation. Consequently, the near-field donut shape in $\boldsymbol{k}$-space transforms into a far-field donut shape in real space.

In practice, the signal output may be a combination of collinearly and noncollinearly phase matched wavelength components. Due to their different $\boldsymbol{k}$-vector orientations, these wavelength components are distributed at different spatial positions in the far field (real space) beam profile. This results in a spatially varying spectral distribution across the beam profile, which is experimentally demonstrated in Fig. 3.6 in Chapter 3.

2.4.5 *Optical Parametric Generation*

In Section 2.4.1 we have discussed the OPA process, where a weak input field (seed) is amplified by energy transfer from a strong pump field. This process, however, is also possible without the presence of an external seed field. Instead, the amplification process can be started spontaneously from quantum noise, also referred to as *spontaneous parametric down conversion* or *parametric fluorescence* [5, 8, 9]. The amplification process initiated by quantum noise is known as optical parametric generation (OPG), see Fig. 2.7. Detailed discussions of the OPG process on a quantum-mechanical as well as on a semi-classical basis can be found in [10, 11]. With a pump field of sufficiently high power level present, the spontaneously generated seed can be amplified to significant power levels. However, the signal output of OPGs is subject to strong fluctuations in the pulse-to-pulse spectra, a high level of intensity noise, and pulse-to-pulse timing jitter, as we will see in Fig. 3.8 in Chapter 3.

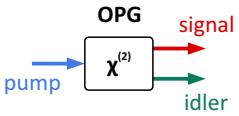

FIGURE 2.7. **Optical parametric generation (OPG) process.** An incoming pump photon is spontaneously converted into a signal-idler photon pair. Essentially, OPG represents an OPA process, where the amplification seed is provided by randomly occurring vacuum fluctuations in the crystal, rather than by an external input field.

This strong stochastic element can be assigned to the random position in the crystal,where the amplification process is initiated. On the one hand, the effective gain length in the crystal varies, resulting in a high uncertainty of the pulse energy. On the other, the random starting position induces a varying effective group delay, which leads to pulse-to-pulse timing jitter.

OPG forms the starting process for optical parametric oscillation, which will be discussed in the following section. The intrinsic randomness associated with the OPG process will be exploited for random bit sampling, as will be demonstrated in Chapter 6.

2.4.6 *Optical Parametric Oscillation*

Apart from employing optical parametric amplification (OPA) in a single-pass configuration, the amplification process can also be placed in a resonator. This is referred

to as an *optical parametric oscillator* (OPO). Here, a part of the generated optical output (signal and/or idler) is fed back as seed for the subsequent amplification process, as schematically depicted in Fig. 2.8. As discussed in the previous section, the initial seed builds up from OPG. From this point, the system will equilibrate after a finite number of roundtrips.

A singly-resonant OPO supports optical feedback for only the signal or the idler, whereas in doubly-resonant operation both channels are fed back into the gain medium. For all further discussions, we will assume a singly-resonant configuration for the signal channel.

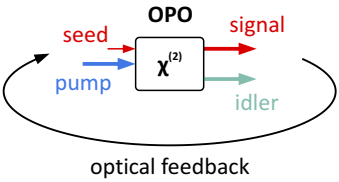

FIGURE 2.8. **Optical parametric oscillation (OPO).** Essentially, an OPO represents an OPA process, with optical feedback. In practice, the parametric gain medium is placed in a resonator and a part of the generated signal and/or idler is fed back as seed for the subsequent amplification process. The semi-transparent idler channel indicates singly-resonant operation for the signal.

For picosecond and femtosecond OPO systems *synchronous pumping* is required, where the cavity length of the OPO is matched exactly to the cavity length of the pump oscillator. This ensures temporal overlap between the pump and the signal feedback, which is required for the amplification process.

Fiber-feedback optical parametric oscillator (FFOPO) systems, as implied by their name, incorporate an optical fiber within their cavity. On the one hand, this significantly reduces the footprint of the system, as free-space propagation is kept at a minimum. On the other hand, it improves wavelength and power stability against changes in ambient conditions. Mainly, the optical fiber adds a large amount of intracavity GDD and induces spectral broadening through SPM (see Section 2.3.2). The dispersive temporal pulse broadening (chirp) separates the spectral components of the feedback pulse. This separation reduces the sensitivity of the temporal overlap of pump and feedback signal in the synchronous pumping scheme, mitigating the impact of vibrations or cavity length drifts caused by temperature changes.

Wavelength tuning in a FFOPO system is achieved by adjusting its cavity length. This essentially shifts the conditions for synchronous pumping, leading to parametric amplification at a different wavelength. Simultaneously, the phase matching condition must be adjusted to support parametric gain for the corresponding wavelength. The choice between normal and anomalous intra-cavity dispersion has implications for both pulse-to-pulse output and wavelength tuning characteristics, as will be discussed in Chapter 3.

For an extensive discussion on FFOPO systems, the reader may refer to the work carried out by T. Steinle [4], where detailed information on the oscillation conditions, power and wavelength stability, and wavelength tuning characteristics for this specific system are provided.

2.5 NONLINEAR DYNAMICS IN OPTICAL SYSTEMS

Nonlinear dynamics can be observed in everyday life in numerous situations. Systems as simple as water droplets dripping from a tap exhibit phenomena such as period doubling bifurcation or chaotic behavior depending on the flow rate [12]. As the name suggests, period doubling refers to a modulation of the outcome of a system in a way that every 2^{nd} output event is identical. Similarly, period doubling can be observed in the retinal response of the human eye upon exposure with bright flickering light [13], where the human brain acts as nonlinear self-feedback element.

Another intriguing example is the simple recursion $x_{n+1} = rx_n(1 - x_n)$, which may be used to model breeding populations. Depending on the growth rate r, period doubling bifurcation or chaotic behavior can be observed as well [14]. The well known FEIGENBAUM diagram provides a visual representation of such a nonlinear behavior [15].

Nonlinearity in combination with a self-feedback mechanism are the key properties for the occurrence of bistability, limit cycles, or chaotic behavior. Due to its nonlinearity and the optical self-feedback, it is not surprising that the FFOPO system employed in this work is subject to bistability and non-periodic pulse output. In the FFOPO system, mainly the intra-cavity nonlinearity level determines the output state. In practice, the signal output coupling ratio as well as the pump power level are the most relevant operational parameters to influence the pulse output behavior.

Fig. 2.9 depicts exemplary time traces together with the corresponding radio frequency (RF) spectra of different pulse patterns generated by the FFOPO system. The

steady state exhibits one peak at the repetition rate in its RF spectrum, in this case located at $f_{\mathrm{rep}} = 41\,\mathrm{MHz}$. Period-$N$ cycles, also known as PN cycles, exhibit additional RF frequency components at the N-th fraction of the repetition rate. Here, modulation cycles up to a P5 state are demonstrated, but also higher-order PN cycles can occur, however, they are usually less stable. The RF spectrum of a limit cycle exhibits sharp peaks as well, but they do not correspond to an integer fraction of the repetition rate. Chaos is characterized by a randomly distributed OPO signal output in terms of pulse-to-pulse energy. Therefore, the RF spectrum exhibits an evenly increased base level across the entire frequency range.

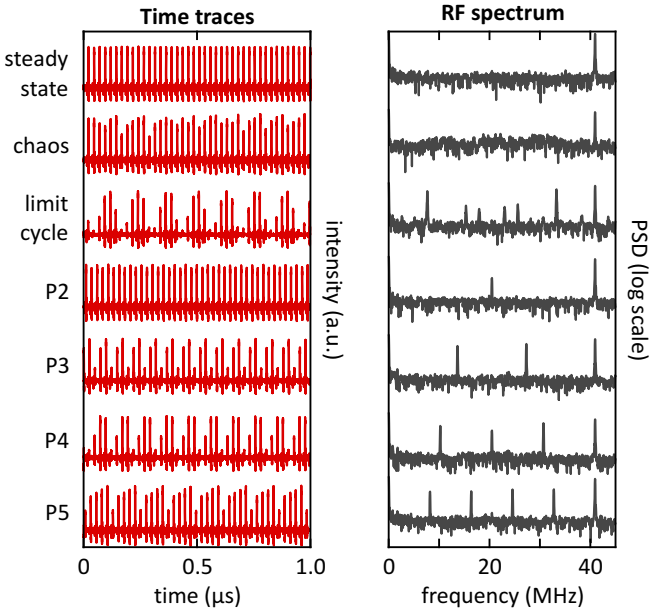

FIGURE 2.9. **Nonlinear attractors** can occur in the signal output of an FFOPO. Measured time traces and the corresponding radio frequency (RF) spectrum are plotted. In the steady state, identical signal pulses are produced at every roundtrip, corresponding to a single peak in the RF spectrum at the repetition rate of $f_{\mathrm{rep}} = 41\,\mathrm{MHz}$. Chaotic behavior is characterized by an overall increased RF base level. Limit cycles exhibit peaks at non-integer fractions of f_{rep}. PN cycles, on the other hand, repeat their output every N-th round trip. Hence, the RF spectrum exhibits $N-1$ additional peaks spaced by f_{rep}/N. Figure adopted from [16].

These output states can be categorized by so-called *attractors*. This term relates to the phase space representation of the observed equilibrium patterns. It refers to

the sub-space the system is 'attracted' to. Fig. 2.10 illustrates four different attractors observed for supercontinuum generation [17]. However, the same holds for the FFOPO system used here. The steady state is represented by one discrete point in phase space. In this context, the phase φ can be understood as the relative phase between a single frequency comb line and a defined position in the resonator. For a steady state, the accumulated phase then amounts to an integer multiple of 2π. Since for PN cycles the system reproduces its output at every N-th round trip, the phase diagram exhibits N distinct points. As mentioned above, limit cycles are characterized by modulation frequencies which are not an integer fraction of the repetition rate. This results in a closed trajectory. Chaotic attractors occupy a volume in phase space.

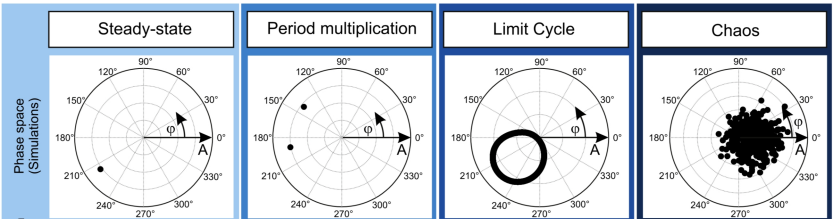

FIGURE 2.10. **Phase space representation** of the four different attractors occurring in the FFOPO. The quantity φ can be understood as the phase between a single frequency component and a defined point in the cavity. The steady state is represented by one single point in phase space. Accordingly, a PN state occupies N discrete points. A limit cycle samples a closed 1-dimensional trajectory, where chaos occupies a 2-dimensional volume. This figure is taken from [17].

2.6 STIMULATED RAMAN SCATTERING MICROSCOPY

This section first provides a short introduction on spontaneous and stimulated RAMAN scattering and their underlying physical mechanisms. Secondly, fundamental GAUSSIAN beam properties are discussed, which are directly associated with the spatial resolution and the concept of the point spread function of the 3D stimulated RAMAN scattering (SRS) microscope system used in this work to investigate biomedical and biological systems.

2.6.1 *Spontaneous Raman Scattering*

When light is scattered upon the interaction with matter, two main types of scattering are differentiated. On the one hand, in an elastic scattering process the frequency of the incident light ω_{in} is unaffected and equals the frequency of the outgoing light

$$\hbar\omega_{\text{out}} = \hbar\omega_{\text{in}}, \tag{2.46}$$

and only the propagation direction is affected. This process is referred to as RAYLEIGH scattering.

On the other hand, the scattering process may be associated with an energy transfer between the incident photon and the medium, involving an energy transition in the scattering medium. This inelastic type of scattering is known as RAMAN scattering. This includes but is not limited to vibrational transitions in molecules. The energy transfer can take place in both directions. Either the incoming photon transfers energy $\Delta E = \hbar\Omega_{\text{vib}}$ to the scattering medium, or the medium transfers energy onto the outgoing photon. This process is schematically depicted in Fig. 2.11. Ω_{vib} denotes the frequency of the oscillating relative distance between the nuclei in a molecule. Therefore, the energy of the outgoing photon can be written as

$$\hbar\omega_{\text{out}} = \hbar\omega_{\text{in}} \pm \hbar\Omega_{\text{vib}}. \tag{2.47}$$

Consequently, two shifted lines occur in the spectrum of the scattered light, known as the STOKES line with lower frequency $(\hbar\omega_{\text{in}} - \hbar\Omega_{\text{vib}})$ and the anti-STOKES line with higher frequency $(\hbar\omega_{\text{in}} + \hbar\Omega_{\text{vib}})$. In the following, we will denote the incoming frequency as 'pump' ($\omega_{\text{in}} = \omega_{\text{p}}$), as usually used in the context of RAMAN scattering.

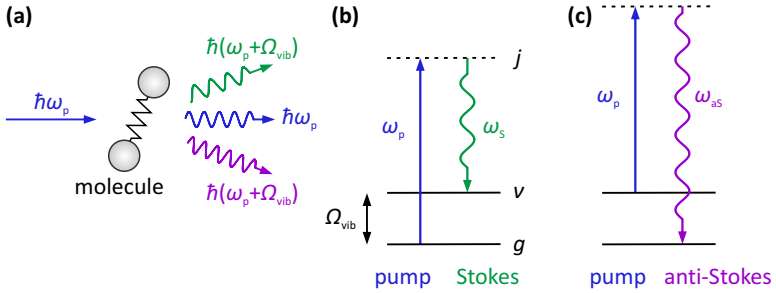

FIGURE 2.11. **Raman scattering. (a)** The incident light is scattered into RAYLEIGH (ω_p), STOKES ($\omega_\mathrm{S} = \omega_\mathrm{p} - \Omega_\mathrm{vib}$), and anti-STOKES ($\omega_\mathrm{aS} = \omega_\mathrm{p} + \Omega_\mathrm{vib}$) components. **(b)** Energy diagram for STOKES RAMAN scattering and **(c)** for anti-STOKES RAMAN scattering. The vibrational transition energy $\hbar\Omega_\mathrm{vib}$ separates the ground state g and the excited state v. Since the intermediate states j are far from electronic resonance, and thus, infinitely short-lived, they can be considered as virtual states. Figure adopted from [18, p. 166].

RAMAN scattering can be described in a classical model based on a simple harmonic oscillator. As this description provides an intuitive picture of the effect, we will shortly address the main aspects. Typically ω_p is located in the visible spectral range, e.g., 532 nm is a commonly used RAMAN pump wavelength. In contrast, the molecular vibrations are typically located in the mid- to far-infrared spectral region corresponding to wavelengths of several µm. As the pump frequency exceeds the vibrational modes by far, the nuclei of the molecule are unable to respond instantaneously to the pump field. Nevertheless, the molecular electron cloud follows the pump field adiabatically. Therefore, the RAMAN effect can be understood as a field-induced spatial modulation of the electron cloud in the molecule, which exhibits shifted frequency components due to the presence of molecular vibrational modes [18, p. 165].

With the incident pump $E(t) = E_0 \cos(\omega_\mathrm{p} t)$ the induced molecular dipole moment can be written as

$$p(t) = \alpha(t)E(t) = \alpha(t)E_0 \cos(\omega_\mathrm{p} t), \tag{2.48}$$

where $\alpha(t)$ denotes the polarizibility of the molecule. The polarizibility can be expanded to the first order in a TAYLOR series as function of the distance R between the nuclei

$$\alpha(R(t), t) = \alpha(R_0) + \frac{\mathrm{d}\alpha}{\mathrm{d}R}(R(t) - R_0) + \ldots \tag{2.49}$$

For the vibrational mode with frequency Ω_{vib}, we can assume a simple harmonic oscillator yielding

$$R(t) = R_0 + q\cos(\Omega_{\text{vib}}t), \tag{2.50}$$

where R_0 denotes the average distance between the nuclei and q represents the oscillation amplitude. With that, we can rewrite Eq. 2.48 to

$$\begin{aligned} p(t) &= \left(\alpha(R_0) + \frac{\mathrm{d}\alpha}{\mathrm{d}R} q\cos(\Omega_{\text{vib}}t)\right) E_0\cos(\omega_{\text{p}}t) \\ &= \alpha(R_0)E_0\cos(\omega_{\text{p}}t) \\ &\quad + \frac{1}{2}\frac{\mathrm{d}\alpha}{\mathrm{d}R}E_0 q\left[\cos\left((\omega_{\text{p}}+\Omega_{\text{vib}})t\right) + \cos\left((\omega_{\text{p}}-\Omega_{\text{vib}})t\right)\right], \end{aligned} \tag{2.51}$$

where the trigonometric identity $\cos x\cos y = 1/2[\cos(x+y)+\cos(x-y)]$ was used in the last step. This result demonstrates that a non-vanishing polarizibility

$$\frac{\mathrm{d}\alpha}{\mathrm{d}R} \neq 0 \tag{2.52}$$

is required for the occurrence of RAMAN sidebands.

This discussion is based on references [18, p. 166] and [19, p. 240]. Especially the latter reference provides further details on RAMAN scattering in molecules.

2.6.2 *Stimulated Raman Scattering*

The ratio of inelastically scattered photons is rather small. Even in case of condensed matter, only 1 in $\sim 10^6$ photons per 1 cm propagation length experiences a RAMAN shift [2]. Thus, if applied to spectroscopic imaging, spontaneous RAMAN scattering imaging is a slow and time consuming method. Nevertheless, the interaction cross-section can be enhanced by utilizing *stimulated* RAMAN scattering (SRS). Here, the sample is not only illuminated with the pump field ω_{p}, but the STOKES field ω_{S} is coherently added to the illumination as well. In case the photon energy difference

$$\Delta E = \hbar\omega_{\text{p}} - \hbar\omega_{\text{S}} \tag{2.53}$$

between pump and STOKES matches a RAMAN-active vibrational mode $\hbar\Omega_{\text{vib}}$, the RAMAN interaction is greatly enhanced. This process is schematically depicted in Fig. 2.12. As discussed above, the RAMAN interaction is mediated by a 'virtual' energy level, which is basically a far off-resonant energy level with an extremely short lifetime. Hence, the interaction can be treated as instantaneous.

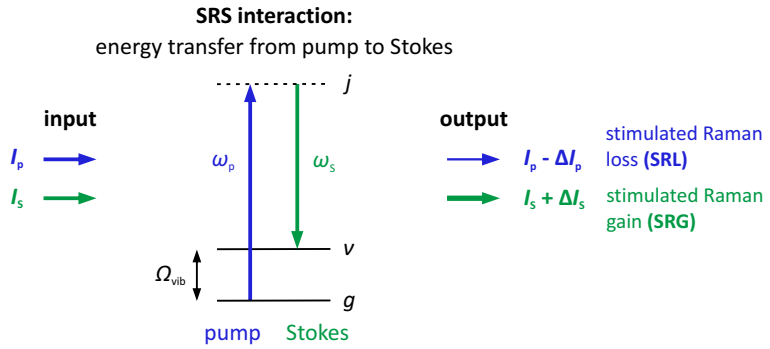

FIGURE 2.12. **SRS process.** Pump and STOKES are simultaneously incident. A vibrational transition can be driven, if the photon energy difference between pump and STOKES matches the transition energy $\hbar\Omega_{vib}$ from the ground state g to the excited state v. The SRS interaction converts a pump photon into a STOKES photon, which causes an intensity change in both channels. Quantifying this intensity change allows to trace back the RAMAN interaction strength.

The presence of the STOKES field greatly increases the probability of the emission of an additional STOKES photon. Thus, the net effect is the conversion of a pump photon into a STOKES photon, and consequently, an intensity change can be observed on the two laser beams. Measuring this intensity change allows to quantify the RAMAN interaction strength in the sample. Here, either the intensity change on the pump beam or on the STOKES beam can be detected, which is referred to as stimulated RAMAN loss (SRL) and stimulated RAMAN gain (SRG) detection, respectively.

However, this relative intensity change is usually on the order of $10^{-7} - 10^{-5}$. In order to detect the effect with high dynamic range, lock-in detection is required. This involves intensity modulation of one of the laser beams. In this work, we operate the SRS system in a SRG detection configuration, which means the pump beam is modulated. To ensure a maximum signal-to-noise ratio for SRS measurements, the intensity noise of the laser source at the modulation frequency has to be considered. Solid-state bulk oscillators have proven to be excellent front-end systems for SRS systems, as they provide shot-noise limited intensity noise performance at frequencies as low as 200 kHz [20].

Sufficient peak intensity levels are required to induce a significant SRS interaction. Hence, ultrashort laser sources are used for this purpose. Typically, pulse durations of the order of 1 ps are used, which provide the best compromise between the SRS interaction efficiency and the spectral resolution. Shorter pulses may enhance the

interaction cross-section, however, the inherently broader pulse spectrum reduces the spectral resolution.

Coherent anti-STOKES RAMAN scattering (CARS) is another coherent RAMAN process, which also requires pump and STOKES fields to be present at the illumination port. In contrast to SRS, CARS is based on the detection of the anti-STOKES line. This has the advantage that the detection channel is spectrally separated from the illumination channel (pump and STOKES). Consequently, the complexity of the detection system is greatly reduced, as a spectral filter and a photo detector suffice and no lock-in detection is required. However, CARS suffers from a non-resonant background, which overlays the anti-STOKES signal. This non-resonant background arises from a four-wave mixing parametric process [21]. Consequently, quantitative signal evaluation is not straightforward.

2.6.3 *Spatial Resolution & Point Spread Function*

Chapter 7 and Chapter 8 will discuss 3D stimulated RAMAN scattering (SRS) imaging on biological systems. In this context, the spatial resolution of the SRS microscope system in lateral as well as in axial direction are of relevance. In particular, the concept of the *point spread function* as well as the RAYLEIGH criterion will be used, which we will shortly introduce in the following.

When imaging an object onto a screen or a camera sensor, the smallest features of the object may not be reproduced accurately. This would even be the case for a perfect imaging system with no aberrations. This limitation in image resolution is intrinsically tied to image formation by means of electromagnetic waves. In particular, interference imposes a resolution constraint on any imaging system, known as the *diffraction limit*.

This can be understood, if we consider the object being made of a set of spatial frequencies, each with their own weight. As known from diffraction of light on a grating, the diffraction angle φ depends on the feature size d of the grating, the wavelength λ, and the refractive index n of the surrounding medium

$$\sin \varphi_m = \frac{m\lambda}{nd}. \tag{2.54}$$

Here, m denotes the diffraction order. Therefore, the information about the object is encoded in the different diffraction orders of different spatial frequencies.

Since an imaging system (e.g., a microscope objective) is only able to collect light up to a maximum diffraction angle, a part of the information about the object is lost. Consequently, any imaging system acts as low-pass filter for spatial frequencies. As a result, the image lacks high frequency content, and thus, fine details can only be restored to a limited extend. The amount of detail that can be retained is determined by the maximum collection angle θ of the imaging optics, which is given by the numerical aperture

$$\mathrm{NA} = n \cdot \sin\theta. \tag{2.55}$$

When imaging a point source using a circular aperture with radius a that restricts the light collection, we obtain a diffraction pattern in the far-field. The associated angular diffraction pattern is known as *Airy disk* or *Airy pattern*. Its angle-dependent intensity distribution is given by

$$I(\varphi) = I(0)\left(\frac{2J_1(ka\sin\varphi)}{ka\sin\varphi}\right)^2, \tag{2.56}$$

where $k = 2\pi/\lambda$ is the absolute value of the wavevector and $I(0)$ denotes the intensity in the center of the spot [22, p. 426]. J_1 denotes the Bessel function of the first kind, which can be found in many textbooks. Fig. 2.13 depicts the individual cross-sectional Airy patterns of two objects close to each other (light blue curves) and the resulting pattern (dark blue curve). The Airy pattern represents the point spread function (PSF) of a circular aperture. It literally states how a point source will be spread out in the far-field. Generally, the spatial low-pass filtering associated with any imaging system together with possible aberrations influence the point spread function of an imaging system. Thus, the PSF can be used to characterize the overall system transfer function for imaging a point source. The PSF finds application in microscopy, astronomy (in this case the PSF becomes directly visible when imaging point-like stars), as well as in lithography. The PSF can not only be given for the lateral direction. In fact, for 3D imaging methods the PSF along the optical axis is relevant as well, as we will see for the case of 3D SRS microscopy.

The Rayleigh criterion states that two objects are resolvable, if the maximum of the first pattern overlaps with the first minimum of the adjacent pattern. This is the case for

$$ka\sin\varphi = 3.83 \tag{2.57}$$

and is associated with in intensity drop of $\Delta = 26.4\%$ half way between the objects with respect to the maximum intensity [23–25]. This intensity modulation criterion

will be used in Section 8.4 to determine the lateral resolution of the SRS microscopy system.

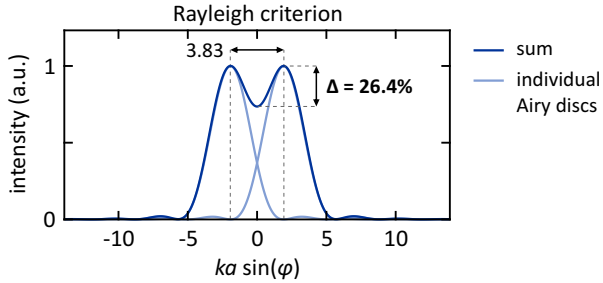

FIGURE 2.13. **Rayleigh criterion.** The Airy patterns of two close-by objects are plotted. In case the maximum of one pattern overlaps with the first minimum of the other pattern (given for $ka \sin \varphi = 3.83$), the two objects are just resolvable according to the Rayleigh criterion. This case is associated with a modulation depth of $\Delta = 26.4\%$.

In the context of SRS imaging, the PSF is only indirectly determined by the individual focal spot size of the two laser beams. In fact, the nonlinear interaction volume defines the spatial resolution, which depends on additional influences apart from the geometric beam properties. In particular, the exact spatial overlap of the two foci in lateral as well as in axial direction strongly influences the resulting 3-dimensional PSF. Furthermore, GAUSSIAN beams are used for the illumination of the samples. In contrast to plane waves, a GAUSSIAN beam exhibits a varying lateral intensity distribution, which causes an additional deviation from the theoretical Airy disk-shaped diffraction pattern. In practice, we will experimentally determine the spatial resolution in lateral and axial direction and apply the RAYLEIGH criterion as measure for the spatial resolution.

2.6.4 *Gaussian beams*

As already mentioned, two laser beams are required for SRS microscopy. They can be described by GAUSSIAN beams. In order to understand the beam geometry and the requirements for optimizing the SRS signal, we will shortly discuss their main characteristics.

The electric field of a GAUSSIAN beam along the propagation axis z and the transversal axis r is given by [26]

$$E(r,z) = E_0 \cdot \frac{w_0}{w(z)} \cdot \mathrm{e}^{-\left(\frac{r}{w(z)}\right)^2} \cdot \mathrm{e}^{-ik\frac{r^2}{2R(z)}} \cdot \mathrm{e}^{-i(kz-\zeta(z))}. \tag{2.58}$$

Considering $I \propto |E|^2$, the corresponding intensity yields

$$I(r,z) = I_0 \cdot \left(\frac{w_0}{w(z)}\right)^2 \cdot \mathrm{e}^{-\frac{2r^2}{w(z)^2}}, \tag{2.59}$$

as plotted in Fig. 2.14.

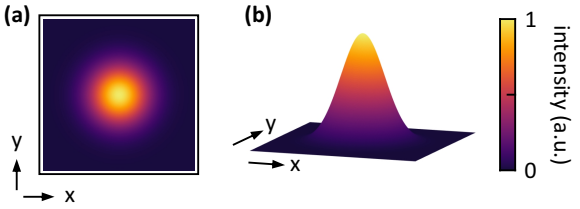

FIGURE 2.14. **Gaussian beam – transversal profile.** **(a)** Top view on the transversal intensity profile. **(b)** Side view.

The beam waist

$$w(z) = w_0\sqrt{1 + \left(z/z_\mathrm{R}\right)^2} \tag{2.60}$$

denotes the distance from the optical axis, for which the intensity drops down to $1/\mathrm{e}^2 \approx 13.5\%$, as depicted in Fig. 2.15(a). At the focal position, i.e., at $z = 0$, the beam waist reaches its minimum w_0. The RAYLEIGH range

$$z_\mathrm{R} = \frac{\pi w_0^2 n}{\lambda} \tag{2.61}$$

denotes the distance along the optical axis from the focal spot at which the waist increases to

$$w(\pm z_\mathrm{R}) = \sqrt{2} \cdot w_0, \tag{2.62}$$

as indicated in Fig. 2.15(a). At this position the beam area increases by a factor of 2 with respect to the beam area in the focal spot. Here, λ and n denote the wavelength and the refractive index, respectively.

The curvature $1/R(z)$ of the wavefronts is often given on terms of the corresponding radius of curvature

$$R(z) = z\left(1 + \left(z_\mathrm{R}/z\right)^2\right), \tag{2.63}$$

as plotted in Fig. 2.15(b). The curvature at the focal spot ($z = 0$) is zero, and therefore, R diverges. At this position, plane wavefronts are present. At positions $z = \pm z_\mathrm{R}$ the curvature reaches is maximum, correspondingly, R exhibits a minimum.

An additional phase shift is picked up by the wavefronts, while propagating through a focal spot. This phase shift is referred to as GOUY phase

$$\zeta(z) = \arctan\left(z/z_\mathrm{R}\right). \tag{2.64}$$

Consequently, a phase shift of π is accumulated between far-field positions on either side of the focal spot.

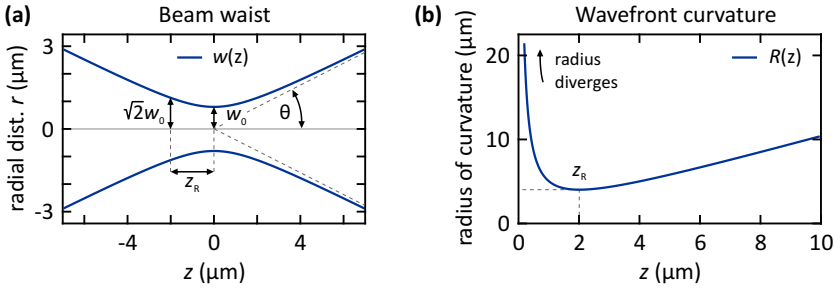

FIGURE 2.15. **Gaussian beam geometry. (a)** The beam waist $w(z)$ along the propagation axis z reaches its minimum value w_0 in the focal spot. The RAYLEIGH range z_R and the divergence angle θ are indicated as well. **(b)** The wavefront curvature is plotted in terms of the radius of curvature. In the focal spot at $z = 0$ plane wavefronts are present. The radius reaches its minimum at $z = \pm z_\mathrm{R}$. Wavelength: 1 µm, w_0: 0.8 µm.

The divergence angle, as indicated in Fig. 2.15(a), is determined by the waist in the far-field

$$\theta = \lim_{z\to\infty} \arctan\left(\frac{w(z)}{z}\right). \tag{2.65}$$

Evaluating the argument yields

$$\begin{aligned}\lim_{z\to\infty}\frac{w(z)}{z} &= w_0 \cdot \lim_{z\to\infty}\frac{\sqrt{1+\left(z/z_\mathrm{R}\right)^2}}{z}\\ &= w_0 \cdot \lim_{z\to\infty}\sqrt{1/z_\mathrm{R}^2+1/z^2}\\ &= \frac{w_0}{z_\mathrm{R}},\end{aligned} \tag{2.66}$$

and hence, the divergence angle yields

$$\theta = \arctan\left(w_0/z_\mathrm{R}\right). \tag{2.67}$$

In the context of laser scanning imaging based on SRS microscopy, the focal spot size depends on the numerical aperture (NA) of the illumination optics. In the following, we will discuss the relationship between the NA and the GAUSSIAN beam waist. For an immersion medium of refractive index n, the NA is given by

$$\mathrm{NA} = n \cdot \sin(\theta). \tag{2.68}$$

For the case of air as immersion medium ($n = 1$), substituting Eq. 2.67 and Eq. 2.61 yields

$$\mathrm{NA} = \sin\left(\arctan\left(w_0/z_\mathrm{R}\right)\right) = \sin\left(\arctan\left(\lambda/(\pi w_0)\right)\right). \tag{2.69}$$

Consequently, the waist w_0 decreases for shorter wavelengths if the NA is kept fix. In case of SRS microscopy, the mode overlap of two laser beams with different wavelengths has to be optimized within the RAYLEIGH range for a maximum SRS signal level. In particular, the waists of both beams have to be matched within the RAYLEIGH range. Therefore, a higher NA is required for the longer wavelength laser beam. In practice, this is achieved with individually tailored beam diameters at the entrance pupil of the microscope objective.

The beam waist can be experimentally determined using the so-called *knife edge* method. Fig. 2.16 depicts the measurement principle. A knife edge is placed in the beam and the transmitted power is measured depending on the exact position of the blade. From the resulting power profile the beam waist can be reconstructed. This method will be used in Chapter 7 to characterize the beam parameters for SRS imaging.

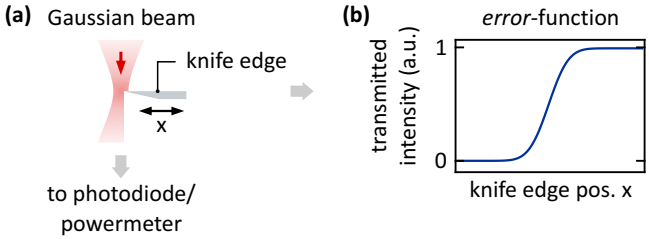

FIGURE 2.16. **Knife edge measurement. (a)** The GAUSSIAN beam is successively blocked by a knife edge, where the transmitted power is monitored depending on the knife edge position x. **(b)** The resulting transmitted intensity profile is analytically given by an *error*-function. From this, the GAUSSIAN beam waist can be extracted.

The transmitted power is given by the 2-dimensional integral of the transversal intensity profile, as given by Eq. 2.59, where the integration in one direction is limited by the knife edge position x. This integral can be expressed in terms of the so-called *error*-function $\mathrm{erf}(x)$

$$P(x) = \int_{-\infty}^{\infty}\int_{-\infty}^{x} I(x',y')\mathrm{d}x'\mathrm{d}y' = \frac{P_0}{2}\left(1+\mathrm{erf}\left(\frac{x-x_0}{w}\right)\right). \tag{2.70}$$

Here, P_0 denotes the total optical power associated with the beam under investigation, x_0 marks the center of the beam, and w denotes the beam waist. In practice, these quantities are used as fitting parameters, yielding the desired beam waist.

Note, that this method is also used to determine the beam quality, i.e., how close the actual beam geometry is to an ideal GAUSSIAN beam. The beam parameter product (BPP) provides a quantitative measure for the beam quality and is defined as

$$\mathrm{BPP} = w_0\theta = M^2\cdot\frac{\lambda}{\pi}. \tag{2.71}$$

An ideal GAUSSIAN mode yields $M^2 = 1$ and allows the smallest possible focal spot size. Deviations from this ideal mode result in values $M^2 > 1$.

2.7 SIGNAL PROCESSING & SAMPLE STATISTICS

In the chapters ahead, several quantities are being used to define measurement accuracy and the spread of data points. Therefore, this section aims to give a short overview on these quantities, which are:

- mean or expectation value,

- variance and standard deviation,
- root mean square (RMS) value,
- full-width at half-maximum (FWHM) value.

Furthermore, we will shortly discuss the signal-to-noise ratio associated with single-photon counting and SRS imaging.

2.7.1 *Mean, Standard Deviation, Variance & RMS*

In the following, we consider a discrete set of data points, i.e., a random variable X, which might represent sampled data points acquired in an experiment. The mean μ, also referred to as the expectation value $\mathrm{E}(X)$, is defined as

$$\mu = \mathrm{E}(X) = \sum_{i=1}^{N} p_i \cdot X_i, \tag{2.72}$$

where p_i denotes the individual probability of the outcome X_i. In case of equal probability for all outcomes, this equation simplifies to

$$\mu = \frac{1}{N} \sum_{i=1}^{N} X_i, \tag{2.73}$$

where N represents the total number of data points/samples. Clearly, the mean value does not make any statement about the spread of the data points. Hence, effects of noise on the accuracy of the measurement are not accounted for. Therefore, the *variance*

$$\begin{aligned} \mathrm{Var}(X) &= \mathrm{E}\left((X-\mu)^2\right) = \frac{1}{N}\sum_{i=1}^{N}(X_i-\mu)^2 \\ &= \mathrm{E}(X^2) - \Big(\mathrm{E}(X)\Big)^2 \\ &= \mathrm{E}(X^2) - \mu^2 \end{aligned} \tag{2.74}$$

can be used, as it measures the average (positive) distance of the data points from the mean value, and thus, the variance directly represents a measure for the spread of the samples. In order to obtain meaningful units, which can be directly compared to the data points or their mean, usually, the *standard deviation* is used instead of the variance. The standard deviation is defined as

$$\sigma_X = \sqrt{\mathrm{Var}(X)}. \tag{2.75}$$

Obviously, σ is measured in the same units as X. For two *uncorrelated* random variables X and Y the variance of their sum can be expressed as the sum of their individual variances

$$\mathrm{Var}(X+Y) = \mathrm{Var}(X) + \mathrm{Var}(Y) = \sigma_X^2 + \sigma_Y^2 = \sigma_{X+Y}^2, \tag{2.76}$$

which allows to disentangle multiple individual contributions to an overall random quantity, as will be discussed in Section 5.7.2 in the context of electronic timing jitter. In literature as well as in device specifications, timing jitter is often given in terms of the *root mean square* (RMS) value. The RMS of a random variable X is defined as

$$X_{\mathrm{RMS}} = \sqrt{\mathrm{E}(X^2)} = \sqrt{\frac{1}{N}\sum_{i=1}^{N} X_i^2}. \tag{2.77}$$

In contrast to the standard deviation, the RMS value also includes bias, which directly follows from Eq. 2.74, Eq. 2.75, and Eq. 2.77

$$X_{\mathrm{RMS}}^2 = \sigma_X^2 + \mu^2. \tag{2.78}$$

Hence, in case of a zero mean value, the RMS value and the standard deviation become identical

$$\sigma_X = \sqrt{\frac{1}{N}\sum_{i=1}^{N}(X_i-\mu)^2}\Bigg|_{\mu=0} = X_{\mathrm{RMS}}. \tag{2.79}$$

Another quantity, that measures the spread of data points is the FWHM value. It is the most intuitive visual measure to characterize the width of a distribution of samples. As its name suggests, it is given by the width at half of its maximum value. In case of a GAUSSIAN (normal) distribution

$$f(x) = \frac{1}{\sigma\sqrt{2\pi}} \exp\left(-\frac{(x-\mu)^2}{2\sigma^2}\right), \tag{2.80}$$

the relation between the FWHM and the standard deviation is given by

$$\mathrm{FWHM} = 2\sqrt{2\ln 2}\cdot\sigma \approx 2.355\cdot\sigma. \tag{2.81}$$

2.7.2 *Signal-to-Noise Ratio & Central Limit Theorem*

Within the scope of this thesis, the measurement sensitivity of SRS imaging (see Chapter 7 and Chapter 8) or single-photon counting (see Chapter 5) is ultimately limited by the signal-to-noise ratio. Inherently occurring random noise imposes a limit

on the detection of weak signals. In this context, it is important to understand the relationship between this noise background and, for instance, the measurement time.

The central limit theorem (CLT) represents one of the key theorems in probability theory. For our purposes, it provides a quantitative description of the properties of random noise. Therefore, the key aspects of the CLT shall be briefly discussed in the following.

The CLT states that for large samples of independent and indentically distributed variables, their sum approaches a normal distribution, as given by Eq. 2.80. This holds even if the original probability of a single sample is not normally distributed. The following discussion is based on [27], where the interested reader may find further details on this topic.

Assume a sequence of *independent* and *identically distributed* variables $\{X_1, \ldots, X_n\}$, where each X_i has a mean value μ and a variance given by σ^2. Both, μ and σ are required to be finite. For n repetitions, the resulting mean value is given by

$$\mu_n = n \cdot \mu. \tag{2.82}$$

The same holds for the variance

$$\sigma_n^2 = n \cdot \sigma^2, \tag{2.83}$$

which implies

$$\sigma_n = \sqrt{n} \cdot \sigma \tag{2.84}$$

for the standard deviation.

3

SPECTRO-TEMPORAL TRANSIENT DYNAMICS IN A FFOPO

This chapter is based on the following published work:

> **M. Floess**, T. Steinle, and H. Giessen
> *Spectrally resolved ultrafast transient dynamics of a femtosecond fiber-feedback optical parametric oscillator*
> Opt. Express **31**, 44680–44692 (2023).

3.1 ABSTRACT

We report on spectrotemporal transient dynamics in a femtosecond fiber-feedback optical parametric oscillator (FFOPO) system. Burst modulation of the pump beam in combination with dispersive FOURIER transformation (DFT) sampling allows to record single-pulse signal spectra at 41 MHz sampling rate. Therefore, each individual pulse of the signal transients can be spectrally resolved. We characterize the signal output behavior for anomalous as well as for normal intra-cavity dispersion. Amongst steady state output we observe period-doubling cycles and other attractors, which occur at higher intra-cavity nonlinearity levels. The experimental findings are supported by numerical simulations, in order to identify the linear and nonlinear effects, which govern the wavelength tuning behavior of this FFOPO system. We find that steady state operation is preferred and that the wavelength tuning stability of the FFOPO dramatically increases when using a normal dispersion feedback fiber.

3.2 INTRODUCTION

Transient dynamics are an inherent part of nonlinear optical systems. Whenever operational conditions change, the system is driven to a new equilibrium state. Stable and repetitive steady state operation may emerge from initially stochastic and chaotic starting conditions. The transient dynamics of numerous different nonlinear systems have been investigated. This includes the buildup of femtosecond mode locking in a Ti:Sapphire oscillator [28], where the transition from cw modes to stable pulsed

operation has been demonstrated. These investigations are not restricted to laser oscillators only, parametric light sources have been investigated as well. In particular, the spectrotemporal buildup of a picosecond free-space optical parametric oscillation (OPO) system based on chirped quasi-phase matching has been reported [29]. They observe oscillatory signal output behavior. Furthermore, O'Donnel et al. reported on the spectrotemporal evolution of femtosecond pulses in a fiber-feedback OPO system in the normal and anomalous dispersion regime [30].

Due to stochastic influences the transients are usually non-repetitive events and may fluctuate statistically over time. This imposes challenges to observe these processes, as real-time sampling on the time-scale of a cavity roundtrip is necessary. Therefore, dispersive FOURIER transformation (DFT) is employed, as it provides sufficiently fast sampling and allows to extract spectral information of single-shot events [31, 32].

In particular, the starting process of optical parametric oscillation is governed by optical parametric generation (OPG), also known as spontaneous parametric down-conversion, where the conversion of a pump photon into a signal-idler photon pair takes place in the nonlinear crystal [11]. During subsequent cavity roundtrips the spontaneously generated signal is being amplified until the system reaches its equilibrium state, where gain and losses balance each other.

In this work, we investigate the ultrafast transient dynamics of a femtosecond FFOPO system as well as its equilibrium wavelength tuning characteristics. We demonstrate how normal dispersion feedback strongly suppresses modulation states in the signal output pulse train as well as how it increases the wavelength stability upon changing pump power levels. Throughout this work, the terms "transient" and "equilibrium" are used to denote the signal buildup process and the final state of the output pulse train, respectively. In particular, the equilibrium may comprise steady state pulse output, i.e., a pulse train of identical pulses, as well as modulated pulse trains such as period-N (PN) cycles. PN cycles are characterized by their signal output being modulated and reproduced after every N^{th} cavity roundtrip. Furthermore, we numerically simulate the FFOPO system in order to identify the dominating effects, which govern the signal output characteristics. In case of anomalous feedback, apart from steady state output, we observe period-doubling and -tripling attractors as well as the formation of limit cycles. In contrast to PN cycles, limit cycles exhibit modulation periods with a non-integer multiple of the roundtrip period [33–35]. Applications, such as nonlinear spectroscopy, sensing, and multi-photon imaging rely on pulse output stability. Therefore, understanding the complex interplay between parametric

gain and nonlinear optical feedback with regard to steady state operation and wavelength tuning characteristics is key. Our results provide insights into how to efficiently stabilize the FFOPO system.

3.3 MATERIALS & METHODS

3.3.1 *Fiber-feedback Optical Parametric Oscillator*

The FFOPO is singly-resonant for the signal and is synchronously pumped by an 8-W, 450-fs Yb:KGW bulk oscillator which operates at 1032 nm center wavelength and at a repetition rate of 41 MHz [36], as depicted in Fig. 3.1(a). The FFOPO is built in linear cavity configuration employing a 10-mm long MgO-doped periodically poled lithium niobate (PPLN) crystal as parametric gain medium [37], as illustrated in Fig. 3.1(b). A variable output coupler allows to adjust the intra-cavity signal power. In the following, the feedback ratio (FBR) is used as a measure for the intra-cavity signal power. It relates to the output coupling ratio (OCR) via

$$\mathrm{FBR} = 1 - \mathrm{OCR}. \tag{3.1}$$

The largest part of the cavity is wound up in a single-mode fiber, which acts as dispersive and nonlinear feedback element. Here, group delay dispersion (GDD) temporally separates the spectral components of the feedback pulse, such that its temporal overlap with the pump pulse effectively determines which wavelength components are being amplified. Hence, wavelength tuning is achieved by adjusting the cavity mismatch between the pump oscillator and the FFOPO cavity, and temperature control of the PPLN crystal for phase matching optimization.

The intra-cavity fiber coupling efficiency of the signal amounts to 40%. Given by the linear cavity configuration, two fiber coupling sites are involved per roundtrip, which results in signal power losses of 84% per roundtrip. The FFOPO system can be operated in the anomalous and in the normal dispersion regime employing a SMF-28 or an UHNA7 feedback fiber, respectively.

As the feedback fiber provides by far the largest contribution to the overall intra-cavity GDD, swapping the fiber allows to investigate the FFOPO dynamics depending on the intra-cavity dispersion. Note, that the material-specific nonlinear refractive index n_2 is the same for both fibers. Hence, switching between the two fibers allows to isolate and measure the influence of the sign of the intra-cavity GDD. Due to different mode field radii (5 µm for SMF-28, 1.6 µm for UHNA7), $\sim$ 10 cm of SMF-28 fiber is spliced to both ends of the UHNA7 fiber. This ensures identical mode matching between pump and signal in the gain crystal for both feedback fibers. Nevertheless, the splices cause increased linear transmission losses for the UHNA7 fiber, which amount to 25% at 1550 nm relative to the SMF-28 fiber. Since the feedback fibers

are not polarization-maintaining, polarization rotation of the signal feedback may occur depending on the fiber bending. Only p-polarized signal feedback components contribute to the polarization-selective parametric conversion process (type-0 phase matching), whereas s-polarized components are rejected as cavity losses. In the following experiments, bending and placement of the feedback fibers are therefore carefully optimized in order to minimize polarization rotation.

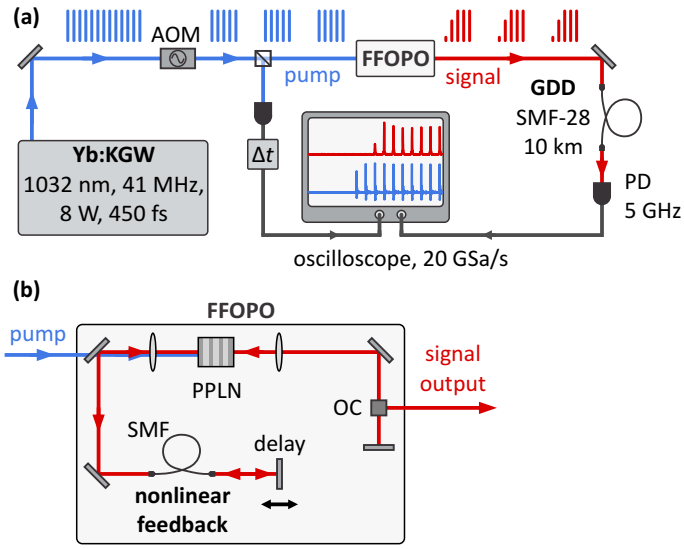

FIGURE 3.1. **Pump burst generation and dispersive Fourier transformation (DFT) sampling of the signal transients. (a)** An Yb:KGW bulk oscillator (1032 nm center wavelength, 41 MHz repetition rate) provides the pump pulses (blue) for a FFOPO. An acousto-optical modulator (AOM) generates pump bursts. The resulting signal transients (red) are recorded using the DFT technique, which employs a 10-km SMF 28 fiber, a 5-GHz photodiode and a 20 GSa/s oscilloscope for sampling of the dispersively time-stretched signal pulses. The corresponding pump burst is recorded as well, where the propagation time difference Δt between pump and signal is compensated in post-processing. **(b)** Detailed schematic of the synchronously pumped FFOPO based on a MgO:PPLN crystal. A variable output coupler (OC) allows to adjust the intra-cavity signal power level. Wavelength tuning is achieved by changing the crystal temperature and a variable end mirror to adjust the cavity mismatch between the FFOPO and the pump oscillator. Most of the FFOPO cavity consists of a single-mode fiber (SMF), which provides nonlinear optical feedback.

3.3.2 *Pump Burst Generation*

In order to investigate its intrinsic transient behavior, the FFOPO has to be driven from its off-state to full pump power availability within one laser cycle. Therefore, the pump laser needs to be switched on the time scale of the temporal pulse spacing, i.e., 24.4 ns. This is realized using an acousto-optical modulator (AOM) in the pump beam. The focal spot size in the AOM crystal is chosen such that the power throughput is optimized and coating damage is avoided, while maintaining a short rise time of $\sim$ 20 ns. This is sufficient to generate pump bursts with minimal depletion of the first pulse, as depicted in Fig. 3.2(a). An arbitrary waveform generator (AWG) (Zurich Instruments, UHFAWG) is employed to provide the electronic control of the AOM.

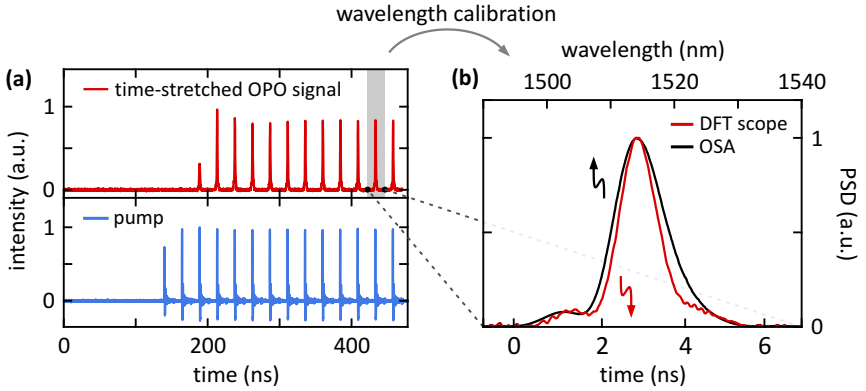

FIGURE 3.2. **DFT wavelength calibration. (a)** Exemplary time traces of the dispersively stretched FFOPO signal and the pump laser after time delay compensation. **(b)** Absolute wavelength calibration of the single-pulse trace is done by matching it with the average spectrum acquired by an optical spectrum analyzer (OSA).

Furthermore, using the first diffraction order of the AOM ensures 100% modulation depth in the pump intensity, such that the FFOPO cavity is emptied completely in between subsequent pump bursts. The driving electronics of the AOM are synchronized to the pump laser repetition rate, in order to ensure precise shuttering between two subsequent pump pulses.

3.3.3 *Single-pulse Spectral Measurements*

In order to quantify the transient dynamics of the FFOPO signal, single-pulse spectra are recorded. This is realized using the dispersive FOURIER transformation (DFT)

technique. Essentially, a large amount of GDD is exerted on the femtosecond signal pulses, such that the pulses are temporally stretched to the nanosecond regime, where electronic sampling of individual pulses becomes feasible, see Fig. 3.3. With this technique, single-pulse spectra can be recorded with an acquisition bandwidth that corresponds to the pulse repetition rate, i.e., 41 MHz in our case.

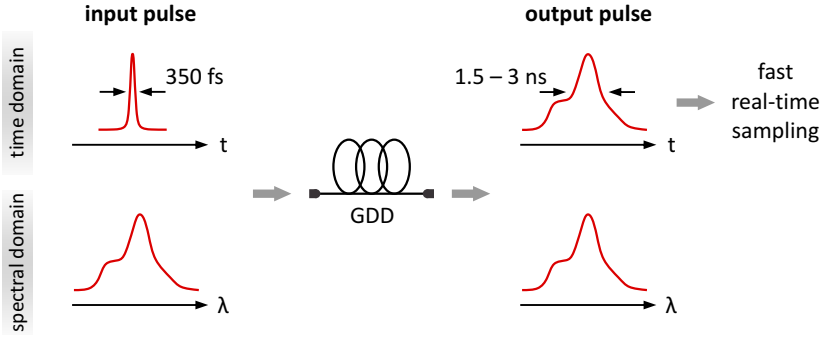

FIGURE 3.3. **DFT – principle.** A femtosecond input pulse propagates through a long single-mode fiber, where it experiences a large amount of group delay dispersion (GDD). The dispersion temporally separates the spectral components by nanoseconds. In this regime, fast electronic sampling allows to measure the relative arrival time of the spectral components, which essentially maps the spectral distribution of the individual pulse into the time domain. During the propagation through the fiber, the pulse does not change its spectral distribution.

We realize the DFT scope using a 10-km long single-mode fiber (SMF-28e, Corning). The temporal separation of the spectral components of a 1520 nm signal pulse amounts to 160 ps/nm. This means the initial 350-fs OPO signal pulses with a typical bandwidth of $10 - 15$ nm are temporally stretched to $1.5 - 3$ ns. The transient is sampled in real time with a fast InGaAs photodiode (5 GHz, Thorlabs, DET08CFC) and a 20-GSa/s oscilloscope (Infiniium DSO9404A). The resulting spectral resolution of $\Delta\lambda = 1$ nm is determined by the overall GDD and the electronic sampling bandwidth. The corresponding pump burst is recorded on a second oscilloscope channel.

As the FFOPO signal pulses propagate through the DFT fiber, their arrival time at the oscilloscope input is delayed by $\Delta t \approx 49$ µs relatively to the corresponding pump burst. Precise temporal matching of the time-stretched signal pulses to the pump burst is done in post processing.

The extraction of the single-pulse spectra from the recorded signal time trace is schematically depicted in Fig. 3.2(a). The wavelength calibration is carried out in two steps. First, the recorded time axis is mapped onto a relative wavelength axis via the GDD characteristics of the 10-km SMF-28 fiber. In the second step, absolute wavelength calibration is achieved by matching the average of several equilibrium single-pulse traces to a time-averaged spectrum acquired by an optical spectrum analyzer (Ando AQ6317), as depicted in Fig. 3.2(b). Further details on the data processing can be found in [16].

3.3.4 *DFT Scope – Spectral Artifacts*

The quantitative agreement between the single-pulse spectra recorded by the DFT scope and the time-averaged spectra acquired by the optical spectrum analyzer decreases for longer wavelengths. This is caused by the formation of donut-shaped

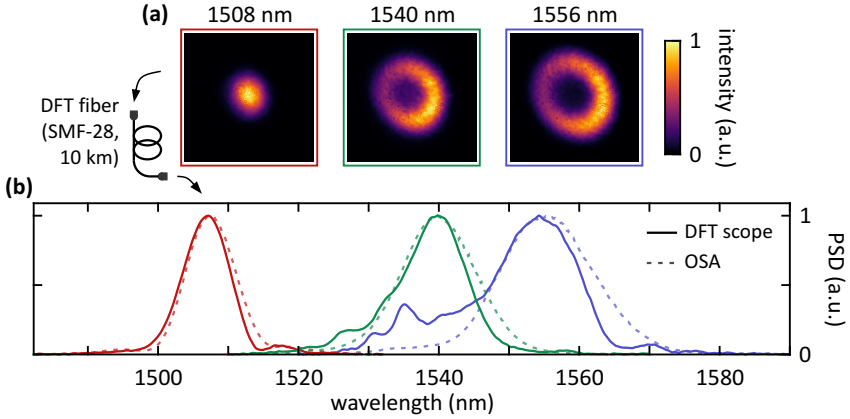

FIGURE 3.4. **DFT scope – spectral distortions due to reduced fiber incoupling efficiency.** **(a)** Signal output beam profiles at different wavelengths. **(b)** Corresponding signal spectra acquired by the DFT scope (solid lines) and by the optical spectrum analyzer (OSA) (dashed lines). Longer wavelengths result in increasingly pronounced donut-shaped beam profiles, which exhibit spectral variations across the mode profile. The resulting inefficient fiber incoupling leads to spatial mode filtering. Therefore, spatial mode filtering translates into unwanted spectral filtering. 1508 nm: the fundamental mode can be efficiently coupled into the DFT fiber, which is confirmed by a good spectral agreement between the DFT scope and the OSA. 1540 nm: spectral deviations arise, which become even more pronounced at 1556 nm. Pump power: 650 mW (unmodulated equivalent), anomalous dispersion feedback. The data points at 1508 nm and 1540 nm correspond to the transients depicted in Fig. 3.9, top row.

transverse modes at longer wavelengths, which cannot be coupled efficiently into the single-mode DFT fiber. As the donut-shaped modes exhibit spectral variations across the beam profile, spectral deviations occur, as demonstrated in Fig. 3.4. However, the transient duration, relative wavelength shifts, and relative spectral changes in the single-pulse spectra can still be assessed qualitatively.

In order to ensure quantitatively meaningful single-pulse spectral measurements, the sampling system itself, i.e., the DFT fiber and the sampling oscilloscope, must not alter the pulse spectra. First, nonlinear interaction between the propagating femtosecond pulses and the DFT fiber may change the spectral distribution, and thus, deteriorate the quantitative data evaluation. For example, self-phase modulation (SPM) causes a nonlinear broadening of the spectrum. Secondly, electronic artifacts may alter the shape of the sampled time traces. In particular, steep slopes resulting from high optical peak power levels on the photodiode cause electronic ring-down. Both effects, optical and electronic nonlinearities, start to influence the measurement for average DFT fiber input power levels of $> 1\,\mathrm{mW}$. Thus, the power level is kept at this value in order to maximize the signal-to-noise ratio (SNR) without deteriorating the measurement.

3.3.5 *Numerical Simulations*

In order to identify the dominant linear and nonlinear optical effects, which govern the dynamics in the FFOPO cavity, we numerically simulate the signal buildup in the FFOPO system, starting from quantum noise until the output reaches its equilibrium. Therefore, the commercially available software *RP Pro Pulse V2* is used, which numerically solves the nonlinear SCHRÖDINGER equation (NLSE) for the pulse propagation in the FFOPO cavity. The simulation uses a 1-dimensional approach, and therefore, spatial effects affecting the beam profile are neglected.

The simulation takes the following aspects into account:

- parametric gain (PPLN crystal),
- group velocity mismatch (GVM) between pump, signal, and idler,
- SPM and GDD in the feedback fiber,
- linear cavity losses.

The refractive index data for the PPLN crystal used in the simulation are taken from [38, 39]. Furthermore, we use the simulation to demonstrate the asymmetry of

the parametric gain with respect to temporal delays of different spectral components, which is depicted in Fig. 3.12 and discussed in Section 3.5. As will be demonstrated in Fig. 3.11, the FFOPO signal output exhibits not only steady state attractors, but also modulated pulse trains, such as period-doubling (P2) states. This behavior is replicated by the simulation as well, as has been demonstrated by Tobias Steinle [4], where further details on the implementation of the simulation of the FFOPO system can be found.

3.4 RESULTS

3.4.1 *Wavelength Tuning Characteristics*

In the first step, the output behavior of the FFOPO system in the equilibrium state is characterized, i.e., a continuous pump pulse train drives the FFOPO without burst generation by the AOM. In particular, the interplay between the phase matching condition and the cavity mismatch, both of which are control parameters for wavelength tuning, and their impact on the signal output characteristics are investigated. Therefore, the phase matching condition in the PPLN crystal is set to one specific working point, i.e., the crystal temperature and the grating period are kept constant, whereas the cavity mismatch is adjusted to sweep the signal wavelength across the spectral gain window. Fig. 3.5(a) depicts an optical parametric generation (OPG) spectrum (black solid line), which is acquired at an average pump power of 650 mW and at a crystal temperature of 40 °C. The OPG spectrum represents the spectral distribution for which the gain crystal supports parametric amplification of the signal for the given parameter set (crystal length, grating period, crystal temperature) without any optical feedback. Its maximum at 1517 nm marks the spectral position with optimal phase matching. At the short-wavelength slope the simulated OPG spectrum agrees well with the measured spectrum. However, the simulation underestimates the gain towards longer wavelengths, since spatial effects are not considered. In particular, the deviation at longer wavelengths arises from noncollinear phase matching (NPM), which will be discussed later.

Fig. 3.6 demonstrates this behavior experimentally. Here, the transversal spectral dependence of the OPG signal is measured employing an aperture in the FOURIER plane. Noncollinear $\boldsymbol{k}$-vector components tend to undergo NPM, and thus, the spectral variations can be spatially assessed in the FOURIER plane. Furthermore, increasing the pump power also increases the relative amount of noncollinearly phase-matched signal components, which results in an overall redshift, see Fig. 3.6(b).

For these fixed phase matching settings, the signal output power level is measured across the signal wavelength tuning range. As mentioned above, the wavelength is changed only by adjusting the cavity mismatch between the FFOPO and the pump oscillator. Fig. 3.5(a) depicts the signal output power for normal (green) and anomalous dispersion (blue) feedback. For both cases, the output power is measured with an optimized feedback ratio (solid lines), and with a feedback ratio of 25% (dashed lines).

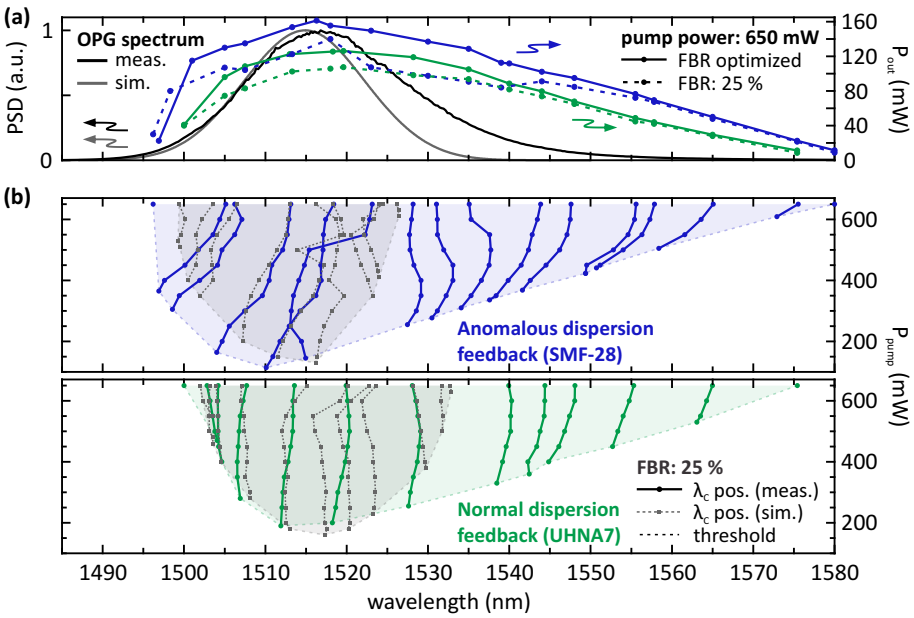

FIGURE 3.5. **Wavelength tuning behavior for normal and anomalous dispersion feedback. (a)** Measured OPG spectrum (black) for 650 mW pump power, 40 °C crystal temperature, and fixed poling period, and simulated OPG spectrum (gray). Signal output power for a fixed feedback ratio (FBR) of 25% (dashed lines), and for an optimized FBR (solid lines) for both, anomalous and normal dispersion feedback (blue and green). In both cases, the maximum signal output power level is reached at the gain maximum, i.e., at $\sim$ 1518 nm. Wavelength tuning is done solely by changing the cavity mismatch. **(b)** Signal center wavelength depending on the pump power level for anomalous dispersion (upper panel) and for normal dispersion (lower panel) feedback at a FBR of 25%. Simulations are plotted in gray. The threshold pump power level corresponds to the envelope (dashed lines).

The anomalous dispersion feedback results in a maximum output power level of 160 mW, where the normal dispersion feedback yields 125 mW. Maximum output occurs at $\sim$ 1517 nm, where the measured OPG spectrum exhibits its peak. Owing to its higher linear transmission losses, operation with the UHNA7 feedback fiber results in slightly reduced output power, higher threshold pump power levels, and a narrower wavelength tuning range compared to the SMF-28 fiber. Fig. 3.5(b) demonstrates the behavior of the signal center wavelength upon pump power variations. The feedback ratio is kept constant at 25%. Each branch corresponds to a fixed cavity mismatch position, for which the pump power is reduced from 650 mW down to the respective

threshold power level. As expected, the lowest threshold is reached in the region around the gain maximum. The signal output is strongly asymmetrically extended towards longer wavelengths up to $\sim$ 1580 nm. In contrast, the simulation yields a symmetrical tuning range, which does not cover signal wavelengths higher than $\sim$ 1530 nm. The implications of spatial effects on this behavior will be discussed later.

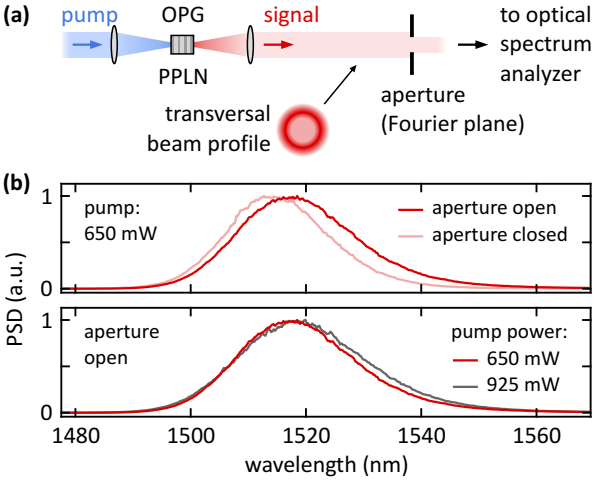

FIGURE 3.6. **OPG spectrum – transversal dependence. (a)** The transversal spectral dependence of the OPG signal is analyzed by placing an aperture in the FOURIER plane, which allows to separate noncollinear k-vector components from collinear components. **(b)** Upper panel: an open aperture allows noncollinearly phase-matched signal components to enter the spectrometer, which shifts the spectral weight towards longer wavelengths (red) with respect to collinear spectral components only (light-red). Lower panel: higher pump power levels increase the relative amount of noncollinearly phase-matched signal components, which also results in an overall redshift (gray).

Furthermore, anomalous dispersion feedback tends to cause skewed branches and mode jumps upon pump power variations. In contrast, normal dispersion feedback exhibits stable signal wavelengths for varying pump power levels. Apart from that, a global wavelength shift is observed between the tuning curves of the anomalous and the normal dispersion case. In particular, the tuning curve for anomalous dispersion is shifted to shorter wavelengths with respect to the normal dispersion case. Both findings, wavelength stability and the global wavelength shift, are reproduced by the simulations.

Signal output beam profiles for several different wavelengths across the tuning range are depicted in Fig. 3.7. Fundamental mode profiles are observed only for shorter wavelengths. For increasing wavelengths, donut-shaped beam profiles emerge and gradually become more pronounced. In case of normal dispersion feedback the donut mode onset occurs at already shorter wavelengths ($\sim$ 1518 nm) than for anomalous dispersion feedback ($\sim$ 1523 nm).

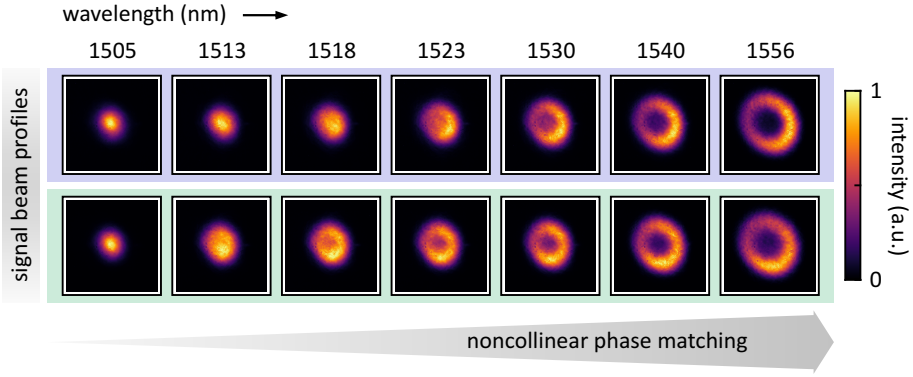

FIGURE 3.7. **Signal output beam profiles** at different wavelength positions for both, normal and anomalous dispersion feedback. Noncollinear phase matching (NPM) asymmetrically extends the parametric gain towards longer wavelengths, which results in donut-shaped beam profiles. In case of normal dispersion feedback, this effect is observed at already shorter wavelengths. The simulations do not include spatial effects, i.e., NPM is neglected. This explains the discrepancy at longer wavelengths between experiment and simulations, as apparent in the OPG spectrum in Fig. 3.5(a) as well as in the wavelength tuning range in Fig. 3.5(b).

3.4.2 *Optical Parametric Generation – Single-pulse Spectra*

In the second step, the starting process of optical parametric oscillation (OPO), i.e., optical parametric generation (OPG) is investigated on the single-shot scale. In particular, single-pulse spectra of the OPG output are recorded using the DFT scope. For this purpose, the FFOPO, as depicted in Fig. 3.1, can be employed. Therefore, the feedback port of the FFOPO is blocked, such that no optical feedback is possible. Hence, each pump cycle drives the OPG process without any seed input. As described in Section 2.4.5 the down-conversion of a pump photon into a signal-idler photon pair is seeded by the vacuum noise present in the crystal. The output coupling ratio is set to 100%, such that the generated signal is fully available at the signal output port, see Fig. 3.1.

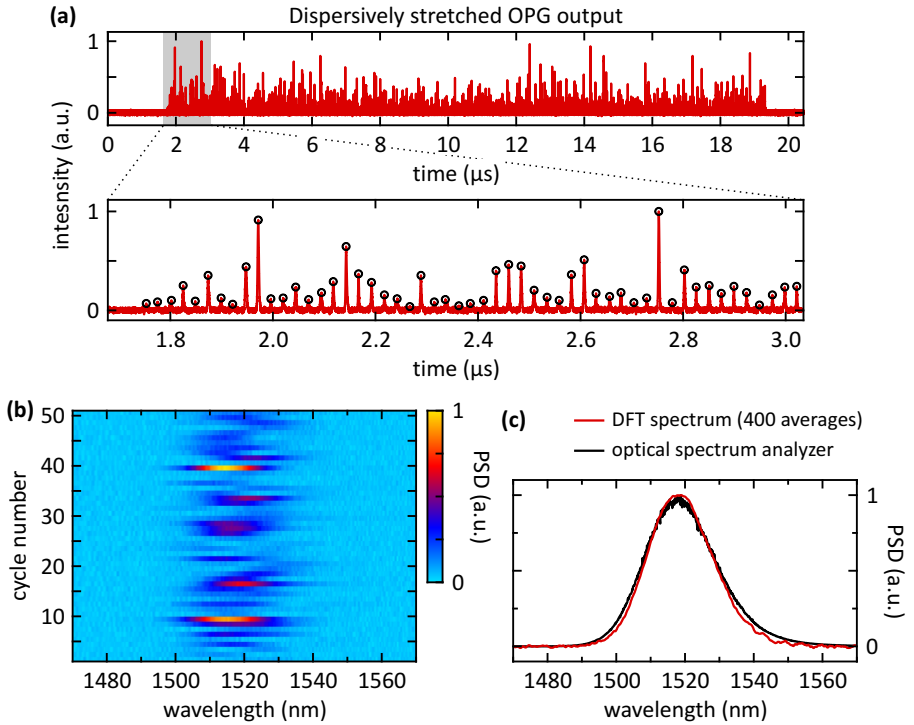

FIGURE 3.8. **DFT spectra of an OPG pulse train. (a)** A dispersively stretched OPG pulse train of 720 pulses is recorded. The first 50 cycles are depicted in the lower panel. The peaks are marked as a guide to the eye, which show the randomly distributed pulse energies. **(b)** Corresponding single-pulse spectra for the first 50 OPG cycles. **(c)** The average of 400 single-pulse spectra agrees well with the (time-averaged) spectrum acquired by an optical spectrum analyzer (free-space incoupling). Pump power: 900 mW, beam waist in the crystal: $\sim 20\,\mu$m, crystal temperature: 40 °C.

Fig. 3.8 depicts single-pulse spectra of the OPG output acquired by the DFT scope. As apparent from the recorded pulse train in panel (a), the pulse energy exhibits strong fluctuations. The same holds for the pulse-to-pulse spectral distribution, as depicted in Fig. 3.8(b). These fluctuations are caused vacuum noise seeding, which occurs randomly at any position in the crystal. Therefore, the further parametric amplification depends on the remaining distance in the gain crystal. Linnenbank et al. [8] demonstrated how cw injection seeding at only low power levels dramatically stabilizes the output characteristics of such an OPG. Fig. 3.8(c) depicts the average spectral distribution of the OPG output, which agrees well with the time-averaged

spectrum acquired with an optical spectrum analyzer. The same is given for the measured OPG spectrum plotted in Fig. 3.5(a). In a sense, the gain spectrum of the gain crystal, i.e., the resulting average OPG spectrum, is mapped out by the randomly distributed individual OPG signal pulse spectra.

3.4.3 *Transient Process – FFOPO Signal Buildup*

In the following, the transient behaviour of the FFOPO signal output is investigated. Therefore, the AOM is used to generate pump bursts, which drive the FFOPO from the off-state into equilibrium. Each individual pulse of the resulting signal transients

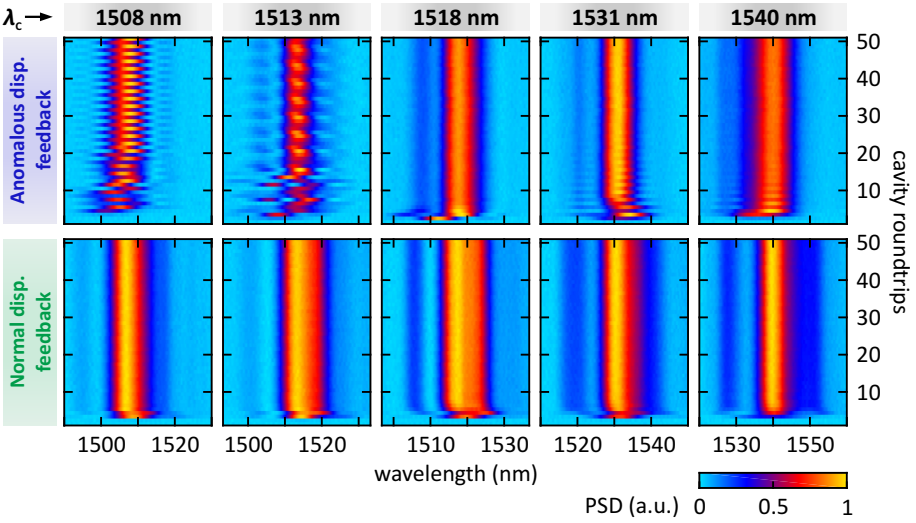

FIGURE 3.9. **Spectrotemporal buildup at different wavelengths measured for anomalous and normal dispersion feedback.** Wavelength tuning is done by adjusting the cavity mismatch only, while the phase matching condition (poling period and crystal temperature) is kept constant. Constant pump power (650 mW, unmodulated equivalent) and constant feedback ratio (25%). The cavity roundtrip count starts with the first pulse of the corresponding pump burst. Amongst steady states, anomalous dispersion feedback tends to support different equilibrium attractors, such as P2 cycles (1508 nm). Furthermore, transient P2 states (1531 and 1540 nm) or limit cycles (1513 nm) are observed, which eventually subside into steady states. Note, that the transient limit cycle at 1513 nm extends across $\sim$ 160 roundtrips, which is fully shown in Fig. 3.10. In contrast, normal dispersion produces stable steady state output across all wavelengths. A high single-pass gain supports ultrafast transients of $<$ 10 roundtrips for normal dispersion, and $<$ 20 roundtrips for anomalous dispersion.

is spectrally resolved using the DFT scope. Fig. 3.9 depicts the spectrotemporal signal buildup process for both, anomalous and normal dispersion feedback, at different wavelengths between 1508 and 1540 nm. The same settings as for Fig. 3.5(a) are used, i.e., the pump power is set to 650 mW (unmodulated equivalent), the feedback ratio is set to 25%, and wavelength tuning is solely achieved by adjusting the cavity mismatch. Hence, Fig. 3.9 depicts the transients which correspond to 5 exemplary working points plotted in Fig. 3.5(a).

The anomalous dispersion feedback tends to support additional attractors rather than steady states only. At this point, one has to differentiate between the equilibrium attractor, i.e., the state which the signal eventually ends up in, and the transient attractor. In this case, different attractors may occur during the transient process, which finally subside into the equilibrium attractor. At 1508 nm a period-2 (P2) cycle emerges, where a signal pulse is reproduced every 2^{nd} roundtrip. An extremely long transient limit cycle is observed at 1513 nm. Note, that only 50 roundtrips are plotted, which do not cover the entire transient in this case. The corresponding full transient is depicted in Fig. 3.10. In contrast, normal dispersion seems to stabilize the signal output to steady state operation across all wavelengths.

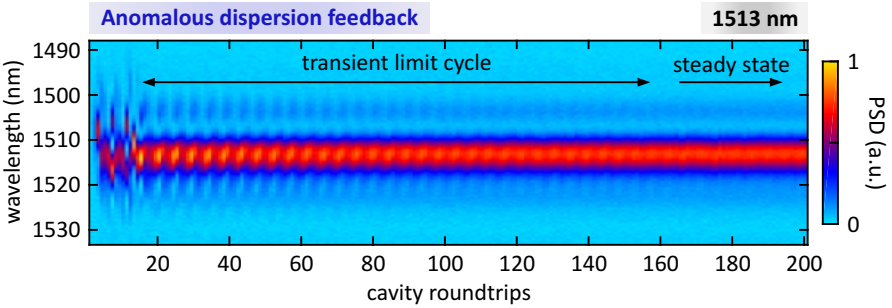

FIGURE 3.10. **Full transient limit cycle at 1513 nm for anomalous dispersion feedback.** Fig. 3.9 depicts only the first 50 cavity roundtrips. However, this limit cycle subsides into a steady state on a timescale of ~ 160 cavity roundtrips. Transients on this timescale are rarely observed. Usually the transient process takes place on timescales of $10 - 20$ cavity roundtrips.

In both cases, ultrafast transients are observed, despite the high intrinsic intra-cavity losses of $> 80\%$ per roundtrip. Anomalous dispersion supports transients with typically only < 20 roundtrips. In case of normal dispersion feedback, the signal output is equilibrated even faster within < 10 roundtrips.

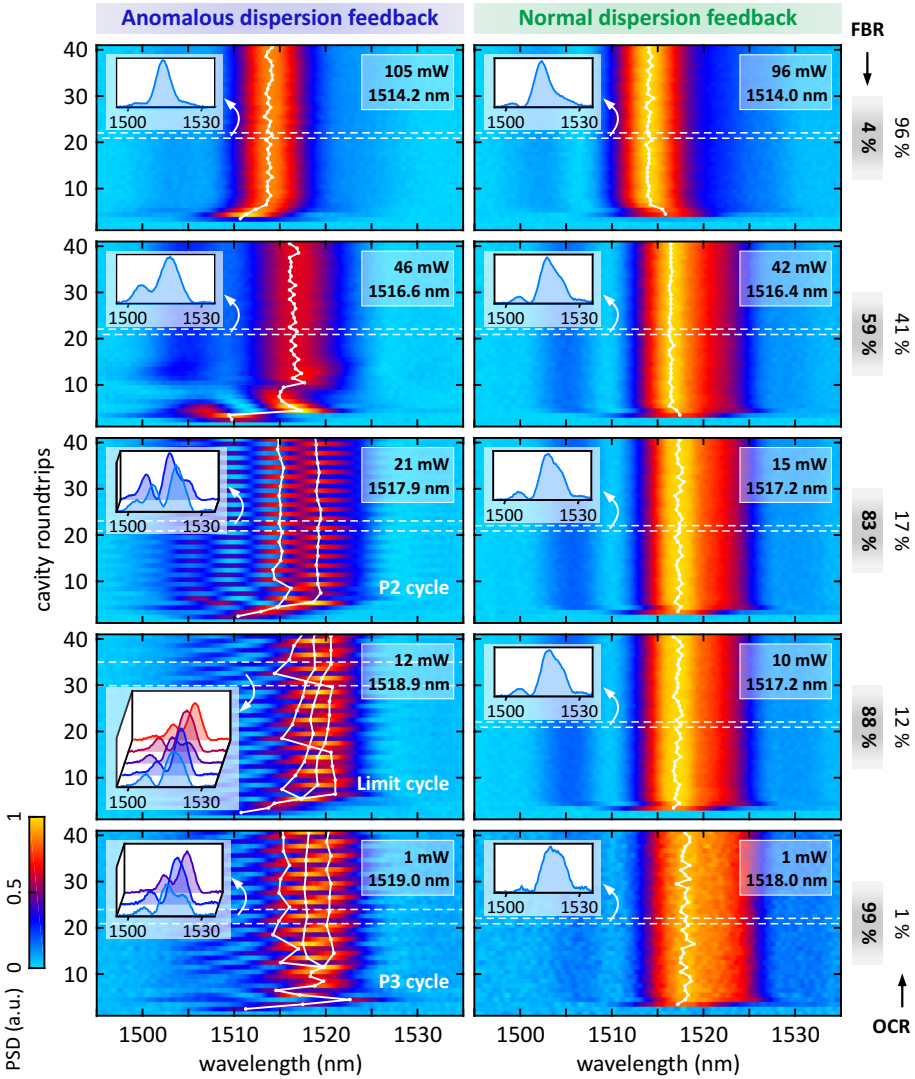

FIGURE 3.11. **Influence of the intra-cavity signal power on the spectrotemporal buildup measured for anomalous and normal dispersion feedback.** Constant pump power (550 mW, unmodulated equivalent), and constant cavity mismatch. The feedback ratio (FBR) is increased from 4% to 99%. Therefore, the intra-cavity signal power, and hence, the nonlinearity increases correspondingly. Equilibrium values for the signal output power and the center wavelength are stated for each measurement. Insets: exemplary individual equilibrium spectra as indicated by the horizontal dashed lines. As a guide to the eye, the spectral peak positions of all individual pulses are marked (white dots) and connected (solid white lines) in order to highlight the different emerging attractors.

In the following, the influence of increasing intra-cavity nonlinearity on the spectrotemporal buildup is investigated. Therefore, the feedback ratio is varied using the variable output coupler. As before, the experiment is carried out for both, anomalous and normal dispersion feedback, as depicted in Fig. 3.11. The pump power is set to a constant value of 550 mW. The cavity mismatch is fixed, such that the signal output runs at $\sim$ 1514 nm at minimum feedback ratio.

In accordance with the previous measurement, the equilibrium states are reached within $5 - 15$ cavity roundtrips. For an increasing feedback ratio, the signal output power drops accordingly. In case of anomalous dispersion feedback, several different attractors arise for increasing intra-cavity signal power levels. In particular, a P2 cycle is observed for a feedback ratio of 83%, as indicated by the branching spectral peak positions. The inset depicts the two corresponding alternating spectra, which exhibit pronounced spectral modulations. A further increase of the intra-cavity signal power leads to the formation of a limit cycle and eventually a P3 state at feedback ratios of 88%, and 99%, respectively. In contrast, normal dispersion feedback exhibits stable steady state operation even at high intra-cavity nonlinearity, which is favored by the smaller mode field radius of 1.6 µm. In both cases, the center wavelength shifts towards the gain maximum at 1517 nm. Interestingly, for each measured transient the first detected signal pulse is centered around $\sim$ 1510 nm and $\sim$ 1517 nm for anomalous and for normal dispersion feedback, respectively. From there, the center wavelength shifts towards its equilibrium value.

3.5 DISCUSSION

In the following, the most significant effects, which govern the equilibrium and the transient signal output behavior of the FFOPO system shall be discussed. As demonstrated in Fig. 3.5(a) and (b), the signal wavelength tuning range and the OPG spectrum are asymmetrically extended towards longer wavelengths. This asymmetry is caused by NPM, as illustrated in Fig. 2.6 in Section 2.4.4. Here, the phase mismatch at longer wavelengths is compensated by the involved $\boldsymbol{k}$-vectors adding up in a noncollinear geometry rather than being aligned [40, 41]. Thus, NPM provides parametric gain beyond the collinear phase matching bandwidth. This effect is governed by the dispersive properties of the lithium niobate crystal in the infrared spectral region, which restricts the gain extension to the long-wavelength side of the gain window. In $\boldsymbol{k}$-space the noncollinear geometry forms a donut-shaped profile in the focal spot. Therefore, NPM manifests in the formation of donut-shaped transversal beam profiles in the far field in real space, as depicted in Fig. 3.7. These donut-shaped beam profiles are associated with a transversal spectral variation, as demonstrated in Fig. 3.6. This effect increases towards longer wavelengths, where parametric gain via NPM dominates. The formation of these modes does not gradually build up across several cavity roundtrips. In fact, it results from each single-pass amplification process, since the signal feedback is spatially filtered by the single-mode feedback fiber at each roundtrip. Since the simulation does not consider spatial effects including NPM, the simulated OPG spectrum as well as the tuning range are limited by collinearly phase matched parametric gain, as depicted in Fig. 3.5(a) and (b), respectively.

Intra-cavity group delay dispersion (GDD) in the feedback fiber introduces a chirp to the feedback pulse, which leads to relative delays in the arrival times in the gain crystal between different spectral components. This has implications on the parametric gain. In particular, leading spectral components experience higher gain than trailing components. This effect is simulated and depicted in Fig. 3.12. Hence, the sign of the intra-cavity GDD determines whether the short- or the long-wavelength components experience higher gain. Effectively, this GDD-induced temporal gain asymmetry leads to a global wavelength shift of the tuning range between normal and anomalous dispersion operation, as evident from Fig. 3.5(b). In particular, normal dispersion feedback causes a redshift with respect to anomalous dispersion feedback. This behavior is reproduced by the simulations, which are plotted and shaded in gray. Furthermore, in case of normal dispersion feedback the temporal gain asymmetry favors NPM at already shorter wavelengths than in case of anomalous dispersion feedback. Hence, donut-shaped beam profiles already occur at 1518 nm for normal dispersion, whereas

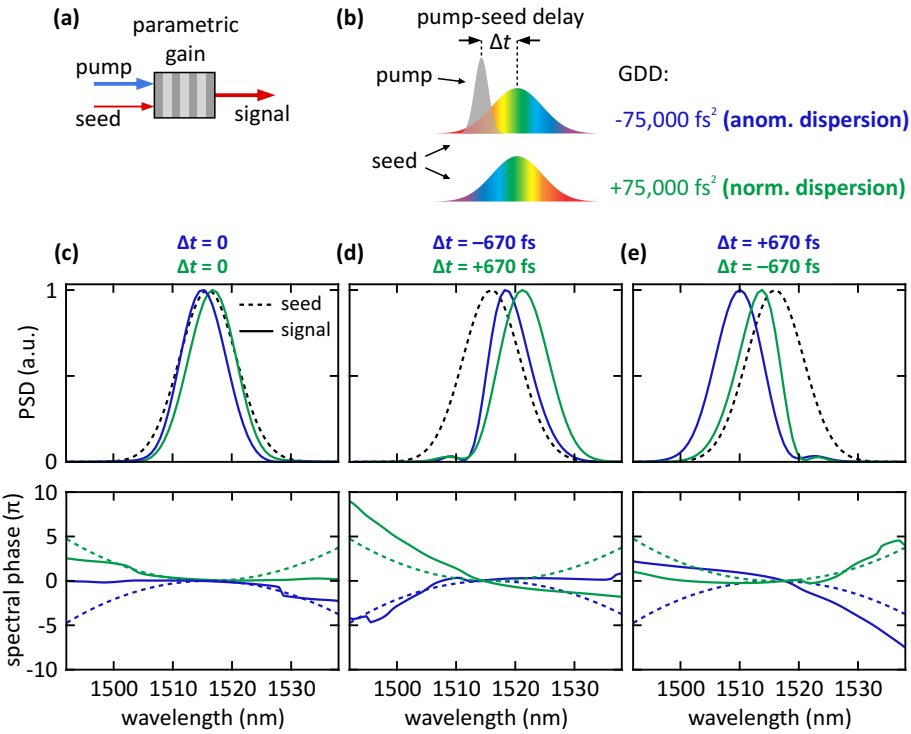

FIGURE 3.12. **Simulation of a single-pass OPA process with chirped seed input** to demonstrate the temporal asymmetry of the parametric gain in the FFOPO, i.e., leading spectral components experience higher parametric gain than trailing components. **(a)** Schematic of the OPA process. **(b)** The simulation considers a FOURIER-limited input pulse to which $\pm 75,000\,\mathrm{fs}^2$ of GDD are applied (normal/anomalous dispersion). The absolute value corresponds to the negative GDD introduced by 4 m of SMF-28 fiber at 1516 nm. Therefore, two cases are considered, i.e., an up-chirped and a down-chirped seed pulse, where the longer wavelength components arrive first and vice versa. Thus, the gain characteristics can be assessed depending on the relative arrival time of the different spectral components of the seed pulse. Adjusting the relative pump-seed timing Δt allows to replicate different cavity mismatch positions in the FFOPO cavity. The pump-seed delay of $\pm 670\,\mathrm{fs}$ corresponds to a cavity mismatch of $\pm 200\,\mu\mathrm{m}$. **(c)** Applying anomalous dispersion to the seed pulse results in a blueshift in the signal output with respect to the case of normal dispersion. This behaviour is reproduced at different working points at higher wavelengths **(d)**, and at lower wavelengths **(e)**. The spectral phase is plotted in the bottom row, where the parabolic curves indicate the linearly chirped seed pulses.

for anomalous dispersion they are observed starting from 1523 nm, as depicted in Fig. 3.7.

The signal wavelength stability upon pump power variation strongly differs between operation with anomalous and normal dispersion feedback, as can be assessed from Fig. 3.5(b). Here, the interplay between GDD and SPM in the feedback and parametric gain dictates the output behavior. Additionally to the chirp caused by GDD, SPM induces an up-chirp to the center part of the feedback pulse. Depending on the sign of the GDD, this SPM-induced chirp further enhances (for positive GDD) or partially counteracts (for negative GDD) the GDD-induced chirp. For increasing pump power, the counteracting chirp arising from SPM increases as well. The SPM-induced chirp shifts longer wavelengths towards the temporal gain window of synchronous pumping, i.e., the pump pulse now overlaps with longer-wavelength parts of the signal feedback pulse. Therefore, the center wavelength of the signal output drifts towards higher values for increasing pump power levels. This behavior can be observed in the measurements (skewed blue branches) as well as in the simulation (gray branches). Furthermore, the nonlinear coupling between gain, SPM, and negative GDD leads to wavelength jumps and even crossing branches, where two cavity mismatch positions lead to the same output center wavelength.

In contrast, the SPM-induced chirp acts in the same direction as the chirp induced by positive GDD. On the one hand, this causes the spectral components of the feedback pulse to separate even faster. On the other hand, the accompanying (faster) decrease in peak power in turn terminates the SPM interaction faster as well. The stronger mode confinement (1.6 µm mode field radius) in the UHNA7 fiber, and therefore, the increased SPM response enhances this mechanism even further. This self-terminating mechanism stabilizes the signal output center wavelength against changing SPM contributions, and thus, against varying pump power levels. Both, measurement (green branches) and simulation, exhibit almost no dependence of the signal center wavelength on the pump power level.

The interplay between SPM and GDD also manifests in the transient process on the timescale of individual signal pulses, as shown in Fig. 3.9. As discussed above, anomalous dispersion feedback gives rise to counteracting chirp contributions from GDD and SPM, which renders the pulse-to-pulse stability sensitive to changing control parameters. In particular, modulation states such as P2 cycles are observed into which the signal output equilibrates. Furthermore, the transients themselves may exhibit clearly patterned attractors, such as P2 states and limit cycles. Interestingly, the

observed limit cycle at 1513 nm represents an unstable intermediate state. The initial buildup takes around $\sim$ 15 roundtrips and launches the limit cycles, which by itself is not long-term stable, but rather subsides into a steady state attractor as the final equilibrium. This happens on a timescale of $\sim$ 160 roundtrips, which is fully plotted in Fig. 3.10. In contrast, normal dispersion feedback seems to stabilize the signal output on the pulse-to-pulse timescale as well, i.e., only steady states are observed. As discussed above for the equilibrium output, SPM and positive GDD both exert chirp on the pulse in the same direction, and therefore, stabilize the pulse-to-pulse spectral evolution. Even though the intra-cavity losses are on the order of 90% per roundtrip including the output coupler [42], the transition from the buildup into equilibrium takes place on the order of 10 roundtrips for normal dispersion feedback, and 20 roundtrips for anomalous dispersion. This ultrafast transient process is facilitated by the extremely high single-pass gain of up to 50 dB [43].

In the next step, the impact of varying intra-cavity signal power on the spectrotemporal buildup will be discussed, as presented in Fig. 3.11. Here, only the output coupling ratio is varied, whereas all other operational parameters are kept constant. As before, the transients exhibit a distinct behavior depending on the sign of the intra-cavity GDD. The gradual increase of the feedback ratio decreases the signal output power from initially $\sim$ 100 mW at a feedback ratio of 4% down to 1 mW at a feedback ratio of 99%. At the same time, SPM in the feedback fiber is being driven more strongly.

In both cases, the first detected signal pulse is centered around 1510 nm for anomalous dispersion feedback, and around 1517 nm for normal dispersion feedback. This behavior is expected and can be understood as follows: The buildup starts from OPG, which is not influenced by the optical feedback. Therefore, the spectral distribution of the initial seed is the same for all cases, and thus, the starting points are expected to be located always at roughly the same spectral position. Subsequently, the feedback fiber directs the temporally asymmetric gain in one or the other direction, depending on the sign of its GDD. During the subsequent roundtrips, the given cavity mismatch enforces a final pump-seed overlap, such that the signal output is directed towards a specific wavelength. Also, in both cases, the competing effect between optimal parametric gain and the center wavelength dictated by the cavity mismatch can be observed. The center wavelength shifts towards the gain maximum at $\sim$ 1518 nm for increasing feedback ratios, where gain saturation sets in. At the same time, spectral backconversion starts, i.e., energy conversion from the signal and idler fields back to the pump field via sum-frequency generation [44–46], which manifests in dips in the signal spectrum, as depicted in the inset spectra in Fig. 3.11. Relatively to these wave-

length components, longer signal wavelengths experience higher gain, and therefore, the spectral weight of the output shifts towards the gain maximum at $\sim 1517\,\mathrm{nm}$. This can be clearly seen in the inset spectra in case of normal dispersion output, where the spectral weight gradually shifts towards longer wavelengths away from the region of spectral backconversion. Thus, steady state operation is favored even at high intracavity nonlinearity levels.

In contrast to that, anomalous dispersion supports higher gain for shorter wavelengths, where spectral backconversion occurs. As evident from the inset spectra, this results in strongly modulated spectra. At some point, this results in different spectra after subsequent amplification cycles, which may lead to the formation of PN states and limit cycles. A P2 state is observed at a feedback ratio of 83%, which is characterized by branching of the spectral peak positions. Accordingly, the P3 cycle at a feedback ratio of 99% exhibits three separate branches of different output spectra. The limit cycle at a feedback ratio of 88%, on the other hand, exhibits crossing branches, which represent the characteristic non-integer period multiplication. Generally, these modulated output attractors are stable over time, given that the ambient conditions are well controlled. Changes in the ambient temperature can suffice to influence the output attractor. In contrast, steady state attractors are usually stable within larger regions of the parameter space given by the operational parameters.

Clearly, the FFOPO signal output exhibits a higher stability when operated with normal dispersion feedback than with anomalous dispersion feedback. This is evident from the wavelength tuning behavior as well as from the dynamics on the pulse-to-pulse timescale. For most applications and measurements, well-defined wavelength tuning characteristics with decoupled control parameters are desirable. Therefore, normal dispersion feedback is the superior choice for this FFOPO system. However, beam profile alterations due to NPM have to be considered and minimized. Therefore, during wavelength tuning the phase matching condition needs to be readjusted carefully, in order to ensure the working point to be located on the short-wavelength side of the spectral gain window.

Nevertheless, the tendency of anomalous dispersion feedback to support P2 cycles may also be employed as a desired feature. In fact, all-optical intensity modulation at the Nyquist frequency is possible without the need for fast electronics, and thus, electronic cross-talk between the modulator and the detection unit is avoided. This scheme can be employed for modulation spectroscopy applications, such as stimulated RAMAN scattering spectroscopy as demonstrated in [47].

3.6 CONCLUSIONS & OUTLOOK

We have presented the transient signal dynamics in a femtosecond FFOPO system. Using pump bursts allows to drive the FFOPO from the cold-cavity state into equilibrium. The resulting ultrafast signal transients have been recorded with the dispersive FOURIER transformation (DFT) technique, which provides spectral resolution for each individual signal pulse. We have demonstrated the impact of intra-cavity normal and anomalous dispersion in the optical feedback on the pulse-to-pulse dynamics, and on the wavelength tuning behavior. Anomalous dispersion feedback gives rise to oscillatory output pulse patterns, such as period-N states and limit cycles. By supporting the experimental data with numerical simulations, we have identified SPM and GDD to be the dominating effects which govern the dynamics of the FFOPO system. Noncollinear phase matching (NPM) asymmetrically extends the wavelength tuning range at the expense of donut-shaped signal beam profiles.

We conclude that normal dispersion feedback stabilizes the pulse-to-pulse output, such that steady state operation is preferred. Additionally, wavelength tuning exhibits uncoupled control parameters and is free of mode jumps and wavelength drifts upon varying pump power levels. This renders operation in the normal dispersion regime to be preferable for most applications.

4

BURST-MODE FIBER-FEEDBACK OPO

This chapter is based on the following published work:

> **M. Floess**, T. Steinle, and H. Giessen
> *Burst-mode femtosecond fiber-feedback optical parametric oscillator*
> Opt. Lett. **47**, 525–528 (2022).

4.1 ABSTRACT

In multiphoton 3D direct laser writing and stimulated RAMAN scattering applications, rapid and arbitrary pulse modulation with an extremely high contrast ratio would be very beneficial. Here, we demonstrate a femtosecond fiber-feedback optical parametric oscillator (FFOPO) system in combination with pulse picking in the pump beam. This allows tunable signal output at variable burst rates from DC all the way up to 5 MHz. Furthermore, arbitrary pulse sequences can be generated. The rapid signal buildup dynamics provide individual full-power pulses with only two prepulses. This is possible without the requirement for additional injection seeding. Here, the intrinsically high intra-cavity losses of the FFOPO system are found to beneficial, as they enable rapid off-switching of the output as signal ring-down is efficiently suppressed. Possible applications are the reduction of the average power while maintaining a high peak power level, as well as tunable arbitrary pulse sequence generation.

4.2 INTRODUCTION

Pulse picking finds numerous applications wherever it is necessary to reduce the repetition rate of a pulsed laser. There may, for instance, be a need to solely pick individual pulses or to generate pulse bursts. In particular, multi-photon direct laser writing benefits from variable pulse repetition rates and burst operation while the pulse energy is kept constant. The spatial resolution of 3D two-photon polymerization writing can be increased by applying femtosecond pulse bursts with pulse energies of a few nanojoules rather than a steady pulse train, since local heat accumulation is minimized [48]. Heat-induced micro-explosions in the photoresist can be avoided

by choosing appropriate pulse sequences [49]. Similarly, the fabrication of integrated optical components using femtosecond laser pulses benefits from burst operation. In this case, avoiding or deliberately introducing heat accumulation enables control over the resulting morphology and optical properties [50, 51]. Also, reducing the repetition rate of the laser is often important for time-resolved fluorescence spectroscopy, where long lifetimes of molecules require quite large temporal pump-pulse separation [52, 53].

Furthermore, coherent laser spectroscopy modalities that are based on lock-in detection rely on laser modulation. For example, stimulated RAMAN scattering spectroscopy requires amplitude modulation of one of the interacting laser pulse trains [21, 54–57], which is usually realized by employing an acousto-optical modulator (AOM). AOMs suffer from wavelength-dependent modulation efficiency with typical maximum modulation depths of approximately 80% in the zeroth diffraction order. Operation in the first diffraction order enables 100% modulation but imposes a reduced maximum power level as well as wavelength-dependent diffraction angles.

In this work, we avoid these problems by combining pulse picking with a subsequent synchronously pumped fiber-feedback optical parametric oscillator (FFOPO). Instead of placing the AOM in the signal output beam, pulse picking is performed in front of the FFOPO in the pump beam. This configuration is advantageous as the wavelength-dependent modulation performance of the AOM is removed from the system.

Parametric fluorescence, the random starting point for optical parametric oscillation, exhibits a strong timing jitter, which limits the effective gain due to a synchronization mismatch. Nevertheless, our system exhibits extremely fast buildup dynamics due to an amplification (small signal) gain of approximately 50 dB in the nonlinear crystal for the synchronized case. As a result, the signal pulse train reaches its steady-state pulse energy within only five pump cycles without any additional injection seeding. Additionally, high resonator losses originating from fiber incoupling and a high output coupling ratio are beneficial for rapid signal turnoff, which enables burst rates of up to 5 MHz. Other burst-mode OPO systems reported in the literature exhibit transients that extend across up to 80 pump cycles [58] and, thus, lack modulation bandwidth.

4.3 INSTRUMENTATION: BURST-MODE FFOPO

The FFOPO is synchronously pumped by an Yb:KGW oscillator that generates 1032 nm, 450 fs pulses at a repetition rate of 41 MHz and 8 W of average output power [36], as depicted in Fig. 4.1. An AOM is placed in the pump beam to act as a pulse picker. The AOM operates in the first diffraction order to ensure the highest possible suppression ratio of undesired laser pulses. The driver electronics for the AOM are synchronized to the pump laser. A frequency divider based on a field-programmable gate array (FPGA) sets the time base by shifting the pump laser repetition rate down. A programmable arbitrary waveform generator (UHF-AWG, Zurich Instruments) drives the AOM. This allows the generation of arbitrary pump pulse sequences. The FFOPO system is

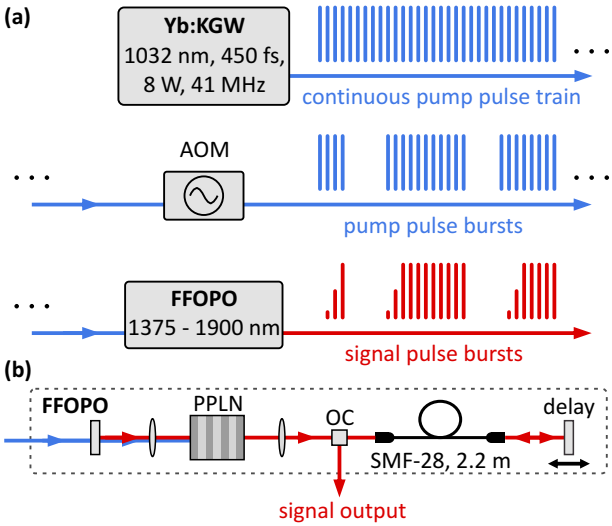

FIGURE 4.1. **Schematic of the burst-mode FFOPO.** An Yb:KGW oscillator synchronously pumps a MgO:PPLN-based FFOPO at 41 MHz repetition rate. The inset depicts the linear cavity design, which incorporates a 2-m-long SMF-28 fiber and a variable-output coupler. An AOM allows the arbitrary generation of pump pulse sequences, each of which drives the FFOPO from its off state into its steady state within only a few cycles.

singly resonant for the signal channel and based on a 10-mm-long, 0.5-mm-thick periodically poled MgO:$LiNbO_3$ (PPLN) crystal with discrete poling periods and anti-reflection coatings at both facets ($R < 2\%$ at 1030 nm, $R < 3\%$ at $1350 - 1900$ nm). The largest share of the FFOPO cavity is wound up in a 2.2-m-long feedback fiber with an effective propagation length of 4.4 m due to the double-pass configuration used. This

imposes a large amount of intra-cavity group-delay dispersion on the signal feedback. The resulting chirp makes the pump-seed overlap insensitive to cavity mismatch fluctuations, and thus enables excellent long-term power and wavelength stability [37]. Even though only a narrow-bandwidth portion of the feedback is therefore available as the seed for the amplification process, the FFOPO generates signal pulses with 350 fs duration [37, 59], which is governed by the nonlinear temporal gain window of the pump (450 fs) in combination with the gain bandwidth. The phase matching is tuned by changing the poling period and the temperature of the PPLN crystal. A moveable end mirror is employed to change the signal wavelength. A variable output coupler allows the adjustment of the intra-cavity signal power in order to optimize the signal buildup time and the output power level. The signal output pulse trains are recorded using a 5 GHz InGaAs photodiode.

4.4 RESULTS AND DISCUSSION: BURST-MODE FFOPO

4.4.1 *Burst Rate Tuning*

Variable pulse burst rates are demonstrated in Fig. 4.2(a). The burst rate is varied from 5 MHz down to 1.25 kHz, measured at a signal wavelength of 1470 nm.

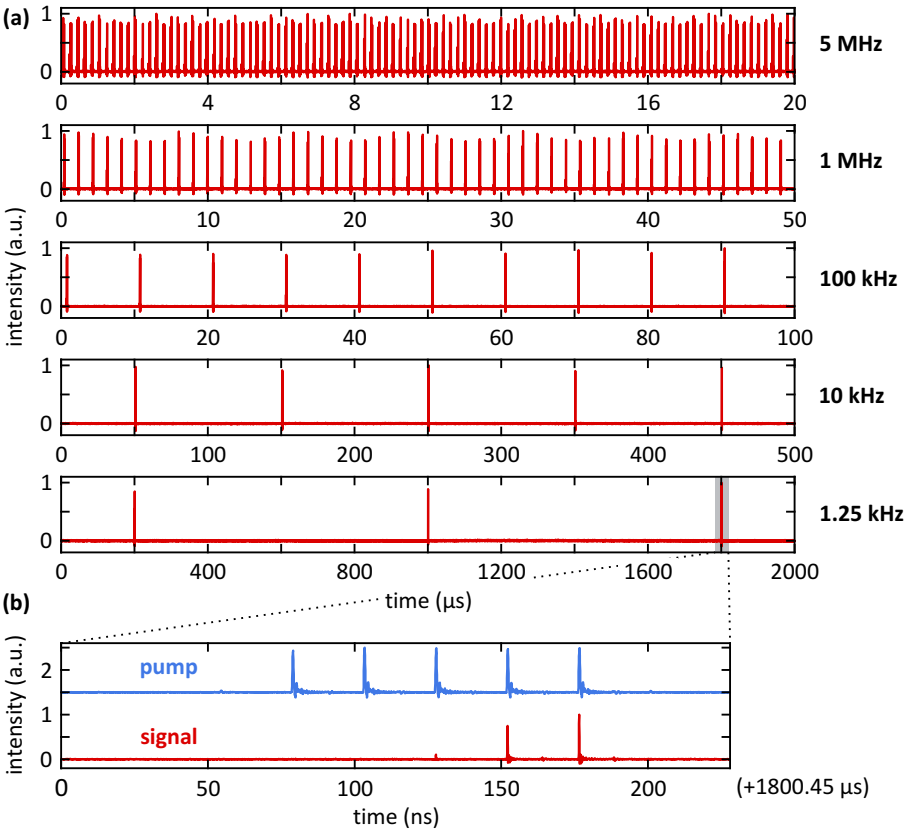

FIGURE 4.2. **Burst rate tuning.** (a) FFOPO signal output at five different burst rates between 1.25 kHz and 5 MHz, as measured at 1470 nm. (b) Zoom of the gray-shaded area in (a). The signal reaches the steady-state pulse energy within five pump cycles, which results in a signal pulse burst that consists of two prepulses followed by the main pulse. This rapid signal buildup enables burst rates of up to approximately 5 MHz. The high intra-cavity losses enable rapid turn-off of the signal output without any ring-down. Pump power: 680 mW (unmodulated); output coupling ratio: 94%.

The pump power level is set to 680 mW, measured at 41 MHz. In principle, there is no lower limit to the burst rate. In this case, the home-made FPGA-based trigger electronics set the lower limit to 1.25 kHz. Fig. 4.2(b) depicts a temporal zoom into one of the signal pulse bursts as well as the corresponding pump burst. The feedback ratio is optimized to 6%, so only five pump pulses are required to drive the FFOPO into its steady state. Gain saturation sets in between pulse sites 4 and 5, which results in only minor amplification. This occurs without any additional injection seeding of the buildup process, which keeps the setup simple and cost efficient.

The fiber-feedback design imposes high intra-cavity losses, mainly caused by the limited fiber incoupling efficiency. In fact, this low Q-factor is advantageous, as it suppresses signal ring-down after the pump beam has been turned off, meaning that the signal output can be completely switched off within one cycle. Thus, skipping only a few pump cycles is sufficient to empty the FFOPO cavity before the next pulse burst is launched. Together with the skipped pump cycles in between subsequent bursts, the upper limit of the burst rate amounts to approximately 5 MHz. The feature between two signal pulse sites is an electronic artifact caused by impedance effects in the signal acquisition chain.

4.4.2 *Wavelength Tunability*

As mentioned before, while single pulse bursts can be generated, arbitrary pump-pulse sequences are possible as well. Fig. 4.3(a) depicts a pump-pulse pattern that consists of three individual pulse bursts. These bursts contain five cycles followed by 13 and 20 cycles. Between the bursts, the AOM suppresses 10 and 20 cycles, respectively. The entire sequence is repeated with a period of 2.3 µs, which corresponds to a sequence repetition rate of approximately 425 kHz. The FFOPO signal output at 1410 nm follows the pump sequence with a delay of approximately five laser cycles. Note that the timing offset between pump and signal due to different optical path lengths to the detectors is compensated for in post processing. Fig. 4.3(b) depicts the signal spectrum as well as the corresponding signal output power. Both are measured while the pump sequence shown in Fig. 4.3(a) is applied. The signal tunability ranges from 1375 to 1835 nm while the burst pattern is preserved. The signal feedback ratio is set to 60% and 20%, respectively. The lowest feedback ratio is reached at 1510 nm (3%). At 1905 nm, the signal time trace cannot be recorded, as the sensitivity of the photodiode ($800 - 1700$ nm) decreases drastically. However, comparing the average output power of burst-pattern operation to that of steady-state operation yields a duty cycle of 23%. This suggests that burst operation still works at this wavelength.

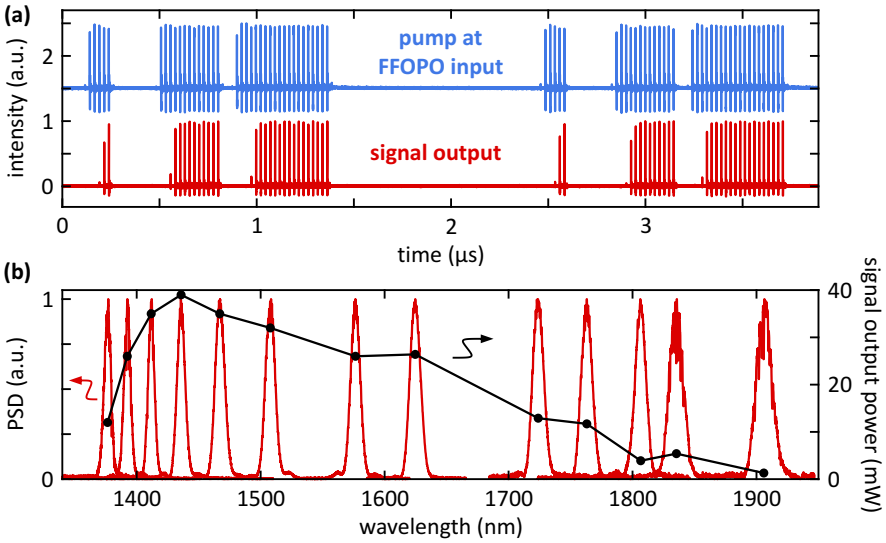

FIGURE 4.3. **Arbitrary burst sequence and wavelength tuning.** (a) An arbitrary pump burst sequence drives the FFOPO. (b) The spectral tunability of the signal output (left y axis) is depicted, as is the corresponding average signal output power (right y axis). Both the spectra and the output power were recorded while the FFOPO was driven by the pulse sequence shown in (a). The measured signal output power therefore corresponds to a duty cycle of approximately 27%. The spectrum at 1410 nm corresponds to the signal burst sequence in (a). Pump power: 680 mW (unmodulated); output coupling ratio: 40 – 97% (optimized for maximum signal output).

The average signal output power stated in Fig. 4.3(b) corresponds to an overall duty cycle of 27%. Exceptions are the operation points at 1375 and 1625 nm, with duty cycles of 20% and 31%, respectively, and the points at 1835 and 1905 nm, with duty cycles of 23%. The maximum output power of 39 mW is reached at 1436 nm, and corresponds to a signal pulse energy of 3.6 nJ, measured with a signal feedback ratio of 4%. This corresponds to a photon conversion efficiency of 31%. The output power drops down to the minimum of 1.3 mW (0.14 nJ pulse energy) at 1905 nm, where temporal walk-off between the pump and the signal reduces the gain.

As each individual signal burst emerges from random parametric fluorescence, there is no coherence between individual bursts. However, there is coherence within a signal burst.

Fig. 4.4 depicts the signal buildup cycles at different wavelengths. The pump time trace corresponds to the 20-cycle burst shown in Fig. 4.3(a), which is launched at

approximately 3.4 µs. The signal reaches its steady-state pulse energy within only $4-6$ pump cycles. As a guide to the eye, the dashed line marks the temporal position of the fifth pump pulse. Only towards the edges of the tuning range is the buildup time slightly increased.

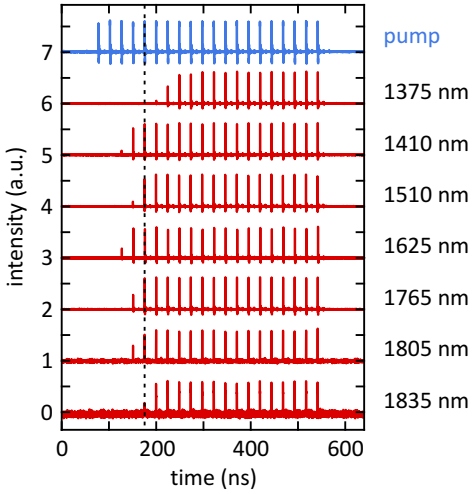

FIGURE 4.4. **Signal buildup at different wavelengths.** The pump trace corresponds to the 20-cycle burst shown in Fig. 4.3(a), which starts at approximately 3.4 µs. As a guide to the eye, the dashed line marks the fifth pump cycle. Except at 1375 nm, the signal output reaches its steady-state pulse energy after a maximum of six cycles. Pump power: 680 mW(unmodulated); output coupling ratio: $40-97\%$ (optimized for maximum signal output).

As mentioned before, no signal ring-down is observed after turning off the pump laser. Thus, burst rates reaching up to the MHz regime can be generated across the entire signal tuning range. Furthermore, using the idler channel as well would extend the tuning range even further towards the IR. Higher pump power levels would extend the wavelength range in which the buildup time is retained at five pump cycles. At the same time, the signal buildup would be even faster for the demonstrated wavelengths due to the increased parametric gain. However, the AOM used for this experiment is not optimized for high power throughput. Tight focusing into the AOM crystal to ensure the maximum modulation bandwidth increases the risk of coating damage. Thus, the available pump power at the FFOPO input is set to 680 mW. In fact, the pump power throughput could be increased by operating the AOM in its zeroth diffraction order, which allows maximum pulse energy transmission. Thereby, the

suppression ratio of unwanted pump pulses deteriorates to approximately 80%, given by the AOM diffraction efficiency. However, the FFOPO threshold suppresses the signal output for these pump cycles and thus maintains the excellent pulse contrast ratio.

4.5 CONCLUSIONS & OUTLOOK

We have demonstrated a femtosecond FFOPO system in combination with pump pulse picking that enables signal output pulse bursts. Exploiting the high single-pass gain and high intra-cavity losses enables rapid signal buildup and fast off-switching, respectively. This allows burst rates from DC up to 5 MHz to be achieved, as well as arbitrary signal pulse sequences. Multi-photon direct laser writing applications could greatly benefit from such a system, as photo damage due to heat accumulation could be minimized via burst rate control. At the same time, the wavelength tunability enables the flexible utilization of photoresists with different polymerization activation energies. Furthermore, stimulated RAMAN scattering applications and time-resolved photoluminescence measurements will tremendously benefit from wavelength-independent modulation performance. The aforementioned lack of coherence between individual signal bursts does not have any impact on any of these applications. Our system is superior to fiber supercontinuum sources, which might also cover this spectral range. However, pulse compression after spectral selection would be necessary. Furthermore, the relative intensity noise of these light sources is detrimental to modulation-based applications, such as stimulated RAMAN scattering spectroscopy. The FFOPO, on the other hand, preserves the excellent noise performance of the solid-state bulk oscillator [14], which enables measurement sensitivities down to the electronic shot-noise limit.

5

EXTENDED-CAVITY FIBER-FEEDBACK OPO

This chapter is based on the following published work:

> **M. Floess**, T. Steinle, I. Gerhardt, and H. Giessen
> *Femtosecond tunable light source with variable repetition rate between 640 kHz and 41 MHz with a 130 dB temporal pulse contrast ratio*
> Opt. Express **30**, 1–11 (2022).

5.1 ABSTRACT

We demonstrate a femtosecond tunable light source with a variable pulse repetition rate based on a synchronously pumped fiber-feedback optical parametric oscillator (FFOPO) that incorporates an extended-cavity design. The repetition rate can be reduced by an acousto-optical modulator in the FFOPO pump beam. The extended FFOPO cavity supports signal oscillation down to the 64^{th} subharmonic. The high nonlinearity of the FFOPO threshold suppresses signal output for residual pump pulses that are transmitted by the pulse picker. We characterize the temporal pulse contrast ratio of the FFOPO signal output with a second-order cross-correlation measurement. This FFOPO system enables pulse picking with extraordinarily high values up to 111 dB suppression of adjacent pulses and exhibits a temporal contrast ratio that exceeds 130 dB. It generates fs-pulses with tunable wavelength from $1415 - 1750$ nm and $2.5 - 3.8$ µm and variable repetition rates ranging from 640 kHz to 41 MHz.

5.2 INTRODUCTION

Laser pulse picking is a widely used concept to decrease the pulse repetition rate or to create bursts by selecting individual pulses from an initial pulse train with a fixed pulse repetition rate. Applications such as fluorescence lifetime imaging microscopy (FLIM) typically require repetition rates in the low MHz-range due to the lifetime of the fluorophores of up to several tens of ns [52]. Ti:sapphire lasers are usually the system of choice since they provide wavelength tunability and ultra-short pulses, both necessary for FLIM applications. However, the repetition rate of commercial systems

is usually in the range of $\sim$ 80 MHz. This limits the relevant observation range to a maximum of $\sim$ 4 ns, considering that the temporal pulse separation should cover at least 3 lifetimes. Pulse picking enables longer lifetimes by reducing the repetition rate and therefore increases the temporal pulse separation [53]. Nonlinear microscopy modalities such as second-harmonic generation and two- or three-photon absorption fluorescence benefit from lower repetition rates as thermal damage is reduced [60, 61]. Typically, the laser pulse contrast ratio of pulse pickers based on acousto- or electro-optic modulators is limited to values of the order of 100:1 for adjacent and 10^4:1 for nonadjacent pulses, see Fig. 5.11 in Section 5.7.1. However, undesired residual pulses during the off-duty cycle can excite the fluorophores partially, create a background signal, and thus deteriorate the signal-to-noise ratio. One possibility to mitigate these effects is cascading pulse pickers. This, however, comes at a cost of electronic complexity, a decrease of the overall transmission efficiency and further narrowing of the spectral operating range due to physical limitations of crystal material transparency, optical coatings, and modulation efficiency. In the realm of high-energy laser pulses in the µJ- to the J-regime used for studying high-field physical processes in solids, an extremely high temporal contrast is required, which is beyond the performance of pulse picker devices. This is crucial to suppress coherent prepulses and thus, to avoid the formation of a preplasma, which alters the entire sample dynamics [62]. Therefore, a number of passive nonlinear temporal pulse cleaning techniques are exploited, such as saturable absorbers [63–66], second-harmonic generation (SHG) [67–69], optical parametric amplification (OPA) [70–76], cross-polarized wave generation (XPW) [77–79], nonlinear birefringence [80–82], as well as self-induced plasma shuttering [83, 84]. These techniques enable measurement-limited contrast ratios of up to 10^{-12} [65], however, some of them like XPW require high-energy pulses. Typically, third-order cross-correlation is employed as temporal pulse characterization technique, as it provides temporal resolution down to the fs-timescale and a dynamic range of $\sim 10^{13}$ [85].

Here, we report on a nJ-level extended-cavity FFOPO system that does not only cover a wide output wavelength range and offers a tunable pulse repetition rate but also reaches an excellent temporal contrast ratio of 130 dB. Adjacent pulses are suppressed by 111 dB. This superior contrast ratio is achieved by modulating the FFOPO pump pulses, and its performance is determined by the threshold of optical parametric oscillation versus residual parametric fluorescence. Thus, the FFOPO enhances the contrast performance of a conventional pulse picker by 9 orders of magnitude in an all-optical manner, whilst offering wavelength tunability with unaltered picking performance. To the best of our knowledge, this temporal pulse contrast is the highest value ever reported for any pulse picking system. This system is therefore suitable

for applications such as nonlinear microscopy and FLIM, and enables access to a large fluorophore lifetime range. Furthermore, it can also be considered as front-end system for high-energy laser systems, as it would provide an extremely high laser pulse contrast ratio already at the front of the amplification chain.

5.3 CONCEPT: EXTENDED-CAVITY FIBER-FEEDBACK OPO

For conventional synchronous pumping schemes the cavity length of the FFOPO matches the cavity length of the pump oscillator

$$L_{\mathrm{OPO}} = L_{\mathrm{osc}}, \tag{5.1}$$

such that subsequent pump pulses coincide with the oscillating signal pulse. This is referred to as a *fundamental cavity* configuration. Consequently, signal pulse P_j at the output directly influences the properties of the following adjacent signal pulse P_{j+1}, as a copy of P_j remains in the FFOPO cavity and serves as the amplification seed for pulse P_{j+1}. Hence, all output signal pulses are directly causally influenced by the preceding pulses. Clearly, this concept holds for free-space OPO systems equally.

In contrast, for an *extended-cavity* configuration the FFOPO cavity length amounts to an *integer multiple* of the oscillator cavity length

$$L_{\mathrm{OPO}} = N \cdot L_{\mathrm{osc}}. \tag{5.2}$$

Fig. 5.1 depicts this situation exemplarily for the case of $N = 4$. Here, N signal pulses can oscillate *independently* at the same time in the FFOPO cavity, where each of them is synchronously amplified at each cavity roundtrip by every N^{th} pump pulse, as depicted in Fig. 5.1(a). Consequently, adjacent signal pulses do not share a causal dependence on each other. In fact, each signal output pulse is causally influenced by every N^{th} preceding signal signal output pulse, i.e., pulse P_j seeds the amplification of pulse P_{j+N}. The resulting FFOPO signal output runs at f_{rep}, and therefore, it does not differ from the case of using a fundamental cavity configuration.
However, the fact that each oscillating signal pulse coincides with every N^{th} pump pulse allows synchronous pumping of the FFOPO using subharmonics of the pulse repetition rate f_{rep}. These subharmonics are generated by employing a pulse picker in the pump beam line, as depicted in Fig. 5.1(b) and (c). The lowest possible pulse repetition rate is given by the cavity extension ratio N. At this point, only one single signal pulse remains oscillating in the FFOPO cavity, as depicted in Fig. 5.1(c).

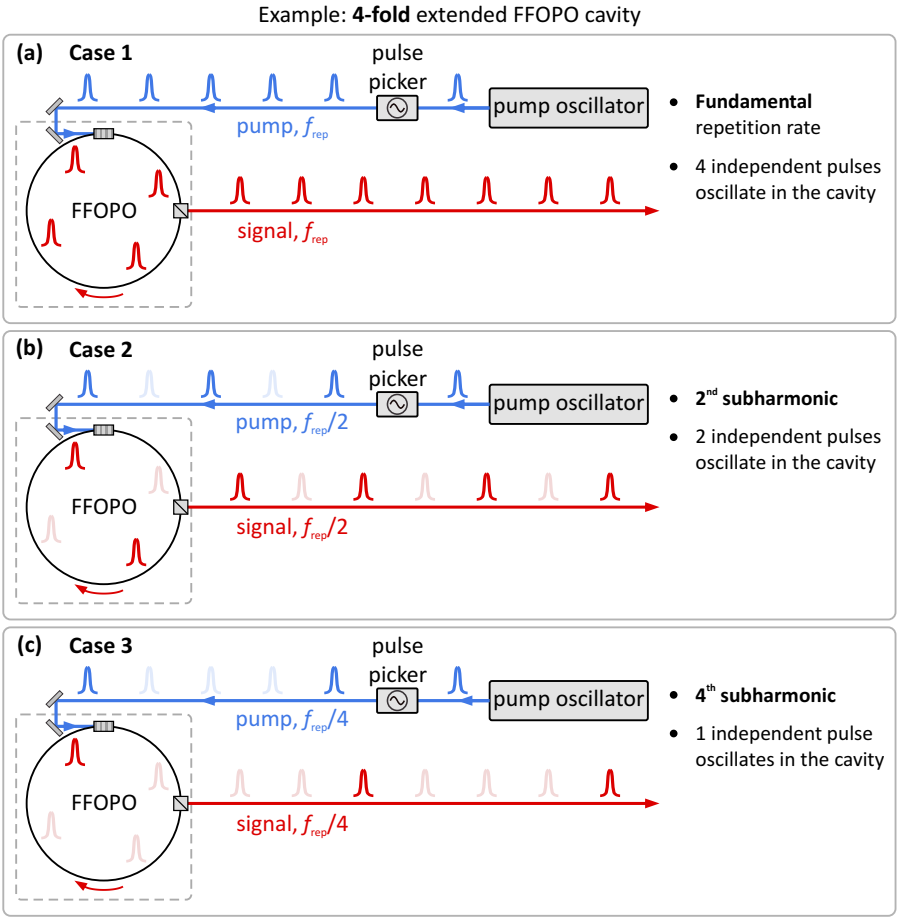

FIGURE 5.1. **Principle of the extended-cavity FFOPO.** A pulse picker generates subharmonics of the repetition rate f_{rep} of the pump oscillator. Multiple *independent* signal pulses oscillate in the FFOPO cavity, each of them is synchronously pumped. This allows for down-conversion of the signal pulse repetition rate, while maintaining synchronous pumping. **(a)** No pulse picking is applied, which results in the fundamental repetition rate at the signal output. **(b)** Every 2nd pump is suppressed, and thus, the signal output runs at $f_{rep}/2$. The cavity extension ratio determines the lower limit for the repetition rate, which amounts to $f_{rep}/4$ in this example, as depicted in **(c)**.

5.4 SETUP: EXTENDED-CAVITY FIBER-FEEDBACK OPO

An Yb:KGW solitary laser oscillator with 8 W of average output power, 40.95 MHz pulse repetition rate at 1032 nm center wavelength and 450 fs pulse duration [36] is used to synchronously pump a singly resonant FFOPO, as shown in Fig. 5.2.

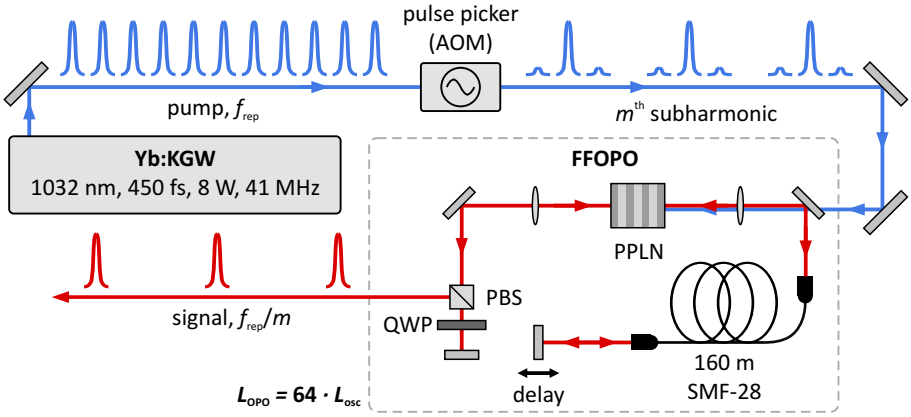

FIGURE 5.2. **Setup extended-cavity FFOPO.** Experimental setup of the FFOPO-based pulse picker. A 450-fs Yb:KGW bulk oscillator is used to synchronously pump an FFOPO based on MgO:PPLN at 1032 nm. An AOM operated in the 1st diffraction order is placed into the pump beam path to generate the m^{th} subharmonic of the fundamental repetition rate (41 MHz) by conventional pulse picking. Here, the leading and trailing pump pulses adjacent to the picked pulse are only suppressed by a ratio of 20:1 due to the AOM rise and fall time. The FFOPO exploits an extended cavity which incorporates a 160-m long fiber such that subharmonics up to $m = 64$ are supported. The FFOPO suppresses any pump input below the threshold pulse energy level and thus provides full modulation depth in its signal output.

A 10-mm long MgO:PPLN crystal with 9 discrete grating periods between 27.91 and 31.59 µm is used as the nonlinear medium. The FFOPO exploits a linear cavity design using a polarizing beam splitter (PBS) in combination with a quarter-wave plate (QWP) for variable output coupling [37]. Coarse wavelength tuning is performed by changing the poling period, and fine tuning is done via temperature control of the periodically poled lithium niobate (PPLN) crystal and by moving one of the end mirrors to adjust the relative temporal pump-signal overlap in the crystal. The coupling efficiency of the signal into the feedback fiber is typically $\sim$ 40%, i.e., the feedback losses introduced by fiber coupling amounts to $1 - 0.42 = 84\%$ (double-pass through the fiber). First, subharmonics of the pulse repetition rate are generated by pulse picking.

Therefore, an acousto-optical modulator (AOM) is placed in the pump beam path prior to the FFOPO. The AOM is driven by an arbitrary waveform generator (AWG), which is electronically synchronized to the pump laser repetition rate ensuring phase-stable operation. The AWG (Zurich Instruments, UHFAWG) applies a low-duty-cycle modulation signal such that individual pump pulses are being transmitted. Hence, the pump pulse repetition rate can be reduced by an integer fraction, which in the following will be denoted by m. The AOM is operated in its 1^{st} diffraction order to ensure highest possible suppression of undesired intermediate pulses. However, the finite AOM rise and fall time leads to a leading and a trailing pulse with residual pulse energies on the order of 5% of the main pulse energy, as schematically shown in Fig. 5.2. These residual pulses are intrinsically suppressed by the FFOPO threshold, which therefore acts as a high-contrast filter mechanism. Later, this will be discussed in more detail. The pump laser power at the AOM input is limited to $\sim 1.25\,\mathrm{W}$ at the given focal spot diameter of $\sim 50\,\mu\mathrm{m}$ in order to avoid coating damage of the AOM crystal. Thus, a pump power level of 750 mW at 41 MHz repetition rate is available at the FFOPO input. The losses are caused by the AOM diffraction efficiency of 80% at 1032 nm and subsequent optics. As mentioned above, the FFOPO is synchronously pumped. However, rather than its cavity optical path length L_{OPO} being fundamentally matched to the optical path length L_{osc} of the pump oscillator cavity, it amounts to an integer multiple thereof, such that $L_{\mathrm{OPO}} = N \cdot L_{\mathrm{osc}}$, as given by Eq. 5.2. Here we choose an extended cavity with $N = 64$.

5.5 RESULTS AND DISCUSSION

5.5.1 *Repetition Rate Tuning*

The extended FFOPO cavity supports n independent signal cycles at the same time, where

$$1 \leqslant n \leqslant N = 64. \tag{5.3}$$

In the following, evenly-spaced pulse trains are being considered, meaning that the possible values for the subharmonic index m restrict the number of independent cycles in the cavity. In particular, the condition N/m being integer-valued determines the number of independent cycles. The choice $N = 64$ therefore allows the subharmonics

$$m = 1, 2, 4, 8, 16, 32, \text{and } 64 \tag{5.4}$$

being supported by the FFOPO cavity. Only at these values the signal pulses are amplified at each roundtrip.

Fig. 5.3 demonstrates the variable signal pulse repetition rate in combination with signal wavelength tunability. The pump pulse energy is set to 17.7 nJ, which corresponds to an average power of 725 mW at $m = 1$ (41 MHz). Fig. 5.3(a) exemplarily shows the signal time traces of the FFOPO operation at subharmonics $m =$ 1, 2, 16, and 64, measured at a signal wavelength of 1518 nm. The time traces are recorded with an oscilloscope (Agilent Technologies, DSO9404A) at 20 GSa/s with 9 bit of vertical resolution using an InGaAs-based photodiode with 5 GHz bandwidth (Thorlabs, DET08CFC). No measurable signature of the 41 MHz fundamental frequency is left in the subharmonic traces since they are strongly suppressed by the FFOPO threshold.

The vertical dashed lines indicate the signal pulses which belong to the same cycle. Thus, each of these signal pulses experience feedback from the respective previous pulse. This is the case for the 64^{th} subharmonic of f_{rep} which marks the fundamental repetition rate of the FFOPO cavity. Thus, at $m = 64$ only a single independent signal cycle is supported. At $m = 16$ four independent cycles are launched, $m = 2$ supports 32 independent cycles, corresponding to Nyquist modulation at $f_{\text{rep}}/2$. Without pump modulation ($m = 1$) the signal output runs at f_{rep}.

Therefore, the signal pulse repetition rate ranges from 640 kHz ($m = 64$) up to 40.95 MHz ($m = 1$). Fig. 5.3(b) demonstrates the wavelength tunability of the system. Signal output time traces are measured at 1415, 1518, 1640, and 1753 nm, where the picking rate is fixed at $m = 16$. The corresponding signal spectra are shown in the

right panel. Pulse picking works over the entire tuning range of the FFOPO system without any residual leading or trailing pulses.

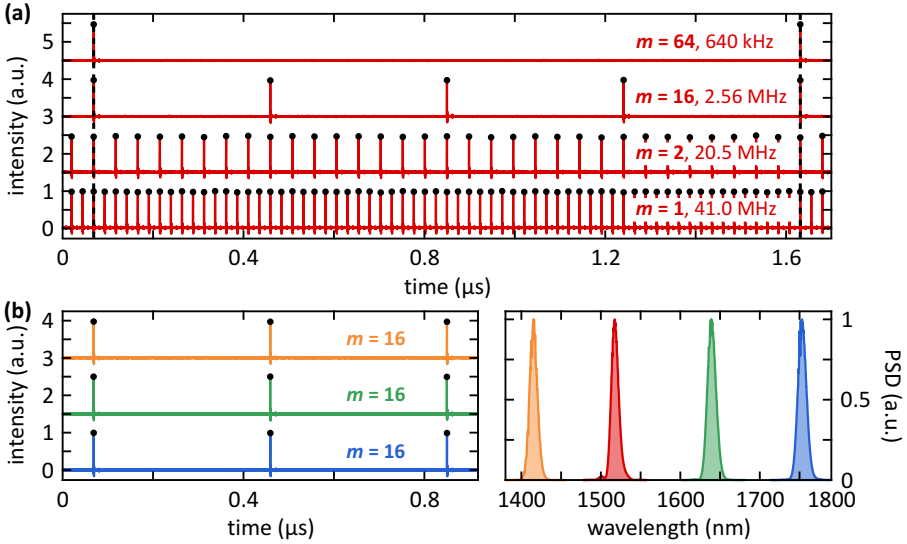

FIGURE 5.3. **Wavelength and repetition rate tuning. (a)** Signal output time traces at 4 different picking rates, $m = 1$, 2, 16, and 64, recorded at a fixed center wavelength of 1518 nm. The vertical dashed lines indicate the signal pulses which belong to the same cycle. At the 64$^{\text{th}}$ subharmonic of the pump oscillator repetition rate only one independent pulse oscillates in the FFOPO cavity. At $m = 16$, four independent pulses are launched, $m = 2$ supports 32 independent pulses, corresponding to Nyquist modulation at $f_{\text{rep}}/2$. The signal pulse repetition rate ranges from 40.95 MHz ($m = 1$) down to 640 kHz ($m = 64$). The feature trailing each signal pulse is an electronic artefact arising from impedance effects. **(b)** Wavelength tuning. Signal output time traces are measured at 1415, 1640, and 1753 nm with fixed picking rate at $m = 16$. The corresponding signal spectra are shown in the right panel. The red spectrum corresponds to the data shown in **(a)**.

Due to the large amount of intra-cavity group delay dispersion (GDD) a cavity length adjustment of $\sim$ 50 cm is necessary to tune the signal wavelength between 1415 and 1753 nm. The measured signal bandwidth is $11 - 12$ nm. In contrast, the calculated spectral acceptance bandwidth of the PPLN crystal is 6 nm at $\lambda_s = 1415$ nm, and 72 nm at $\lambda_s = 1753$ nm. These deviations arise from a peak-intensity dependent acceptance bandwidth and spectral filtering due to dispersion in the fiber, respectively. The latter contribution also explains the absence of strong spectral modulations in the output which might be expected from self-phase modulated feedback pulses. The

corresponding pulse durations fall in the range between 320 and 400 fs, as depicted in Fig. 5.4. This suggests that the output pulse duration is close to the FOURIER limit, assuming a time-bandwidth product of

$$\mathrm{TBP} = 0.441, \tag{5.5}$$

which corresponds to a GAUSSIAN temporal profile. Reference [59] reports signal pulse durations between 250 and 400 fs for this FFOPO system using the fundamental cavity configuration.

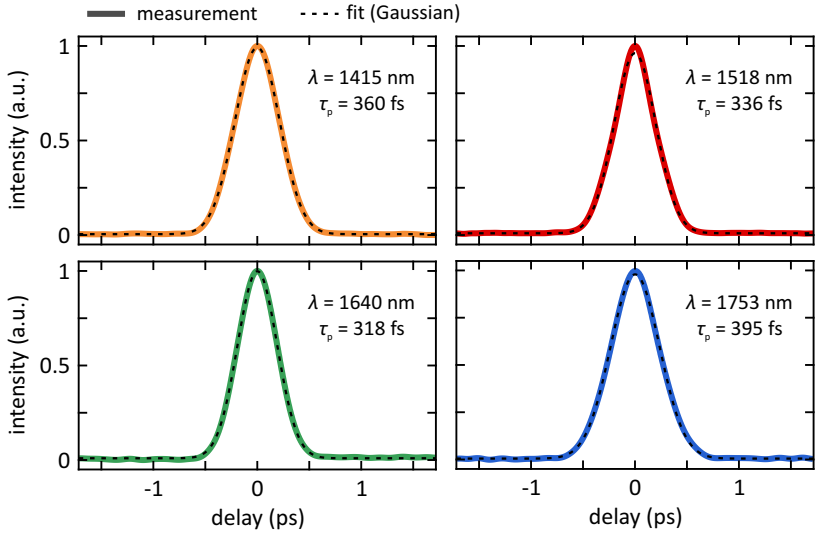

FIGURE 5.4. **Auto-correlation traces – FFOPO signal.** The auto-correlation traces of the extended-cavity FFOPO signal (solid lines) are measured across the wavelength tuning range at the spectral positions, which are depicted in Fig. 5.3(b). Here, the same color code is used. The Gaussian fit curves (dashed lines) agree well with the measurements.

An auto-correlation trace is exemplarily shown in Fig. 5.10(c) which will be discussed below. The idler channel extends the tunability even further towards the mid-IR region (2509 – 3813 nm) with identical repetition rate and the superior contrast ratio. This is due to the inherent presence of an idler photon for each generated signal photon.

The timing jitter of the signal pulses depends on both, the timing jitter of the pump oscillator and the FFOPO resonator. Passively mode-locked solid-state oscillators typically exhibit integrated root mean square (RMS) timing jitters of a few femtoseconds

and well below. The FFOPO is optically synchronized and must therefore show similar performance. Otherwise, the temporal mismatch between pump and seed pulse would induce significant relative intensity noise (RIN), which is not the case, as shown in Fig. 5.5. Here, the RIN curves of the FFOPO signal are depicted for operation with the extended and the fundamental cavity, respectively. In this case, the extended cavity is operated at $m = 1$, i.e., the signal pulse train runs at $f_{\mathrm{rep}} = 40.95\,\mathrm{MHz}$ for both cavity configurations. The extended cavity exhibits only a marginal increase in the noise level compared to the fundamental cavity. Thus, the extended cavity design has no detrimental effect on the pulse energy stability. As expected however, the fundamental repetition rate of the extended cavity, i.e., $f_0 = f_{\mathrm{rep}}/64$ appears in the noise spectrum as a small peak at 640 kHz. Its higher harmonics are visible as well, as indicated in Fig. 5.5(b).

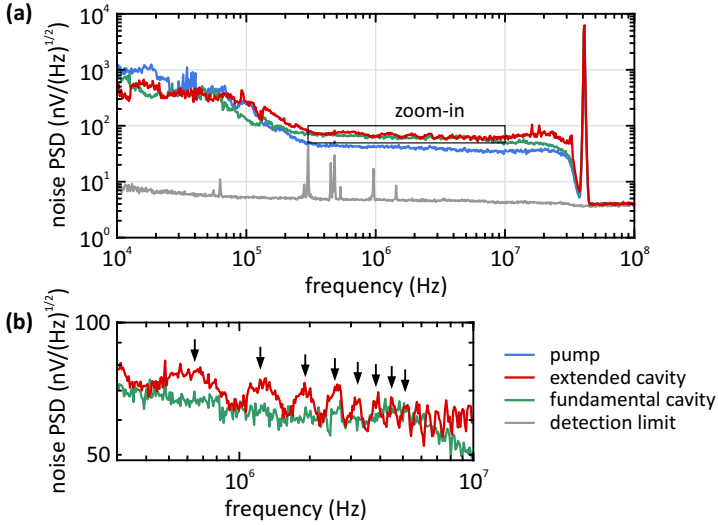

FIGURE 5.5. **Relative intensity noise: extended vs. fundamental cavity. (a)** The signal intensity noise level using the extended cavity (red) is increased only marginally compared to the fundamental cavity (green). Blue: noise curve of the pump laser as reference; gray: noise floor of the photo detector. A 25-MHz low-pass filter is used to suppress the peak at the repetition rate (40.95 MHz), in order to maintain the highest possible sampling dynamic range. Pump power: 780 mW; signal wavelength: 1605 nm. **(b)** Zoom-in to the indicated area in **(a)**. The fundamental repetition rate $f_0 = f_{\mathrm{rep}}/64 = 640\,\mathrm{kHz}$ of the extended cavity along with its harmonics appear in the noise spectrum. Harmonics $1-8$ are indicated by the black arrows.

Thermal expansion of the 160-m long feedback fiber causes an effective change of the cavity length and thus, a wavelength change. Thermal stabilization of the fiber could be implemented to prevent long-term wavelength drifts. The extended cavity configuration does not alter the GAUSSIAN-shaped beam profiles of signal and idler compared to fundamental cavity operation, since only the propagation length in the single-mode fiber is increased, whereas the free-space part of the cavity remains unchanged.

So far, only evenly spaced pulse trains have been considered. However, arbitrary signal pulse sequences can also be produced, e.g., bursts consisting of a few single pulses. This works if the burst periodicity corresponds to $N = 64$ pump cycles, i.e., steady-state operation is given. Furthermore, arbitrary N-values can be chosen in order to access any specific subharmonic of f_{rep}.

5.5.2 *Temporal Pulse Contrast Ratio*

We now focus our investigation on the modulation contrast ratio by analyzing the threshold and energy filter behavior of the FFOPO. Fig. 5.6(a) depicts the signal output pulse energy depending on the pump pulse energy in the range between 9.6 and 15.6 nJ. Below a pump level of 12.8 nJ no signal output occurs apart from parametric fluorescence. Here, the output coupling ratio is set to 75%. Fig. 5.6(b–e) demonstrate the pulse suppression behavior in the output time trace by reducing the pump pulse energy in a controlled manner. Therefore, pump and signal time traces are shown for three different pump pulse energies as indicated in Fig. 5.6(a).

The AOM generates a subharmonic at $m = 8$ (5.1 MHz), such that the picked pulses are separated by several AOM rise time constants ($\sim$ 15 ns). Additionally, every 2$^{\mathrm{nd}}$ pump pulse is partially attenuated such that the pulse suppression behavior due to the OPO threshold can be investigated, while the unattenuated pulse train serves as reference. As a guide to the eye the corresponding signal pulses are alternatingly shown in red (reference) and green (attenuated) to indicate their relationship to the modulated pump pulse train. Without attenuation (15.6 nJ, Fig. 5.6(b)) a steady state signal output at $m = 8$ is observed. Reducing the pulse energy to slightly above the threshold (13.0 nJ, Fig. 5.6(c)) leads to four individual signal cycles with different pulse energies, each corresponding to $m = 64$. Below the threshold at 12.8 nJ (Fig. 5.6(d)) no signal output occurs. The zoom-in (Fig. 5.6(e)) depicts the region between two subsequently detected signal pulses recorded at high resolution. This confirms that the signal output is suppressed for pump levels below the threshold.

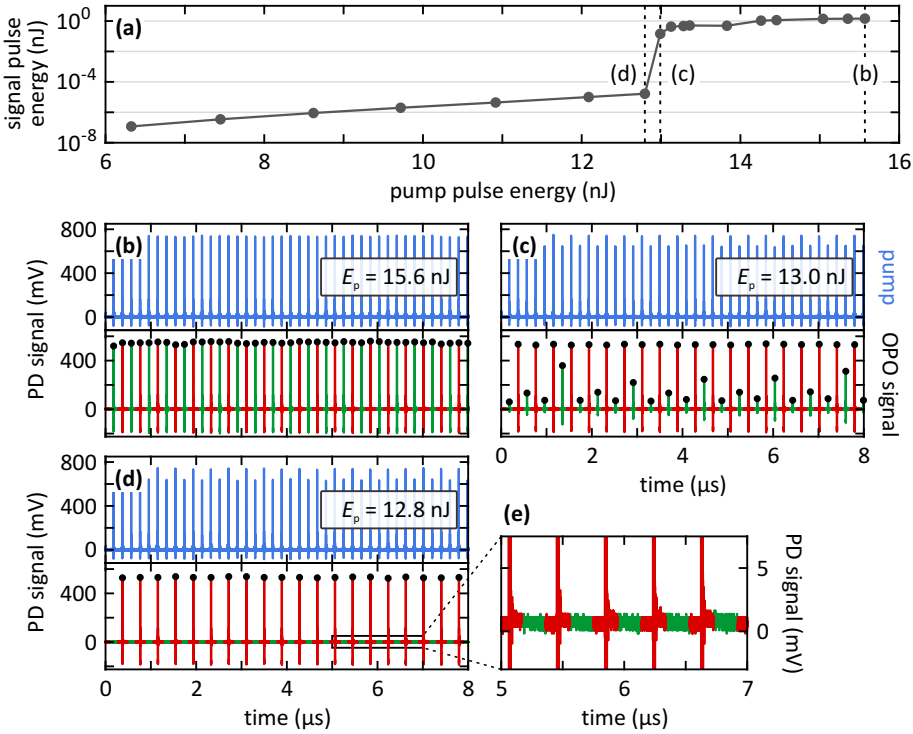

FIGURE 5.6. **OPO threshold behavior.** Contrast ratio investigation to demonstrate the efficiency of the pulse suppression mechanism. **(a)** Signal output pulse energy depending on the pump pulse energy. The FFOPO threshold is between 12.8 and 13.0 nJ below which no signal oscillation occurs, only parametric fluorescence is present. **(b)** The time traces of pump and signal output are shown for three different pump pulse energy levels as indicated in **(a)**. The AOM operates at $m = 8$ and hence, 8 independent signal cycles are launched. Additionally, every 2^{nd} pump pulse is variably attenuated such that the pulse suppression behavior due to the FFOPO threshold can be investigated. The unattenuated pulse train (red) serves as reference for the attenuated pulse train (green). Both pulse trains are equal in panel **(b)** for identical pump energy of 15.6 nJ. Reducing the pump energy near the FFOPO threshold **(c)** leads to decreasing energy in the attenuated pulse trains. Interestingly, the four independent pulse trains also oscillate with different pulse energy. Already slightly below the oscillation threshold **(d)** only the reference pulse train remains, while any intermediate pulses vanish completely. PD: photodiode.

So far, the characterization of the suppression of the signal output at intermediate pulse sites was based on the measurement using a photodiode and an oscilloscope. This method clearly lacks sensitivity and dynamic range (~ 30 dB), even if the analog

input gain of the oscilloscope is increased to its maximum. Since a much higher pulse contrast is expected for the FFOPO due to the complete absence of amplified spontaneous emission, we employ a single photon counting module (SPCM). This approach, in principle, allows to scan the entire temporal region of one pulse cycle when combined with a time tagger. In practice, these devices are limited to similar 30 dB contrast ratio due to 0.1% electronic after-pulsing and damage threshold (10^4 photons/pulse), and, suffer from a 25-ns dead time window after a detected event, during which no data can be acquired.

A scanning scheme based on nonlinear optical gating overcomes this dynamic range problem by mapping the signal into a different spectral channel, which thus can be spectrally separated from the fundamental and can be detected by the SPCM. This measurement scheme circumvents the limitations of after-pulsing and detector dead time. At gate positions with high nonlinear yield, e.g., the main pulse at time-zero, attenuation of the optical power using neutral density (ND) filters is introduced prior to the SPCM in order to avoid photo damage, and, to extend the dynamic range arbitrarily. Additionally, the temporal resolution is not limited by electronic jitter anymore. It is now given by the gating laser pulse duration, i.e., 450 fs. Thus, the temporal resolution is enhanced by ~ 3 orders of magnitude.

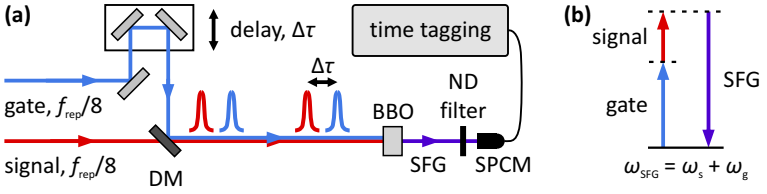

FIGURE 5.7. **Cross-correlation scheme. (a)** The sum-frequency generation (SFG) cross-correlation between the FFOPO signal output and the pump laser (gate) is generated in a β-barium borate (BBO) crystal and acquired using a SPCM and a time tagging unit. An optical delay line allows to adjust the relative delay $\Delta\tau$ between the gating pulse and the signal pulse. DM: dichroic mirror, BBO: β-barium borate, ND: neutral density, SPCM: single-photon counting module. **(b)** Energy diagram of the SFG mixing process. 1032 nm and 1584 nm are converted into 625 nm.

We realize this scheme with a second-order cross-correlation measurement based on SFG in a BBO crystal (2 mm, $\theta = 23\,^\circ$) as depicted in Fig. 5.7. The FFOPO signal at 1584 nm and $m = 8$ (5.13 MHz) is being correlated with a portion of the laser oscillator which serves as 450-fs optical gate with a center wavelength of 1032 nm. This yields a center wavelength of 625 nm for the SFG channel. Delaying the gating laser with

respect to the signal allows scanning of the temporal region between two subsequent signal pulses for any residual optical power at the spectral position of the FFOPO signal.

The detection is performed using a SPCM in combination with a time tagging unit (Swabian Instruments, Time Tagger 20, 8.5 Mtags/s max. bandwidth). The SFG signal is spectrally separated from all other spectral components before it is sent into the SPCM. The SPCM (Excelitas, SPCM-AQRH-15-FC) exhibits an extremely low dark count rate of only 20 counts/s, and a dead time after a detected event of 25 ns. Thus, at the gating rate of 5.13 MHz the SPCM is fully recovered between possibly occurring events. The photon detection efficiency exceeds 70% at 650 nm. Therefore, the SFG wavelength of 625 nm employed in this experiment is optimally detected by the SPCM. The FFOPO pump pulse train serves as trigger, such that all signal events are binned into a narrow time range of the acquired histogram. This enhances the signal-to-noise ratio even further as randomly occurring dark counts are equally distributed across all time bins. In combination with accurate ND filtering this method provides an extremely high dynamic range.

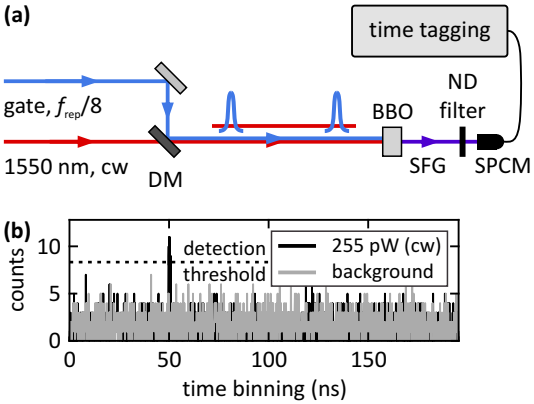

FIGURE 5.8. **Cross-correlation detection threshold.** (b) Sensitivity check using a 1550-nm cw-laser instead of the FFOPO signal. The SFG at a cw-power level of 255 pW is still detectable at 10 mW of gating laser power and 100 s integration time.

The sensitivity limit of this method is characterized by replacing the FFOPO signal with a 1550-nm cw laser, as depicted in Fig. 5.8(a). Thus, the resulting SFG signal originates from 1550-nm photons which temporally overlap with the 450-fs gating laser pulses. The cw-laser power is attenuated using ND filters until the SFG signal is

not detectable anymore in the timing histogram. Prior to this measurement, the ND filters were carefully characterized for their optical density at 1550 nm.
As depicted in Fig. 5.8(b), a cw power level of only 255 pW is still detectable at 100 s integration time per data point. Considering the low gating laser duty cycle of

$$\frac{\tau_\mathrm{p}}{T_\mathrm{p}} = \tau_\mathrm{p} \cdot \frac{f_\mathrm{rep}}{8} = 450\,\mathrm{fs} \cdot 5.13\,\mathrm{MHz} = 2.3 \cdot 10^{-6}, \tag{5.6}$$

statistically ~ 1100 gating cycles are required until one single 1550-nm photon coincides with a gating pulse at the given power level of 255 pW. Inversely, one gating pulse samples

$$N_\mathrm{limit} = 8.95 \cdot 10^{-4} \tag{5.7}$$

photons on average. Thus, within 100 s integration time, a total number of $\sim 4.6 \cdot 10^5$ 1550-nm photons on average are gated which leads to ~ 90 detected SFG events, as extracted from the integrated signal peak in Fig. 5.8(b). The main signal pulse energy level of 1.2 nJ (6 mW at 5.13 MHz, 1584 nm) corresponds to a total number of photons of

$$N_\mathrm{main\,pulse} = 9.3 \cdot 10^9 \tag{5.8}$$

per pulse. Relating the number of photons yields

$$\frac{N_\mathrm{limit}}{N_\mathrm{main\,pulse}} = \frac{8.95 \cdot 10^{-4}}{9.3 \cdot 10^9} = 9.6 \cdot 10^{-14}, \tag{5.9}$$

which corresponds to a sensitivity limit of -130 dB with respect to the main signal pulse energy level, and hence, this surpasses the sensitivity in the measurement shown in Fig. 5.6(e) by *10 orders of magnitude*.

At a repetition rate of 5.13 MHz ($m = 8$), the optical path length between two subsequent pulses amounts to

$$l = \frac{c}{f_\mathrm{rep}/m} \overset{(m=8)}{=} \frac{8c}{f_\mathrm{rep}} = 59\,\mathrm{m}, \tag{5.10}$$

where c denotes the speed of light. Covering this range using an optical delay line only is unfeasible. Therefore, an additional synchronized AOM is used, which selects the actual gating pulse from the 40.95-MHz pulse train, and thus, allows for discrete 7.3-m steps, as depicted in Fig. 5.9. The corresponding temporal delay $\Delta\tau_\mathrm{AOM}$ enabled by the AOM is given by integer-multiples of the fundamental pulse roundtrip time

$$\Delta\tau_\mathrm{AOM} = \frac{n}{f_\mathrm{rep}}. \tag{5.11}$$

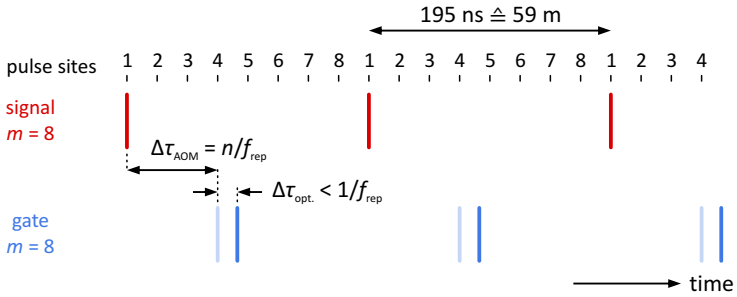

FIGURE 5.9. **Cross-correlation delay tuning.** The free-space optical path length at $m = 8$ amounts to $l = 59\,\text{m}$, which renders a solely optical delay line unfeasible. Therefore, pulse picking of the gating laser is employed to create delay values of an integer-multiple of the roundtrip time, i.e., $\Delta\tau_{\text{AOM}} = n/f_{\text{rep}}$. The remaining path length is covered using an optical delay line, which covers the distance between two subsequent pulses (7.3 m), i.e., $\Delta\tau_{\text{opt.}} > 1/f_{\text{rep}}$. Hence, the total delay $\Delta\tau_{\text{tot}} = \Delta\tau_{\text{AOM}} + \Delta\tau_{\text{opt.}}$ enables access to any arbitrary position between two pulses.

In order to access the range between these discrete time delay steps, a 7.3-m (40.95 MHz) folded optical delay stage is employed, which introduces an additional temporal delay of $\Delta\tau_{\text{opt.}}$. A micrometer stage is mounted on top of the delay stage, such that a temporal resolution of $\sim 100\,\text{fs}$ is achieved by translating the gating pulse with respect to the FFOPO signal pulse. Therefore, the overall temporal delay yields

$$\Delta\tau_{\text{tot}} = \Delta\tau_{\text{AOM}} + \Delta\tau_{\text{opt.}}. \tag{5.12}$$

Fig. 5.10(a) depicts the optically gated SFG trace, which covers one entire FFOPO signal cycle. The respective SFG level at $\Delta\tau = 0$ is set as the reference level to 0 dB. During most of the off-duty cycle the measured SFG level falls below the sensitivity limit, which statistically corresponds to $8.95 \cdot 10^{-4}$ photons per gating window, as explained above. In this case, the sensitivity limit at $-130\,\text{dB}$ is assigned to the respective data points as an upper bound level.
The black dots indicate the temporal position of the 7 suppressed pump pulses during one subharmonic cycle ($m = 8$). At the pulse sites adjacent to the main pulse two peaks arise at a level of $-111\,\text{dB}$. As indicated in Fig. 5.2, the limited switching bandwidth of the AOM leads to residual pump pulses which generate parametric fluorescence. Thus, the initial contrast ratio of the AOM of 20:1 is enhanced to $1.3 \cdot 10^{11}$ by the intrinsic threshold characteristics of the FFOPO. All other pump pulse sites do not exhibit any residual optical power above the sensitivity limit.

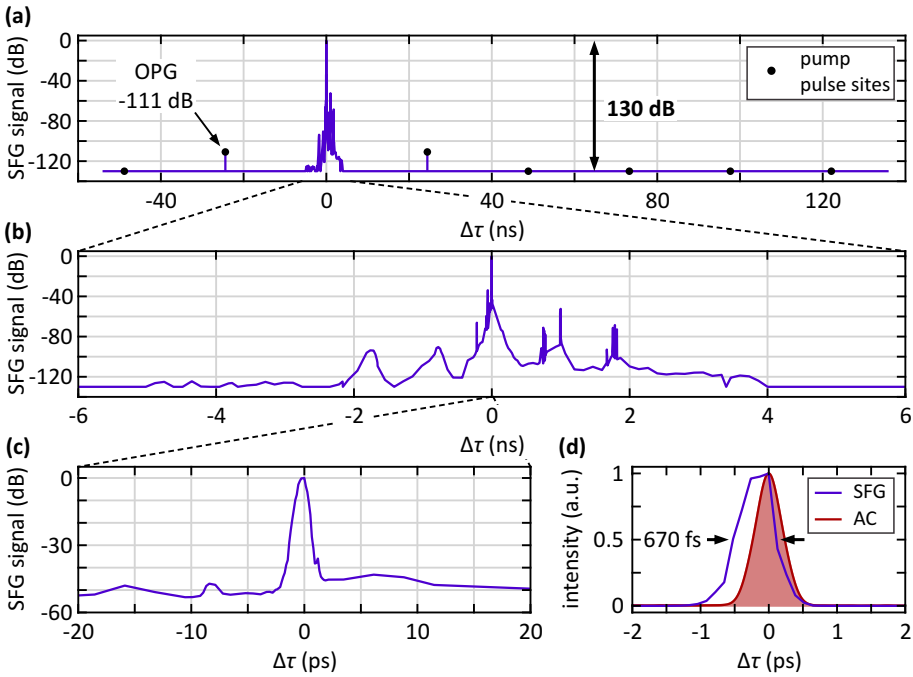

FIGURE 5.10. **Cross-correlation measurement.** Temporal pulse contrast ratio of the FFOPO signal output at 1584 nm and $m = 8$ (195.4 ns pulse spacing). **(a)** SFG cross-correlation trace. At 6 mW of signal power (1.2 nJ pulse energy) a sensitivity level of -130 dB relative to the maximum signal is reached. The black dots mark the positions of the pump pulse sites. Residual adjacent pump pulses generate parametric fluorescence (OPG) at -111 dB. **(b)** Zoom-in to the ns-timescale. Multiple reflections of the signal at optical elements within the FFOPO cavity cause leading and trailing peaks. **(c)** The ps-timescale reveals the main peak. The background level of -50 dB can be assigned to the dispersively stretched part of the signal feedback which does not experience parametric gain. **(d)** SFG cross-correlation on a linear scale, which exhibits a width of 670 fs at FWHM. Red curve: corresponding auto-correlation (AC) trace of the FFOPO signal, which yields 338 fs pulse duration assuming a Gaussian temporal profile.

Special caution is required when measuring the suppression ratio of the optical parametric generation (OPG) pulses adjacent to the main pulse. As depicted in Fig. 5.11, the gating laser as well exhibits unwanted leading and trailing pulses, which originate from the finite extinction ratio of the AOM. Hence, probing either of the OPG pulse sites with the main gating pulse, inevitably leads to one of the *adjacent* gating laser pulses overlapping with the *main* FFOPO signal pulse. This in turn produces a strong SFG signal that exceeds the signal of interest by orders of magnitude. Hence, the

dynamic range is largely consumed by this unwanted SFG signal. In order to circumvent this problem, the main signal pulse is suppressed by selectively attenuating its corresponding pump pulse below the OPO threshold. This main pulse suppression preserves the dynamic range and the OPG pulses can be sampled with high accuracy.

Leading and trailing pulses at levels between -90 and -60 dB are detected within $1-5$ ns temporal separation from the main peak symmetrically to both sides as depicted in Fig. 5.10(b). These peaks arise from back-reflections of the feedback pulse at optical elements in the FFOPO cavity, even though angled physical contact fiber optics with high return losses are used. The free-space path length between fiber coupler and delay mirror amounts to $\sim$ 60 cm, which explains the $\sim$ 2 ns temporal separation between reflected pulse and the main pulse. Further suppression of back-reflections would be possible by changing from a linear cavity to a ring-cavity design, where reflections propagating in backward direction do not appear in the output.

Optimally, the gating laser would consist of only one single laser pulse, which defines the gating window. However, due to unavoidable reflections at optical elements a number of weak ghost pulses accompany the main gating pulse. These ghost pulses undergo the SFG process with the FFOPO signal pulse as well, given that they overlap temporally. Clearly, these ghost pulses cause SFG events with advanced or delayed arrival time at the SPCM, and hence, they can be temporally separated from the main gating window within the timing histogram. But if this temporal separation falls below the temporal resolution of the electronic gating ($\sim$ 1 ns, corresponding to $\sim$ 30 cm spatial separation), these undesired events are convoluted into the main gating window and cannot be separated anymore. For further details on the electronic timing jitter refer to Section 5.7.
Fig. 5.10(c) depicts the ps-range around the main pulse, where pedestals to both sides at a level of -50 dB are observed. The signal feedback propagates through 320 m of single-mode fiber, where dispersion causes temporal stretching to $\sim$ 70 ps at the given signal bandwidth of 12 nm. Only the part which temporally overlaps with the pump pulse experiences a single-pass gain of $\sim$ 50 dB. In Fig. 5.10(d) the SFG cross-correlation is depicted on a linear scale together with the auto-correlation (AC) trace of the signal (red curve). A pulse duration of 338 fs is extracted assuming a GAUSSIAN temporal profile. A numerical convolution of such a signal pulse with the gate (sech^2, 450 fs) yields a cross-correlation trace with a width of 590 fs. This value is in good agreement with the measured width (670 fs).

Subsequent pulse cleaning of the FFOPO signal output via second-harmonic generation (SHG) would enhance the temporal contrast ratio even further due to its quadratic

intensity dependence. Even intense reflections at relative levels of −50 dB would be suppressed down to approximately −100 dB. The same holds for the ps-pedestals at −50 dB around the main pulse. The leading and trailing parametric fluorescence would be suppressed beyond the sensitivity limit.

5.6 CONCLUSIONS & OUTLOOK

We have demonstrated a wavelength-tunable pulse picking system based on an extended FFOPO cavity, which provides an extremely high (measurement-limited) temporal contrast ratio which exceeds 130 dB. Adjacent pulses are suppressed by 111 dB which offers a superior modulation depth at the Nyquist frequency, as the comparison with a commercially available pulse picking system demonstrates, see Table 5.1. The picking performance is independent of the signal output wavelength. Additionally, the tunability extends across the idler wavelength range as well, i.e., 2510 − 3815 nm for the given signal tuning range.

	Commercial pulse picker (Coherent)	**Extended-cavity FFOPO**
Max. picking rate	4.75 MHz	20.5 MHz
Contrast ratio (adjacent pulses)	10^{2}:1	**10^{11}:1**
Operation wavelength	700 – 1000 nm	1415 – 1750 nm (signal) 2510 – 3815 nm (idler)

TABLE 5.1. **Pulse picking performance comparison.** Performance comparison of a commercially available pulse picking system (Coherent, Pulse Picker) with the extended-cavity FFOPO system. Not only allows the FFOPO a significantly higher picking rate, but also the contrast ratio of adjacent pulses is 9 orders of magnitude higher than for the commercial system. Furthermore, the picking performance is independent of the signal (or idler) output wavelength.

The system has its fundamental pulse repetition rate at the 64^{th} subharmonic of the pump oscillator. Thus, the tunable output pulse train can be varied between 640 kHz and 41 MHz, which enables fluorescence lifetime imaging microscopy (FLIM) measurements with extremely long lifetimes. Effectively, the performance of the pulse picker in the pump beam is enhanced by the subsequent FFOPO system exploiting its nonlinear characteristics. For an existing synchronously pumped FFOPO system the extended-cavity approach presented in this work offers an easy-to-implement, low-cost upgrade possibility, such that the FFOPO capabilities are extended to variable

repetition rates. Further suppression of reflections can be achieved by changing to a ring cavity, such that backwards-propagating reflections do not appear in the signal output. Additionally, subsequent temporal pulse cleaning via SHG would increase the minimum contrast ratio to $\sim 100\,\mathrm{dB}$. Residual wing pulses caused by parametric fluorescence would be suppressed below the detection limit. Therefore, this system could also be used as front-end system for high-power laser applications which aim for extremely high temporal contrast ratios.

5.7 EXPERIMENTAL DETAILS

These experiments involve numerous aspects, which have not been described in detail in the previous sections. Thus, this section shall provide deeper insights into the experimental details for the interested reader. For instance, the impact of electronic timing jitter on the temporal resolution of the cross-correlation scan is being discussed, as well as its influence on the signal-to-noise ratio. Furthermore, a detailed assessment of the conversion and detection efficiency of the cross-correlation system is presented.

5.7.1 *AOM Suppression Ratio in the Gating Channel*

In this subsection the extinction ratio of the pulse picking system in the *gating channel* is quantitatively determined. In particular, the suppression ratio of the unwanted remaining pulses is measured relatively to the desired main pulse.

Therefore, the AOM (operated in 1^{st} diffraction order) is set to generate the 8^{th} subharmonic of the gating laser, which is spatially overlapped with a 1550-nm cw laser, as depicted in Fig. 5.11(a). As illustrated in Fig. 5.8, the sum-frequency of the two channels is generated and measured with the SPCM and the time tagging unit. The resulting timing histogram is plotted in Fig. 5.11(b), from which the suppression ratio can directly be determined. Adjacent pulses are suppressed by 560:1, whereas nonadjacent pulses are two orders of magnitude weaker. In this case, the resulting suppression ratio amounts to 56,000:1. The residual diffraction of unwanted pulses into the 1^{st} diffraction order is caused by spurious RF power, which is still applied to the AOM.

In contrast, the suppression ratio for adjacent pulses of the AOM in the *pump channel* of the FFOPO only amounts to 20:1, as stated in the caption of Fig. 5.2. Weaker focusing, and therefore, higher power throughput increase the AOM rise time, which results in a reduced extinction ratio for unwanted adjacent pulses. For the cross-correlation gating channel, on the other hand, lower power levels are sufficient, such that a smaller focal waist can be used and optimal AOM rise times are achieved.

For the evaluation of the suppression ratios, the *leading* pulses relatively to the main pulse in the timing histogram are considered. Aforementioned after-pulsing, an inherent phenomenon in SPCMs, following the main pulse imposes a background signal onto the *trailing* pulses.

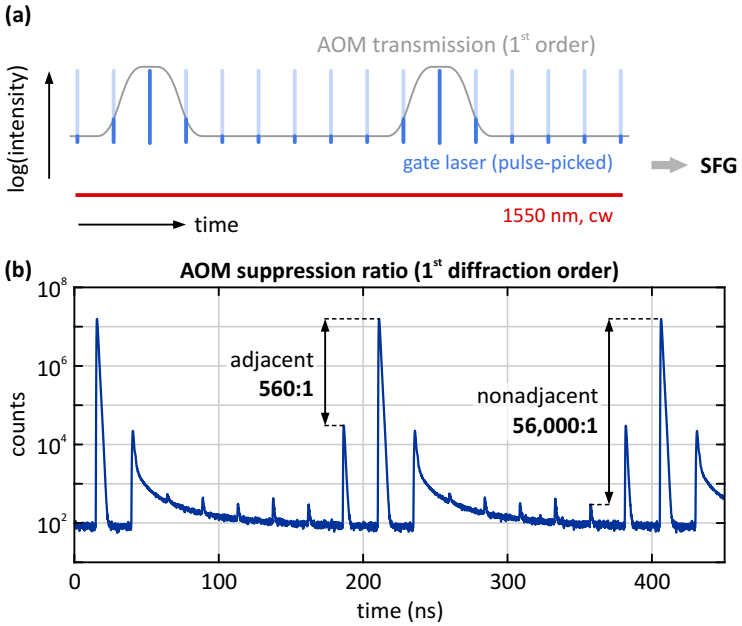

FIGURE 5.11. **AOM suppression ratio in the gating laser. (a)** Schematic of the pulse-picked gating laser pulse train. Gray line: AOM transmission window in 1st diffraction order operation. Its finite switching time leads to partial transmission of adjacent pulses. Nonadjacent pulses are efficiently suppressed. A 1550-nm cw laser is collinearly combined with the gating laser. **(b)** SFG signal between the pulse-picked gating laser and the cw laser (1550 nm). Suppression ratios of 560:1 (adjacent pulses) and 56,000:1 (nonadjacent pulses) are reached. 10 mW gating laser power at the 8th subharmonic (5.13 MHz), 58 μW cw laser power, 60 min integration time, 100 ps histogram bin width.

5.7.2 *Electronic Timing Jitter*

As described in Section 5.5.2 in the discussion of Fig. 5.10, the temporal resolution of the cross-correlation trace is ultimately dictated by the pulse duration of the gating laser (450 fs). Since the entire system is operated by the same front-end, i.e., the Yb:KGW oscillator, the relative timing between signal and gating pulses is intrinsically synchronized. Possible *optical* pulse-to-pulse jitter is of the order of only a few femtoseconds, and therefore, it does not affect the temporal resolution of the cross-correlation measurement.

Nevertheless, unwanted ghost pulses accompanying the main gating pulse in combi-

nation with *electronic* timing jitter in the acquisition chain impose a limitation on the *minimum temporal separation* of optical features in the FFOPO signal trace.
These weak ghost pulses, which originate from unavoidable reflections at optical elements, may undergo the SFG process as well. These SFG events are detected by the SPCM with advanced or delayed arrival times. This arrival time difference is sampled in the timing histogram as well. However, if the temporal separation between the main events and the unwanted events is smaller than the overall electronic timing jitter, the undesired events are convoluted into the main gating window and cannot be rejected anymore.

It shall be emphasized at this point, that the temporal resolution of $\sim 100\,\mathrm{fs}$ is not compromised by the electronic timing jitter. Only unwanted events may contribute to the signal peak at a given point in the cross-correlation trace.

In the following, the electronic jitter is investigated in more detail and its individual contributions are discussed. Table 5.2 lists the individual contributions and the overall electronic timing jitter.

		FWHM	RMS	
δt_{TT}	(time tagging unit)	80 ps	34 ps	(device specs)
$\delta t_{trig.}$	(trigger signal, pulse-to-pulse)	103 ps	44 ps	(directly measured)
δt_{SPCM}	(SPCM response)	–	607 ps	(derived)
δt_{tot}	(total timing jitter)	**910 ps**	**609 ps**	(directly measured)

TABLE 5.2. **Electronic timing jitter.** Root mean square (RMS) and FWHM values are given for each contribution. The SPCM response timing jitter represents the largest contribution. An overall FWHM timing jitter of 910 ps is observed. Here, the FWHM values for δt_{TT} and $\delta t_{trig.}$ are calculated from the respective RMS values according to Eq. 2.79 and Eq. 2.81 (both contributions are Gaussian distributed).

The overall electronic timing jitter δt_{tot} manifests in the finite width of the signal peak in the timing histogram, as depicted in Fig. 5.12. A full-width at half-maximum (FWHM) value of

$$\delta t_{tot} = 910\,\mathrm{ps} \tag{5.13}$$

is extracted. Therefore, optical features in the FFOPO signal trace separated by $< 30\,\mathrm{cm}$ may not be rejected from the resulting signal peak.

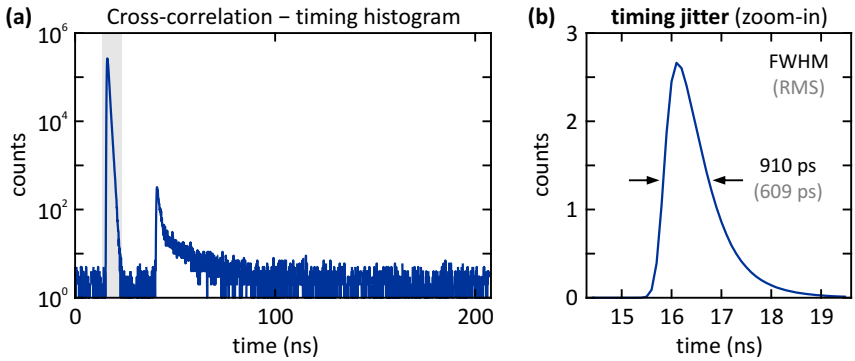

FIGURE 5.12. **Overall electronic timing jitter. (a)** Measured timing histogram, which corresponds to one data point of the cross-correlation trace, as depicted in Fig. 5.10. Logarithmic y-axis. **(b)** Zoom-in of the signal peak, as indicated by the gray shaded area. Linear y-axis. The FWHM of the signal peak amounts to 910 ps, the corresponding rms value yields 607 ps. This temporal spread is caused by timing jitter in the electronic acquisition chain, where the individual contributions are discussed below.

In the following, the individual contributions to the overall electronic jitter, as listed in Table 5.2, will be discussed.

(1) The intrinsic timing jitter of the **time tagging unit** (Swabian Instruments, Time Tagger 20) amounts to $\delta t_{\mathrm{TT}} = 34\,\mathrm{ps}\,(\mathrm{RMS})$ jitter, as given in the device specifications. Therefore, this contribution plays a subordinate role compared to the overall timing jitter.

(2) The pump oscillator provides the time base to which relative arrival times are measured by the time tagging unit. A photodiode is used to poll the trigger signal. In order for the time tagging unit to detect the trigger events reliably, the corresponding electronic pulses must exceed a minimum pulse duration of 1 ns. This directly translates to a finite rise time, which in turn causes a **trigger** timing inaccuracy $\delta t_{\mathrm{trig.}}$ in the comparator circuit of the time tagging unit.

(3) The **SPCM response** is subject to timing jitter δt_{SPCM} between the arrival time of a photon at the SPCM and the output of an electronic click.

The individual contributions $(1) - (3)$ are uncorrelated. According to Eq. 2.76, their individual variances therefore add up to the overall variance

$$\sigma_{tot}^2 = \sigma_{\mathrm{TT}}^2 + \sigma_{\mathrm{trig.}}^2 + \sigma_{\mathrm{SPCM}}^2. \tag{5.14}$$

The following measurement decouples contributions (2) and (3). Therefore, the electronic auto-correlation of the trigger signal is measured using the time tagger unit. For this purpose, the photodiode signal of the gating laser (pump oscillator) is used as the trigger signal and as the signal input for the time tagger unit at the same time. The resulting signal peak width in the timing histogram is a direct measure for the electronic timing jitter, which originates from the uncertainty of the trigger slope readout by the time tagger. Clearly, the intrinsic jitter of the time tagger enters the measurement as well. However, contributions (1) and (2) can be separated in post processing, as both are uncorrelated.

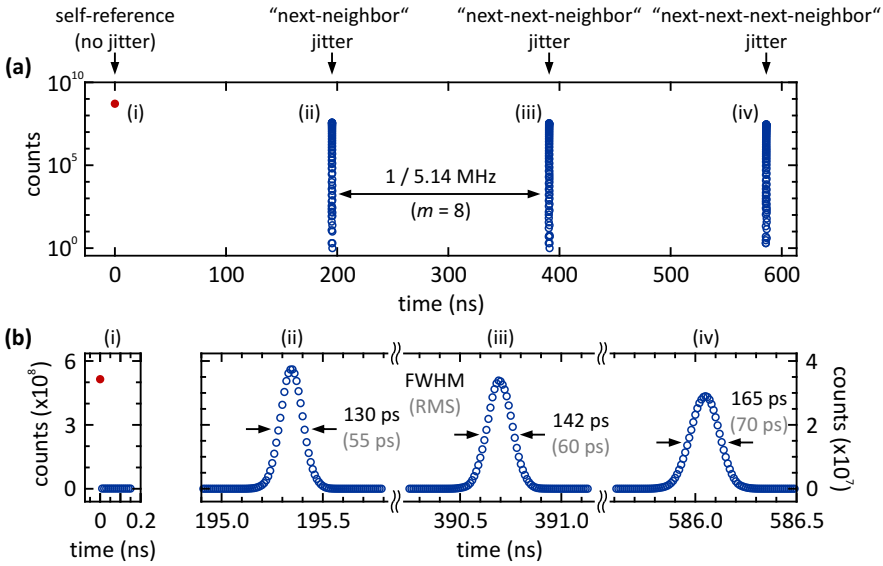

FIGURE 5.13. **Trigger signal – electronic timing jitter. (a)** Timing histogram of the electronic autocorrelation across three laser cycles, logarithmic y-axis. 5.135 MHz repetition rate ($m = 8$), 100 s integration time, 10 ps bin size for the timing histogram (well below the 30-ps intrinsic jitter of the time tagger). **(b)** Temporal zoom-ins for all four peak, linear y-axes. The first peak does (red dot) not exhibit any timing jitter, as this measures the relative arrival time between the trigger signal and itself. The other peaks measure the "n^{th}-neighbor" jitter, which increases with increasing separation between the trigger events, as given by the FWHM, and the RMS values, respectively. The total amount of detected events for the first peak is given in Table 5.3. Note, that the intrinsic timing jitter of the time tagger unit itself is contained in the measured signal.

Fig. 5.13(a) depicts the timing histogram for a 600-ns window. The repetition rate is set to 5.14 MHz ($m = 8$). Hence, three laser cycles are sampled within this time frame.

Fig. 5.13(b) depicts the signal peaks on a linear scale.

The first peak does not exhibit any timing jitter, as it measures the relative arrival time between the trigger signal and itself, which of course is zero. Hence, all n_0 detected events fall into one single time bin in the histogram. Its value measures the number of detected trigger events within the given integration time T_{int}

$$n_0 = \frac{f_{\text{rep}}}{8} \cdot T_{\text{int}}, \tag{5.15}$$

which is given in Table 5.3. The number of detected events decreases by exactly 1 for each next signal peak. This can be understood as follows: Within the time span T_{int} (integration time) n_0 trigger events occur. As peak (i) measures the relative arrival between each trigger event and itself (which of course is zero), peak (i) intrinsically samples the total number of trigger events. Peak (ii), on the other hand, measures the relative arrival time between two adjacent trigger events. Consequently, in order to acquire n_0 samples, a total measurement time of $T_{\text{int}} + 8/f_{\text{rep}}$ would be required. Hence peak (ii) acquires exactly $(n_0 - 1)$ samples within T_{int}. Therefore, for every further higher-order correlation peak the number of samples decreases by exactly 1, as listed in Table 5.3.

peak	number of detected events *n*
(i)	513,523,313 (:= n_0)
(ii)	513,523,312 ($n_0 - 1$)
(iii)	513,523,311 ($n_0 - 2$)
(iv)	513,523,310 ($n_0 - 3$)

TABLE 5.3. **Number of detected events.** Signal peaks (i)–(iv) depicted in Fig. 5.13 are integrated in order to obtain the total number of detected events, respectively. As expected, the number of detected events for next-neighbor correlations decreases by steps of 1. Dividing n_0 by the integration time of 100 s directly yields the pulse repetition rate in units of 1 Hz.

As depicted in Fig. 5.13(b), peak (ii) yields an RMS jitter of 55 ps. Note, that the mean of the peak has been shifted to $t = 0$ for this evaluation, i.e., the RMS value corresponds to the standard deviation. As mentioned above, both, the intrinsic jitter of the time tagging unit and the jitter of the trigger signal, enter this value. According to Eq. 2.76, the RMS jitter for the trigger signal, therefore, is given by

$$\sigma_{\text{trig.}} = \sqrt{\sigma^2_{\text{TT+trig.}} - \sigma^2_{\text{TT}}} = \sqrt{(55\,\text{ps})^2 - (34\,\text{ps})^2} = 44\,\text{ps}. \tag{5.16}$$

Finally, according to Eq. 5.14, the RMS jitter of the SPCM response can be determined to

$$\sigma_{\mathrm{SPCM}} = \sqrt{\sigma_{\mathrm{tot}}^2 - \sigma_{\mathrm{trig.}}^2 - \sigma_{\mathrm{TT}}^2} = 607\,\mathrm{ps}, \tag{5.17}$$

which thus is the largest contribution to the overall timing jitter.

5.7.3 *SFG Conversion Efficiency*

In this section the *optical conversion efficiency* of the sum-frequency generation (SFG) process between the OPO signal and the gating laser is determined.

The optical conversion efficiency η_{BBO} in the β-barium borate (BBO) crystal is given by the ratio of the photon numbers at the output channel n_{SFG} (SFG photons) and at the input channel n_{s} (OPO signal photons)

$$\eta_{\mathrm{BBO}} = \frac{n_{\mathrm{SFG}}}{n_{\mathrm{s}}}. \tag{5.18}$$

Note, that n_{s} is number of *gated* signal photons, i.e., temporal overlap with the gating laser is required. Thus, for η_{BBO} being meaningful, the laser power levels of the interacting channels have to be stated. In this case the laser power levels are set as given in Table 5.4.

P_{gate}	75 mW	1032 nm
P_{s}	43 mW	1584 nm
P_{SFG}	470 µW	625 nm

(measured at m = 1)

TABLE 5.4. **Average laser power levels** and center wavelengths of the interacting channels. The repetition rate is set to 41 MHz ($m = 1$).

In the following, *complete temporal overlap* of the signal pulses with the gating pulses is assumed. Considering typical signal pulse durations of 320 – 400 fs (see Fig. 5.4) and a gating pulse duration of 450 fs, this is a valid assumption. Hence, all signal photons are considered to be able to undergo an interaction with the gating laser mode in the BBO crystal.
For simplicity, we further assume, that the pulse energy E_{pulse} can be expressed as an equivalent number of photons n at the center wavelength λ_{c}

$$E_{\mathrm{pulse}} = n \cdot \hbar\omega_{\mathrm{c}} = n \cdot \frac{hc}{\lambda_{\mathrm{c}}}, \tag{5.19}$$

where h denotes Planck's constant. Furthermore, we can relate the number of photons to the average laser power P_{avg}

$$E_{\text{pulse}} = n \cdot \frac{hc}{\lambda_c} = \frac{P_{\text{avg}}}{f_{\text{rep}}}, \tag{5.20}$$

where f_{rep} represents the pulse repetition rate. From this, we deduce

$$n = \frac{P_{\text{avg}} \cdot \lambda_c}{f_{\text{rep}} \cdot hc} \propto P_{\text{avg}} \cdot \lambda_c. \tag{5.21}$$

Further, energy conservation demands

$$\hbar\omega_{\text{SFG}} = \hbar\omega_{\text{gate}} + \hbar\omega_s, \tag{5.22}$$

which can be rewritten in terms of the corresponding center wavelengths to

$$\frac{1}{\lambda_{\text{SFG}}} = \frac{1}{\lambda_{\text{gate}}} + \frac{1}{\lambda_s}. \tag{5.23}$$

This yields for the optical conversion efficiency

$$\begin{aligned} \eta_{\text{BBO}} &= \frac{P_{\text{SFG}} \cdot \lambda_{\text{SFG}}}{P_s \cdot \lambda_s} \\ &= \frac{P_{\text{SFG}}}{P_s} \cdot \frac{1}{1 + \lambda_s/\lambda_{\text{gate}}} \\ &= 4.312 \cdot 10^{-3}. \end{aligned} \tag{5.24}$$

Hence, for 1000 incoming signal photons, ~ 4 SFG photons are generated on average, which corresponds to a conversion efficiency of 0.4%.

5.7.4 *Detection Efficiency SPCM*

In the following, the detection effiency η_{SPCM} of the SPCM is evaluated. The overall detection efficiency η_{tot} is given by the product of the optical conversion efficiency via the SFG process in the BBO crystal and the detection efficiency of the SPCM

$$\eta_{\text{tot}} = \eta_{\text{BBO}} \cdot \eta_{\text{SPCM}}. \tag{5.25}$$

The optical conversion efficiency η_{BBO} is known as given by Eq. 5.24. The SPCM detection efficiency can be further decoupled into the quantum efficiency η_{QE} ($> 70\%$ at 650 nm) of the SPCM itself, and the incoupling efficiency $\eta_{\text{incoupl.}}$ of the optical mode into the detector, which yields

$$\eta_{\text{tot}} = \eta_{\text{BBO}} \cdot \eta_{\text{QE}} \cdot \eta_{\text{incoupl.}}. \tag{5.26}$$

Further, the overall efficiency can be measured, which allows to determine $\eta_{\text{incoupl.}}$ as

$$\eta_{\text{incoupl.}} = \frac{\eta_{\text{tot}}}{\eta_{\text{BBO}} \cdot \eta_{\text{QE}}}. \tag{5.27}$$

The overall detection efficiency η_{tot} can be expressed as

$$\eta_{\text{tot}} = \frac{N_{\text{det. events}}}{N_{\text{photons}}}, \tag{5.28}$$

where $N_{\text{det. events}}$ denotes the number of events detected by the time tagging unit, and N_{photons} represents the number of 1550-nm photons (cw laser), which are gated by the gating laser across the integration time T_{int}. The experiment is carried out using the parameters as stated in the following Table 5.5. The corresponding timing histogram is depicted in Fig. 5.8(b).

$\boldsymbol{P}_{\text{gate}}$	10 mW	1032 nm
$\boldsymbol{P}_{\text{cw}}$	255 pW	1550 nm
$\boldsymbol{\Delta t}_{\text{int}}$	100 s	

(measured at m = 8)

TABLE 5.5. **Measurement parameters – sensitivity limit.** Average laser power levels and center wavelengths of the interacting channels used to determine the sensitivity limit. The repetition rate is set to 5.13 MHz ($m = 8$). The corresponding measurement is depicted in Fig. 5.8(b).

First, the number of 1550-nm photons (cw laser), which fall into one single gating time window of $\Delta\tau_{\text{gate}} = 450\,\text{fs}$ is estimated. Statistically, a cw power level of $P_{\text{cw}} = 255\,\text{pW}$ yields an *average* number of photons per gating pulse of

$$\begin{aligned} n_{\text{photons}} &= \frac{P_{\text{cw}}}{E_{\text{photon}}} \cdot \Delta\tau_{\text{gate}} \\ &= \frac{P_{\text{cw}}}{hc/\lambda} \cdot \Delta\tau_{\text{gate}} \\ &= 8.95 \cdot 10^{-4}\ \frac{\text{photons}}{\text{gating pulse}}, \end{aligned} \tag{5.29}$$

where E_{photon} denotes the energy of a photon with a wavelength $\lambda = 1550\,\text{nm}$, h and c represent Planck's constant and the speed of light, respectively. Considering the repetition rate f_{rep} ($m = 8$), the total number of gating pulses within the integration time window T_{int} amounts to

$$N_{\text{pulses}} = f_{\text{rep}} \cdot T_{\text{int}} = 5.13 \cdot 10^{8}. \tag{5.30}$$

Therefore, the number of gated 1550-nm photons (cw laser) within the integration time T_{int} can be deduced

$$N_{\text{photons}} = n_{\text{photons}} \cdot N_{\text{pulses}} = 4.59 \cdot 10^5. \tag{5.31}$$

Integration of the signal peak of the timing histogram yields the number of detected events

$$N_{\text{det. events}} = 90. \tag{5.32}$$

Hence, the *total* detection efficiency is determined to

$$\eta_{\text{tot}} = \frac{N_{\text{det. events}}}{N_{\text{photons}}} = 1.96 \cdot 10^{-4}. \tag{5.33}$$

Equations Eq. 5.24, Eq. 5.27, and Eq. 5.33 yield

$$\eta_{\text{incoupl.}} = \frac{\eta_{\text{tot}}}{\eta_{\text{BBO}} \cdot \eta_{\text{QE}}} = 6.5\% \tag{5.34}$$

for the incoupling efficiency.

5.7.5 *Signal-to-noise Ratio – Timing Histogram*

In this section the signal-to-noise ratio (SNR) obtained from the timing histogram is assessed. The SNR ultimately determines the sensitivity, which can be reached by the measurement, i.e., down to which level spurious photons can still be detected. Therefore, this section aims to provide insights on the behavior of the signal and the noise level depending on the integration time.

Fig. 5.14 depicts an exemplary timing histogram, which shall support the following discussion on how the signal and the noise level are determined.

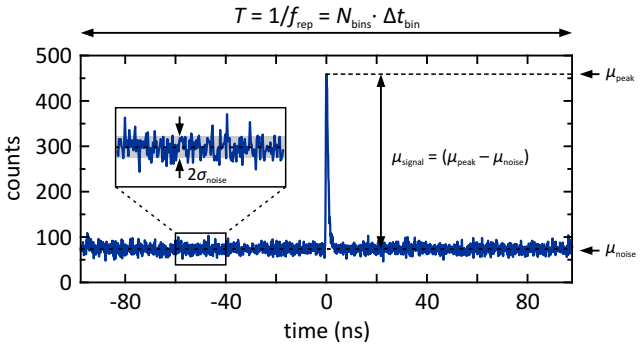

FIGURE 5.14. **Signal-to-noise ratio – timing histogram.** Exemplary timing histogram to demonstrate how the SNR is determined from the respective mean signal level μ_{signal} and the noise standard deviation σ_{noise}. The plotted time frame corresponds to exactly one single pulse cycle $T = 195.4\,\text{ns}$, where the corresponding repetition rate is set to $f_{rep} = 5.13\,\text{MHz}$ $(m = 8)$. The time bin width is set to $\Delta t_{bin} = 100\,\text{ps}$, which corresponds to $N_{bins} = 1954$. Integration time $T_{int} = 90\,\text{min}$.

After an integration time T_{int} a total number of SFG events

$$N_{signal} = R_{signal} \cdot T_{int} \tag{5.35}$$

form the signal peak in the timing histogram. These SFG events are temporally correlated with the laser repetition rate, and therefore, these clicks are binned into a narrow region in the timing histogram. In this context, R_{signal} denotes the rate of signal (SFG) events. At the same time, a total number of unwanted dark counts

$$N_{dark} = R_{dark} \cdot T_{int}, \tag{5.36}$$

detected at a dark count rate R_{dark}, cause a noise background. These dark counts, which are temporally uncorrelated to the laser repetition rate, form a *discrete uniform distribution* [86, p. 215] across all time bins

$$N_{bins} = \frac{T}{\Delta t_{bin}} = \frac{1}{f_{rep} \cdot \Delta t_{bin}} \tag{5.37}$$

in the histogram, where Δt_{bin} represents the width of an individual time bin, see Fig. 5.14. The laser pulse roundtrip time T can be expressed in terms of the inverse pulse repetition rate f_{rep}. The SPCM used in this experiment (Excelitas, SPCM-AQRH-15-FC) exhibits an extremely low dark count rate of only $R_{dark} = 20\,\text{counts/s}$. The signal count rate, on the other hand, is given by

$$R_{signal} = f_{rep} \cdot \eta_{tot} \cdot N_{fund.}, \tag{5.38}$$

where η_{tot} denotes the overall efficiency, as given by Eq. 5.26. Furthermore, $N_{\text{fund.}}$ represents the number of *gated* (fundamental) OPO signal photons.

The SNR is can be expressed as

$$\text{SNR} = \frac{\mu_{\text{signal}}}{\sigma_{\text{noise}}} = \frac{(\mu_{\text{peak}} - \mu_{\text{noise}})}{\sigma_{\text{noise}}}, \tag{5.39}$$

where μ_{peak} denotes the mean count level of the signal peak, which is formed by the total number of signal events N_{signal}. However, the relevant quantity is the signal peak prominence relative to the surrounding mean background level μ_{noise}, which is accounted for by subtracting it accordingly, as depicted in Fig. 5.14. The *standard deviation* of this baseline signal σ_{noise} characterizes the noise floor, as denoted in the inset of Fig. 5.14.

In the following, these three quantities will be discussed individually. The mean peak level is given by

$$\mu_{\text{peak}} = \frac{N_{\text{signal}}}{N_{\text{bins, peak}}}. \tag{5.40}$$

Timing jitter, as discussed in Section 5.7.2, causes the signal peak to spread across $N_{\text{bins, peak}}$ time bins in the timing histogram. We assume, that the signal events are *uniformly distributed* within the signal peak region, i.e., the peak forms a rectangular shape. Clearly, the electronic timing jitter reduces the peak signal level, and thus, limits the achievable SNR. The number of bins, which contain the signal peak is given by

$$N_{\text{bins, peak}} = \frac{\Delta\tau}{\Delta t_{\text{bin}}}, \tag{5.41}$$

where $\Delta\tau$ denotes the temporal width of the peak. The mean signal peak level yields

$$\mu_{\text{peak}} = \frac{R_{\text{signal}}}{N_{\text{bins, peak}}} \cdot T_{\text{int}}. \tag{5.42}$$

Analogously, the mean background level yields

$$\mu_{\text{noise}} = \frac{N_{\text{dark}}}{N_{\text{bins}}} = \frac{R_{\text{dark}}}{N_{\text{bins}}} \cdot T_{\text{int}}, \tag{5.43}$$

where N_i denotes the number of dark counts in the i^{th} time bin in the histogram. Consequently, the mean signal can be written as

$$\mu_{\text{signal}} = \mu_{\text{peak}} - \mu_{\text{noise}} = \left(\frac{R_{\text{signal}}}{N_{\text{bins, peak}}} - \frac{R_{\text{dark}}}{N_{\text{bins}}} \right) \cdot T_{\text{int}}. \tag{5.44}$$

Obviously, an increasing peak width $\Delta\tau$ leads to a higher number of bins $N_{\text{bins, peak}} = \Delta\tau / \Delta t_{\text{bin}}$ (Eq. 5.41), where the signal peak is spread across. This reduces the signal level μ_{signal}, and thus, the resulting SNR. The signal peak width $\Delta\tau$ is directly governed by the electronic timing jitter, as depicted in Table 5.2.
Furthermore, the number of bins N_{bins} has to be chosen such that the signal peak is resolved by at least a few time bins, i.e.,

$$\Delta t_{\text{bin}} < \Delta\tau. \tag{5.45}$$

Otherwise, the number of bins containing the signal peak $N_{\text{bins, peak}}$ saturates at 1 and dark counts accumulate in the same bin, while the total number of bins N_{bins} decreases. This results in a saturating peak level μ_{peak}, while the noise level μ_{noise} increases, see Eq. 5.44. Hence, the SNR deteriorates.
The noise level σ_{noise} is essentially the standard deviation of the number of counts N_i within the i^{th} time bin. According to Eq. 2.74 and Eq. 2.75, this can be written as

$$\begin{aligned} \sigma^2_{\text{noise}} &= \sigma^2(N_i) \\ &= \mathrm{E}(N_i^2) - \Big(\mathrm{E}(N_i)\Big)^2 \\ &= \frac{1}{N_{\text{bins}}} \sum_{j=1}^{N_{\text{bins}}} N_j^2 - \mu^2_{\text{noise}}. \end{aligned} \tag{5.46}$$

This expression cannot be further simplified. However, as discussed in Section 2.7.2, the *central limit theorem* provides the scaling behavior of the standard deviation with increasing sample size, i.e., increasing integration time T_{int}. According to Eq. 2.84, the standard deviation scales with

$$\sigma_{\text{noise}} \propto \sqrt{N_{\text{dark}}} \propto \sqrt{T_{\text{int}}}. \tag{5.47}$$

Additionally, the scaling behavior of the mean and the standard deviation is demonstrated by the following simulation depicted in Fig. 5.15. As apparent from the extracted slopes (note the double-logarithmic axes), the expected behavior as stated by the central limit theorem is reproduced. This simulation can also be used to extract explicit numbers for the expected noise standard deviation σ_{noise}.

Finally, according to Eq. 5.44 and Eq. 5.47, the resulting SNR scales as

$$\text{SNR} \propto \frac{T_{\text{int}}}{\sqrt{T_{\text{int}}}} = \sqrt{T_{\text{int}}}. \tag{5.48}$$

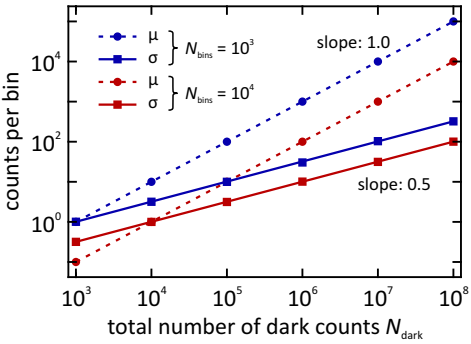

FIGURE 5.15. **Simulation – noise floor of the timing histogram.** Mean μ and standard deviation σ of the background arising from dark counts are simulated for a varying total number of dark counts N_{dark}. The simulation is carried out for two different number of bins N_{bins} in the timing histogram. As given by the extracted slope, the standard deviation, i.e., the noise level, increases with $\propto \sqrt{N_{\text{dark}}} \propto \sqrt{T_{\text{int}}}$. In contrast, the mean value increases with $\propto N_{\text{dark}} \propto T_{\text{int}}$. Simulation: MATLAB, uniformly distributed pseudo-random numbers.

5.7.6 *Suppression of Intra-cavity Backreflections*

The measured cross-correlation trace depicted in Fig. 5.10 exhibits peaks to both sides of time-zero, which arise from single or even mulitple backreflections at the surfaces of intra-cavity optical components. For this measurement angled physical contact (APC) intra-cavity fiber optics have been used.
The following Fig. 5.16 depicts the original cross-correlation trace (purple). Additionally, the gray curve shows the cross-correlation trace when using physical contact (PC) optics instead. As expected, the lower return loss for APC optics significantly reduces the backreflections.

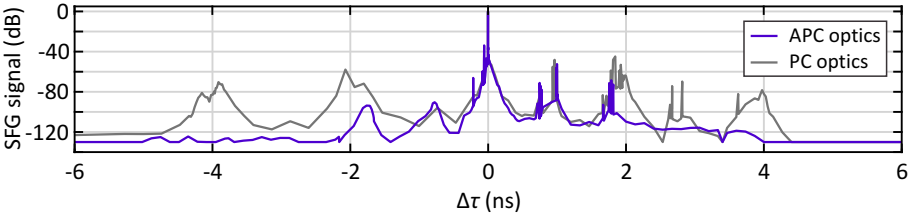

FIGURE 5.16. **Suppression of backreflections.** The use of APC intra-cavity fiber optics (purple) reduces backreflections substantially. PC fiber optics with 0° surfaces (gray), on the other hand, cause multiple backreflections which are spread across ± 4 ns.

Further suppression of intra-cavity reflections could be achieved by changing to a ring cavity configuration, such that backwards-propagating reflections do not appear in the signal output.

5.7.7 *Further Sensitivity Enhancement*

The sensitivity of the cross-correlation approach could be further enhanced by optimizing the operational parameters. Table 5.6 summarizes the potential sensitivity enhancement for this system, which will be briefly discussed in the following.

			enhancement factor
repetition rate	f_{rep}	5.13 MHz ⟶ 41.0 MHz	8
gate laser power	P_{gate}	10 mW ⟶ 50 mW (at m = 8)	5
electr. jitter SPCM	Δt_{SPCM}	1 ns ⟶ 0.5 ns	2
incoupling efficiency into SPCM	$\eta_{incoupl.}$	6.5% ⟶ 20 – 50%	3 – 8
optical conversion efficiency	η_{BBO}	0.4% ⟶ ~4%	10
		overall:	**2,400 – 6,400**

TABLE 5.6. **Potential sensitivity enhancement** for the cross-correlation system.

Increasing the repetition rate f_{rep} from 5.13 MHz ($m = 8$) to 41.0 MHz ($m = 1$, no pulse picking) would directly translate into an increased acquisition speed by a factor of 8. Therefore, a time tagging unit with increased bandwidth would be required (8.5 Mtags/s max. bandwidth were available for these experiments).
The gating laser power is limited to 10 mW at $m = 8$, which corresponds to 80 mW at $m = 1$. This limitation is imposed by the damage threshold of the AOM crystal coating. Hence, increasing the repetition rate up to 41.0 MHz would allow to remove the AOM from the gating laser beam line, and therefore, its maximum power throughput does not impose a limitation anymore.

The electronical timing jitter of the SPCM output determines the temporal spread of the signal peak in the timing histogram, and therefore, its prominence relative to the noise floor. In this case, the electronical timing jitter amounts to ~ 1 ns (FWHM). Improved electronics might reduce by a factor of ~ 2, and thus, increase the signal peak prominence, and eventually the signal-to-noise ratio. As shown in Eq. 5.34, the

optical incoupling efficiency into the SPCM is only $\eta_{\text{incoupl.}} = 6.5\%$. Using appropriate focusing optics would easily increase the incoupling efficiency up to $\sim 50\%$.

Furthermore, the optical conversion efficiency of $\eta_{\text{BBO}} = 0.4\%$ may also be increased by choosing a different crystal material for sum-frequency generation. In particular, the conversion efficiency may be increased by a factor of the order of ~ 10 using KTA ($KTiOAsO_4$) as nonlinear material, as reported in [87].

Overall, applying these measures may increase the signal by a factor of $2400 - 6400$, while keeping the integration time at the same value (100 s). Clearly, the integration time can be increased as well, which leads to a linear increase in the signal level, and therefore, in sensitivity.

6

ALL-OPTICAL RANDOM NUMBER GENERATION

In Chapter 3, the buildup process of the fiber-feedback optical parametric oscillator (FFOPO) signal upon instantly turning on the pump pulse train has been investigated in detail. Spontaneous parametric down-conversion provides the initial seed for this transient process. Furthermore, we have demonstrated the emergence of different attractors in the FFOPO signal output. In particular, period doubling and tripling as well as limit cycles have been observed. In this chapter, we will combine the transient process and period doubling output as equilibrium state to generate sequences of random binary numbers in an all-optical manner. The intrinsic bias in the binary distribution will be characterized and we will discuss different approaches to minimize this bias.

6.1 INTRODUCTION

Random numbers are of high importance in our everyday life. The most critical aspect probably is encryption to ensure secure money transfer, communication, and data transfer and storage. The underlying encryption keys are based on random numbers. The level of security against undesired decryption depends on the quality of the randomly generated keys. In this context, the term 'quality' is related to the number of possible outcomes of the random number generator for a given bit string length N. Optimally, each individual bit of the random sequence is independent from the other bits, i.e., 2^N outcomes are possible. In case of weak random number quality, where the number of outcomes is significantly reduced, minimal computational effort might be sufficient for successful decryption.

Due to the deterministic nature of computer algorithms, computer-generated random sequences will eventually repeat, even though they may exhibit very long seemingly random sequences. Therefore, these generators are referred to as *pseudo-random number generators*. For applications such as computer-based simulations of physical systems, pseudo-random numbers can be beneficial, as they provide reproducibility. For encryption, however, hardware true random number generators based on random physical processes are indispensable.

Ideally, hardware true random number generators have the following characteristics:

- Random physical process as source (radioactive decay, atmospheric noise, thermal noise, quantum noise ...).
- Unbiased equally distributed outcome.
- Robustness against changes of ambient conditions.
- Ambiguity-free extraction of random bits (a measurement that has two (or more) definite outcomes, which cannot be confused due to technical issues of the measurement apparatus).
- Pass random number tests.
- High entropy per bit (ideally, every individual bit represents an independent fair coin toss).

Furthermore, a high sampling speed is desired to generate long random sequences in a short time.

Period doubling states, also denoted as period-2 or P2 states, exhibit an alternating output, where every 2^{nd} output event is identical. It occurs in nonlinear systems featuring self-feedback, as discussed in Section 2.5. Thus, the emergence of period doubling bifurcation in the output pulse train of a FFOPO system is not surprising, as its nonlinearity and optical feedback offer the prerequisites for this phenomenon.

The bistable output can be employed to realize an all-optical hardware random number generator, as reported by T. Steinle et al. [88]. They utilize a P2 attractor as binary sampling mechanism, as schematically illustrated in Fig. 6.1. The P2 state allows the unambiguous detection of two distinct phase values against a global reference. The exact measurement scheme will be introduced in Section 6.3.

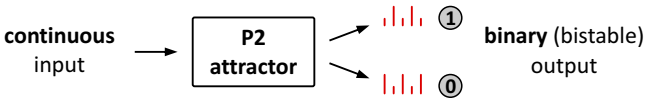

FIGURE 6.1. **P2 attractor as binary sampling mechanism.** A continuous random input is mapped onto a binary output. For this purpose, the bistable outcome of a P2 attractor serves as binary sampling mechanism.

The bit sequences generated by T. Steinle et al. pass a large set of random number tests. In combination with an entropy assessment, these bit sequences have been

verified to be flawless. It should be noted that randomness cannot be proved. A bit sequence can only be tested for flaws, which indicate a lack of randomness. However, sequences such as the binary representation of π pass all these tests, although being perfectly deterministic.

As the quality of randomness has been demonstrated by T. Steinle et al., we will not focus on random number testing. However, the original measurement scheme does not allow to separate the influence of the unsynchronized modulator phase on the outcome. To solve this, we introduce an improved modulation scheme with phase-stable pump burst generation, which allows to disentangle the influences of the modulator and of the intrinsic system dynamics on the binary distribution.

6.2 GENERATING AND DETECTING P2 CYCLES

As discussed in detail in Chapter 3, P2 cycles can be accessed by operating the FFOPO in the anomalous dispersion regime using the SMF-28 feedback fiber. Furthermore, rather high intra-cavity nonlinearity levels are required for P2 cycles to emerge, as demonstrated in Fig. 3.11. This can be achieved using high feedback ratios and/or high pump power levels. The cavity mismatch should be chosen such that the output wavelength is located at the short-wavelength slope of the phase matching spectral bandwidth window, see Fig. 3.5 and Fig. 3.9. In this region, the FFOPO exhibits a high tendency to produce in PN cycles, limit cycles, or chaos attractors. The detection sensitivity of P2 cycles can be increased by employing dispersive pulse stretching prior to electronic sampling, as will be discussed in more detail in the following.

First, the P2 cycles have to be identified and stabilized. We employ the 5-GHz InGaAs photodiode, the 20-km long SMF-28 fiber, and the 20-GSa/s oscilloscope, as we have used for the single-pulse spectral measurements, see Section 3.3.3 in Chapter 3. The presence of a P2 state can easily be assessed from the radio frequency spectrum of the signal output pulse train. Therefore, the FFT (fast FOURIER transform) functionality of the oscilloscope is used. Additionally to the prominent peak at the repetition rate of $f_{\mathrm{rep}} = 41\,\mathrm{MHz}$, a second peak at exactly $f_{\mathrm{rep}}/2$ arises in the radio frequency spectrum if a P2 cycle is present.

Period doubling may manifest not only in alternating pulse energies, but also in alternating pulse spectra. Hence, the P2 detection sensitivity using the radio frequency spectrum can be increased by accessing single-pulse spectra. Dispersive pulse stretching reveals alternating pulse output with higher sensitivity than relying on the

detection of alternating pulse energy only. In fact, P2 cycles with equal pulse energies but alternating spectra could not be detected without employing dispersive pulse stretching.

6.3 ALL-OPTICAL RNG – INSTRUMENTATION & MEASUREMENT PRINCIPLE

In the following, the principle of bit sequence generation will be described, which is largely based on and adopted from the measurement scheme employed by T. Steinle et al. [88].

Fig. 6.2 depicts the operation principle and the P2 phase detection scheme to generate bit sequences from the FFOPO. As described in Section 3.3.2 in Chapter 3, an acousto-optical modulator (AOM) is utilized for pump burst generation. Each pump burst produces a FFOPO signal burst, where the P2 cycle emerges from parametric fluorescence via a transient, as indicated at the bottom of the schematic. The FFOPO is turned off between each pulse burst.

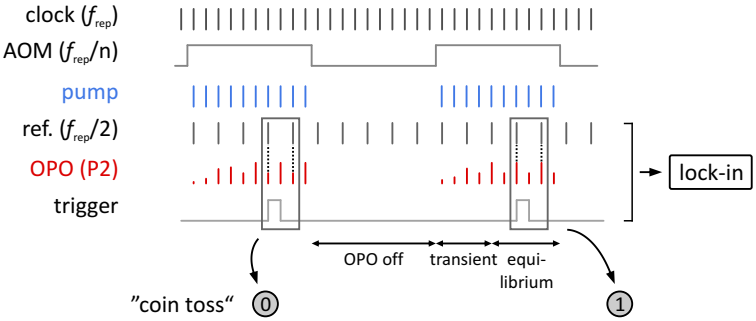

FIGURE 6.2. **P2 phase measurement.** The pump oscillator serves as the global clock operating at $f_{rep} = 41\,\text{MHz}$ to which all subsequent components are synchronized. The AOM generates pump bursts at an integer fraction of the repetition rate f_{rep}/n driving the FFOPO from its off-state into the P2 state. A reference signal at $f_{rep}/2$ is derived from the clock. The P2 state demodulation is triggered once the FFOPO reaches equilibrium. As the relative position between the reference and the P2 can only take two distinct values, the demodulated phase results in two discrete values separated by exactly 180 °. Figure adopted from [88] and [16].

The repetition rate f_{rep} of the pump oscillator is monitored and serves as the global clock to synchronize the entire measurement system. The electronic measurement control is realized within one single device (Zurich Instrument, UHFLI, AWG option installed) comprising the lock-in amplifier unit, as well as an arbitrary waveform

generator (AWG) to provide the phase-stable modulation sequence driving the AOM and the demodulation trigger signal. A reference signal for the P2 phase detection is directly derived from the clock and runs at $f_{\mathrm{rep}}/2$.

The idea is to compare the P2 cycle of each individual burst to the global reference ($f_{\mathrm{rep}}/2$) and to determine their relative phase. As indicated in Fig. 6.2, the reference signal coincides with either the high or the low pulse of the P2 state ('high' and 'low' encode alternating pulse properties). The lock-in amplifier is employed to extract this relative phase, which can take two distinct values, i.e., $\{0, \pi\}$. These two phase values can be interpreted as binary values. Therefore, each signal buildup into an equilibrated P2 state represents a coin toss with two outcomes. Since the relative phase between the P2 cycle and the reference can only take two defined values, *unambiguous* bit extraction is inherent to this scheme.

The main difference between this experimental scheme and the one reported by T. Steinle et al. is the phase-stable pump burst generation. Utilizing an electronically synchronized modulator rather than an independently running chopper wheel, allows to disentangle the influence of the modulator and the FFOPO dynamics themselves on the generated bit sequences.

6.4 INTRINSIC BIAS

As depicted in Fig. 6.3(a), the lock-in phase measurement of the P2 cycle against the $f_{\mathrm{rep}}/2$-reference results in two discrete outcomes, which are separated by exactly $\Delta\varphi = 180\,^{\circ}$. Note, that the absolute position of the phase values is given by the global phase between the lock-in amplifier and the reference signal. However, this value is not of interest. Fig. 6.3(b) depicts the corresponding phase histogram. The width of the two phase peaks is determined by the analog gain at the device input (which should be optimized in order to ensure optimal data sampling), the integration time (set to 1 µs for all measurements), and the modulation depth of the P2 pulse train itself. As mentioned in Section 6.2, the latter is improved by employing dispersive pulse stretching to increase the contrast between the alternating signal pulses. Each of the two phase peaks can be interpreted as binary outcome ('0' and '1'). Thus, the phase peaks are integrated and the resulting binary distribution is plotted in a histogram, as depicted in Fig. 6.3(c).

In contrast to the equally distributed bit strings reported by T. Steinle et al., this sequence exhibits a deviation of 5.314% from an equal distribution. This result confirms

the findings as presented in [16]. The bit sequences generated with phase-stable burst modulation are intrinsically biased. In the following, we will introduce modifications in the pump sequence to minimize this bias.

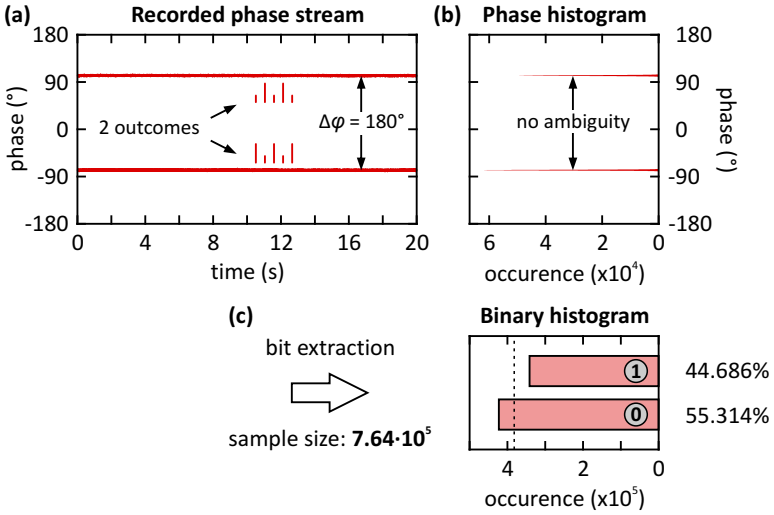

FIGURE 6.3. **Bit extraction. (a)** Raw data stream of the demodulated phase. Sampling rate: 38.2 kHz (given by the frequency divider), lock-in integration time per sample: 1 µs. The two outcomes are separated by exactly 180 °. **(b)** Histogram of the measured phase values, bin size 0.5 °. Each peak is interpreted as binary outcome, i.e., "0" and "1". The sharp distribution of the two occurring phase values allows ambiguity-free bit extraction. **(c)** The phase peaks are integrated and plotted in a binary histogram. The dashed line indicates the point of equal distribution. Here, a deviation from an equal distribution of 5.314% is observed. The sample size of $7.64 \cdot 10^5$ results from the sampling rate and the total measurement time of 20 s.

6.5 BIAS REDUCTION IN THE BINARY OUTCOME

As we have seen in Fig. 6.3, the bit sequences produced by the FFOPO system are intrinsically biased. In the following, we will apply different pump pulse sequences and monitor the influence on the bias in the binary distribution. Ideally, the output distribution is equalized by finding the right starting conditions for the signal buildup.

Fig. 6.4 depicts two concepts to influence the binary outcome. First, the starting condition of the signal transient is varied by selectively controlling the pulse energy of the first pump pulse of each pump burst, see Fig. 6.4(a). Since the first pump

pulse generates the initial seed for the upcoming roundtrip, varying its pulse energy may impact the buildup behavior, and therefore, the binary distribution. Secondly, a pre-conditioning sequence is applied prior to the P2 sequence. Rather than driving the FFOPO directly into the P2 sequence via the signal transient, an intermediate chaotic pulse sequence is applied. Generally, chaos attractors are located close to P2 cycles in terms of variations in the operational parameters. In this case, the average pump power level is selectively adjusted to access a close-by chaos attractor, as depicted in Fig. 6.4(b)

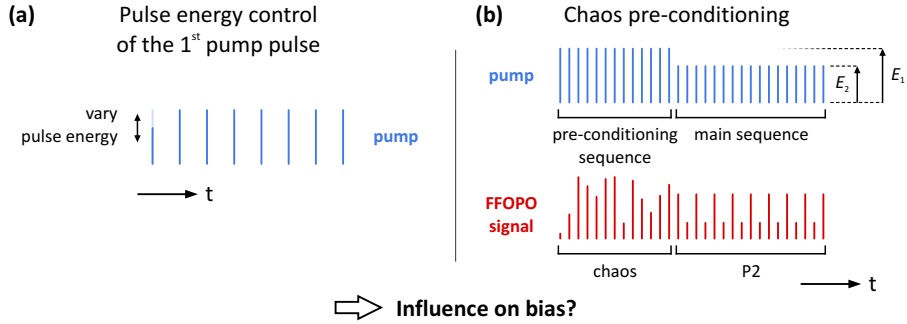

FIGURE 6.4. **Methods to influence the bias. (a)** Varying the pulse energy of the first pump pulse allows to control the starting condition for the FFOPO signal buildup into the P2 state. **(b)** A chaos attractor is employed as pre-conditioning sequence prior to the P2 sequence, which might reduce the bias. The chaos attractor can be accessed by applying a different pump pulse energy E_1 (pulse energy E_2 generates the P2 cycle). Clearly, both methods can be combined.

6.5.1 *Pulse Energy Control of the First Pump Pulse*

As illustrated in Fig. 6.4, the pulse energy of the first pump pulse is varied in order to influence the transient signal buildup process. Experimentally, this is realized by the precise timing control between the AOM and the pump pulse train. Basically, we exploit the finite rise time of the AOM to selectively and partially suppress the first pump pulse. The corresponding measurement is depicted in Fig. 6.5. To achieve this, we use the AWG to apply a precise time delay between the rising slope of the AOM and the pump laser. The AWG maximum sample rate of 1.8 GSa/s defines the time delay step size to 0.55 ns. Thus, 44 AWG samples replicate a time delay of 24.4 ns, which corresponds to the temporal separation of two subsequent laser pulses.

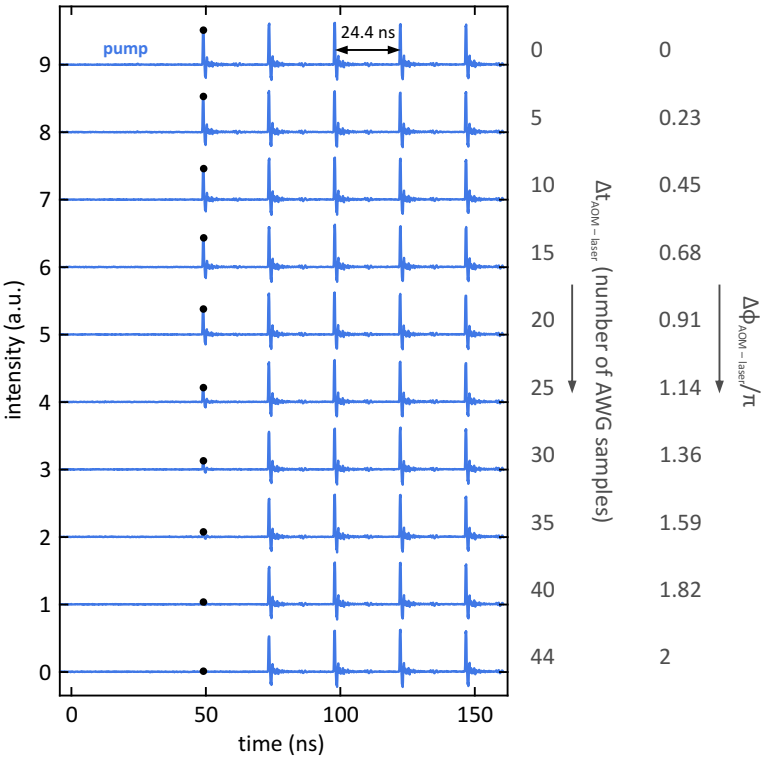

FIGURE 6.5. **Pulse energy control using the AOM.** The pulse energy of the 1st pump pulse can be selectively varied by shifting the relative phase $\Delta\phi_{\mathrm{AOM-laser}}$ between the AOM and the pump laser pulse train. To achieve this, the AWG sequence is used to shift the electronic control signal for the AOM. Each time trace shows the pump pulse sequence for a different number of AWG samples, which introduce an electronic time delay. The black dots indicate the subsequently suppressed 1st pump pulse. The AWG sample rate is set to 1.8 GSa/s, i.e., the temporal AWG sample spacing corresponds to 0.55 ns. Hence, 44 AWG samples correspond to the temporal laser pulse separation of 24.4 ns, and thus, to $\Delta\phi_{\mathrm{AOM-laser}} = 2\pi$.

The pulse energies of the first two pump pulses are extracted and plotted versus the applied time delay between the AOM and the pump laser, see Fig. 6.6. This yields the AOM response for the partial pulse attenuation. Ideally, the second pump would be unaffected. However, the finite switching speed of the AOM (given by the speed of sound in the AOM and the laser spot size) slightly attenuates the second pump pulse as well.

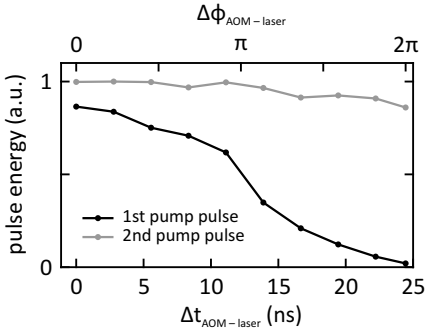

FIGURE 6.6. **AOM response – pulse attenuation.** The pulse energy of the first (black) and the second (gray) pump pulse are plotted as extracted from Fig. 6.5. Bottom x-axis: relative delay between the AOM rising slope and the pump laser, top x-axis: their relative phase (24.4 ns $\widehat{=} 2\pi$). As evident from the partial attenuation at $\Delta t_{\mathrm{AOM-laser}} \geqslant 15$ ns, the second pump pulse is slightly influenced by the limited switching speed of the AOM. Equally, the first pump pulse does not exhibit full pulse energy at $\Delta t_{\mathrm{AOM-laser}} = 0$.

6.5.2 *Pre-sequence with Chaotic Attractor*

Fig. 6.7 depicts the recorded time traces of the pump bursts and the corresponding

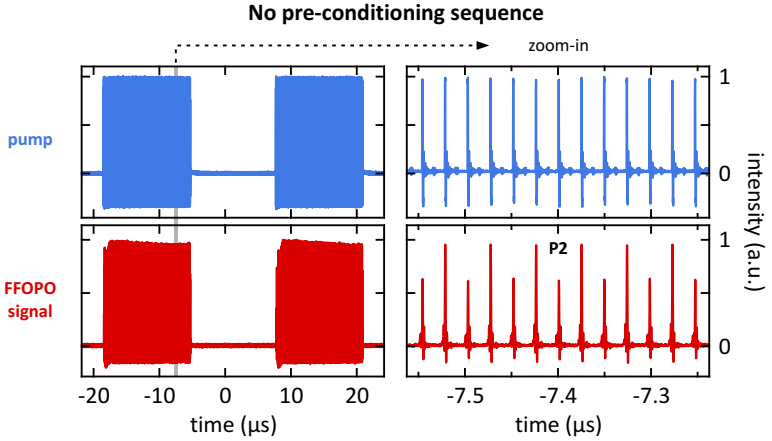

FIGURE 6.7. **P2 sequence only.** Two subsequent pulse bursts are recorded. A constant pump pulse energy across the burst is chosen, such only the P2 sequence is generated. The zoom-in plots on the right depict the equilibrated P2 cycle and the corresponding pump pulse train.

signal bursts, which are used as sequence to perform optical random bit generation. In this case, no pre-conditioning sequence is applied prior to the P2 sequence.

As illustrated in Fig. 6.4(b), a chaos pre-conditioning sequence might be beneficial to reduce the bias in the generated bit sequences. The measured time traces are presented in Fig. 6.8. An increased pump power level during the beginning of each pump burst is realized using the AWG, which drives the AOM. As evident from the FFOPO signal burst, a chaos attractor with large pulse-to-pulse fluctuations is generated by the increased pump power level.

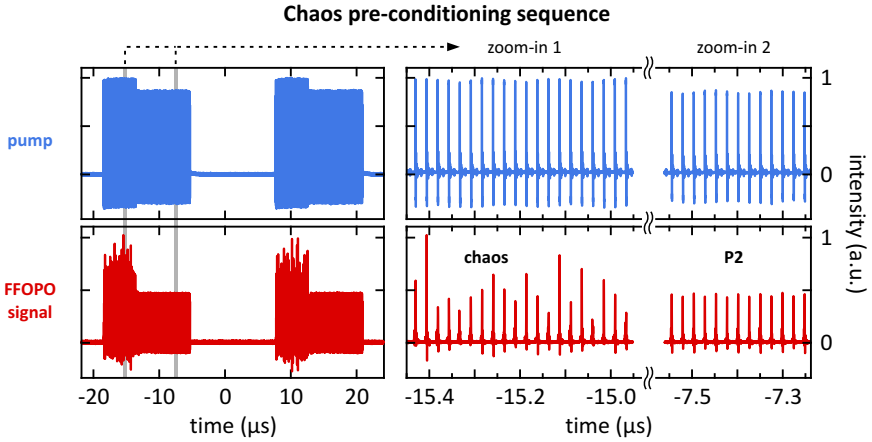

FIGURE 6.8. **Chaos pre-conditioning.** The pump pulse energy is increased at the beginning of each pulse burst. The increased pump level drives a chaos attractor, as clearly visible in the zoom-in plot on the right panel. The chaos attractor is followed by the P2 sequence once the pump pulse energy level is reduced.

6.5.3 *Results and Discussion*

In the previous sections, we have introduced and discussed two concepts to influence the bias in the binary outcome. First, we can use precise temporal control of the pulse picker for selective pulse energy control, and secondly, changing the pump power level during the pulse burst allows to generate a chaos attractor prior to the P2 state. The idea is to further randomize the starting condition for the P2 cycle, and therefore, to reduce the bias. In the following experiment, both concepts will be combined to assess their influence on the bias.

Fig. 6.9 plots the bias depending on the relative time delay between the AOM and the pump laser. Hence, the pulse energy of the first pump pulse is varied according to Fig. 6.6. The relative occurrence of the binary value '1' is plotted on the vertical axis. Please note, that the axis is shifted by 50%, such that the zero-line marks the point of equally distributed binary outcomes (dashed line). Two cases are plotted. First, only the P2 sequence is used (blue curve), and secondly, chaos pre-conditioning is applied (green curve) according to Fig. 6.8.

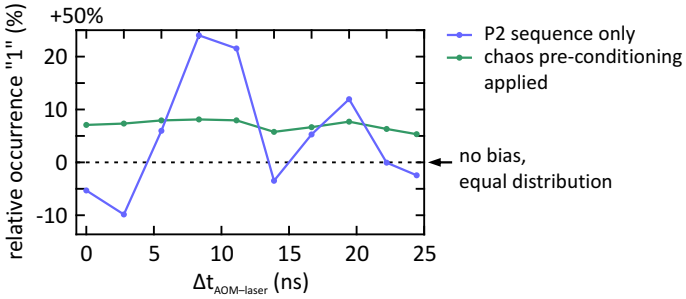

FIGURE 6.9. **Bias depending on the first pump pulse.** The pulse energy of the first pump pulse is varied by attenuating it using the AOM, see Fig. 6.6. The binary distribution strongly fluctuates if no pre-conditioning sequence is applied (blue). On the other hand, pre-conditioning with a chaos attractor renders the distribution independent from the first pump pulse (green), yet the bias does not vanish. The dashed line marks the point of equal distribution. Chaos sequence length: 200 pulses. Sample size per data point: $7.64 \cdot 10^5$.

In the first case without pre-conditioning, the bias fluctuates strongly in both directions and reaches deviations of $> 20\%$ from an equal distribution. The bias may reach almost zero for specific pulse energies, as it is the case at $\Delta t_{\mathrm{AOM-laser}} = 22.2\,\mathrm{ns}$. However, these points are not stable and slight changes in the operational parameters as well as in the ambient conditions are sufficient to induce a deviation from the equal distribution.

In case a chaos pre-conditioning sequence is applied, the bias becomes independent of the pump pulse energy of the first pump pulse, yet the bias does not vanish. This result indicates, that the buildup from quantum noise is not the decisive influence. Rather the feedback pulse directly preceding the P2 sequence determines the bias. On average, the chaos sequence provides the same starting conditions for the P2 cycle, and therefore, renders the bias insensitive to the very first pump pulse of the burst sequence.

In the following, the bias is characterized depending on the length of the chaos pre-conditioning sequence, see Fig. 6.11. The first data point (chaos sequence length: 0) yields a strong bias, as expected from Fig. 6.9. For varying lengths of the chaos pre-conditioning sequence, we observe an almost constant bias. This also indicates that the feedback pulse preceding the P2 sequence is decisive for the resulting binary distribution.

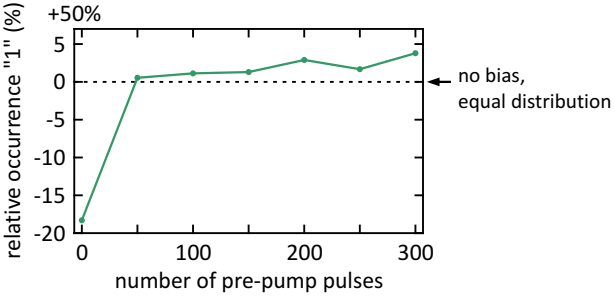

FIGURE 6.10. **Bias depending on pre-conditioning sequence length.** A chaos attractor is employed as pre-conditioning sequence. The bias is mostly independent of the length of the pre-conditioning sequence, indicating that the feedback pulse that precedes the P2 sequence is decisive for the binary outcome. Without pre-conditioning (the first data point), a strong bias is observed. This aligns with the results from Fig. 6.9. The dashed line marks the point of equal distribution. Sample size per data point: $7.64 \cdot 10^5$.

The residual bias observed in this measurement is lower than in Fig. 6.9. The reason is that chaos attractors at different FFOPO working points are employed. This results in slightly different average starting conditions for the P2 cycle, and thus, alters the bias. Consequently, one could argue to choose the operational parameters (e.g., the pump power) of the FFOPO such that the chaos attractor yields a bias of zero. However, this again is unstable against changes in the ambient conditions.

6.5.4 *Cavity Cold-start vs. Running Cavity*

The previously presented experiments and results indicate, that the binary distribution depends on the seed pulse preceding the P2 sequence. This raises the question of whether the starting process itself, namely amplified vacuum noise, introduces the randomness, or if the randomness is attributed to the nonlinear feedback by means of operating in a chaotic state.

Therefore, we remove the influence of the starting process in the following experiment. Fig. 6.11(a) depicts the control experiment, where the buildup from amplified vacuum noise is followed by a chaos pre-conditioning sequence and the P2 attractor. This replicates the situation as depicted in Fig. 6.8. Although we only skip 50 pump cycles between the bursts, this is still sufficient to turn off the FFOPO. Due to the high intra-cavity losses, the signal ring-down after turning off the pump takes place within a few cavity roundtrips. We observe a small bias of 0.08%.

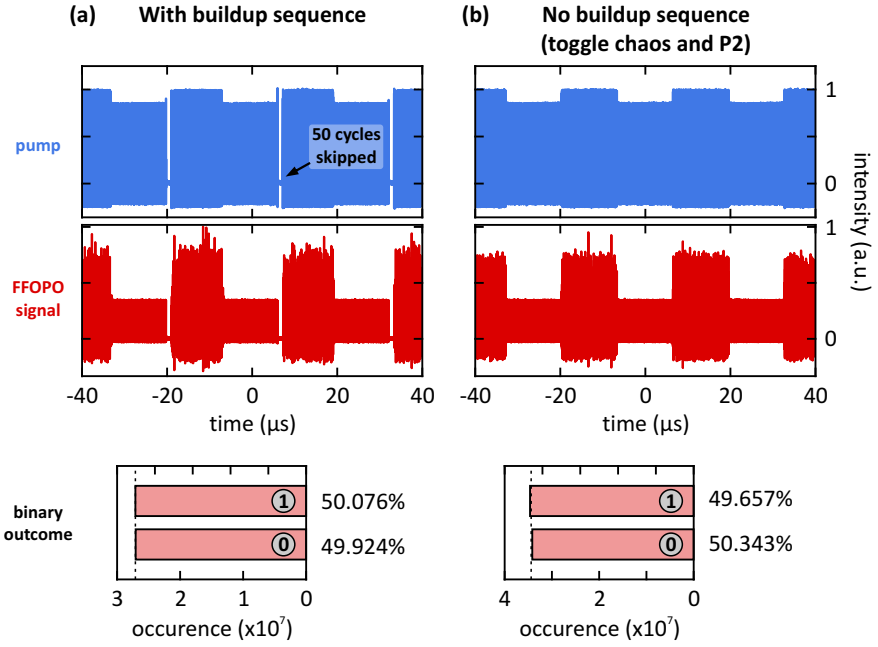

FIGURE 6.11. **Bias depending on the presence of a buildup sequence. (a)** Signal buildup into a chaos pre-conditioning sequence, followed by the P2 sequence. 50 pump cycles are skipped between each burst to ensure a 'cold-cavity' start from vacuum noise. A small bias is observed. **(b)** The pump power is toggled between two power levels without turning off the FFOPO between subsequent bursts. This removes the influence of the signal buildup. The resulting bit sequence exhibits only a slightly increased bias. Sample sizes: $6.87 \cdot 10^7$ and $5.42 \cdot 10^7$.

In Fig. 6.11(b), the pump power is toggled between two levels without turning off the FFOPO. The signal output therefore toggles between chaos and the P2 state. The resulting binary distribution deviates only slightly from the control experiment. In fact, changes in ambient temperature in the course of these experiments are enough

to induce this deviation. This result suggests, that the randomness mainly arises from the chaotic state, i.e., the interplay between the nonlinear feedback, parametric gain, cavity losses, and intensity noise carried by the pump beam. In the context of the latter, T. Steinle et al. demonstrate that the measured relative intensity noise of the pump integrated between 10 kHz and 20 MHz is a factor of ~ 50 too small to be the relevant driver of the randomness generation [88]. However, this holds for the case that no chaotic attractor is involved. In our case, the pump intensity noise may suffice to introduce enough randomness via the chaotic attractor. To confirm this assumption, further investigations including pulse propagation simulations would be necessary.

6.6 CONCLUSIONS & OUTLOOK

In conclusion, we find that the FFOPO system is intrinsically biased. Synchronization of the pump burst generation to the pump oscillator removes the influence of an unstable modulator and reveals the intrinsic bias of this system. We demonstrate the strong influence of the first pump pulse of the pump burst on the resulting binary distribution. Applying pre-conditioning pulse sequences based on a chaotic attractor removes the sensitivity of the bias to the pulse energy of the first pump pulse. Yet, the bias does not vanish. Thus, the signal roundtrip prior to the start of the P2 sequence seems to be decisive for the binary distribution.

We furthermore isolate the influence of the signal buildup process from vacuum noise from the influence of the chaotic attractor on the outcome. Our findings suggest that chaos mediated by the interplay between the nonlinear feedback, parametric, cavity losses, and pump intensity noise may introduce enough randomness to the system to be used for random number generation. Nevertheless, further investigations of the exact influence of the chaotic attractor on the randomness are necessary. Especially the remaining bias has to be suppressed for the system to be of broad interest for applications such as encryption.

Another approach towards fast unbiased true random number generation could be the original scheme, employing the unsynchronized beating between the modulator and the repetition rate of the pump oscillator combined with high modulation frequencies, and thus, increased sampling rates. Operating the AOM at burst frequencies, which are not synchronized to the laser oscillator could, on the one hand, restore the unbiased output of the original scheme published by T. Steinle et al. and, on the other hand, increase the sampling rate from originally 10 kHz up to several 100 kHz.

7

3D STIMULATED RAMAN SCATTERING IMAGING

In the previous chapters the nonlinear dynamics of the fiber-feedback optical parametric oscillator (FFOPO) system have been studied extensively. The following two chapters discuss stimulated Raman scattering (SRS) microscopy for biomedical and biological applications as direct application of the FFOPO as tunable light source.

This chapter is based on the following published work:

> **M. Floess**, T. Steinle, F. Werner, Y. Wang, W. L. Wagner, V. Steinle, B. S. Liu, Y. Zheng, Z. Cheng, M. Ackermann, S. J. Mentzer, and H. Giessen
> *3D stimulated Raman spectral imaging of water dynamics associated with pectin-glycocalyceal entanglement*
> Biomed. Opt. Express **14**, 1460–1471 (2023).

7.1 ABSTRACT

Pectin is a heteropolysaccharide responsible for the structural integrity of the cell walls of terrestrial plants. When applied to the surface of mammalian visceral organs, pectin films form a strong physical bond with the surface glycocalyx. A potential mechanism of pectin adhesion to the glycocalyx is the water-dependent entanglement of pectin polysaccharide chains with the glycocalyx. A better understanding of such fundamental mechanisms regarding the water transport dynamics in pectin hydrogels is of importance for medical applications, e.g., surgical wound sealing. We report on the water transport dynamics in hydrating glass-phase pectin films with particular emphasis on the water content at the pectin-glycocalyceal interface. We used label-free 3D SRS spectral imaging to provide insights into the pectin-tissue adhesive interface without the confounding effects of sample fixation, dehydration, shrinkage, or staining.

7.2 INTRODUCTION

Defined as three-dimensional hydrophilic polymer networks, hydrogels provide a promising tool in biomedical applications such as wound healing, drug delivery and

tissue repair [89–91]. A particularly intriguing hydrogel is the plant-derived heteropolysaccharide pectin. Structurally, pectin has a high content of partially esterified linear chains of (1,4)-α-D-galacturonic acid residues. Functionally, the pectin chains contribute to the structural integrity of the middle lamella between plant cells by entangling with other pectin chains and cellulose microfibrils [92]. Structurally, pectin is similar to the extracellular surface layer of mammalian cells [93] and pectin chains also entangle with the glycocalyx of visceral organs [94], thereby providing a structural scaffold for wound healing and an opportunity to facilitate tissue repair [95–97].

A distinctive property of polysaccharide polymers, including pectin and the glycocalyx, is the alteration of structural and physical properties with changes in water content [98]. Pectin can demonstrate striking and reversible changes in its physical properties with even small changes in the amount of polymer hydration [99]. The loss of water from a disperse solution of pectin can lead to a change in the physical properties from a viscous liquid to a soft and rubbery gel. With ongoing water loss, the physical properties change from a soft gel to a hard and glassy film. These phase transitions have functional and microstructural implications that remain unclear because of the difficulty in detecting the time-dependent water content in the native pectin polymer.

To identify the water transport dynamics in glass-phase pectin films, we measured water movement in pectin films using 3D SRS microscopy. SRS is an ideal modality as it enables label-free imaging without the need for tissue dehydration, exogenous tracers or chemical fixation [100]. Hence, the addition of chemical fixatives, fluorophores, or tracers is unnecessary. In addition to morphological assessments, quantitative temporal and spectral data evaluation is possible because the SRS signal scales linearly with the concentration of the specimen. Moreover, SRS is free of a non-resonant signal contribution that is present in coherent anti-Stokes Raman scattering (CARS) microscopy [21, 101–104]. In contrast to conventional Raman scattering, SRS exhibits a drastically increased interaction cross-section owing to the simultaneous presence of the pump and Stokes fields. This allows very fast data acquisition speeds up to video rate imaging [105, 106], which is ideal to capture the water transport processes.

Using hyperspectral 3D SRS imaging we depict the interface of pectin polymer biomaterial and serosal tissue. This provides, for the first time, quantitative insights into the structural transition zone between pectin and the serosal tissue, as well as the water-dependent entangling phenomenon between a plant-derived polysaccharide network and the mammalian glycocalyx.

7.3 MATERIALS & METHODS

7.3.1 *3D SRS Microscope System with Active Humidity Control*

The laser system used for this work is based on a Yb:KGW solid-state oscillator that operates at 41 MHz repetition rate at 8 W average output power and 450 fs pulse duration [36, 57], as depicted in Fig. 7.1. Both, pump and STOKES beams are derived from this oscillator, which intrinsically ensures temporal synchronization.

A part of the oscillator directly serves as the STOKES beam at a fixed wavelength of 1041 nm. Spectral filtering with an etalon tailors its bandwidth to 10 cm^{-1}, which results in a pulse duration of $\sim$ 1 ps.
In order to obtain a tunable pump beam, and therefore, access to different RAMAN bands, a fiber-feedback optical parametric oscillator (FFOPO) is employed. Its signal channel (1350 – 1900 nm) is post-amplified by an optical parametric amplifier (OPA). Details on this laser system can be found in [107]. Subsequent second-harmonic generation (SHG) employing a 10-mm long periodically poled lithium niobate (MgO:PPLN) crystal provides the RAMAN pump beam with a wavelength between 760 and 803 nm. This corresponds to a pump-STOKES detuning range of 2850 – 3550 cm^{-1}.

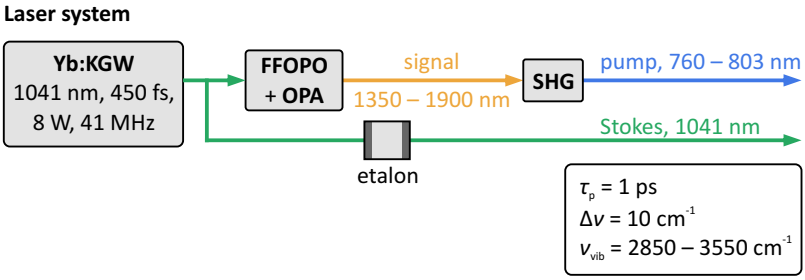

FIGURE 7.1. **Laser system.** An Yb:KGW oscillator pumps a fiber-feedback optical parametric oscillator (FFOPO). Its signal channel (1350 – 1900 nm) is amplified by an optical parametric amplifier (OPA). Subsequent second-harmonic generation (SHG) provides the tunable RAMAN pump beam, i.e., 760 – 803 nm. At the same time, the SHG process is used to control the pulse duration via spectral filtering. A part of the oscillator directly serves as the STOKES beam at 1041 nm after spectral filtering using an etalon. Both, pump and STOKES exhibit a pulse duration of $\sim$ 1 ps, and thus, 10 cm^{-1} bandwidth. The tuning range allows to access RAMAN bands between 2850 and 3550 cm^{-1}.

The SRS interaction manifests as an energy transfer from the pump to the STOKES beam, and thus, as an intensity change thereof. Hence, the SRS signal is intrinsically

imprinted on the input wavelength channels, and thus, cannot be retrieved by spectral separation as it is possible with, e.g., CARS. Furthermore, the relative intensity change is typically within a range of $10^{-7} - 10^{-5}$. In order to measure these small intensity changes, lock-in amplification is employed. This requires intensity modulation of one of the beams, where the respective other beam is detected. In this system the stimulated RAMAN gain (SRG) of the STOKES beam is detected, as depicted in Fig. 7.2. Intensity modulation of the pump is realized using an acousto-optical modulator (AOM), which operates at 200 kHz modulation frequency. At this frequency the relative intensity noise of the laser system approaches the electronic shot noise limit, and hence, provides the maximum possible signal-to-noise ratio.

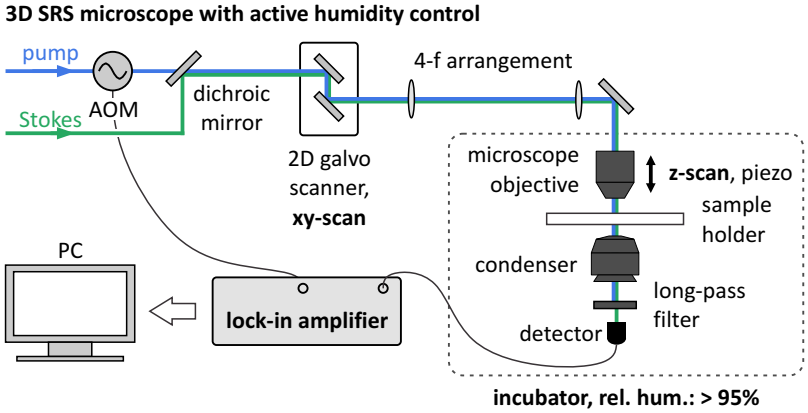

FIGURE 7.2. **3D microscope system.** The setup operates in stimulated RAMAN gain (SRG) configuration. Therefore, an acousto-optical modulator (AOM) modulates the pump beam at 200 kHz, whereas the STOKES beam is being detected using a single-channel photodiode and a lock-in amplifier. A 2D galvo mirror system allows to scan the sample in lateral direction. Thereby, a 4-f arrangement translates the lateral beam displacement into an angular displacement at the entrance pupil of the microscope objective. Scanning along the beam axis is realized using a closed-loop piezo actuator at the microscope objective mount. The pump beam is spectrally separated from the STOKES beam in front of the detector. The entire microscope is enclosed into an incubator, such that the relative humidity can be kept at high levels in order to prevent sample dehydration, and therefore, shrinkage.

Lateral scanning is enabled by a pair of galvanometric mirrors. Here, a 4f-arrangement translates the lateral beam displacement into an angular displacement at the entrance pupil of the microscope objective. Axial scanning is realized using a piezoelectric actuator (120 µm travel range), which translates the microscope objective along the

beam axis.

The microscope objective (Nikon S Plan Fluor ELWD 60×, NA = 0.7) features a high working distance of 1.8 − 2.6 mm and is used in air as immersion medium. An oil-immersion condenser with a working distance of 1.6 mm (Nikon C-AA Achromat/Aplanat Condenser, NA = 1.4) is used to collect as much of the transmitted laser light as possible. Since the resulting image quality is solely determined by the microscope objective, the condenser is used in air as immersion medium.

Biological systems typically require specific ambient conditions in order to maintain steady state and prevent the sample from degradation, which especially becomes important during long measurements. In this case, the ambient relative humidity is the critical system parameter, which has to be controlled. Therefore, the entire microscope unit is enclosed in an incubator. A self-designed humidity control system allows to keep the ambient atmosphere at high relative humidity levels close to 100%.

7.3.2 *Lateral and Axial Resolution*

Ultimately, the resulting spatial resolution is determined by the volume pixel (voxel) size, where the laser intensities are high enough to drive the SRS interaction. Clearly, this is dictated by the mode matching of pump and STOKES, and the diffraction limit, i.e., the numerical aperture (NA) of the microscope objective and laser wavelength. In order to obtain a quantitative figure of merit for the spatial resolution, the nonlinear point spread function (PSF) is measured in lateral as well as in axial direction. Especially the axial resolution is of interest as the transition zone of pectin placed on top of serosal tissue was analyzed.

First, the geometric properties of the pump and STOKES modes in the focal region of the SRS microscope are determined. Therefore, the *knife-edge* method is employed, where a blade is moved transversally across the beam profile, as illustrated in Fig. 7.3(a). In this case, rather than moving the blade, the beam is scanned across the blade employing the galvanometric scanner system, see Fig. 7.2. This enables extremely fast and automated knife-edge scans. As the angular displacement of the galvanometric mirrors is small, geometric distortions are negligible.

As described in Section 2.6.4, for a GAUSSIAN mode the transmitted intensity follows an *error-function* profile, which is evident from Fig. 7.3(b). The relative z-position between the focal spot and the blade can be varied using the piezo device, which is

also used for 3D SRS scans. From this z-dependent knife-edge scan, the waist along the beam axis can be determined, see Fig. 7.3(c).

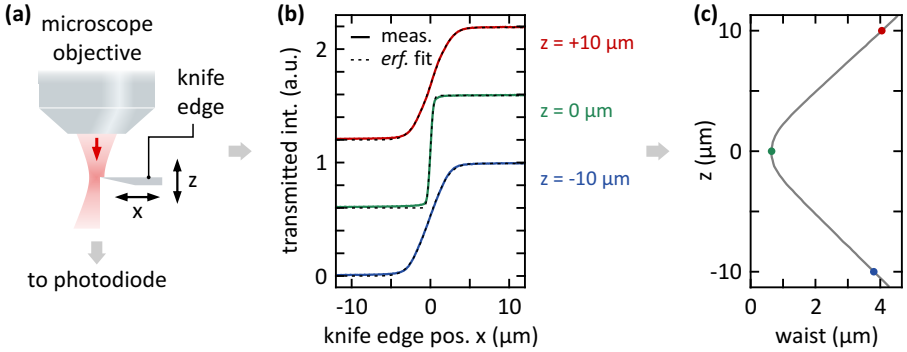

FIGURE 7.3. **Beam waist measurement in the SRS microscope. (a)** The knife-edge method is employed to determine the beam waist at different positions along the beam axis. A photo detector is used to measure the transmitted intensity. **(b)** Exemplary knife-edge scans at different z-positions. Excellent agreement between the measurement and the *erf*-fit for a GAUSSIAN mode. **(c)** At each z-position the beam waist is extracted from the fitted model, which yields the beam waist along the beam axis. Colored dots: corresponding scans in **(b)**.

Fig. 7.4(a) depicts the measured beam waists of pump and STOKES along the optical axis, which clearly demonstrates mode matching in the focal spot. From the extracted focal beam waists

$$\begin{aligned} w_{0,\text{pump}} &= 575\,\text{nm} \\ w_{0,\text{Stokes}} &= 650\,\text{nm}, \end{aligned} \tag{7.1}$$

as given in Fig. 7.4(b), the effective numerical aperture (NA) values are calculated according to Eq. 2.69 in Section 2.6.4. As expected for mode matching, the shorter pump wavelength (here: 784 nm) requires a lower NA, i.e., a smaller beam diameter at the entrance pupil of the microscope objective, than the STOKES beam with a longer wavelength (1041 nm). The effective NA values

$$\begin{aligned} \text{NA}_{\text{pump}} &= 0.40 \\ \text{NA}_{\text{Stokes}} &= 0.45 \end{aligned} \tag{7.2}$$

are smaller than the nominal numerical aperture of the microscope objective (NA = 0.7), as the beam diameter in front of the microscope objective is restricted by other components. An optimized optical design of the SRS microscope would enable even higher effective NA values.

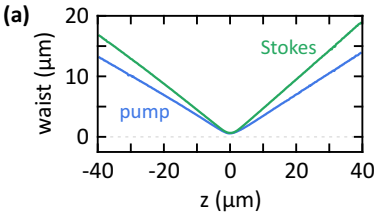

(b)

λ	784 nm	1041 nm
w_0	575 nm	650 nm
NA	0.40	0.45

FIGURE 7.4. **Beam waists pump and Stokes. (a)** Knife edge scans. The slight asymmetry of the curves is caused by piezo creeping (open-loop operation) in positive z-direction. **(b)** Extracted beam waists w_0 at the focal position and the corresponding NA values. Similar beam waists ensure sufficient mode overlap for an optimized SRS interaction.

In the following, the automated knife-edge scan capability is used to determine the temporal positioning stability of the piezo actuator, and thus, of the focal spot. Especially for time consuming 3D SRS scans, stable and reproducible focus positioning is essential. Fig. 7.5(a) depicts the effect of piezo creeping, which is the inherent relaxation of piezoelectric materials upon a changing externally applied voltage. This effect takes place on the order of minutes. Closed-loop operation compensates for these positioning drifts, as apparent from Fig. 7.5(b).

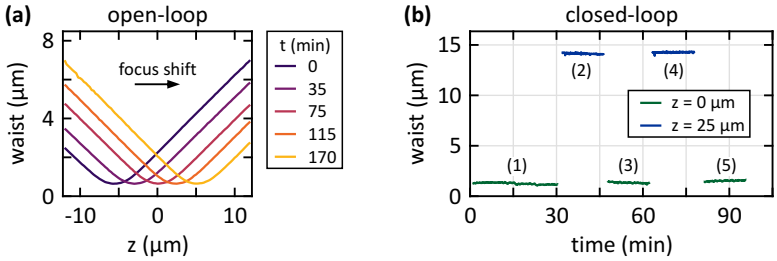

FIGURE 7.5. **Focus positioning stability.** The STOKES beam waist is tracked over time, in order to evaluate the positioning stability of the laser focus. **(a)** In open-loop operation, piezo creeping is not compensated, which leads to a focus shift along the beam axis. **(b)** Closed-loop piezo operation ensures positioning stability of the focal spot. The beam waist is reproducibly stable over time at two different z-positions.

In the next step, the nonlinear PSF is determined. Therefore, a sample of polystyrene (PS) beads with a known diameter of 500 nm in aqueous solution is used to measure the lateral PSF, see Fig. 7.6(a). A lateral scan at the RAMAN resonance of PS (3066 cm^{-1}) is depicted in Fig. 7.6(b). Fig. 7.6(c) depicts SRG signal cross-sections taken along the x-direction, as indicated by the dashed lines. From this, the full-width at half-maximum (FWHM) is extracted, where the reference signal level is set to zero rather than the

background noise level. This results in a conservative value for the width of the lateral PSF of 900 nm and ensures unambiguous separation of spatial features.

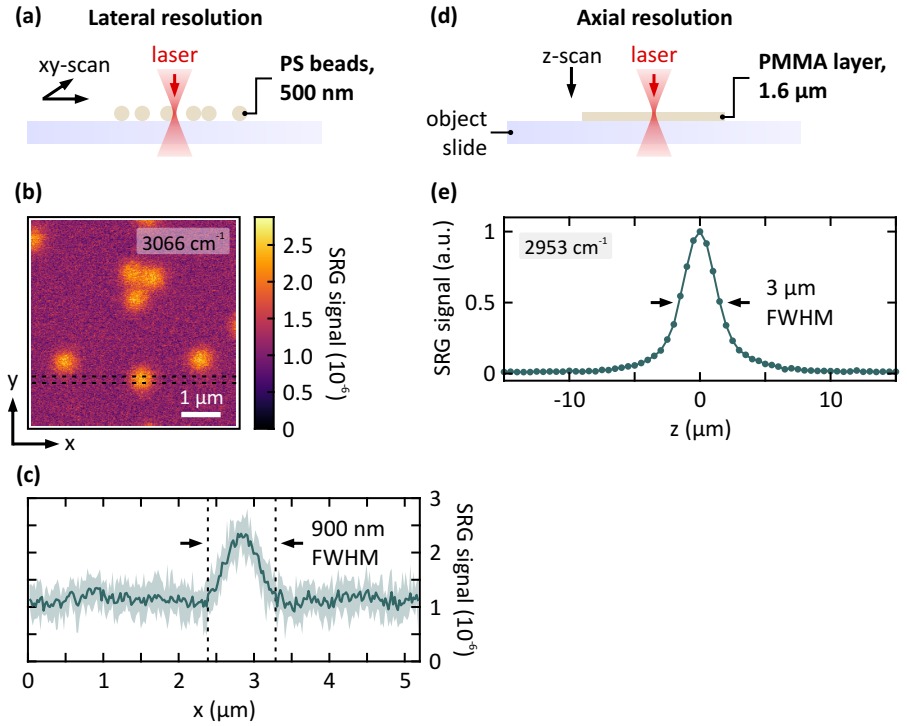

FIGURE 7.6. **Spatial resolution – 3D SRS microscope.** Characterization of the nonlinear point spread function of the SRS microscope in both, lateral and axial, directions. **(a)** 500-nm polystyrene (PS) beads are imaged in order to determine the lateral resolution. **(b)** SRS scan at 3066 cm^{-1} with 250 × 250 pixels resolution and 3 ms pixel integration time. **(c)** Signal cross-sections are extracted from **(b)** as indicated by the dashed lines. Minimum and maximum values are plotted in light green, the average is given by the solid green line. This yields a full-width at half maximum (FWHM) of 900 nm. **(d)** A 1.6 µm thick spin-coated PMMA film is scanned along the beam axis. **(e)** Resulting SRG signal at the PMMA resonance at 2953 cm^{-1}, which yields a FWHM of 3 µm in axial direction.

The axial resolution is characterized using a spin-coated PMMA film with a thickness of 1.6 µm and by measuring the SRG signal along the beam axis as depicted in Fig. 7.6(d). The FWHM value amounts to 3 µm. Hence, the axial resolution is sufficient

to resolve the interlink range between pectin and tissue, which is expected to be on the order of $10 - 20\,\mu m$.

7.3.3 *Sample Characterization*

In order to investigate the interaction of pectin with mammalian serosal tissue, a sample of porcine intestinal serosa is covered with a patch of pre-hydrated pectin, as

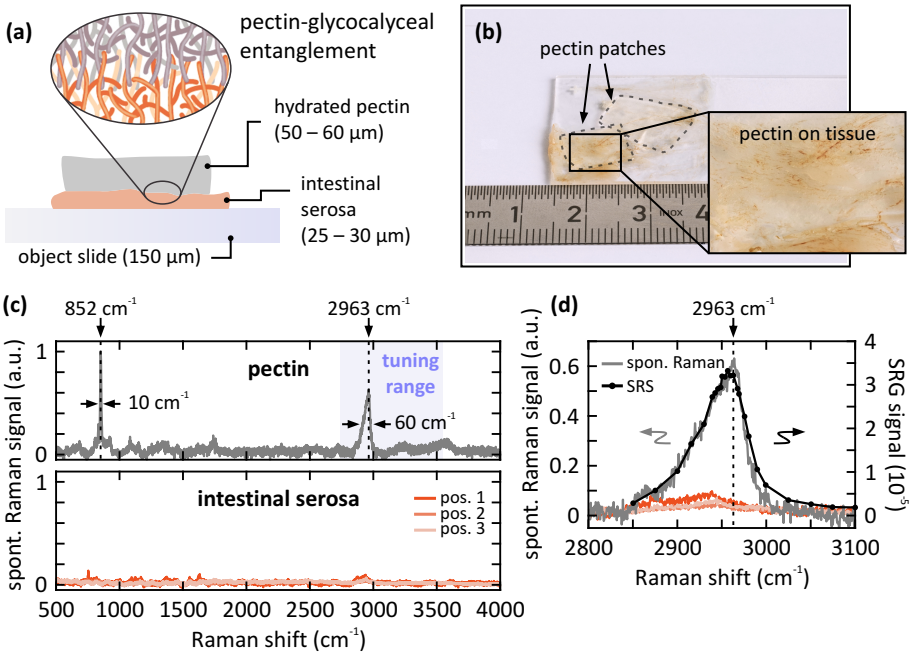

FIGURE 7.7. **Pectin sample. (a)** Schematic side view of the sample. Porcine intestinal serosa is covered with a hydrated pectin patch. Inset: schematic of the entanglement between pectin and the glycocalyceal surface of the intestinal serosa. **(b)** Close-up photograph of the sample, top view. Two pectin patches (dashed lines) are applied to the tissue. **(c)** Spontaneous RAMAN spectra of hydrated pectin (upper panel) and intestinal serosa at three different positions (lower panel). Pectin exhibits two prominent peaks at $852\,cm^{-1}$ and $2963\,cm^{-1}$, where the latter is accessible by the laser system (corresponding pump wavelength: 795.6 nm). In contrast, the intestine tissue shows a broad RAMAN response without any prominent feature. Thus, the peak at $2963\,cm^{-1}$ is ideal to distinguish pectin from the tissue. **(d)** Zoom-in of the RAMAN peak of hydrated pectin at $2963\,cm^{-1}$ and the corresponding SRS spectrum.

indicated by the dashed lines in Fig. 7.7(b).

Hydrated pectin is much more transparent for pump and STOKES wavelengths than the intestinal tissue. This, in combination with its structural homogeneity, minimizes laser wavefront distortions during propagation. Since SRS is a phase-sensitive process, these wavefront distortions deteriorate the signal level. Therefore, the pectin polymer was placed on top of the tissue, as depicted in Fig. 7.7(a), in order to maintain high imaging quality in deeper sections of the sample.

First, the RAMAN responses of pectin as well as of the intestinal tissue were characterized. Therefore, broadband spontaneous RAMAN spectra are acquired, as depicted in Fig. 7.7(c). Pectin exhibits two prominent RAMAN resonances, located at 852 cm^{-1} in the fingerprint spectral region, and at 2963 cm^{-1} in the C–H stretch region (upper panel). The shaded area indicates the accessible spectral range of the laser system. The intestinal serosa, on the other hand, does not exhibit any prominent specific spectral features (lower panel). Thus, the RAMAN peak at 2963 cm^{-1} is being used to track the pectin concentration. As a cross-check, a stimulated RAMAN spectrum of the pectin resonance is additionally acquired, as depicted in Fig. 7.7(d). Both, the resonance position as well as the spectral shape agree well. Note, that the pectin resonance partially overlaps with the protein signal, which is located around 2950 cm^{-1}.

7.4 RESULTS AND DISCUSSION

7.4.1 *Hydrophilicity of the Hydrogel Network*

Hydrating the dry pectin prior to applying it onto pleural tissue is required to initiate pectin-glycocalyceal entanglement in vitro. In situ, the secretory lubricating properties of mesothelial cells facilitate the initial hydration process and microstructural entanglement. This hydration process and interrelated water transport dynamics within the pectin polymer are not yet well understood. Here, we use SRS to determine the hydrophilicity by quantitatively monitoring the spatial water content over time within the pectin hydrogel network.

In this context, two mechanisms are investigated, namely, the water absorption from a humid ambient atmosphere, and the water transport within the pectin polymer by direct contact with the liquid water. Both mechanisms are involved in the hydration process of the pectin polymer in biomedical use, and hence, it is important to determine their respective time scales.

For practical reasons the water absorption from ambient atmosphere is measured in vertical geometry, whereas the water transport from direct contact is measured in horizontal geometry, as depicted in Fig. 7.8(a) and (c). Since the hydration takes place directionally, e.g., from the top as shown in Fig. 7.8(a), the pectin polymer bends due to the expanding hydrogel network. In order to avoid motion artifacts by pectin bending during the measurement, the pectin patch was fixed to the object slide by double-sided tape with an aperture for the laser to be transmitted, see the schematics in Fig. 7.8.

The SRS signal scales linearly with the oscillator concentration, i.e., the water concentration in this case. However, it is necessary to also track the pectin signal channel simultaneously as the pectin polymer expands during hydration, and therefore, the overall oscillator concentration changes. Therefore, the relative signal level between water and pectin is the significant measure, as shown in the lower panel of Fig. 7.8(b). The laser focus is positioned at a constant z-position beneath the interface between pectin and the air. Notably, the focal position relative to the interface changes over time due to the volume expansion of the pectin polymer.

The relative SRS signal follows the ambient relative humidity (black line) with a delay, which is caused by the slow water absorption. The overall absorption dynamics

spans across $\sim 5\,\mathrm{h}$. Here, a relative mass change of 24% is measured between $t = 0$ and the steady state at $t = 335\,\mathrm{min}$.

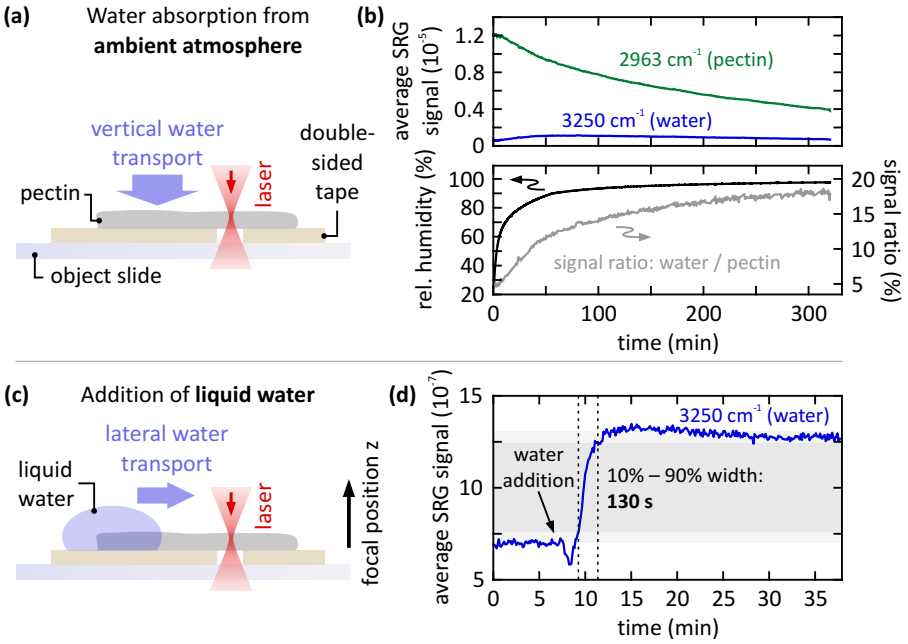

FIGURE 7.8. **Water transport dynamics.** Water absorption and transport dynamics in pectin are measured by tracking the SRS signal levels at the water and pectin resonance. For this, the pump-STOKES detuning is automatically switched between $2963\,\mathrm{cm}^{-1}$ and $3250\,\mathrm{cm}^{-1}$. Pump power: 5 mW, STOKES power: 4.5 mW. The temperature is constant at 24 °C. **(a)** Water absorption from the ambient atmosphere at high relative humidity. **(b)** Upper panel: individual signal traces for pectin and water. Lower panel: signal ratio between water and pectin, as well as the ambient relative humidity in the microscope incubator. In this case, hydration takes place on the time scale of $\sim 5\,\mathrm{h}$. Each data point corresponds to the average signal obtained from a $50 \times 50\,\mu\mathrm{m}^2$ FOV with $20 \times 20\,\mathrm{px}^2$. 8 s acquisition time per data point, 4 s effective integration time. **(c)** Liquid water is applied to the pectin patch and the water transport is tracked in lateral geometry. **(d)** For lateral water transport, the hydration process takes place on the time scale of $\sim 2\,\mathrm{min}$ (10% – 90% width, indicated by dashed lines and grey shaded area). Each data point corresponds to the average signal obtained from a $50 \times 5\,\mu\mathrm{m}^2$ FOV with $50 \times 5\,\mathrm{px}^2$, where the water transport is directed along the short edge of the FOV. Hence, the corresponding diffusion coefficient amounts to $D = \langle x^2 \rangle / 2t \sim 10^{-13}\,\mathrm{m}^2/\mathrm{s}$. 5 s acquisition time per data point, 2.5 s effective integration time.

The water transport dynamics is measured by applying a liquid drop of water to a dry patch of pectin polymer, which immediately starts to absorb the liquid water (real-time video footage of this process can be found in the supplementary material of [108]). A well-defined waterfront passes through the field of view ($50 \times 5\,\mu m$, details can be found in Fig. A.1(b) in appendix A) along its short edge, i.e., across a distance of $5\,\mu m$. The SRS signal is recorded at the water resonance at a constant z-position within the pectin. In this measurement, only the water signal is monitored, since only the relative change of the local water content is of interest. As determined from the $10\% - 90\%$ width, the waterfront traverses the field of view within 130 s. Assuming simple diffusion, the corresponding diffusion coefficient amounts to

$$D = \langle x^2 \rangle / 2t \sim 10^{-13}\,m^2/s \tag{7.3}$$

at 24 °C, where $\langle x^2 \rangle$ denotes the average square of the traversed distance within the time t [109]. Thus, the water transport dynamics within the pectin is $\sim$ 2 orders of magnitude faster than the water absorption from the ambient atmosphere. This large difference between these two time scales also manifests in the signal ratio being independent of the z-position within the pectin, as depicted in Fig. 7.9.

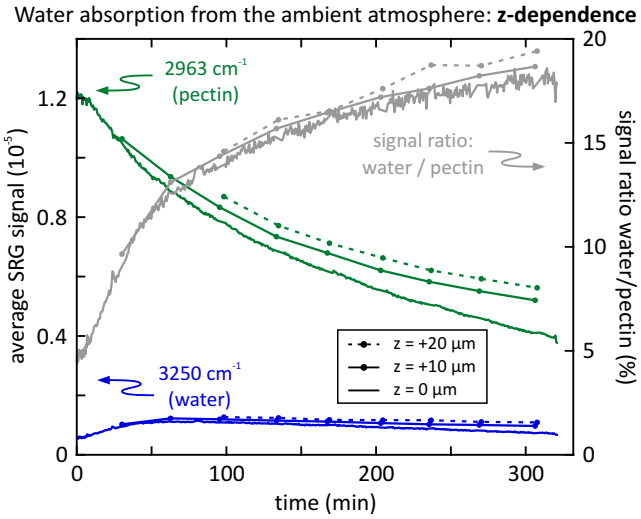

FIGURE 7.9. **Water absorption – z-dependence.** Additional z-dependence of the water content within the pectin polymer. Solid line: data shown Fig. 7.8, measured at a constant z-position, which is used as the reference position. Additionally, the signal levels are measured 10 µm and 20 µm above the reference level.

Both individual signal levels, water and pectin, decrease for lower z-positions, whereas their signal ratio does not change. Hence, this signal decrease does not originate from a z-dependent water content within the pectin polymer. Rather, it is caused by a laser power drop due to the absorption and/or scattering and by wavefront distortions arising from inhomogeneities in the pectin bulk material. The latter deteriorates the phase-sensitive SRS signal level.

Since the water transport dynamics within the pectin are much faster than the absorption from the ambient atmosphere (Fig. 7.8), no temporal delay between the signal ratio curves at different z-positions is observed. Furthermore, no structured water channels in the pectin hydrogel are visible, as depicted in Fig. A.1 in the appendix A. Hence, the water transport takes place homogeneously on a molecular scale or, on the other hand, potential water channels are well below the diffraction limit.

7.4.2 *Pectin-glycocalyceal Transition Zone*

In the following, the structural transition and the interlink length between the pectin hydrogel and intestinal serosa tissue is measured using 3D SRS imaging. Therefore, the sample is prepared as shown in Fig. 7.7 and placed in the incubator $\sim 1.5\,\mathrm{h}$ before the SRS scan is started. This ensures that the water uptake from the ambient atmosphere is equilibrated, and thus, the sample is in a steady state. A range of $\sim 100\,\mu\mathrm{m}$ in z-direction is scanned, where the zero position is set to be within the object slide directly beneath its interface to the intestinal tissue. Since hydrated pectin is highly transparent for the employed wavelengths, and the intestinal serosa tissue is only $\sim 25\,\mu\mathrm{m}$ in thickness, no corrections for depth-dependent signal attenuation are necessary. Fig. 7.10 depicts a part of the hyperspectral data set. In particular, 2D cross-sections at $z = 14$, 18, 57, and $100\,\mu\mathrm{m}$ for three RAMAN resonances are shown, each image covers a field of view of $50 \times 50\,\mu\mathrm{m}^2$. For each z-position, the three spectral channels (unsaturated lipids at $2850\,\mathrm{cm}^{-1}$, pectin at $2963\,\mathrm{cm}^{-1}$, and water at $3250\,\mathrm{cm}^{-1}$) are combined into an RGB overlay, where each spectral position corresponds to one color channel.

With the pectin placed on top of the tissue, in order to evaluate the signal transitions and the interface, the average SRS signals are plotted against their respective z-position, see Fig. 7.11. In particular, each 2D scan is averaged across the entire field of view (right panel). Locally resolved averaging is done according to regions (i)–(iii) as indicated in the RGB overlay at $z = 18\,\mu\mathrm{m}$ in Fig. 7.10. The center area of the field of view at $z = 14\,\mu\mathrm{m}$ exhibits a strong signal, which is independent of the spectral position. This

spectrally independent signal is usually caused by parasitic cross-phase modulation (XPM) between pump and STOKES, which enters the same detection channel as signals, that arise from SRS interaction. Therefore, XPM intrinsically cannot be rejected by the detection unit.

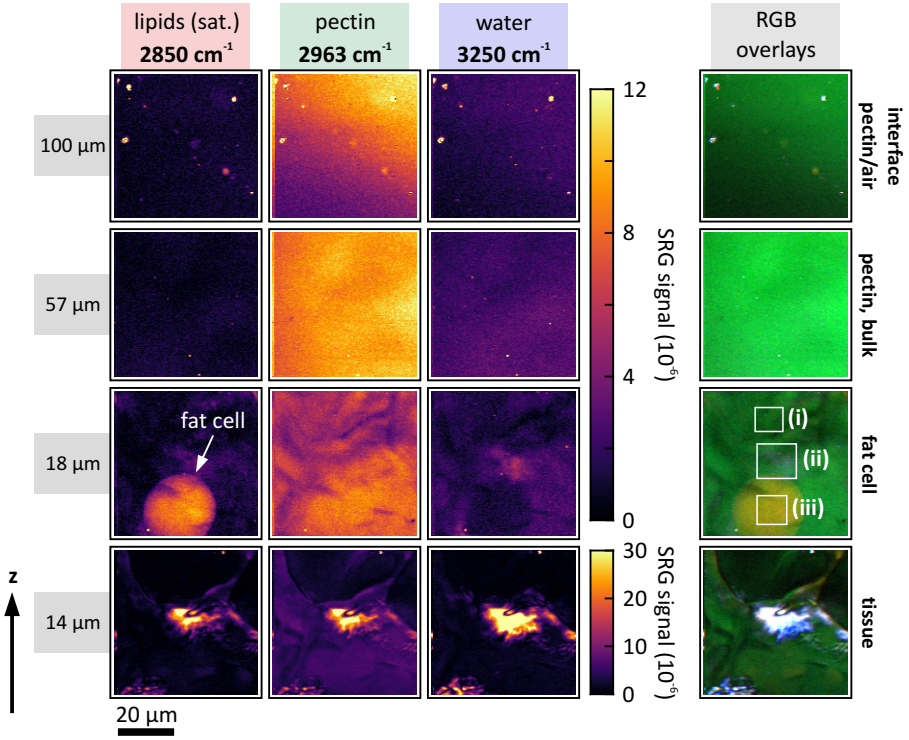

FIGURE 7.10. **3D SRS scan – pectin-pleura interface.** Composition of the pectin mesothelial interface. Hyperspectral 3D SRS scan through the sample, measured at three RAMAN bands: 2850 cm^{-1} (saturated lipids), 2963 cm^{-1} (pectin), and 3250 cm^{-1} (water). 2D scans at $z = 14$, 18, 57, and 100 µm are depicted as well as RGB overlays thereof, where each of the three resonance positions is encoded as one color channel. The pleural tissue ($z = 14$ µm) exhibits structures in the pectin channel, which mainly originates from the close-by protein band at 2950 cm^{-1}. At $z = 18$ µm a mesenteric fat cell with a diameter of 25 µm is revealed at the resonance of saturated lipids. The pectin bulk material at $z = 57$ µm causes a homogeneous signal distribution, which extends up to the pectin-to-air interface at $z = 100$ µm.

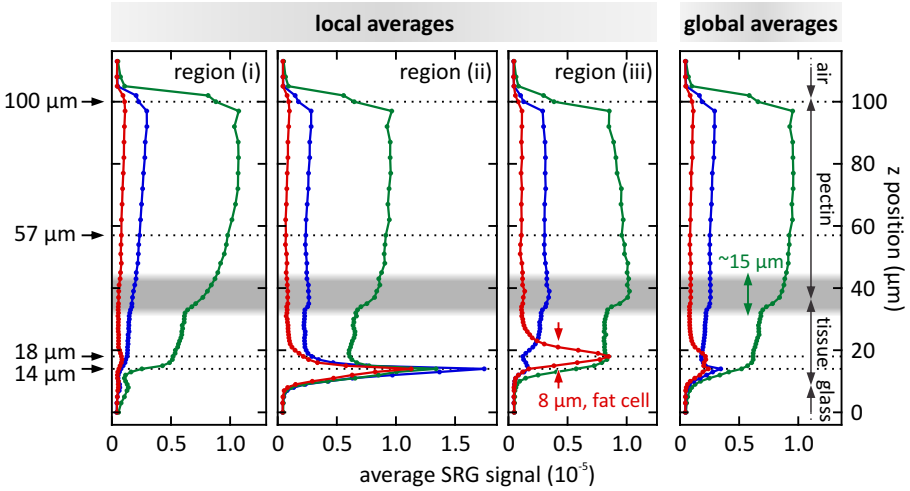

FIGURE 7.11. **3D SRS scan – signal cross-sections.** Signal cross-sections along the z-axis for each of the three RAMAN bands. Local averages are calculated for the rectangular regions (i)–(iii) as indicated in Fig. 7.10, global averages take into account one entire image for each data point. As shown by the green curves, the pectin layer exhibits a thickness of $\sim$ 65 µm, which extends from $z = 35 - 100$ µm. Region (iii) shows the axial dimension of the mesenteric fat cell, i.e. 8 µm. On average, the interlink length (gray shaded area) between tissue and pectin amounts to $\sim$ 15 µm. Imaging parameters: 12 mW pump power, 4.5 mW STOKES power, $50 \times 50\,\mu m^2$, $150 \times 150\,px^2$, 2.5 ms pixel dwell time, 1 ms integration time per pixel, $\sim$ 1 min acquisition time per image. Ambient conditions: 25 °C, 96% relative humidity.

At $z = 18$ µm, a fat cell with a diameter of $\sim$ 25 µm is revealed at the resonance of saturated lipids (2850 cm^{-1}). Its thickness amounts to 8 µm as extracted from the axial signal trace for region (iii), see the red curve in Fig. 7.11. These dimensions match the typical size of fat cells. In contrast, the fat cell does not exhibit any substantial signal at the water resonance (3250 cm^{-1}). Hence, this demonstrates an off-resonant case for the RAMAN transitions in saturated lipids. Furthermore, the pectin channel at $z = 18$ µm exhibits a strong signal, which can be traced back to the overlapping protein resonance at 2950 cm^{-1}, see Fig. A.2 (appendix A). In the pectin bulk material, the SRS signal level is clearly dominated by the resonance at 2963 cm^{-1}. Here, the signal is homogeneously distributed across the field of view, as evident at $z = 57$ µm. As expected, the water channel also exhibits a homogeneous signal distribution, caused by water molecules being incorporated within the pectin polymer. At $z = 100$ µm the pectin polymer interfaces the air. Apparently, the pectin surface is slightly tilted with

respect to the object slide, which causes the signal gradient in the image.

From the axial signal traces in Fig. 7.11, the interface between pectin and the glycocalyx as well as the pectin-glycocalyceal entanglement length can be extracted. Between $z = 35$ and 97 µm all signal channels, including protein and unsaturated lipids (see Fig. A.2 in the appendix A), exhibit constant signal levels. Hence, this range contains the structurally homogeneous pectin layer. In contrast, within the intestinal tissue the signal levels vary more strongly due the more inhomogeneous distribution of the chemical constituents.

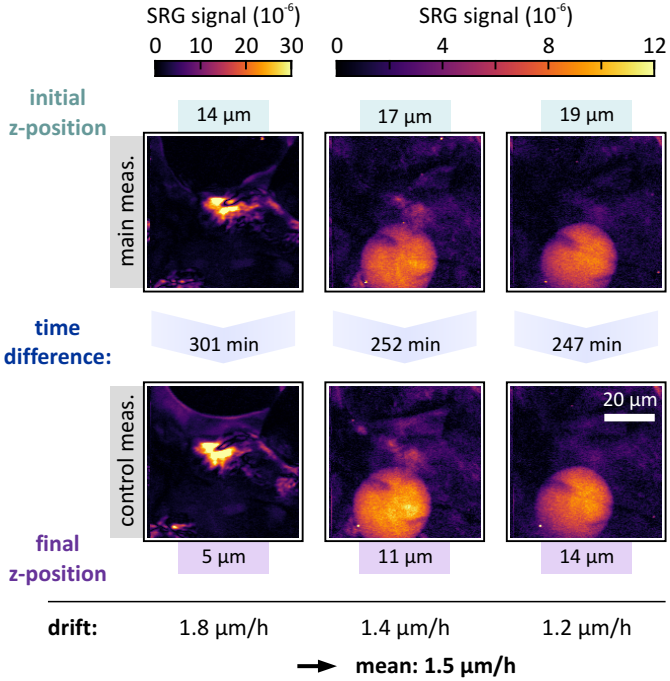

FIGURE 7.12. **Positioning reproducibility.** Quantitative analysis of the vertical positioning drift due to sample dehydration. After the main measurement run, three structures within the tissue are located again in order to quantify vertical sample shrinkage. The mean drift amounts to $\sim 1.5\,\mu m/h$. All images are acquired at $2850\,cm^{-1}$ (saturated lipids).

The zone of pectin-glycocalyceal entanglement can be extracted from the width of the signal transition from the tissue to the pectin hydrogel, as indicated by the gray shaded area. In particular, the interlink length amounts to $\sim 15\,\mu m$ on average, which

is well in line with recent data we derived from high pressure freezing transmission electron microscopy, which estimates the thickness of the mammalian visceral glycocalyx to a thickness of $\sim 13\,\mu m$ [93]. Clearly, this value varies locally as evident from the first three plots in Fig. 7.11.

Additionally to unsaturated lipids, pectin, and water, the signal is also acquired for proteins at $2950\,cm^{-1}$ as well as for unsaturated lipids at $3015\,cm^{-1}$. Both resonances are included in Fig. A.2 in the appendix A. In particular, the protein resonance is located close to the pectin resonance.

The total acquisition time for the entire data set amounts to 5 h 45 min. Hence, the incubation unit of the SRS system is crucial to ensure sample stability over this period of time. The absolute positioning drift of the sample due to dehydration across the measurement time is determined to a very low value of $1.5\,\mu m/h$ on average, as can be seen in Fig. 7.12. This low drift also suggests that the incident laser does not have any substantial impact on the water content.

7.4.3 *Limitations of this Study*

Technical restrictions impose limitations on this study, which are discussed here. For instance, the signal-to-noise ratio (SNR) ultimately determines the acquisition time. The SNR scales linearly with the laser power in each of the two wavelength channels. However, the laser power is limited to several milliwatts, otherwise photo damage as well as dehydration due to local heating occur in the sample. The impact of the incident laser on the water content could be quantified using hydrated pectin in a steady state, i.e., all processes associated with material-specific water transport dynamics are equilibrated. A power-dependent measurement of the signal ratio between water and pectin would provide a figure of merit for laser power-dependent effects on the water content. Regions closer to the surface are expected to be more susceptible to dehydration than the bulk material. Due to the restricted laser power level, very fast sample dynamics, such as early aspects of the pectin-glycocalyceal entanglement process itself may not be resolved temporally, or only with limited spatial resolution and/or with a limited number of spectral positions. Resolving the entanglement process is particularly challenging, as it additionally involves a volume change, and therefore, a non-steady z-position. For a further in-depth understanding of these specific aspects of the process, we plan to correlate the SRS-derived data to non-time resolved, but very spatially resolved electron microscopy in the future.

As SRS is phase-sensitive, the sample thickness is limited by its scattering properties. Especially inhomogeneous biological samples tend to deteriorate the wavefronts, such that the sample thickness is limited to a few tens of microns. This was sufficient for our study, because our focus was on the superficial surface layer of the organ, but may limit wider applications in other studies that involve thick tissues.

7.5 CONCLUSIONS & OUTLOOK

In this work, we investigated the hydrophilicity of a plant-derived pectin hydrogel using 3D stimulated RAMAN scattering (SRS) microscopy. The two hydration mechanisms, water absorption from ambient atmosphere and hydration by direct contact with the liquid water, exhibit largely different time scales, separated by nearly two orders of magnitude. These findings are of importance especially for wound healing, since the structural and physical properties of this hydrogel network are strongly dependent on its water content. In particular, optimal adhesive properties of pectin on organ surfaces require a correct hydration level. Furthermore, we used 3D SRS imaging in order to quantify the interlink length of hydrated pectin and mammalian glycocalyx. In the future, we plan to measure the volume expansion of the pectin hydrogel associated with hydration. Thereby, the position of the interface between pectin and the air can be tracked with high precision using the z-scan capability of our SRS microscope. Our study will provide new quantitative insights into the structural transition zone between pectin and the serosal tissue, as well as the water-dependent entangling phenomenon between pectin and the mammalian glycocalyx, which can further enable medical applications such as serosal wound healing and visceral tissue repair.

8

LIMITS OF DETECTION OF MICROPLASTICS IN FISH TISSUE USING SRS MICROSCOPY

This chapter is based on the following published work:

> **M. Floess**, M. Fagotto-Kaufmann, A. Gall, T. Steinle, I. Ehrlich, and H. Giessen
> *Limits of detection of microplastics in fish tissue using stimulated Raman scattering microscopy*
> Biomed. Opt. Express **15**, 1528–1539 (2024).

8.1 ABSTRACT

We demonstrate the detection sensitivity of microplastic beads within fish tissue using stimulated Raman scattering (SRS) microscopy. The intrinsically provided chemical contrast distinguishes different types of plastic compounds within fish tissue. We study the size-dependent signal-to-noise ratio of the microplastic beads and determine a lower boundary for the detectable size. Our findings demonstrate how SRS microscopy can serve as a complementary modality to conventional Raman scattering imaging in order to detect and identify microplastic particles in fish tissue.

8.2 INTRODUCTION

In recent years, the contamination of drinking water supplies and the food chain with micro- and nanoplastics has become an increasingly recognized problem. Enormous amounts of plastic waste worldwide find their way into the environment and ecosystems. Waste dumping into rivers constitutes the largest source of plastic waste in the oceans [110, 111]. Over time, environmental weathering causes plastic parts to continuously fragment into smaller debris, so-called secondary microplastics, which can reach the micrometer or even the nanometer scale [112, 113]. In addition, microplastic additives in cosmetic products, i.e., primary microplastics, find their way directly into local water supply systems [114–116]. Through uptake by, e.g., seashells or fish, these micro- and nanoplastic particles enter the food chain and may end up in our food,

and finally, in our digestive system [117, 118].

The exact physiological consequences of micro- and nanoplastics in the human body are still not clear and are currently under extensive investigation [119, 120]. However, it is assumed that the potential health risks increase as the particle size decreases [121]. Below certain dimensions, nanoplastics may be able to traverse the intestinal barrier and enter the bloodstream [122]. In order to assess these potential health risks, in a first step, the detection and characterization of micro- and nanoplastics is necessary. Therefore, suitable detection and imaging methods to monitor the abundance of micro- and nanoplastics in the food chain are of high demand. Combined systems of dark-field imaging and spontaneous RAMAN spectroscopy, which are commercially available, are employed to screen drinking water supplies for contamination with microplastics [123, 124].

However, conventional RAMAN micro-spectroscopy suffers from low acquisition speeds, which renders it unfeasible to scan entire samples without first determining the location of the plastic particles using an additional imaging modality, such as dark-field imaging. In order to overcome these speed limitations, stimulated RAMAN scattering (SRS) microscopy can be employed. SRS provides images with intrinsic chemical contrast, i.e., no additional labels are required, at up to video-rate acquisition speeds [105]. SRS micro-spectroscopy has been employed to estimate the relative abundance of synthetic microfibers in environmental samples [125]. Furthermore, SRS has been used to identify and distinguish microfibers of natural and synthetic origin from different geographical areas and environments, including microfibers from deep-sea sediments [126].

In this work, we investigate the detection of microplastics in fish tissue, which may ultimately pave the way to screen for microplastics contamination in fish populations. For this purpose, microplastic beads serve as well-controlled model system for microplastic debris occurring in environmental samples. In particular, we determine the detection limit of polystyrene (PS) and poly(methyl methacrylate) (PMMA) microplastic particles under optimal conditions, i.e., in aqueous solution, using SRS microscopy in the C–H stretch spectral range. We demonstrate that the two different plastic compounds can be distinguished in fish muscle tissue based on their characteristic RAMAN responses. As for other types of tissue, muscle tissue contains the main chemical compounds (proteins, lipids, etc.), and thus, is well-suited to serve as test system to characterize the detection limits of microplastics. Furthermore, we show that microplastics can be detected and localized within bulk tissue employing

the 3D imaging capability of our SRS system. Finally, we determine the limit for unambiguous detection and characterization of microplastic particles in fish tissue for our SRS microscope, which results in 1 μm particle size and a pixel integration time (T_{int}) of 30 μs. Our findings can be extended to other plastic compounds, which occur in environmental samples.

Our SRS approach is intrinsically orders of magnitude faster than RAMAN microspectroscopy, due to the increased interaction cross-section. It is one of the tasks of this work to find out about the signal-to-noise ratio of SRS microscopy of micro- and nanoplastics in-situ in a relevant fish tissue environment.

8.3 MATERIALS & METHODS

8.3.1 *Laser System and SRS Microscope*

Pump and STOKES beams are both provided from the same solid-state laser system, as depicted in Fig. 8.1. An 8-W Yb:KGW oscillator with a pulse repetition rate of 41 MHz serves as front-end and directly provides the STOKES channel at a fixed wavelength of 1041 nm. A part of the oscillator is used to operate an optical parametric oscillator [107] and a subsequent second-harmonic generation stage, which provides the tunable RAMAN pump with a wavelength in the range between 760 and 803 nm.

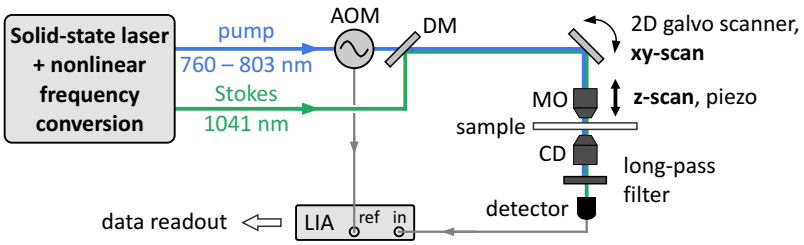

FIGURE 8.1. **SRS microscope.** The pump and STOKES beams are provided by a solid state laser system (Yb:KGW oscillator: 8 W, 450 fs, 41 MHz, and 1041 nm) with subsequent nonlinear frequency conversion. SRG detection of the STOKES is employed, where an acousto-optical modulator (AOM) is used to modulate the pump beam. 3D scanning is realized using a 2D galvo scanner unit in combination with a piezo actuator, which enables z-scan capability. DM: dichroic mirror, MO: microscope objective, CD: condenser.

Thus, the pump-STOKES detuning allows to access RAMAN bands in the range of $2850 - 3550\,\mathrm{cm}^{-1}$. As both channels are provided by the same front-end, their pulse repetition rate is intrinsically synchronized, and therefore, the system is free of relative pump-STOKES timing jitter. The pulse duration of ~ 1 ps corresponds to a spectral bandwidth of $\sim 10\,\mathrm{cm}^{-1}$, which directly translates to the spectral resolution of this system. A modulation frequency of 2.6 MHz is chosen, where the relative intensity noise (RIN) of the laser system enables shot-noise limited detection, see Fig. 8.2, and electronic cross-talk is minimized. A home-built low-noise detector based on a transimpedance amplifier design (Texas Instruments, OPA843) is used for detection [4]. A lock-in amplifier (Zurich Instruments, UHFLI) is employed for signal extraction.

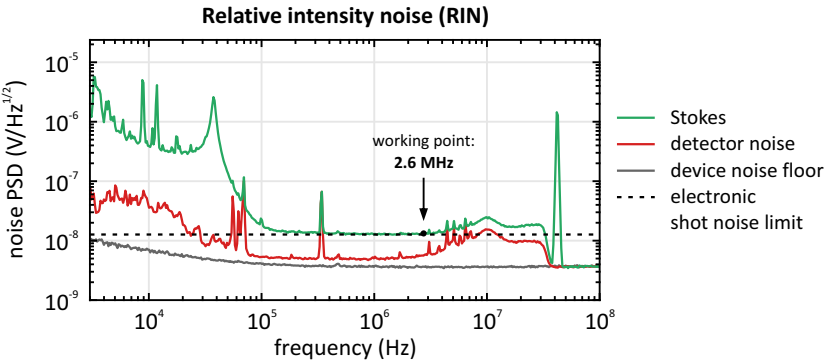

FIGURE 8.2. **Relative intensity noise (RIN) spectra.** The RIN of the STOKES reaches the electronic shot noise limit (dashed line) at 200 kHz. Data acquired using the *Noise Amplitude Sweep* functionality of the Zurich Instruments UHFLI device. DC at the device input channel, external AC coupling using a 2-kHz high-pass filter. In order to preserve dynamic range, an external 25-MHz low-pass filter is employed to suppress the repetition rate peak at 41 MHz of the STOKES laser. Photo current: 2 mA.

3D SRS imaging is realized using a 2-axis galvanometric mirror scanner (Cambridge Technology, 6220HM44B) for lateral scanning and a piezo actuator (Physik Instrumente, P-721-17) for axial scanning, as already introduced in Section 7.3 of Chapter 7. Here, the positive z-direction points upwards, as indicated in Fig. 8.3. This convention is used for all following experiments. A microscope objective (Nikon S Plan Fluor ELWD 60×, NA = 0.7) with a long working distance of 1.8 − 2.6 mm using air as imaging medium is used for laser illumination of the sample. An oil-immersion condenser (Nikon C-AA Achromat/Aplanat Condenser, NA = 1.4) collects as much of the transmitted STOKES light as possible. The condenser is used in air as immersion medium, as the image quality solely depends on the illumination with the microscope objective. The moderate numerical aperture of NA = 0.7 of the microscope objective provides the best compromise between maximum spatial resolution and the ability to image inside of scattering tissue. In fact, high-NA illumination is more susceptible to scattering and wavefront distortions, which eventually reduces the coherence at deeper positions in the tissue, and thus, deteriorates the SRS signal.
The spatial resolution is given by the volume pixel element (voxel), in which the SRS interaction takes place, i.e., the nonlinear 3D point spread function. The lateral resolution is experimentally determined to $w_{\text{voxel}} = 450\,\text{nm}$, as depicted in Fig. 8.4(b). The axial resolution yields $l_{\text{voxel}} = 3\,\mu\text{m}$, as we have reported in [108]. Therefore, particles which fall below the lateral resolution cannot be separated unambiguously from adjacent structures.

Apart from the SRS signal, the detected Stokes beam also carries the linear transmission properties of the sample. In particular, the DC voltage level at the detector is a direct measure thereof and is used to acquire linear transmission images at the Stokes wavelength.

8.3.2 *Sample Preparation*

Our strategy was to apply microplastic beads with defined dimensions onto thin slices of fish tissue, in order to systematically study the detection capabilities and signal-to-noise ratios of our SRS microscope system.

In the first step, fresh mackerel fish muscle tissue was obtained from commercial vendors and transported to the laboratory. In the laboratory, tissue was cut into cubes of $\sim 1\,\mathrm{cm}^3$ and fixed in a fixation buffer containing 4% Paraformaldehyde (Roth, Germany) in phosphate-buffered saline (PBS) of the following composition: 140 mM NaCl, 15 mM phosphate buffer (3 mM NaH_2PO_4, 12 mM Na_2HPO_4) (Roth, Germany) at a pH of 7.4 (pH was adjusted with NaOH or HCl). Initial fixation was carried out at room temperature ($20 - 24\,^\circ\mathrm{C}$) for 1 hour, followed by post-fixation for $\sim$ 16 hours at $4\,^\circ\mathrm{C}$. Afterwards, the tissue was washed three times for 10 min with PBS and stored in PBS supplemented with 0.1% Sodium-Azide (NaN_3, Sigma-Aldrich, Germany) at $4\,^\circ\mathrm{C}$ until further processing.

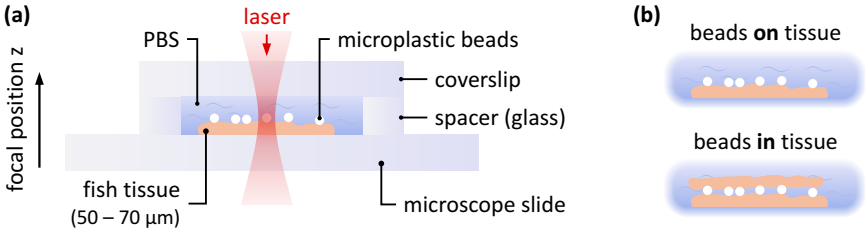

Figure 8.3. **Sample geometry.** **(a)** The fish tissue is kept in physiologically neutral phosphate-buffered saline (PBS). Microplastic beads are placed on top of the fish tissue. The microscope slide, the spacer, as well as the coverslip have a thickness of 170 µm. Laser illumination from the top, detection in transmission. **(b)** Microplastic beads may either be placed on top of one tissue slice, or may be sandwiched between two slices. The muscle structures of the stacked tissue slices are deliberately oriented in different directions.

In the second step, the tissue was sectioned into thin slices using a vibratome (Leica VT1200S, Leica Microsystems, Germany). The blocks of fish tissue were embedded

into 2% agar (Agar-Agar, Roth, Germany) in order to stabilize the tissue during slicing. Tissue slices were cut at a thickness varying between 50 and 70 µm. The slices were collected and stored in PBS at 4 °C.

Fig. 8.3(a) depicts the sample geometry. Glass spacers with a thickness of 170 µm were glued on top of the microscope slide to form a closed container for the tissue. The tissue slices were placed onto the microscope slide within the spacer containment. Diluted microplastic bead solutions (0.25% microplastic particles) were prepared in PBS from a 2.6% PS bead stock solution (Polysciences, USA), and from a 10% PMMA bead stock solution (microParticles GmbH, Germany), respectively. 5 µl of the diluted microplastic beads solution were applied onto the tissue using a syringe. Depending on the experiment, a second tissue slice was sandwiched on top, as depicted in Fig. 8.3(b). The remaining containment volume was filled with PBS to ensure that no air bubbles were present. In the final step, a coverslip was placed on top and sealed using 2-component epoxy glue in order to prevent the sample from dehydrating.

8.4 RESULTS

The signal-to-noise ratio (SNR) scales as

$$\mathrm{SNR} \propto \sqrt{N}, \tag{8.1}$$

where N denotes the number of photons which are involved in the SRS interaction. However, we use an alternative form

$$\mathrm{SNR} = \frac{\mu_{\mathrm{signal}} - \mu_{\mathrm{bg}}}{\sigma_{\mathrm{noise}}}, \tag{8.2}$$

where $\mu_{\mathrm{signal,bg}}$ and σ_{noise} denote the mean values of signal and background, and the noise standard deviation, respectively. This allows the direct assessment of the SNR as these quantities can be extracted directly from the resulting images. First, an upper boundary for the achievable SNR was determined. For this purpose, PS beads in aqueous solution (deionized water) without any tissue involved were prepared. This provides a reference system with optimal conditions, i.e., a low background signal level μ_{bg}, from which a benchmark for the achievable SNR can be deduced. Beads with diameters between 200 nm and 10 µm were imaged using the SRS microscope. A separate sample was prepared for beads of different diameters. For each bead diameter, a pixel integration time sweep between $T_{\mathrm{int}} = 100$ and 3000 µs was carried out (for larger bead diameters T_{int} was varied down to 3 µs), and the resulting SNR was extracted from the SRS images, as plotted in Fig. 8.4(a). The corresponding raw data are depicted in Fig. 8.5.

The axial voxel size $l_{\mathrm{voxel}} = 3$ µm divides the range of particle sizes into two regimes, where the SNR scales differently with the bead diameter. A linear behavior (note the double-logarithmic axes) is observed for this particle size range, which we define as the *particle regime*. For this regime, the fitted slope values range from 1.75 to 1.86, as indicated in Fig. 8.4(a). In contrast, for bead diameters $d > l_{\mathrm{voxel}}$ the SNR exhibits only a minor increase and almost saturates at values of ~ 300 at a pixel integration time of 3 ms. At $T_{\mathrm{int}} = 3$ µs the SNR reaches values of ~ 10. We define this range as the *bulk regime*. For large beads with dimensions in this range even shorter integration times are sufficient for detection of the beads. The raw data set depicted in Fig. 8.5 is extended to extremely short integration times as short as 100 ns, see Fig. 8.6.

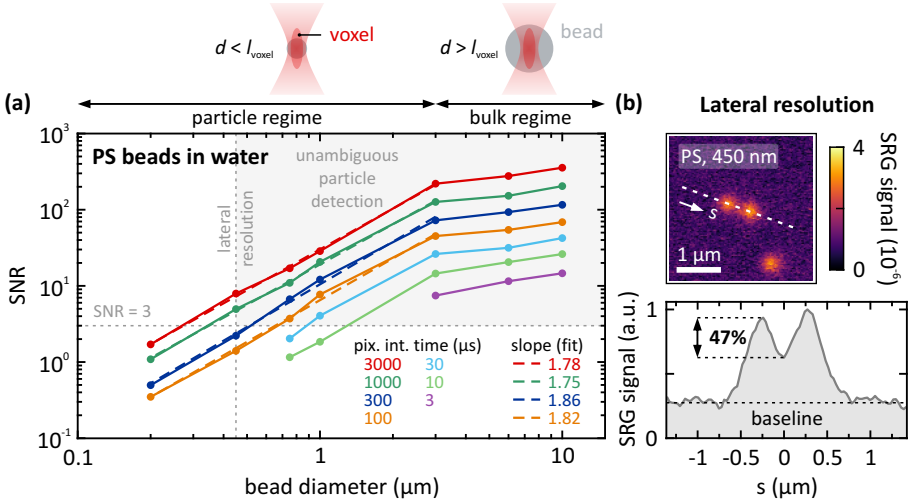

FIGURE 8.4. **Signal-to-noise ratio (SNR) depending on the diameter of the microplastic beads and lateral resolution. (a)** PS beads in aqueous solution are used as reference system, in order to obtain an upper boundary for the achievable SNR. Given *a priori* knowledge about the microplastic particles and optimal conditions, beads down to 200 nm diameter are detectable. However, for unambiguous detection of microplastic particles with unknown dimensions, a minimum required SNR of 3 and a minimum size of > 0.45 µm (lateral resolution of the SRS microscope) are defined, as indicated by the gray shaded area. Hence, the detection limit is reached for 450-nm beads at a pixel integration time of 1000 µs, which yields a SNR of 5. The axial voxel size of $l_{\text{voxel}} = 3$ µm divides the range of particle sizes into two regimes, in which the SNR scales differently: particle regime for beads with $d < l_{\text{voxel}}$ (SNR increases linearly on double-logarithmic axes), and bulk regime for beads with $d > l_{\text{voxel}}$ (SNR almost saturates). Pump power: 10 mW, STOKES power: 9.5 mW. **(b)** 450-nm PS beads are imaged to determine the lateral resolution. Pixel integration time: 3 ms. The signal cross-section along the dashed line yields a modulation depth of 47% with respect to the noise baseline, therefore satisfying the Rayleigh criterion, which requires a modulation depth of 26.4% for two objects to be resolvable.

Fig. 8.4(b) depicts the cross-sectional signal of two 450 nm PS beads to assess the lateral resolution limit. The resulting modulation depth of 47% satisfies the RAYLEIGH criterion, which states that the intensity in the area between the overlapping Airy disks of two close-by objects has to be decreased by $> 26.4\%$ [23–25], see Fig. 2.13. Thus, the lateral resolution of the SRS system reaches ~ 450 nm at $T_{\text{int}} = 3$ ms. For shorter integration times the lateral resolution degrades, as the noise level increases.

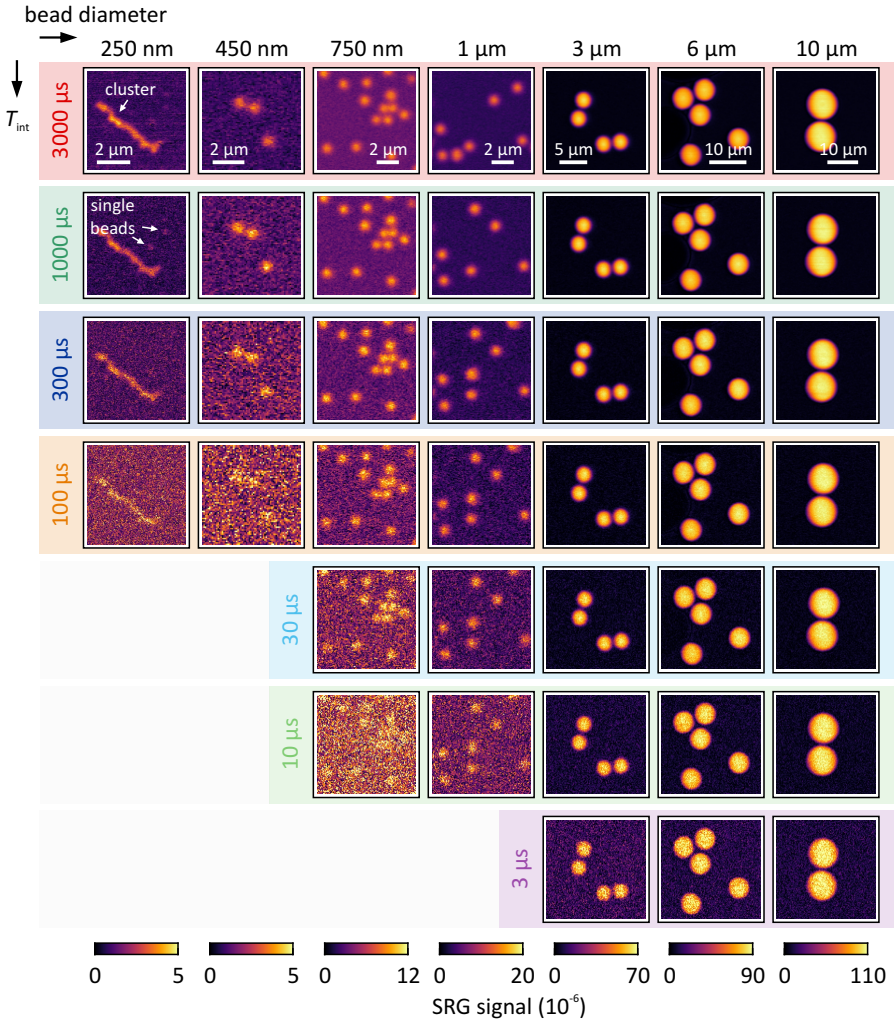

FIGURE 8.5. **SRS scans of PS beads of varying diameter** in aqueous solution. The data depicted in Fig. 8.4(a) are extracted from these SRS scans. In case of the 200-nm beads several individual beads conglomerate into a cluster. Two single beads are located on the right of the field of view, as indicated by the arrows. The number of 1-µm beads changes, as individual beads are dragged into and out of the field of view by the scanning laser focal spot, which acts as an optical tweezer.

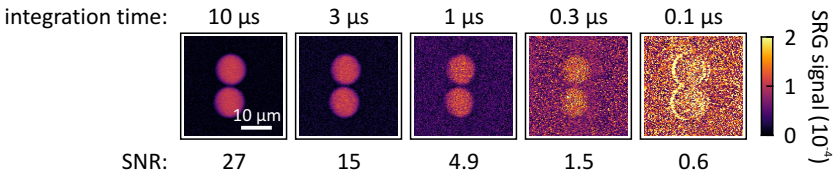

FIGURE 8.6. **SRS signal at extremely short integration times.** Two 10-µm PS beads are imaged at pixel integration times down to 100 ns. Once the integration time reaches the time scale of one modulation cycle (1/2.6 MHz ≈ 400 ns), image artifacts occur. The SNR values of the first two images are included in Fig. 8.4(a).

The lateral resolution of this SRS system has already been characterized in the previous chapter in Section 7.3.2. However, there a 500-nm PS bead is imaged, and from that, the point spread function is determined. Since the assumption of a 500-nm PS bead being a point-like object is not entirely valid, the determined lateral resolution is a rather conservative value. In order to obtain a more precise value for the lateral resolution, here we use the RAYLEIGH criterion as a measure for the lateral resolution.

As one of the benefits of SRS imaging is the intrinsic chemical selectivity, we measure the SRS spectra of PS and PMMA beads, as depicted in Fig. 8.7(a). The peak positions as well as the peak ratios agree well with the corresponding spontaneous RAMAN spectra. Due to the spectral resolution of $\sim 10\,\mathrm{cm}^{-1}$, sharp spectral features appear smoothed in the SRS spectra. Fig. 8.7(b) depicts exemplary SRS scans at four different spectral positions. At the resonance of saturated lipids ($2850\,\mathrm{cm}^{-1}$), PS and PMMA beads exhibit comparable residual signal levels. The PS beads show a remaining signal at $2953\,\mathrm{cm}^{-1}$. The highest chemical contrast is reached at $3066\,\mathrm{cm}^{-1}$. At $3250\,\mathrm{cm}^{-1}$, the SRS signal of the surrounding water exceeds the response of the beads.

In the next step, we demonstrate chemical contrast between PS and PMMA beads of 6 µm of diameter in fish tissue environment, as depicted in Fig. 8.8. A bead cluster of both plastic types in tissue was imaged at their respective RAMAN resonances at 3066, and $2953\,\mathrm{cm}^{-1}$, respectively. Additionally, images at the RAMAN band of saturated lipids at $2850\,\mathrm{cm}^{-1}$ were acquired. As control measurements, linear transmission images at the STOKES wavelength were acquired, which reveal the cluster of beads as well. The PMMA beads are well visible at $2953\,\mathrm{cm}^{-1}$. Nevertheless, the PMMA RAMAN resonance overlaps with the protein resonance, which also highlights tissue structures, and therefore, limits the contrast of the PMMA beads against the background, yielding a SNR of 25.

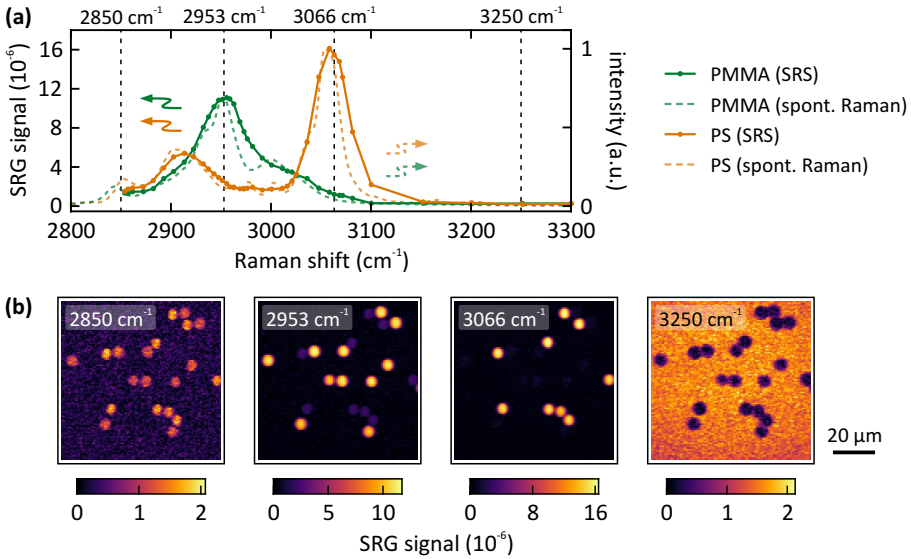

FIGURE 8.7. **SRS spectra. (a)** Measured SRS spectra of PS and PMMA beads, both 6 µm diameter. The SRS spectra agree well with the literature spontaneous RAMAN spectra (dashed lines). **(b)** Exemplary SRS scans at the spectral positions indicated by the vertical dashed lines in (a). Pixel integration time: 3 ms, pump power: 6 mW, Stokes power: 10 mW.

On the other hand, excellent contrast with almost no background signal is observed for the PS beads, resulting in a SNR of 43. In agreement with Fig. 8.7, the SRS signatures of both, PMMA and PS beads, almost vanish at the lipids resonance at 2850 cm^{-1}, which demonstrates the chemically selective imaging capability of our SRS system. As expected, the bead cluster vanishes at deeper z-positions in the tissue, as evident from the scans at $z = 50$ and 60 µm.

Further down in the sample, two PS beads are revealed between the two tissue slices at $z = 0$. In this case, the signal level dropped by a factor of ~ 15 compared to the signal originating from the beads on top of the tissue. An integration time of 1 ms (3.3 ms pixel dwell time) yields a SNR of 4.2. Again, the linear transmission image confirms the location of the beads.

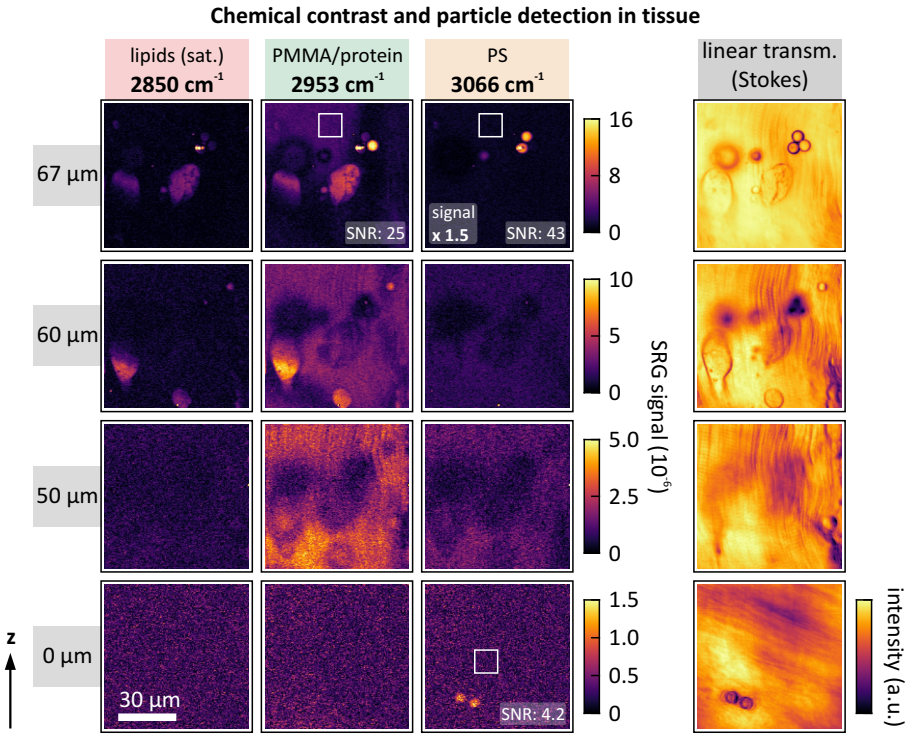

FIGURE 8.8. **Chemical contrast between PS and PMMA beads in fish tissue environment.** Bead diameter: 6 µm. Two tissue slices are stacked on top of each other, as depicted in Fig. 8.3(b). SRS images are acquired at 2850 cm^{-1} (saturated lipids), 2950 cm^{-1} (PMMA/protein), and 3066 cm^{-1} (PS) for four different z-positions. The corresponding linear transmission (STOKES channel) images are depicted on the right. Note the different orientation of the muscle tissue at $z = 0$ (at the interface between the tissue slices, Fig. 8.3(b)). PS and PMMA beads can be distinguished by their respective RAMAN resonances. Especially PS exhibits excellent contrast against the tissue environment. SNR values are determined for the brightest beads and the noise regions marked by the white squares, respectively. The three beads at $z = 67$ µm are located on top of the tissue. A laser-induced defect at one of the beads causes a strong spectrally independent signal, which arises from cross-phase modulation. In contrast, the PS beads at $z = 0$ µm are located within the tissue, i.e., in between two tissue slices. At this position, the SRS signal level drops by a factor of ~ 15 as the laser propagates through ~ 65 µm of tissue, resulting in a SNR of 4.2. Note the signal multiplication factor for the upper right image. Pump power: 7 mW, STOKES power: 9.5 mW, 150×150 px^2, pixel integration time: 300 µs (1 ms at $z = 0$), pixel dwell time: 1 ms (3.3 ms at $z = 0$), acquisition time per image: 25 s (75 s at $z = 0$).

Fig. 8.9(a) demonstrates the unambiguous particle size detection limit in fish tissue environment. In this experiment, PS beads with a diameter of 1 µm were placed on top of a slice of fish tissue. In order to account for the increased noise level at an integration time of only 300 µs, 1 µm beads are used to ensure unambiguous separation of the particles. The PS resonance (3066 cm^{-1}) at $z = 6$ µm clearly reveals the beads. At the water resonance at 3250 cm^{-1}, the beads appear as shadows surrounded by the water signature., while at the protein resonance (2950 cm^{-1}), the beads are not detectable. As control measurement, images were acquired 6 µm below the bead location within the tissue ($z = 0$ µm), where the protein signature reveals the presence of tissue bulk material. The SNR is analyzed depending on the pixel integration time, as depicted in Fig. 8.9(b). The resulting slope (note the double-logarithmic axes) of 0.54 agrees well with the expected square-root scaling behavior of the SNR. At an integration time as short as 30 µs (100 µs pixel dwell time) a SNR of 2.9 is reached, as depicted in the inset in Fig. 8.9(b).

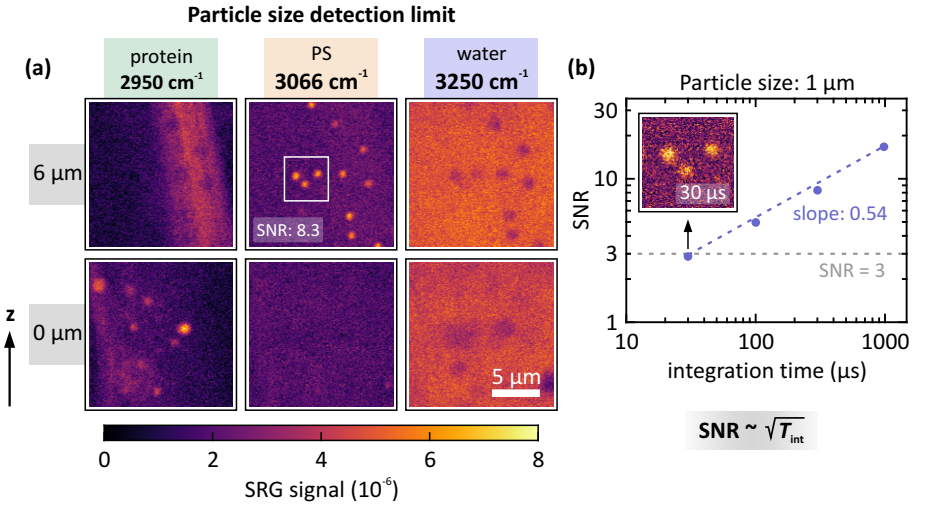

FIGURE 8.9. **Detection of PS beads with 1 µm diameter on fish tissue. (a)** SRS images are acquired at 2950 cm^{-1} (PMMA/protein), 3066 cm^{-1} (PS), and 3250 cm^{-1} (water) for two different z-positions. The 1-µm PS beads are clearly distinguishable. Pump power: 7 mW, STOKES power: 9.5 mW, 150 × 150 px^2, pixel integration time: 300 µs, pixel dwell time: 1 ms, acquisition time per image: 25 s. **(b)** Signal-to-noise ratio (SNR) for varying integration times (T_{int}). The white square at $z = 6$ µm indicates the analyzed region. The resulting slope agrees well with the expected square-root scaling. Inset: a SNR of 2.9 is reached at an integration of only $T_{int} = 30$ µs (pixel dwell time: 100 µs).

8.5 DISCUSSION

8.5.1 *Detection Limit of PS Beads Under Optimal Conditions*

Generally, the detection limit for structural features such as microplastic particles using SRS microscopy is dictated by two factors. First, the signal-to-noise ratio (SNR) must be sufficient in order to obtain contrast against the noise floor. Secondly, the spatial resolution of the imaging setup determines whether individual particles can be spatially distinguished, and imposes a lower boundary on the minimum detectable particle size. Both conditions have to be met to ensure unambiguous particle detection. Consequently, particle sizes below the resolution limit cannot be directly assessed, even though the SNR level might be sufficient, and vice versa.

Nevertheless, given a priori knowledge about the microplastic particles, beads down to 200 nm diameter are detectable under optimal conditions, although they are well below the spatial resolution limit, as depicted in Fig. 8.4(a). Thus, in order to reach this sensitivity level, the bead dimensions must be known beforehand. Additionally, clustering of individual beads cannot be ruled out, as bead clusters may still be sized below the spatial resolution limit. The integrated signals of several potential clusters exhibit discrete differences in the signal level from which the number of beads within the clusters can be extracted. Furthermore, the detection with a SNR below 1 is possible only if the bead location is exactly known.

However, for unambiguous detection of microplastic particles with unknown dimensions and location, a minimum required SNR of 3 is defined and a minimum size of $> 0.45\,\mu m$ (lateral resolution of the SRS microscope) is necessary, as indicated by the gray shaded area in Fig. 8.4(a). As a result, we demonstrate that the detection limit for PS beads is reached, e.g., for a diameter of 1 µm with $T_{int} = 30\,\mu s$, or for 450 nm beads with $T_{int} = 1\,ms$, at the given laser power levels of 10 mW in the pump channel, and 9.5 mW in the STOKES channel. Increasing the pump power level would yield a linear increase in the SNR. However, the damage threshold of the sample imposes a limitation on the power level to $\sim 10\,mW$.

For beads with $d < l_{voxel}$, the filling factor of the voxel scales with the bead volume (particle regime). Thus, the number of excited molecular oscillators N increases with

$$N \propto d^3. \tag{8.3}$$

Since the SNR scales with $\sqrt{N}$, the SNR is expected to increase with

$$\mathrm{SNR} \propto d^{3/2}. \tag{8.4}$$

This is well reproduced by the mean slope value of 1.8 which is extracted from the linear fit curves. In contrast, for beads with diameters of $> 3\,\mu m$ (bulk regime), the voxel fully overlaps with the material independently of the bead diameter, and thus, the SRS signal almost saturates.

8.5.2 *Chemical Contrast and Detection of Microplastics in Fish Tissue*

As depicted in Fig. 8.8, PS exhibits excellent contrast against the background, as the tissue does not respond at $3066\,cm^{-1}$. Conversely, the PMMA resonance largely overlaps with the protein resonance at $2950\,cm^{-1}$, and thus, the tissue response at this spectral position limits the contrast of the detected PMMA beads against the background. Therefore, SRS imaging in the fingerprint spectral region would be beneficial, as it provides improved chemical specificity. Nevertheless, PS and PMMA beads can be clearly distinguished, even if they conglomerate within the same cluster. Off-resonant imaging, in this case at the RAMAN band of saturated lipids at $2850\,cm^{-1}$, indicates that the signal originates from SRS interaction rather than parasitic effects, such as cross-phase modulation (XPM).

SRS detection of microplastic particles within fish tissue is demonstrated at $z = 0$. Imaging of the $6\,\mu m$ PS beads through the upper tissue slice still yields clear images with low distortions. However, deterioration of the SRS signal is observed, as evident from the signal level at $z = 0$. This is likely due to inhomogeneities in the tissue that cause wavefront distortions and scattering, both of which decrease the SRS efficiency, as it is a phase-sensitive process. In this specific case, the signal level drops by a factor of ~ 15 after the propagation through $\sim 65\,\mu m$ of tissue. Thus, while we demonstrate that SRS imaging can be employed to screen fish tissue for microplastic contamination, it is apparent that the penetration depth into the bulk tissue strongly depends on the local tissue composition and its overall transparency.

8.5.3 *Particle Size Detection Limit*

As demonstrated in Fig. 8.4(a), unambiguous PS bead detection under optimal conditions demands a minimum bead diameter of $1\,\mu m$ when using a minimum pixel integration time of $30\,\mu s$, which yields a SNR of 4.1. This could be replicated in fish tissue, where $1\,\mu m$ PS beads, due to the low signal background level at $3066\,cm^{-1}$, are detected with an only slightly reduced SNR of 2.9 at a pixel integration time of $30\,\mu s$, as depicted in the inset in Fig. 8.9(b). As this is right at the lower SNR limit of 3, it marks the detection threshold for PS in fish tissue and indicates that it is feasible to

detect 1 µm particles under more realistic conditions.

Clearly, this assessment holds for the specific case of PS microplastic particles. Other plastic compounds with different RAMAN response levels may exhibit deviating figures of merit, and thus, may be harder to detect. As in the case of PS, disjoint RAMAN resonances between the microplastic particles and the surrounding tissue are highly beneficial for optimized chemical contrast. As apparent from Fig. 8.8, PMMA microplastics detection in the C–H stretch spectral region suffers from the overlapping protein resonance, which highlights surrounding tissue as well.

8.5.4 *Limitations of SRS Microscopy for the Detection of Microplastics*

The spatial resolution imposes a lower boundary on the minimum detectable particle size of $\sim 450\,\mathrm{nm}$. Below that, the actual particle size cannot be assessed. Furthermore, in this particle size range the SNR drops with decreasing particle volume ($\mathrm{SNR} \propto \sqrt{V}$). Therefore, individual nanoplastic particles with dimensions significantly smaller than 1 µm cannot be detected using SRS imaging, unless several smaller particles are conglomerated within a cluster.

Furthermore, the penetration depth into the tissue we demonstrate is on the order of $\sim 65\,\mu\mathrm{m}$. Although higher penetration depths may be possible, this would strongly depend on the tissue texture and composition. On the one hand, limited tissue transparency hinders imaging deep inside the tissue without the laser power exceeding the tissue damage threshold. On the other hand, a loss of coherence is induced by scattering. Especially inhomogeneous tissue could deteriorate the wavefronts of the incident laser beams, which in turn decreases the SRS interaction efficiency, as observed in Fig. 8.8 at $z = 0$. Hence, careful tissue preparation is necessary prior to the imaging process. In particular, thin slicing may be required, as demonstrated in this work.

SRS imaging is well suited for imaging of biological systems with high resolution and detail within fields of view below $1\,\mathrm{mm}^2$. However, large area or even large volume scans using SRS microscopy would require image stitching, and as a result, the overall acquisition time would increase drastically. Therefore, the region of interest within a large sample should be known or determined in advance to enable directed SRS imaging within this region. Consequently, unbiased monitoring of large volumes for traces of microplastics based on SRS imaging remains not yet feasible.

8.5.5 *SRS Imaging as Complementary Technique to Conventional Raman Imaging*

Conventional RAMAN imaging provides the entire RAMAN spectrum per pixel with high spectral resolution, which renders this technique ideal for the identification of unknown compounds [127, 128]. SRS in its original scheme, on the other hand, intrinsically probes one resonance at a time only. In principle, spectral multiplexing is possible to certain extent, but it requires increased technical effort, and thus, adds cost and complexity [129–131]. Additionally, the spectral resolution of SRS is intrinsically limited, as pulse duration requirements impose a limitation to narrow-band detection.

However, owing to its significantly enhanced interaction cross-section, SRS enables much faster image acquisition than conventional RAMAN imaging [100]. In order to reduce the acquisition time, conventional RAMAN imaging is combined with dark-field imaging, which is employed to detect the location and the size distribution of microplastic particles in advance [124, 132]. With that, the subsequent RAMAN spectroscopic measurement can be used specifically at the regions of interest only. However, this combined technique can only be employed in situations, where the microplastic particles can be isolated from their surrounding medium and prepared accordingly, such as filtered particles for monitoring of microplastic contamination in drinking water.

SRS imaging is a superior choice for tissue screening for microplastic contamination, as it does not require filtration and extraction of the plastic particles by elaborate chemical treatment in advance [133, 134]. Additionally, SRS microscopy reveals the location of the microplastic particles in the surrounding tissue, which will be useful to unravel precise patterns of accumulation in diverse tissue types and organisms, and thus, enables investigations into its physiological consequences in the future.

8.6 CONCLUSION & OUTLOOK

We have demonstrated microplastics detection in fish tissue based on SRS spectral imaging and determined an upper boundary for the achievable signal-to-noise ratio for PS microplastic beads. Considering the spatial resolution of the SRS microscope, we have defined the requirements on unambiguous microplastic particle detection. For PS particles the detection limit is reached for a diameter of 1 μm and a pixel integration time of 30 μs at 10 mW of pump power. Other plastics compounds, such as PMMA, exhibit lower contrast against the tissue background due to spectrally overlapping RAMAN responses.

Extending the wavelength tuning range to the fingerprint spectral region would enable access to RAMAN bands with increased specificity, and thus, to increase the contrast between microplastics signatures and the surrounding tissue.

The sensitivity could be further enhanced by utilizing a high-NA water immersion microscope objective for the laser illumination of the sample to increase the SRS signal level as well as the spatial resolution. However, the imaging performance within scattering and absorbing tissue would deteriorate, and therefore, limit this approach to microplastic detection close to the tissue surface.

The SRS image acquisition speed could be further enhanced by increasing the modulation frequency up to 20.5 MHz. Such Nyquist modulation schemes have been reported for SRS [47, 106], as well as for stimulated emission microscopy [135]. This could be realized using an extended-cavity design for the fiber-feedback optical parametric oscillator (FFOPO) in combination with pump modulation to provide maximum modulation depth [42]. However, the expected increase in the noise level at higher acquisition speeds would limit the detection to larger microplastic debris on the order of 10 μm diameter.

In conclusion, SRS spectral imaging is an ideal complementary modality to conventional RAMAN scattering imaging for the detection and identification of microplastic particles. In particular, SRS is superior for imaging microplastics contamination in tissue, where the particle extraction from the tissue prior to chemical identification and particle size assessment is unfeasible. Currently, there is no single detection technique available, which combines all requirements, i.e., high acquisition speed, chemical specificity, high 3D spatial resolution, large-area fields of view, and large penetration depth. Consequently, for every specific use case, the detection methodology has to be chosen

accordingly. We believe that 3D SRS spectral imaging holds the potential to be an important tool for the assessment of possible health risks imposed by microplastics in our food chain.

A

APPENDIX

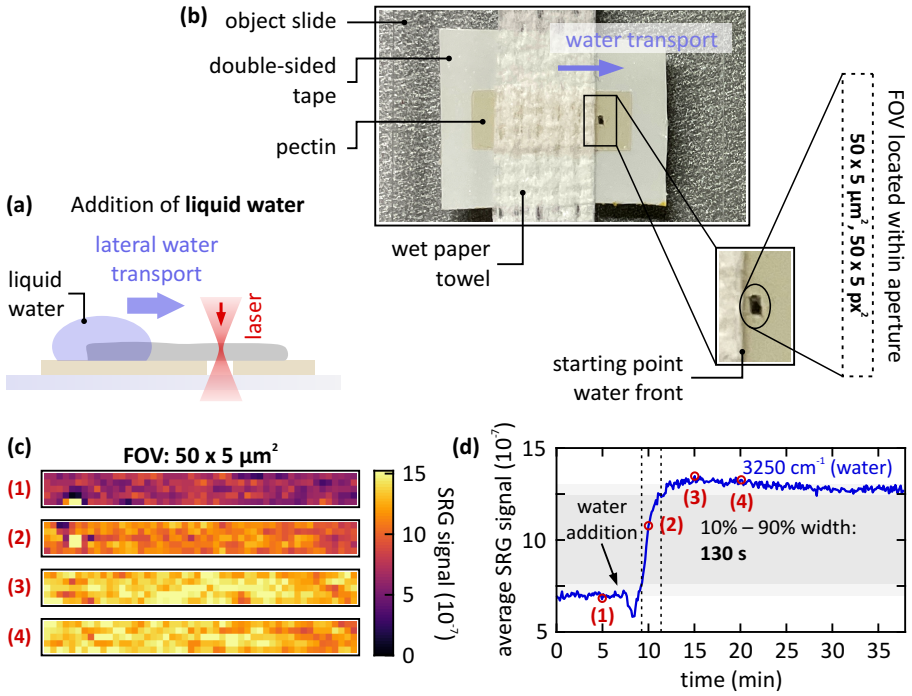

FIGURE A.1. **Setup horizontal water transport. (a)** Schematic for measuring the water transport in the pectin, as shown in Fig. 7.8. **(b)** Close-up photograph of the pectin patch which is glued on double-sided tape. An aperture in the tape enables the SRS signal detection. A wet water towel on top of the pectin polymer delivers a defined water front, which traverses the field of view (transport direction indicated by the blue arrow). **(c)** Exemplary individual raw data scans, which are obtained at $t = 5$, 10, 15, and 20 min, as indicated in **(d)**. No structured water channels are visible. Therefore, the water transport takes place either homogeneously on the molecular scale or within small water channels which are well below the diffraction limit. Each data point in **(d)** corresponds to the average of one entire raw data scan.

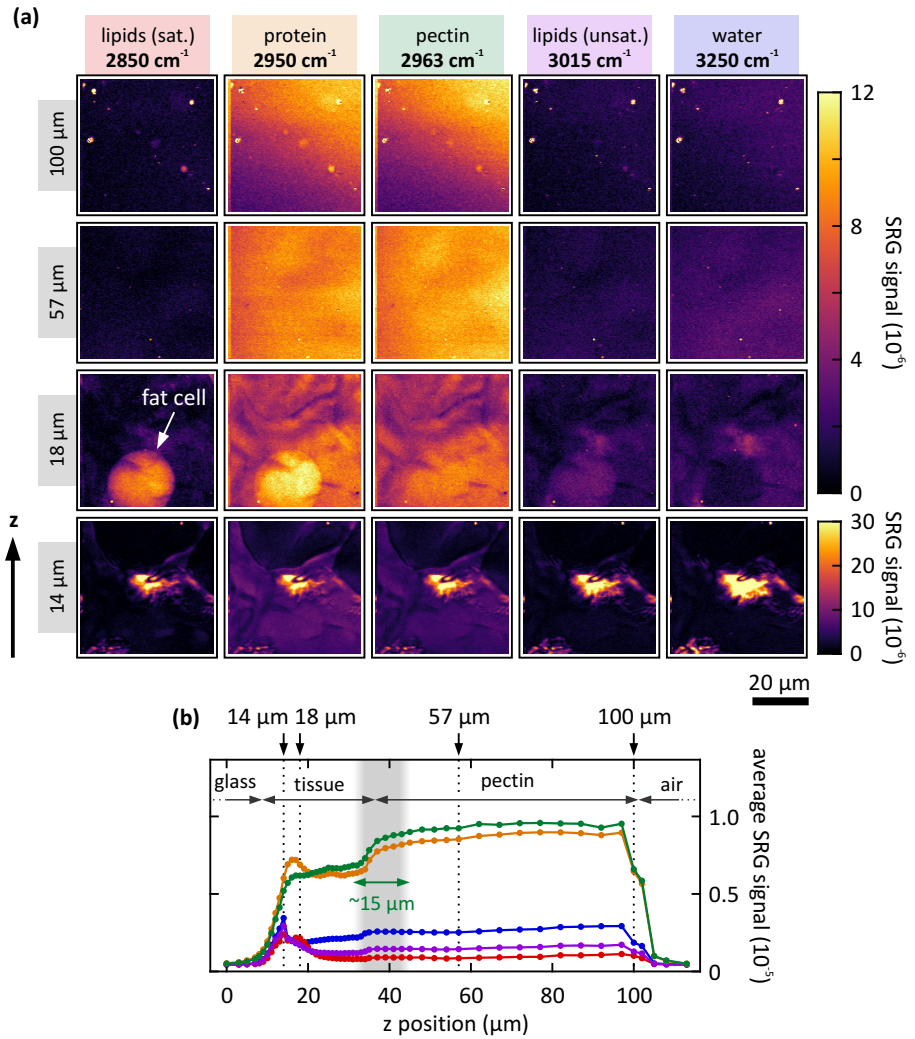

FIGURE A.2. **3D SRS scan, all resonances.** Two additional RAMAN bands are shown, i.e., protein at 2950 cm^{-1} and unsaturated lipids at 3015 cm^{-1} (see Fig. 7.10). The protein resonance overlaps with the pectin resonance, as their peak positions are separated by only 13 cm^{-1}. **(a)** A large amount of protein is present in the intestinal tissue at $z = 14\,\mu m$. The fat cell at $z = 18\,\mu m$ mainly consists of saturated lipids, as evident from the significantly lower signal level in the channel of unsaturated lipids. **(b)** As expected from their spectral vicinity, the average signal levels along the z-axis of pectin (green) and protein (yellow) are closely correlated. However, in the tissue at $z = 15\,\mu m$ the protein signal exceeds the pectin signal level. Correspondingly, this behaviour is switched in the pectin bulk material. Total acquisition time for the entire data set: 5 h 45 min.

ACRONYMS

AC	auto-correlation.
AOM	acousto-optical modulator.
APC	angled physical contact.
AWG	arbitrary waveform generator.
BBO	β-barium borate.
CARS	coherent anti-Stokes Raman scattering.
CLT	central limit theorem.
DFG	difference frequency generation.
DFT	dispersive Fourier transformation.
FBR	feedback ratio.
FFOPO	fiber-feedback optical parametric oscillator.
FLIM	fluorescence lifetime imaging microscopy.
FWHM	full-width at half-maximum.
GDD	group delay dispersion.
GVD	group velocity dispersion.
GVM	group velocity mismatch.
KTA	potassium titanyl arsenate.
$LiNbO_3$	lithium niobate.
NA	numerical aperture.
ND	neutral density.
NLSE	nonlinear Schrödinger equation.
NPM	noncollinear phase matching.
OCR	output coupling ratio.
OPA	optical parametric amplification.
OPG	optical parametric generation.
OPO	optical parametric oscillation.

OSA	optical spectrum analyzer.
PBS	polarizing beam splitter.
PBS	phosphate-buffered saline.
PC	physical contact.
PMMA	poly(methyl methacrylate).
PPLN	periodically poled lithium niobate.
PS	polystyrene.
PSF	point spread function.
QPM	quasi phase matching.
QWP	quarter-wave plate.
RIN	relative intensity noise.
RMS	root mean square.
SFG	sum-frequency generation.
SHG	second-harmonic generation.
SNR	signal-to-noise ratio.
SPCM	single photon counting module.
SPM	self-phase modulation.
SRG	stimulated RAMAN gain.
SRL	stimulated RAMAN loss.
SRS	stimulated RAMAN scattering.
XPM	cross-phase modulation.
XPW	cross-polarized wave generation.

LIST OF FIGURES

LIST OF TABLES

BIBLIOGRAPHY

[1] J. D. Jackson, *Classical electrodynamics*, New York: Wiley, 1999, ISBN: 9780471309321.

[2] R. W. Boyd, *Nonlinear Optics, Third Edition*, New York: Academic Press, Inc., 2008, ISBN: 0123694701.

[3] U. Keller, *Ultrafast Lasers*, Springer, 2021, ISBN: 9783030825324.

[4] T. Steinle, *Ultrafast near- and mid-infrared laser sources for linear and nonlinear spectroscopy*, PhD thesis, University of Stuttgart, 2016.

[5] G. Cerullo and S. De Silvestri, *Ultrafast optical parametric amplifiers*, Review of Scientific Instruments **74**, 1–18 (2003).

[6] D. S. Hum and M. M. Fejer, *Quasi-phasematching*, Comptes Rendus Physique **8**, 180–198 (2007).

[7] D. H. Jundt, *Temperature-dependent Sellmeier equation for the index of refraction, n_e, in congruent lithium niobate*, Optics Letters **22**, 1553–1555 (1997).

[8] H. Linnenbank and S. Linden, *High repetition rate femtosecond double pass optical parametric generator with more than 2 W tunable output in the NIR*, Optics Express **22**, 18072 (2014).

[9] H. Linnenbank, T. Steinle, and H. Giessen, *Narrowband cw injection seeded high power femtosecond double-pass optical parametric generator at 43 MHz: Gain and noise dynamics*, Optics Express **24**, 19558 (2016).

[10] W. H. Louisell, A. Yariv, and A. E. Siegman, *Quantum fluctuations and noise in parametric processes. I.* Physical Review **124**, 1646–1654 (1961).

[11] G. Arisholm, *Quantum noise initiation and macroscopic fluctuations in optical parametric oscillators*, Journal of the Optical Society of America B **16**, 117–127 (1999).

[12] R. Shaw, *The Dripping Faucet as a Model Chaotic System*, Aerial Press Inc., 1984, ISBN: 0942344057.

[13] D. W. Crevier and M. Meister, *Synchronous Period-Doubling in Flicker Fision of Salamander and Man*, Journal of Neurophysiology **79**, 1869–1878 (1998).

[14] R. M. May, *Simple mathematical models with very complicated dynamics*, Nature **261**, 459–467 (1976).

[15] M. J. Feigenbaum, *Quantitative Universality for a Class of Nonlinear Transformations*, Journal of Statistical Physics **19**, 25–52 (1978).

[16] M. Floess, *Lock-in camera-based stimulated Raman scattering imaging and synchronized pump modulation in an optical parametric oscillator*, Master's thesis, University of Stuttgart, 2019.

[17] P. Groß, N. Haarlammert, M. Kues, T. Walbaum, and C. Fallnich, *Effects of optical feedback on femtosecond supercontinuum generation*, Optical Fiber Technology **18**, 290–303 (2012).

[18] B. R. Masters and P. T. C. So, *Handbook of Biomedical Nonlinear Optical Microscopy*, New York: Oxford University Press, Inc., 2008, ISBN: 9780195162608.

[19] H. Haken and H. C. Wolf, *Molekülphysik und Quantenchemie: Einführung in die experimentellen und theoretischen Grundlagen*, Berlin Heidelberg: Springer, 2006, ISBN: 3540303146.

[20] H. Linnenbank et al., *Robust and rapidly tunable light source for SRS/CARS microscopy with low-intensity noise*, Advanced Photonics **1**, 1–7 (2019).

[21] W. Min, C. W. Freudiger, S. Lu, and X. S. Xie, *Coherent Nonlinear Optical Imaging: Beyond Fluorescence Microscopy*, Annual Review of Physical Chemistry **62**, 507–530 (2011).

[22] K. K. Sharma, *Optics - Principles and Applications*, Academic Press, Inc., 2006, ISBN: 9780123706119.

[23] H. H. Hopkins and P. M. Barham, *The Influence of the Condenser on Microscopic Resolution*, Proceedings of the Physical Society. Section B **63**, 737–744 (1950).

[24] X. Michalet and S. Weiss, *Using photon statistics to boost microscopy resolution*, Proceedings of the National Academy of Sciences **103**, 4797–4798 (2006).

[25] C. J. R. Sheppard, *Resolution and super-resolution*, Microscopy Research and Technique **80**, 590–598 (2017).

[26] A. E. Siegman, *Lasers*, University Science Books, 1986, ISBN: 0935702113.

[27] P. Billingsley, *Probability and Measure*, New York: Wiley, 1995.

[28] G. Herink, B. Jalali, C. Ropers, and D. R. Solli, *Resolving the build-up of femtosecond mode-locking with single-shot spectroscopy at 90 MHz frame rate*, Nature Photonics **10**, 321–326 (2016).

[29] D. Descloux et al., *Spectrotemporal dynamics of a picosecond OPO based on chirped quasi-phase-matching: erratum*, Optics Letters **40**, 280–283 (2015).

[30] C. F. O'Donnell, S. C. Kumar, T. Paoletta, and M. Ebrahim-Zadeh, *Widely tunable femtosecond soliton generation in a fiber-feedback optical parametric oscillator*, Optica **7**, 426 (2020).

[31] P. Kelkar, F. Coppinger, A. Bhushan, and B. Jalali, *Time-domain optical sensing*, Electronics Letters **35**, 1661–1662 (1999).

[32] K. Goda and B. Jalali, *Dispersive Fourier transformation for fast continuous single-shot measurements*, Nature Photonics **7**, 102–112 (2013).

[33] M. Kues, N. Brauckmann, T. Walbaum, P. Groß, and C. Fallnich, *Nonlinear dynamics of femtosecond supercontinuum generation with feedback*, Optics Express **17**, 15827–15841 (2009).

[34] N. Brauckmann, M. Kues, T. Walbaum, P. Groß, and C. Fallnich, *Experimental investigations on nonlinear dynamics in supercontinuum generation with feedback*, Optics Express **18**, 7190–7202 (2010).

[35] M. Kues, N. Brauckmann, P. Groß, and C. Fallnich, *Basic prerequisites for limit-cycle oscillations within a synchronously pumped passive optical nonlinear fiber-ring resonator*, Physical Review A **84**, 033833 (2011).

[36] A. Steinmann, B. Metzger, R. Hegenbarth, and H. Giessen, *Compact 7.4 W femtosecond oscillator for white-light generation and nonlinear microscopy*, *CLEO:2011 - Laser Applications to Photonic Applications*, Optica Publishing Group, 2011, CThAA5, DOI 10.1364/CLEO_SI.2011.CThAA5, https://opg.optica.org/abstract.cfm?URI=CLEO_SI-2011-CThAA5.

[37] T. Steinle, F. Mörz, A. Steinmann, and H. Giessen, *Ultra-stable high average power femtosecond laser system tunable from 1.33 to 20 µm*, Optics Letters **41**, 4863–4866 (2016).

[38] R. DeSalvo, A. A. Said, D. J. Hagan, E. W. Van Stryland, and M. Sheik-Bahae, *Infrared to Ultraviolet Measurements of Two- Absorption and n_2 in Wide Bandgap Solids*, IEEE Journal of Quantum Electronics **32**, 1324–1333 (1996).

[39] D. H. Jundt, *Temperature-dependent Sellmeier equation for the index of refraction, n_e, in congruent lithium niobate*, Optics Letters **22**, 1553–1555 (1997).

[40] P. Tzankov et al., *300 μJ noncollinear optical parametric amplifier in the visible at 1 kHz repetition rate*, Optics Letters **31**, 3629–3631 (2006).

[41] G. Cirmi et al., *Few-optical-cycle pulses in the near-infrared from a noncollinear optical parametric amplifier*, Optics Letters **32**, 2396–2398 (2007).

[42] M. Floess, T. Steinle, I. Gerhardt, and H. Giessen, *Femtosecond tunable light source with variable repetition rate between 640 kHz and 41 MHz with a 130 dB temporal pulse contrast ratio*, Optics Express **30**, 1 (2022).

[43] M. Floess, T. Steinle, and H. Giessen, *Burst-mode femtosecond fiber-feedback optical parametric oscillator*, Optics Letters **47**, 525–528 (2022).

[44] G. Arisholm, G. Rustad, and K. Stenersen, *Importance of pump-beam group velocity for backconversion in optical parametric oscillators*, Journal of the Optical Society of America B **18**, 1882–1890 (2001).

[45] C. R. Phillips and M. M. Fejer, *Efficiency and phase of optical parametric amplification in chirped quasi-phase-matched gratings*, Optics Letters **35**, 3093–3095 (2010).

[46] J. Moses, N. Flemens, and X. Ding, *Back-conversion Suppressed Parametric Frequency Conversion for Ultrawide Bandwidth and Ultrahigh Efficiency Devices*, Proc. SPIE **11264**, 112640B (2020).

[47] T. Steinle et al., *Stimulated Raman Scattering Microscopy with an All-Optical Modulator*, Physical Review Applied **11**, 044081 (2019).

[48] T. Baldacchini, S. Snider, and R. Zadoyan, *Two-photon polymerization with variable repetition rate bursts of femtosecond laser pulses*, Optics Express **20**, 29890 (2012).

[49] J. Fischer et al., *Three-dimensional multi-photon direct laser writing with variable repetition rate*, Optics Express **21**, 26244 (2013).

[50] S. M. Eaton et al., *Heat accumulation effects in femtosecond laser-written waveguides with variable repetition rate*, Optics Express **13**, 4708 (2005).

[51] R. R. Gattass, L. R. Cerami, and E. Mazur, *Micromachining of bulk glass with bursts of femtosecond laser pulses at variable repetition rates*, Optics Express **14**, 5279 (2006).

[52] S. Lévêque-Fort, D. N. Papadopoulos, S. Forget, F. Balembois, and P. Georges, *Fluorescence lifetime imaging with a low-repetition-rate passively mode-locked diode-pumped Nd:YVO_4 oscillator*, Optics Letters **30**, 168 (2005).

[53] A. Major, V. Barzda, P. A. E. Piunno, S. Musikhin, and U. J. Krull, *An extended cavity diode-pumped femtosecond Yb:KGW laser for applications in optical DNA sensor technology based on fluorescence lifetime measurements*, Optics Express **14**, 5285 (2006).

[54] A. Gambetta et al., *Fiber-format stimulated-Raman-scattering microscopy from a single laser oscillator*, Optics Letters **35**, 226 (2010).

[55] C. W. Freudiger et al., *Stimulated Raman scattering microscopy with a robust fibre laser source*, Nature Photonics **8**, 153–159 (2014).

[56] C. H. Camp and M. T. Cicerone, *Chemically sensitive bioimaging with coherent Raman scattering*, Nature Photonics **9**, 295–305 (2015).

[57] T. Steinle et al., *Synchronization-free all-solid-state laser system for stimulated Raman scattering microscopy*, Light: Science and Applications **5**, 1–6 (2016).

[58] S. Cai, M. Ruan, B. Wu, Y. Shen, and P. Jiang, *High Conversion Efficiency, Mid-Infrared Pulses Generated via Burst-Mode Fiber Laser Pumped Optical Parametric Oscillator*, IEEE Access **8**, 64725–64729 (2020).

[59] F. Mörz, T. Steinle, A. Steinmann, and H. Giessen, *Multi-Watt femtosecond optical parametric master oscillator power amplifier at 43 MHz*, Optics Express **23**, 23960 (2015).

[60] B. R. Masters et al., *Mitigating thermal mechanical damage potential during two-photon dermal imaging*, Journal of Biomedical Optics **9**, 1265 (2004).

[61] P. G. Antal and R. Szipocs, *Tunable, low-repetition-rate, cost-efficient femtosecond Ti:sapphire laser for nonlinear microscopy*, Applied Physics B: Lasers and Optics **107**, 17–22 (2012).

[62] G. A. Mourou, T. Tajima, and S. V. Bulanov, *Optics in the relativistic regime*, Reviews of Modern Physics **78**, 309–371 (2006).

[63] J. Itatani, J. Faure, M. Nantel, G. Mourou, and S. Watanabe, *Suppression of the amplified spontaneous emission in chirped-pulse-amplification lasers by clean high-energy seed-pulse injection*, Optics Communications **148**, 70–74 (1998).

[64] S. Fourmaux et al., *Pedestal cleaning for high laser pulse contrast ratio with a 100 TW class laser system*, Optics Express **19**, 8486 (2011).

[65] H. Kiriyama et al., *Temporal contrast enhancement of petawatt-class laser pulses*, Optics Letters **37**, 3363 (2012).

[66] T. J. Yu et al., *Generation of high-contrast, 30 fs, 1.5 PW laser pulses from chirped-pulse amplification Ti:sapphire laser*, Optics Express **20**, 10807–10815 (2012).

[67] Z. Zhao, K. Mernick, M. Costanzo, and M. Minty, *An ultrafast laser pulse picker technique for high-average-current high-brightness photoinjectors*, Nuclear Instruments and Methods in Physics Research, Section A: Accelerators, Spectrometers, Detectors and Associated Equipment **959**, 163586 (2020).

[68] Y. Huang et al., *Ultrashort pulse temporal contrast enhancement based on noncollinear optical-parametric amplification*, Optics Letters **36**, 781 (2011).

[69] P. Yuan, G. Xie, D. Zhang, H. Zhong, and L. Qian, *High-contrast near-IR short pulses generated by a mid-IR optical parametric chirped-pulse amplifier with frequency doubling*, Optics Letters **35**, 1878 (2010).

[70] I. Jovanovic, C. P. J. Barty, C. Haefner, and B. Wattellier, *Optical switching and contrast enhancement in intense laser systems by cascaded optical parametric amplification*, Optics Letters **31**, 787 (2006).

[71] C. Dorrer, I. A. Begishev, A. V. Okishev, and J. D. Zuegel, *High-contrast optical-parametric amplifier as a front end of high-power laser systems*, Optics Letters **32**, 2143 (2007).

[72] H. Kiriyama et al., *High-energy, high-contrast, multiterawatt laser pulses by optical parametric chirped-pulse amplification*, Optics Letters **32**, 2315 (2007).

[73] H. Kiriyama et al., *High-contrast, high-intensity laser pulse generation using a nonlinear preamplifier in a Ti:sapphire laser system*, Optics Letters **33**, 645 (2008).

[74] R. C. Shah et al., *High-temporal contrast using low-gain optical parametric amplification*, Optics Letters **34**, 2273 (2009).

[75] I. Musgrave et al., *Picosecond optical parametric chirped pulse amplifier as a preamplifier to generate high-energy seed pulses for contrast enhancement*, Applied Optics **49**, 6558–6562 (2010).

[76] E. Cunningham, E. Galtier, G. Dyer, J. Robinson, and A. Fry, *Pulse contrast enhancement via non-collinear sum-frequency generation with the signal and idler of an optical parametric amplifier*, Applied Physics Letters **114**, (2019).

[77] A. Jullien et al., 10^{-10} *temporal contrast for femtosecond ultraintense lasers by cross-polarized wave generation*, Optics Letters **30**, 920 (2005).

[78] A. Cotel et al., *Nonlinear temporal pulse cleaning of a 1-μm optical parametric chirped-pulse amplification system*, Applied Physics B: Lasers and Optics **83**, 7–10 (2006).

[79] H. Liebetrau et al., *Ultra-high contrast frontend for high peak power fs-lasers at 1030 nm*, Optics Express **22**, 24776 (2014).

[80] J.-L. Tapié and G. Mourou, *Shaping of clean, femtosecond pulses at 1053 μm for chirped-pulse amplification*, Optics Letters **17**, 136 (1992).

[81] Y. Beaudoin, *Ultrahigh-contrast Ti:sapphire/Nd:glass terawatt laser system*, Optics Letters **17**, 865–867 (1992).

[82] D. Homoelle, A. L. Gaeta, V. Yanovsky, and G. Mourou, *Pulse contrast enhancement of high-energy pulses using a gas-filled hollow waveguide*, Optics Letters **27**, 1646–1648 (2002).

[83] H. C. Kapteyn, A. Szoke, R. W. Falcone, and M. M. Murnane, *Prepulse energy suppression for high-energy ultrashort pulses using self-induced plasma shuttering*, Optics Letters **16**, 490 (1991).

[84] A. Lévy et al., *Double plasma mirror for ultrahigh temporal contrast ultraintense laser pulses*, Optics Letters **32**, 310 (2007).

[85] V. A. Schanz et al., *High dynamic range, large temporal domain laser pulse measurement*, Applied Physics B: Lasers and Optics **125**, 1–7 (2019).

[86] A. Lawrence, *Probability in Physics - An Introductory Guide*, Cham: Springer, 2019.

[87] Z. G. Figen and O. Aytur, *Simultaneous optical parametric oscillation and sum-frequency generation within a single crystal for converting 1064 nm into 627 nm*, *Pacific Rim Conference on Lasers & Electro-Optics*, 2005, pp. 1665–1666.

[88] T. Steinle, J. N. Greiner, J. Wrachtrup, H. Giessen, and I. Gerhardt, *Unbiased all-optical random-number generator*, Physical Review X **7**, 1–9 (2017).

[89] A. Bordbar-Khiabani and M. Gasik, *Smart Hydrogels for Advanced Drug Delivery Systems*, International Journal of Molecular Sciences **23**, 3665 (2022).

[90] M. Vázquez-González and I. Willner, *Stimuli-Responsive Biomolecule-Based Hydrogels and Their Applications*, Angewandte Chemie - International Edition **59**, 15342–15377 (2020).

[91] A. Gupta et al., *The production and application of hydrogels for wound management: a review*, European Polymer Journal **111**, 134–151 (2019).

[92] S. E. Broxterman and H. A. Schols, *Interactions between pectin and cellulose in primary plant cell walls*, Carbohydrate Polymers **192**, 263–272 (2018).

[93] W. L. Wagner et al., *Mesopolysaccharides: The extracellular surface layer of visceral organs*, PLoS ONE **15**, 1–15 (2020).

[94] A. Pierce et al., *Visualizing pectin polymer-polymer entanglement produced by interfacial water movement*, Carbohydrate Polymers **246**, 116618 (2020).

[95] A. B. Servais et al., *Structural heteropolysaccharide adhesion to the glycocalyx of visceral mesothelium*, Tissue Engineering Part A **24**, 199–206 (2018).

[96] A. B. Servais et al., *Structural heteropolysaccharides as air-tight sealants of the human pleura*, Journal of Biomedical Materials Research - Part B Applied Biomaterials **107**, 799–806 (2019).

[97] A. B. Servais et al., *Functional mechanics of a pectin-based pleural sealant after lung injury*, Tissue Engineering Part A **24**, 695–702 (2018).

[98] A. Pierce et al., *Pectin biopolymer mechanics and microstructure associated with polysaccharide phase transitions*, Journal of Biomedical Materials Research - Part A **108**, 246–253 (2020).

[99] A. F. Pierce et al., *Optical and Mechanical Properties of Self-Repairing Pectin Biopolymers*, Polymers **14**, 1–11 (2022).

[100] C. W. Freudiger et al., *Label-Free Biomedical Imaging with High Sensitivity by Stimulated Raman Scattering Microscopy*, Science **322**, 1857–1861 (2008).

[101] A. Zumbusch, G. R. Holtom, and X. S. Xie, *Three-Dimensional Vibrational Imaging by Coherent Anti-Stokes Raman Scattering*, Physical Review Letters **82**, 4142–4145 (1999).

[102] A. Volkmer, *Vibrational imaging and microspectroscopies based on coherent anti-Stokes Raman scattering microscopy*, Journal of Physics D: Applied Physics **38**, R59–R81 (2005).

[103] C. L. Evans and X. S. Xie, *Coherent Anti-Stokes Raman Scattering Microscopy: Chemical Imaging for Biology and Medicine*, Annual Review of Analytical Chemistry **1**, 883–909 (2008).

[104] M. Marangoni et al., *Fiber-format CARS spectroscopy by spectral compression of femtosecond pulses from a single laser oscillator.* Optics letters **34**, 3262–3264 (2009).

[105] B. G. Saar et al., *Video-rate molecular imaging in vivo with stimulated Raman scattering*, Science **330**, 1368–1370 (2010).

[106] C. Riek, *Stimulated Raman Scattering microscopy by Nyquist modulation of a two-branch ultrafast fiber source*, Optics letters **41**, (2016).

[107] T. Steinle, F. Mörz, A. Steinmann, and H. Giessen, *Ultra-stable high average power femtosecond laser system tunable from 1.33 to 20 µm*, Optics Letters **41**, 4863 (2016).

[108] M. Floess et al., *3D stimulated Raman spectral imaging of water dynamics associated with pectin-glycocalyceal entanglement*, Biomedical Optics Express **14**, 1460–1471 (2023).

[109] A. Einstein, *Über die von der molekularkinetischen Theorie der Wärme geforderte Bewegung von in ruhenden Flüssigkeiten suspendierten Teilchen*, Annalen der Physik **4**, (1905).

[110] W. C. Li, H. F. Tse, and L. Fok, *Plastic waste in the marine environment: A review of sources, occurrence and effects*, Science of the Total Environment **566-567**, 333–349 (2016).

[111] L. Lebreton et al., *Evidence that the Great Pacific Garbage Patch is rapidly accumulating plastic*, Scientific Reports **8**, 4666 (2018).

[112] M. Arhant, M. Le Gall, P.-Y. Le Gac, and P. Davies, *Impact of hydrolytic degradation on mechanical properties of PET - Towards an understanding of microplastics formation*, Polymer Degradation and Stability **161**, 175–182 (2019).

[113] K. Zhang et al., *Understanding plastic degradation and microplastic formation in the environment: A review*, Environmental Pollution **274**, 116554 (2021).

[114] A. van Wezel, I. Caris, and S. A. Kools, *Release of primary microplastics from consumer products to wastewater in the Netherlands*, Environmental Toxicology and Chemistry **35**, 1627–1631 (2016).

[115] M. Shen et al., *Removal of microplastics via drinking water treatment: Current knowledge and future directions*, Chemosphere **251**, 126612 (2020).

[116] Y. L. Cheng et al., *Occurrence and removal of microplastics in wastewater treatment plants and drinking water purification facilities: A review*, Chemical Engineering Journal **410**, 128381 (2021).

[117] P. Bonfanti et al., *Microplastics from miscellaneous plastic wastes: Physico-chemical characterization and impact on fish and amphibian development*, Ecotoxicology and Environmental Safety **225**, 112775 (2021).

[118] N. Piyawardhana et al., *Occurrence of microplastics in commercial marine dried fish in Asian countries*, Journal of Hazardous Materials **423**, 127093 (2022).

[119] K. Yin et al., *A comparative review of microplastics and nanoplastics: Toxicity hazards on digestive, reproductive and nervous system*, Science of The Total Environment **774**, 145758 (2021).

[120] P. Stapleton, *Microplastic and nanoplastic transfer, accumulation, and toxicity in humans*, Current Opinion in Toxicology **28**, 62–69 (2021).

[121] V. K. Sharma, X. Ma, E. Lichtfouse, and D. Robert, *Nanoplastics are potentially more dangerous than microplastics*, Environmental Chemistry Letters **21**, 1933–1936 (2023).

[122] N. J. Clark, F. R. Khan, D. M. Mitrano, D. Boyle, and R. C. Thompson, *Demonstrating the translocation of nanoplastics across the fish intestine using palladium-doped polystyrene in a salmon gut-sac*, Environment International **159**, 106994 (2022).

[123] I. Chakraborty et al., *Raman spectroscopy for microplastic detection in water sources: a systematic review*, International Journal of Environmental Science and Technology **20**, 10435–10448 (2023).

[124] L. Maurizi, L. Iordachescu, I. V. Kirstein, A. H. Nielsen, and J. Vollertsen, *Do drinking water plants retain microplastics? An exploratory study using Raman micro-spectroscopy*, Heliyon **9**, e17113 (2023).

[125] S. P. Laptenok, C. Martin, L. Genchi, C. M. Duarte, and C. Liberale, *Stimulated Raman microspectroscopy as a new method to classify microfibers from environmental samples*, Environmental Pollution **267**, 115640 (2020).

[126] L. Genchi et al., *When microplastics are not plastic: Chemical characterization of environmental microfibers using stimulated Raman microspectroscopy*, Science of the Total Environment **892**, 164671 (2023).

[127] C. F. Araujo, M. M. Nolasco, A. M. Ribeiro, and P. J. Ribeiro-Claro, *Identification of microplastics using Raman spectroscopy: Latest developments and future prospects*, Water Research **142**, 426–440 (2018).

[128] D. Schymanski, C. Goldbeck, H.-U. Humpf, and P. Fürst, *Analysis of microplastics in water by micro-Raman spectroscopy: Release of plastic particles from different packaging into mineral water*, Water Research **129**, 154–162 (2018).

[129] D. Fu et al., *Quantitative chemical imaging with multiplex stimulated Raman scattering microscopy*, Journal of the American Chemical Society **134**, 3623–3626 (2012).

[130] D. Fu, G. Holtom, C. Freudiger, X. Zhang, and X. S. Xie, *Hyperspectral Imaging with Stimulated Raman Scattering by Chirped Femtosecond Lasers*, Journal of Physical Chemistry B **117**, 4634–4640 (2013).

[131] K. C. Huang, J. Li, C. Zhang, Y. Tan, and J. X. Cheng, *Multiplex Stimulated Raman Scattering Imaging Cytometry Reveals Lipid-Rich Protrusions in Cancer Cells under Stress Condition*, iScience **23**, 100953 (2020).

[132] J. R. Peller et al., *Facile nanoplastics formation from macro and microplastics in aqueous media*, Environmental Pollution **313**, 120171 (2022).

[133] J. Li, D. Yang, L. Li, K. Jabeen, and H. Shi, *Microplastics in commercial bivalves from China*, Environmental Pollution **207**, 190–195 (2015).

[134] A. Karami et al., *A high-performance protocol for extraction of microplastics in fish*, Science of the Total Environment **578**, 485–494 (2017).

[135] S. Das, Y.-C. Liang, S. Tanaka, Y. Ozeki, and F.-J. Kao, *Synchronized subharmonic modulation in stimulated emission microscopy*, Optics Express **27**, 27159–27167 (2019).

ACKNOWLEDGMENTS

This work would not have been possible without the help of many people in our group as well as outside the institute.

I would especially like to thank:

- Prof. Dr. Harald Giessen for giving me the opportunity to work on my PhD thesis at the 4th Physics Institute. I thank you for all your support throughout my entire time in your group, for making it possible to work on such exciting projects, and for providing a high-quality scientific environment.
- Prof. Dr. Peter Michler for being my co-examiner.
- Prof. Dr. Christian Holm for being the head of my examination committee.
- Dr. Tobias Steinle for introducing me to the field of nonlinear optics, ultrafast lasers, SRS microscopy, and the general work in the laser lab, for the countless helpful discussions over the years, and for always providing helpful tips and hints. Without your input this work would not have been possible.
- Dr. Mario Hentschel for all your valuable input regarding general scientific questions, talk preparation, and aesthetic data representation, for all the on- and off-topic discussions, the countless Schokoriegel from your Schrank, and of course for being a good friend.
- Dr. Christine von Rekowski for always reliably taking care of all my administrative matters, paying the countless bills, and for being the place to go for everything concerning university.
- Dr. Julian Karst for being a great colleague and friend throughout the years as well as for all the fruitful discussions and good laughs in the lab, after work, and during late-night hat building sessions.
- Dominik Ludescher for being an incredible office mate and for the great atmosphere in our office.
- Dr. Andy Steinmann for taking care that the countless member photos I took throughout the years find their way on the PI4 website.

- Dr. Florian Sterl for teaching me a lot about microscopy, Matlab, and providing valuable tips and tricks in CorelDraw saving countless hours of work.
- Our collaborators Prof. Dr. Ingrid Ehrlich, Marie Fagotto-Kaufmann, Andrea Gall, Prof. Dr. Monilola Olayioye, Dr. Cristiana Lungu, Stella Asmanidou, Prof. Dr. Steven Mentzer, and Dr. Willi Wagner for the great work together.
- Dr. Axel Griesmaier and his team for providing essential electronic components for my experiments.
- Ralf Kamella and his team for providing me with many mechanical parts over the years, indispensable for various experiments.
- My former fellow student and good friend Ralf Albrecht for all our chats and discussions during our inter-institutional coffee breaks and of course for being a good friend.
- My former fellow student and good friend Dr. Lucca Kühner for many good discussions and his encouragement during my PhD.
- My former colleagues Dr. Joachim Krauth and Dr. Asa Asadollahbaik for the countless beer-and-burger evenings.
- All my current and former colleagues at PI4, who made the last years not only incredibly interesting but also incredibly fun. Especially the 9 group trips I had the pleasure of joining over the years will be in good memory.

Furthermore, I want to thank all my friends outside the institute for the distraction from my everyday life working on my PhD thesis. Especially, I want to thank Dr. David Weißhaupt, one of my best friends for many years and the best roommate one can think of, for all the years together in Stuttgart-Süd. My deepest thanks go to my parents and my entire family, who always supported and encouraged me during my studies and throughout my PhD. Without you all this would not have been possible, I am incredibly grateful for your support. And, of course, Claudi. There is no doubt the last three years have been the best years of my PhD. Without your support, encouragement, and patience this thesis would not have been possible. Thank you for everything.